# TWO PHASE FLOW VISUALIZATION IN EVAPORATOR TUBE BUNDLES USING EXPERIMENTAL AND NUMERICAL TECHNIQUES

by

JASON SCHLUP

B.S., Kansas State University, 2011

---

A THESIS

submitted in partial fulfillment of the
requirements for the degree

MASTER OF SCIENCE

Department of Mechanical and Nuclear Engineering
College of Engineering

KANSAS STATE UNIVERSITY
Manhattan, Kansas
2013

| Approved by: | Approved by: |
|---|---|
| Co-Major Professor | Co-Major Professor |
| Steven Eckels | Mohammad Hosni |

# Copyright

# Abstract

This research presents results from experimental and numerical investigations of two-phase flow pattern analysis in a staggered tube bundle. Shell-side boiling tube bundles are used in a variety of industries from nuclear power plants to industrial evaporators. Fluid flow patterns in tube bundles affect pressure drop, boiling characteristics, and tube vibration. R-134a was the working fluid in both the experimental and computational fluid dynamics (CFD) analysis for this research. Smooth and enhanced staggered tube bundles were studied experimentally using a 1.167 pitch to diameter ratio. The experimental tube bundles and CFD geometry consist of 20 tubes with five tubes per pass.

High speed video was recorded during the experimental bundle boiling. Bundle conditions ranged in mass fluxes from 10-35 $kg/m^2 \cdot s$ and inlet qualities from 0-70% with a fixed heat flux. Classification of the flow patterns from these videos was performed using flow pattern definitions from literature. Examples of smooth and enhanced bundle boiling high speed videos are given through still images. The flow patterns are plotted and compared with an existing flow pattern map. Good agreement was found for the enhanced tube bundle while large discrepancies exist for the smooth tube bundle.

The CFD simulations were performed without heat transfer with non-symmetrical boundary conditions at the side walls, simulating rectangular bundles used in this and other research. The two-phase volume of fluid method was used to construct vapor interfaces and measure vapor volume fraction. A probability density function technique was applied to the results to determine flow patterns from the simulations using statistical parameters. Flow patterns were plotted on an adiabatic flow pattern map from literature and excellent agreement is found between the two. The agreement between simulation results and experimental data from literature emphasizes the use of numerical techniques for tube bundle design.

# Table of Contents

# List of Figures

# List of Tables

# Nomenclature

**Roman Symbols**

D Diameter

P Tube pitch

**Abbreviations**

CFD Computational fluid dynamics

DNS Direct numerical simulation

DOV Direction of view

FOV Field of view

FPS Frames per second

LES Large-eddy simulation

LSF Level-set function

P/D Pitch-to-diameter ratio

PC Polycarbonate

PDF Probability density function

PFD Process flow diagram

PIV Particle image velocimetry

RANS Reynolds averaged Navier-Stokes

RNG Renormalized group

RSM Reynolds stress model

SRANS Steady Reynolds averaged Navier-Stokes

RTD Resistance temperature detectors

URANS Unsteady Reynolds averaged Navier-Stokes

SST Shear stress transport

VFD Variable-frequency drive

VI Virtual instrument

**Greek Symbols**

$\alpha$ Volume fraction

$\Delta$ Difference

$\epsilon_{ij}$ Dissipation of Reynolds stresses

$\Gamma$ Zero level-set

$\nu$ Specific volume

$\omega$ Specific turbulent dissipation

$\phi_{ij}$ Pressure strain from Reynolds stresses

$\rho$ Density

$\varepsilon$ Turbulent dissipation

$\varepsilon$ Void fraction

$\varphi$ Level-set function

**Subscripts**

$ave$ Average

$f$ Face value

$i$ Inlet

k Individual water channel

$lm$ Log mean condition

| | |
|---|---|
| $min$ | Minimum |
| $o$ | Outlet |
| $out$ | Outside |
| $PB$ | Preboiler |
| $q$ | Phase |
| $R$ | Refrigerant |
| $sat$ | Saturation condition |
| $TS$ | Test section |
| $W$ | Water |
| $x$ | X-component |
| $y$ | Y-component |
| $z$ | Z-component |

**Mathematical Symbols**

| | |
|---|---|
| $A$ | Area |
| $a$ | Acceleration |
| $c_p$ | Specific heat at constant pressure |
| $C_{ij}$ | Convection of Reynolds stresses |
| $C_{M3}$ | Coefficient of skewness |
| $C_{M4}$ | Coefficient of kurtosis |
| $D$ | Diameter |
| $d$ | Distance from interface |
| $D_{L,ij}$ | Molecular diffusion of Reynolds stresses |
| $D_{T,ij}$ | Turbulent diffusion of Reynolds stresses |
| $\mathbf{f}$ | Body force per unit mass |
| $F_b$ | Body force |
| $F_s$ | Surface force |
| $F_{ij}$ | Production of Reynolds stresses by system rotation |
| $G$ | Mass flux |
| $G_{ij}$ | Buoyancy production of Reynolds stresses |
| $i$ | Specific enthalpy |
| $k$ | Turbulent kinetic energy |
| $\ell$ | Turbulent length scale |
| $L$ | Length |
| $\dot{m}$ | Mass flow rate |
| $m$ | Mass |
| $p$ | Pressure |
| $P_{ij}$ | Production of Reynolds stresses |
| $q$ | Heat transfer rate |
| $q''$ | Heat flux |
| $R$ | Resistance |
| Re | Reynolds number |
| $S_{user}$ | Source terms of Reynolds stresses defined by user |
| $\overline{\overline{\tau}}$ | Shear stress tensor |
| $\tau$ | Shear stress |
| $T$ | Temperature |
| $t$ | Time |
| $\boldsymbol{u}$ | Velocity vector |
| $U$ | Overall heat transfer coefficient |
| $U$ | Volume flux, based on normal velocity |

| | | | |
|---|---|---|---|
| $u$ | Uncertainty | $v$ | Y-component of velocity |
| $u$ | X-component of velocity | $w$ | Z-component of velocity |
| $V$ | Volume | $x$ | Thermodynamic quality |

# Acknowledgments

This thesis could not have been possible without the support of my instructors, family, and friends. I would first like to acknowledge Dr. Steve Eckels, my co-advisor, who taught me throughout my undergraduate career and into my graduate schooling and offered to support me through this research. I would also like to thank Dr. Mohammad Hosni who co-advised this research and provided me access with the high speed visualization equipment, and Dr. Larry Glasgow for beginning my instruction on computational techniques and serving on my committee. I'd also like to thank Dr. Evraam Gorgy, who's Ph.D. dissertation did a significant amount of the initial construction and problem solving of the testing facility, Garrett Mann and Jacob Wagner for helping construct and troubleshoot the testing facility, and Eric Wagner for machining many of the experimental components.

Finally, I'd like to thank my family and friends. My parents taught me the importance of education, learning, exploring, and cooperating. My brother and sister provided a significant amount of support during the frustrating parts of this research. And finally, I'd like to thank my wife, who listened to many complaints of faulty equipment, slow testing days, and long nights while encouraging me to strive for the best results.

# Dedication

This work is dedicated to my family; beginning with my parents who instilled in me the desire to do my best and learn as much as possible, to my brother and sister who put me in my place when I needed it, and finally my wife, whose never-ending love, support, and encouragement motivated me through all difficult points of the past two years.

# Chapter 1

# Introduction

This document presents research done on experimental and numerical analysis of flow patterns in horizontal evaporator tube bundles under vertical cross-flow. The research was funded by the Institute for Environmental Research under the direction of Dr. Steve Eckels at Kansas State University.

## 1.1 Background

Evaporator tube bundles are seen throughout many industries, ranging from chemical processing plants, HVAC&R applications, to nuclear power plants. In many of these cases, the boiling fluid flows on the shell-side of the tube bundle with the primary purpose of removing heat from a secondary fluid. In the HVAC&R industry, evaporator tube bundles play an integral part in countless applications in residential, commercial, and industrial fields. The nuclear power industry relies on the boiling fluid to remove heat from fuel rods and to power turbines.

In these industries, the flow pattern characteristics can greatly affect the performance of a tube bundle. Through the last several decades, research has documented the flow pattern effects on pressure drop, heat transfer, and bundle dryout mechanism. Tube vibration is another important issues as the flow velocities can be quite large, and with improper bundle design, cause catastrophic mechanical failures through tube excitation or significantly increase power requirements for pumping the working fluid.

Recent research concerning flow pattern classification by measuring pressure drop and void fraction in a tube bundle have attempted to create flow pattern maps for bundle designs. The change of bundle pitch, tube type, working fluid, mass velocities, and many other parameters make creating a general flow pattern map difficult. The difficulty in creating a general flow pattern model causes expensive experimental tests to be conducted. These tests provide results for only one specific bundle design.

## 1.2 Significance of Research

The design and production of nearly any tube bundle can be very expensive. The cost includes testing of prototype units or the use of models based on extensive experimental results from decades of research. For many bundle properties, such as heat transfer coefficients and pressure drop, empirical models do an adequate job of modeling the bundle operating conditions. However, the influence of flow patterns on pressure drop and bundle vibration is not well modeled and has comparatively fewer experimental data sets to support empirical models.

The increasing amount of computational power in personal computers, clusters, and supercomputers has allowed for very detailed numerical simulations in a variety of fields. Adapting these techniques to the design of tube bundles could significantly reduce design costs and improve the understanding of the flow pattern dynamics in the bundle. As numerical simulations become more accurate with smaller mesh sizes and improved turbulence, heat and mass transfer, two phase flow and phase change modeling, the use of computational techniques will become crucial in designing tube bundles.

## 1.3 Objective of Research

There are two primary objectives to this research; 1) obtain an experimental data set of flow pattern observations and compares results with existing flow pattern maps, and 2) predict flow patterns in an evaporator tube bundle using CFD techniques.

These two objectives explore various operating conditions of an evaporator tube bundle. The diabatic experimental facility varies refrigerant mass flux and inlet vapor quality to produce different flow patterns at the observation point. The adiabatic numerical simulations documents vapor volume fractions at specific points in the tube bundle under various mass fluxes and inlet vapor qualities.

## 1.4 Scope of Research

This research focuses on one tube bundle design using two tube types and one refrigerant type. The two experimental tube bundles have a pitch to diameter ratio (P/D) of 1.167 using either smooth or enhanced tubes with the refrigerant R-134a as the working fluid. The bundle test section is rectangular with inactive half-rounds mounted to the insert plates to simulate a small portion of a much larger tube bundle. The tube outside diameter is 19.05 mm (0.75 in). The refrigerant is boiled at a saturation temperature of 4.4 °C (40 °F). A polycarbonate tube replaces one active tube in the bundle; this clear plastic tube allows visualization access to the inside of the bundle using a borescope and high speed camera.

The testing conditions for both bundles include mass fluxes at 10, 15, 20, 25, and 35 $kg/m^2 \cdot s$, a heat flux at the polycarbonate tube row of 20 $kW/m^2$, and a range of vapor qualities at the polycarbonate tube from 30-100%. The test matrix is completed for each bundle with high speed video recorded at a test condition. The video is analyzed and a flow pattern is determined according to definitions given in the literature. The resulting flow patterns are plotted on a flow pattern map and qualitative comparisons are made.

The numerical simulations studied use the same mass flux conditions as the experimental work. No heat transfer is analyzed in the simulations. Bundle inlet qualities from 10% to 82% are simulated. The computational fluid dynamics (CFD) flow patterns are characterized by a statistical method of the vapor volume fraction past a location in the simulation domain. The determined flow patterns are also plotted on a flow pattern map, and qualitative comparisons are once again made.

## 1.5 Outline of Document

This document consists of nine chapters and six appendices. Following this introduction chapter is a literature review on experimental flow pattern analysis and numerical simulations of tube bundles and topics related to the simulations performed in this work. Chapter 3 provides a facility description for the experimental portion of this research. Details on the test section, plumbing, and instrumentation is given here.

Chapter 4 contains the derivations of the governing equations for general fluid motion. These equations are then applied to CFD techniques. The extension of general fluid motion equations to CFD applications is built from years of research, so the models used in the CFD software are only briefly presented from the software documentation. An explanation of the simulation setup used for this work follows.

Chapter 5 provides the method of data reduction. This chapter explains how the recorded experimental measurements produce vapor quality and heat flux values. Uncertainty analysis is also given here for the appropriate measured and calculated values.

Chapters 6 and 7 present the results from the experimental flow visualization and CFD simulations, respectively. Each chapter details how the flow patterns are determined, give an example of the analysis method, and present the results on a flow pattern map. A brief qualitative comparison of the results concludes each chapter.

Following the presentation of the analysis techniques, Chapter 8 summarizes the findings of this research. In this chapter, the results from the experimental and numerical simulations are examined. Trends in the flow pattern map comparisons are also given, with recommendations on reconciling differences between the results of this research and existing flow pattern maps. Finally, suggestions for future research, directly following the current results, are proposed. Chapter 9 concludes the document and provides a summary of each chapter. The appendices at the end of this document provide dimensioned drawings of the test facility, pictures of the facility and equipment, properties of the instrumentation, complete results from the CFD simulation statistical analysis, and an example uncertainty

calculation file.

# Chapter 2

# Literature Review

## 2.1 Introduction

Flooded evaporators and tube bundles have been an emphasized research area for many years. Research on flooded evaporators dates back to Nukiyama's pool boiling work (Nukiyama, 1934) creating the boiling curve for saturated water. The pool boiling curve was created for saturated water at atmospheric pressure by controlling the power running through submerged wires. There are many factors that influence and change the boiling curve, including surface material and roughness, fluid properties, thermodynamic quality, and heat flux. Extensive work has been done exploring the effects of surface roughness which eventually led to the creation of enhanced tubes to control and optimize heat fluxes in shell side heat transfer.

This literature review will focus primarily on external boiling flow visualization in vertical cross-flow over tube bundles, which builds from early in-tube flows and in-line tube bundles. Due to the relatively low number of flow visualization results of R-134a boiling on staggered tube bundles, literature has been included summarizing many different visualization experiments and methods regardless of fluid type. In addition to a general overview on boiling flow visualization, literature covering void fraction, specific visualization techniques, and numerical analysis of flow patterns have also been included.

## 2.2 Void Fraction and Flow Patterns

Local void fraction measurements are now recognized as an important tool for flow pattern identification. However, acquiring void fraction measurements can be difficult and their use in flow pattern identification is relatively new. Many methods exist for measuring void fraction, including quick-close valve systems for volume average void fraction measurements and x-ray absorption, gamma ray attenuation, electrical resistivity probe, and optical probe systems for local void fraction measurements. In this section, a review of void fraction measurement techniques is presented while the following section reviews flow pattern identification with emphasis on incorporating void fraction measurements to obtain objective flow regimes.

### 2.2.1 Void Fraction Measurements for Flow Pattern Identification

One of the first attempts at objectively determining local void fraction in a two-phase flow was undertaken by Jones Jr. and Zuber (1975). Their experimental setup consisted of acrylic plates with porous stainless steel plates mounted at even intervals in the test section, resulting in a vertical rectangular test section. Air was injected either through the stainless steel plates with water injected through the bottom of the test section for bubbly flow, or vice versa for other flow pattern experiments. X-ray measurements of the void fraction were taken for flow velocities ranging from 0.0 to 37 $m/s$ (0.0 - 121.4 $ft/s$). The authors find that bubbly flow was generally uniform throughout their test section, annular flow contained ripples along the wall, while slug flow appeared to be a combination of bubbly and annular flow. They analyzed their results using probability density functions (PDFs) of the void fraction and found that bubbly flow consists of a single, high-valued peak at low void fractions and annular flow consists of a single, high-valued peak at high void fractions. Additionally, they described the appearance of the PDF typical of slug flow to be a combination of bubbly and annular flow, having peaks at both low and high void fractions. From these results, they conclude slug flow can be considered a transitional flow

from bubbly to annular conditions. The authors construct a flow pattern map based on their PDF measurements with liquid flux density as a function of void fraction.

Kondo and Nakajima (1980) used quick closing solenoid valves below their mixing section to determine void fraction in their tube bundle for an air-water two-phase mixture. This volume average void fraction was used to formulate a simple empirical void fraction model for their experimental results. The test section was a staggered equilateral triangular bundle with three different tube P/D ratios and six different number of tube rows. Their void fraction model in the test section agrees well with their experimental data in the bubbly, slug, and froth flow regimes. Additionally, they find that as the vapor superficial velocity increases, the void fraction inside the bundle also increases.

Although in-tube air-water flow was used in Vince and Lahey (1982), they employed a PDF method similar to Jones Jr. and Zuber (1975) and included an analysis of the void fraction PDF statistical moments. Using X-ray attenuation techniques, chordal average void fraction measurements were made in a 2.54 cm (1 in) diameter plexiglas tubes. 12800 instantaneous chordal average void fractions, at a sampling frequency of 200 Hz, were measured at each of six chordal locations for each test run. Coefficients of variance, skewness, and kurtosis were determined for the resulting PDFs of area and chordal average void fraction. The authors suggest using variance as a flow regime indicator, specifically a variance greater of 0.04 indicating slug flow in the pipe. A variance less than 0.04 indicates either bubbly or annular flow dependent on area average void fraction. The authors also mention the variance is independent of liquid superficial velocity, a conclusion many authors arrive at. A new flow pattern map was also developed based on the variance and observed flow regimes with many variance determined flow regimes agreeing with visual observations.

A quick closing valve technique with air-water mixtures was used by Schrage et al. (1987) to find volume average void fractions in their 27 row in-line tube bundle. The authors reported void fractions increase with increasing mass flow rates at a given quality and note that the homogeneous void fraction model significantly over predicts the void fraction at all

test conditions. A void fraction model is formed that fits a majority of their data within ±20%. Flow pattern identification was based on the flow pattern map presented in Grant and Chisholm (1979).

Dowlati et al. (1988) used a 10 row, in line, rectangular test section with an air-water mixture to find bundle average void fractions. Gamma ray densitometry was used to measure chordal void fractions above, below, and throughout the tube bundle. Volume average void fractions were obtained by averaging the chordal void fractions taken at four locations. Chordal void fraction values at various heights were found to be uniform for a given mass flow rate, with occasional sudden increases or decreases above and below the tube bundle. Volume average void fractions were found to be much lower than the homogeneous void fraction model predicts, similar to other authors results. The authors develop a void fraction model based on the Wallis parameter, $j_g^*$, that predict their entire set of data with a standard deviation of 0.052.

Hahne et al. (1990) used an optical probe within 6 row in-line and staggered tube bundles. Copper tubes were used to boil R11 using electrical heaters with P/D = 1.3 and 1.15. Saturated R11 at 1 bar and 23.31 °C (14.5 psi and 74.0 °F) was injected through the bottom of the rectangular test section. The optical probe, encased in a steel sheath, transmitted light from an emitter to the tube bundle. If the probe tip resided in liquid, the light signal continues through into the liquid. If the probe tip was in vapor, the light was reflected back to a recording station. The signal was integrated at 0.01 second intervals to determine local void fraction. The probe tip was positioned at 13 various vertical locations. They used a Fast Fourier Transformation analyzer to generate PDFs of the void fraction measurements. Their results indicate increasing local void fractions with heat flux and height inside the bundle but they record no slug or annular flow within the bundle. Their statistical analysis suggests classifications for slug and annular flow based on the coefficient of skewness, $C_{M3}$, and coefficient of kurtosis, $C_{M4}$, but instead of seeing these flow regimes, they find bubbles at the top of the tube bundle are distributed by a Gaussian curve in both quantity and size.

Ali et al. (1993) provides experimental results of flow patterns in a rectangular channel using air-water as their two-phase fluid and resistivity probes for void fraction measurements. The test channel width was no greater than 1.465 mm (0.058 in) with no obstructions in the flow path. The authors find local, cross-sectional averaged, and test section averaged void fractions. Using PDFs similar to Jones Jr. and Zuber (1975), the authors are able to find void fractions of their narrow-channel arrangement based on measurements taken at 2 kHz for 3 seconds. These flow patterns and instantaneous test section averaged void fraction are also determined with photographs. Flow pattern maps are created for their various experimental configurations from the PDF results. It is important to note their resistivity probes were mounted flush to the walls of the test section channel, thus reducing the influence of the probe on flow patterns.

Inside a 13 row in-line kettle reboiler model, Gebbie and Jensen (1997) measured void fraction values of boiling R113 at various row and column locations throughout the bundle. The horizontal tube bundle was composed of 75 electrically-heated brass alloy tubes with a length-to-diameter ratio of 10.6. The authors state this length-to-diameter ratio is large enough to neglect axial effects at the midplane of the bundle. Void fraction measurements were made using a hot-wire anemometer with a voltage level indicating the presence of either vapor or liquid at the probe tip. With this method, instantaneous void fractions are not acquired; instead, time average void fractions at each location are recorded. The authors use these measurements to determine where high void fraction regions reside throughout the reboiler model. Their results show little horizontal void fraction variation at the interstices between tubes on the same tube row, while significant horizontal void fraction variation exists between two vertically-adjacent tube rows. Additionally, void fractions generally increased with vertical position in the bundle with faster increasing void fraction rates at lower bundle positions.

Using two different tube bundles in an in-line and staggered bundle arrangement with

P/D = 1.47, Noghrehkar et al. (1999) measured local void fraction using a resistivity probe. Due to the resistive probe, their working fluid was an air-water mixture. Water entered the test section through an inlet nozzle and air was injected through two porous tubes at the bottom of the test section. Their resistivity probe was installed in the tube gap at the fifth or sixth tube row dependent on bundle geometry. The authors do note that changing the probe height did not appreciably change the PDFs obtained, indicating the flow pattern was uniform throughout the entire height of the bundle. Their experimental results generated two flow pattern maps with flow classification dependent on the PDFs of void fraction measurements. They compare their flow pattern maps with previous maps in literature and find significantly different results, but the authors mention previous flow pattern maps relied on subjective visual flow pattern identification only. Additionally, the authors also recognize the flow patterns near the shell wall may vary significantly from the flow deep in a bundle.

Aprin et al. (2007) also used an optical probe to take local void fraction measurements at the center of the tube bundle. Their experiments used three different hydrocarbons (propane, iso-butane, and n-pentane) as the working fluid, boiling from a bundle with P/D = 1.33. While the optical probe geometry is slightly different, the infrared light responds in a manner similar to Hahne et al. (1990). They are capable of sampling up to 5 kHz to allow for 6.4 s of data acquisition for two of the three hydrocarbons with longer data acquisition for the third hydrocarbon. A cross-correlation analysis was performed to determine an optimal $\Delta t$ for sample averaging, with a $\Delta t$ of 0.02 s deemed appropriate. Further information on the statistical moments of the PDFs is given, including important values of the third and fourth moment in determining flow pattern. They indicate a coefficient of skewness $C_{M3} <$ 0 indicates a large number of events at low values while $C_{M3} < 0$ indicates a large number of events at high values of the variable. Further, a coefficient of kurtosis, $C_{M4} > 3$ indicates a concentrated peak of events, $C_{M4} < 3$ indicates events spread through a larger range about a peak with $C_{M4} = 3$ indicates a Gaussian distribution of events.

Their resulting PDFs echo previous studies in that bubbly and annular flow show large peaks at low and high void fractions, respectively, and an intermediate, transitional region with peaks at each end representing slug flow. Investigation of their PDF results for bubbly, intermittent, and annular-dispersed flow shows that lower mass fluxes have a higher count of detected events at lower void fractions, indicating that increased mass flux causes bubbles to coalesce into large vapor structures more easily. Additionally, higher heat fluxes at constant mass fluxes generate higher bubble counts, meaning higher heat fluxes generates more vapor causing an earlier transition than adiabatic two-phase flow. Finally, flow pattern maps of their P/D ratio and working fluids are presented.

A more recent study by van Rooyen et al. (2012) explored a new visualization method for observing flow patterns as well as using laser signal attenuation and PDF techniques to determine void fraction for two different flow channels. In their air-water mixture instrumentation tests performed for an in-tube flow, they found their laser instrumentation PDF analysis results were in good agreement with the results of Jones Jr. and Zuber (1975), Vince and Lahey (1982), and Tutu (1982). However, the staggered tube bundle results with R-134a and R236fa showed little agreement with previous bundle research. Four rows of adiabatic tubes were installed above two passes of five water heated smooth copper tubes. In two of the adiabatic tubes, mirrors were installed to provide high-speed camera visualization and two other tubes provided access to the laser and photodiode system. PDF analysis of the laser signal showed that, for nearly all mass fluxes and vapor qualities tested, skewness and kurtosis were greater than zero and tended towards zero as vapor quality increased. The authors note their PDF analysis showed little correlation for various flow patterns, although a question is raised on the ability of their laser system to return void fraction similar to gamma-ray and X-ray techniques. As vapor quality approached 1.0, peaks at high voltages indicated a presence of large amounts of vapor. The author contributes this to onset of dry-out. The authors conclude their laser PDF analysis is therefore well suited to determining onset of dryout but does not accurately predict flow patterns.

Other researchers have presented similar methods for measuring void fraction using optical probes, electrical probes, and various non-invasive methods. These include Ali and Kawaji (1991), who used electrical probes between flat plates to measure void fractions resulting in PDFs assisting in flow pattern identification, Haquet and Gouirand (1995), who employed a bi-optical probe to find 150 void fraction measurements in a tube bundle channel between four neighboring tubes, Bertola (2003), who utilized an optical probe to create PDFs based on the phase density functions, and Ueno et al. (1997), who used a bi-optical probe for R123 boiling and an electrical probe for water boiling in a tube bundle to find void fractions and velocities.

For this work, the void fraction measurement method presented by Aprin et al. (2007) will be simulated using the numerical CFD techniques. Additionally, their $C_{M3}$ and $C_{M4}$ values for PDF analysis will also be used in classifying flow patterns from the CFD results.

### 2.2.2 Flow Pattern Definitions and Classification Techniques

In addition to their void fraction model, Kondo and Nakajima (1980) provide definitions for flow pattern identification in vertical cross-flow tube bundles. Their definitions for each flow pattern can be summarized as follows:

- Bubble—The height and width of a bubble is much smaller than the tube outside diameter. Bubbles are elliptical when their size is less than the interstitial spacing.
- Slug—The maximum height and width of a bubble is approximately equal to the tube pitch, with smaller sizes and individual bubbles still visible. Reverse flow of smaller bubbles is found trailing larger vapor slugs.
- Froth—The height and width of vapor regions span multiple pitch lengths. As air flow rates increase, an increase in the number of large bubbles is found.

While neither a definition nor pictures for spray flow are given, the authors mention that spray flow is detected with high air flow rates. Their definition of bubbly flow has

an extremely large diameter for many applications; typically, bubbles smaller than the gap between tubes can also be seen. Alternate definitions incorporating smaller bubble diameters are given in subsequent articles. Additionally, they mention that for spray flow, a liquid film forms around the tube surface, indicating that their classification of spray flow may also be considered annular flow. Finally, their classification is based purely on visual observation and no attempt was made to quantitatively determine the flow pattern.

Ulbrich and Mewes (1994) give similar definitions for the three predominant flow patterns in vertical cross-flow. Their definitions are summarized as:

- Bubble—Liquid phase is the continuous phase; discrete, elliptical bubbles are small and diameter is less than the interstitial spacing between tubes.
- Intermittent—Irregular, alternating motion of the liquid and gas. Liquid direction can alternate between upward and downward flow. Both large regions of liquid or vapor exist. Liquid regions can fill interstice or act as just film. Vapor regions can have heights greater than the tube diameter or small elliptical bubbles.
- Dispersed—Droplets carried by vapor, but liquid can flow as continuous units (intermittent-dispersed) or as a film wetting the tube walls (annular-dispersed).

The authors also specify that spray flow can exist but is difficult to achieve. They compare their flow pattern identification results with those from numerous other authors and create a general flow pattern map for bubbly and dispersed flow conditions in cross-flow tube bundles.

Analysis of the high-speed video recorded by van Rooyen et al. (2012) showed bubbly flow with bubbles much larger than the intertube spacing for vapor qualities greater than 0.1. Additionally, they identified that bubbles interact significantly with the tube bundle and are constricted in one dimension by the intertube spacing but not in the bundle axial direction. This led to coalescing of the bubbles into larger structures. An additional note about flow patterns changing throughout the bundle was also made. They found that their

flow patterns did not agree with maps presented by Noghrehkar et al. (1999) and Ulbrich and Mewes (1994). From their conclusions about broad flow pattern transition regions and their note about the limited mass flux range and single P/D ratio of their data limiting the applicability of a new flow pattern map, no new map was presented.

Other sources give definitions for flow patterns, such as Xu et al. (1998). Additionally, further work in identifying flow patterns has been performed by multiple investigators. One of the first flow pattern maps for tube bundles was proposed by Grant and Chisholm (1979) who created an experimental bundle allowing for upward, downward, horizontal flow of an air-water mixture. Two flow pattern maps, one each for vertical and horizontal flow, was produced based on superficial velocities. Tutu (1982) explored using PDFs of pressure drop to determine flow patterns in a vertical in-tube air-water two-phase mixture by analyzing the skewness of the pressure drop and the root mean square of a pressure ratio. Lu et al. (2010) investigated flow patterns in a vertical parallel flow tube bundle using high speed videography and propose flow pattern definitions and a new flow pattern map for their boiling tube bundle.

The flow pattern map presented by van Rooyen (2011) will be used to plot the experimental results from this research and for the verification of the numerical results presented later in this work. For the experimental results, the transition vapor velocities for their diabatic bundle will be used, while their adiabatic vapor velocity transition values will be used for the CFD results.

### 2.2.3 Visualization Techniques

A brief review of various visualization techniques is given below. A number of visualization techniques have been developed to assist in flow pattern identification in tube bundles; these methods include external visualization by creating the tube bundle out of transparent materials, and internal visualization using borescopes or fiberscopes.

Cornwell et al. (1980) constructed a 2.54 cm (1 in) thick kettle reboiler section with the tube ends against glass such that flow patterns between tubes could be viewed looking axially down the bundle. Flow patterns were captured using a video camera with paper discs flowing in the fluid. Burnside et al. (2005) also tested a thin slice kettle reboiler with a glass endplate, but their flow pattern identification was performed with spherical particles inserted into the flow and particle image velocimetry (PIV) techniques were used to capture the velocities in the bundle. Chen et al. (2005) use a sight glass next to their boiling tube and a high speed camera to capture the bubble growth and departure from the smooth and enhanced tube surfaces. Another thin section experiment was performed by Iwaki et al. (2005) using glass tubes 50 mm (1.97 in) in length and 15 mm (0.60 in) in outer diameter. Viewing from the end plate allowed for PIV measurements of the bubbly flow through the tube bundles.

For internal visualization, Mizutani et al. (2007) used a fiberscope running through one of their clear FEP tubes filled with water to capture subchannel flow patterns. Additional video was captured of overall flow patterns by situating their camera outside the test section, similar to the studies above. van Rooyen (2011) and van Rooyen et al. (2012) used a borescope inserted into one of their adiabatic tubes with a clear section situated deep in the bundle. Light was provided through the borescope to illuminate the flow leaving the boiling section of their tube bundle.

In this work, a flow visualization method similar to van Rooyen (2011) will be used. A borescope is inserted into the test section through a clear polycarbonate tube and light is provided through the same borescope. Video will be captured at various high frame rates and analyzed to determine the flow patterns in the boiling section of the tube bundle.

## 2.3 Numerical Techniques for Tube Bundle Analysis

The applicability of numerical techniques in fluid flows range from external flows around airfoils to internal flows in buildings, and more recently with the increased availability of

computing power, heat transfer and phase change problems. In this section, literature dealing with the numerical techniques used throughout this research will be reviewed, focusing mainly on CFD analysis of tube bundles, but also in turbulence modeling of small passages, multiphase modeling, and boiling.

### 2.3.1 Turbulence in Small Channels

In the first part of their research, Ridluan and Tokuhiro (2008a) explored different steady Reynolds averaged Navier-Stokes (SRANS) turbulence models in a staggered tube bundle for a single phase. Their 2D geometry of the region immediately surrounding a single tube included a quarter of the four nearest neighbor tubes consisting of 25000 total mesh elements. Periodic boundary conditions were applied at the inlet and outlet in the streamwise direction, as well as in the spanwise boundaries vertical direction. An inlet Reynolds number (Re) of $Re = 1.8 \times 10^4$ was used. The turbulence models used in the simulations were the $k - \varepsilon$, renormalized group (RNG) $k - \varepsilon$, shear stress transport (SST), and the Reynolds stress model (RSM). Their results showed that some velocities are accurately predicted by some turbulence models such as the $k - \varepsilon$ model, while other locations give very poor agreement with all turbulence models. Additionally, none of the SRANS methods adequately calculated Reynolds stresses when compared to experimental data sets.

In their article addressing unsteady RANS models (URANS), Ridluan and Tokuhiro (2008b) modeled the same flow region as described above for a staggered tube bundle of a single phase fluid with similar mesh size and inlet conditions. Their time-dependent solutions show much better agreement with averaged velocities, though they note that average velocity conclusions may be misleading for oscillating flows. They note that the trailing wake flow behind the cylinder oscillates with the RSM URANS model, and marginal to excellent agreement of Reynolds stresses were found at all measurement locations. The authors recommend the use of the RSM URANS model for simulating the turbulence found in their tube bundle.

An investigation of nuclear fuel rod cooling by Lávička (2011) implemented single phase flow heat transfer of the fluid surrounding a fuel rod with various spacers with a computational grid consisting of over 1 million cells. The fluid chosen is water with a flow rate of 2.5 $L/hr$ (0.088 $ft^3/hr$) (Re=45) and a heat flux from the fuel rod and spacer of 5 $kW/m^2$ (1585 $BTU/hrft^2$). The RSM turbulence model was used for the calculation and the transient simulation was run for 4000 total time steps. The parallel flow around the fuel rod was heated, and velocity and temperature plots at various cross sections were extracted to determine the difference between three different spacer designs.

A very recent study by Dehbi and Badreddine (2013) explored a steam generator of a PWR plant. Their study looked at tube side flows from an inlet mixing section where a hot fluid was injected towards the tube bundle. The primary goal of their analysis was comparing the results of a fully modeled tube bundle and a porous approximation of the tube flows, but it is of interest in this study as their channel flows had an internal diameter of 5 mm (0.17 in) and pitch of 17 mm (0.67 in). Their mesh consisted of 700000 cells after a grid independence study and the RSM turbulence model was used for its ability to handle complex recirculation flows in the inlet plenum. Temperature plots of the in-tube flow shows reasonable agreement between the full geometry and porous model while saving 50% computational power for the porous model. They do note that velocities for the porous model are an order of magnitude lower than the full geometry bundle, indicating that the current porous model treatment is unsatisfactory for a transient simulation as the time required to reach steady state would be significantly skewed.

Further work showing different turbulence models in subchannels include Benhamadouche and Laurence (2003) who explored large-eddy simulation (LES), coarse LES, and RANS turbulence models in a single-phase tube bundle. Their conclusions show reasonable agreement between the three for 3D flows but severe over-prediction of turbulent kinetic energy with the RANS model in 2D flows. Banerjee and Isaac (2003) used the standard and RNG $k-\varepsilon$ and RSM models to simulate 2D and 3D two-phase stratified channel flows using the vol-

ume of fluid (VOF), finding that the RNG $k-\varepsilon$ model produces the best overall results of the four methods. Yeh and Ferng (2012) used a 3D single-phase cross-flow staggered tube bundle with the RSM model, obtaining reasonable agreement with experimental results over a number of measured parameters. A tube bundle with air flowing over elliptic tubes was modeled by Ibrahim and Gomaa (2009). Using a $k-\varepsilon$ RNG turbulence model, they found the simulation results over-predicted various flow quantities for the elliptic bundle.

### 2.3.2 Multiphase CFD Simulations

Multiphase CFD simulations may or may not include heat transfer; in the case that they do not, there can be no mass transfer between the two phases and the energy equation is generally not solved. Many techniques exist for approaching multiphase simulations, including modeling the two-phases as a continuous-discrete pair with given droplet diameter for the discrete phase and VOF techniques that fully separate the two-phases. This section explores literature of CFD simulations containing two-phase flows with or without heat transfer. A special section on VOF techniques is given as well.

Using air as a continuous phase and water droplets as a discrete phase, Gan et al. (2000) modeled 24 rows of 10 mm (0.39 in) diameter tubes in a closed wet cooling tower and calculated the pressure drop across the tube bundle with Re=2677 and various tube P/D. They justify the use of a 2D model through the large ratio of length-to-width of the bundle and model half of the bundle with a symmetry boundary condition. Their findings on the effects of water droplets on pressure drop show that water falling through the heat exchanger section causes an increased pressure loss. Their simulations also show that flow bypass, a common occurrence in many tube bundles, reduces pressure loss. Their final conclusions show that introducing water droplets, changing the air-to-water flow ratio, and the arrangement of tubes causes changes in pressure drop, and that the simulations prove to be a useful modeling tool for creating new approximations for pressure drop.

Lo and Osman (2012) modeled a steady state, 3D 5x5 tube bundle with heat transfer,

simulating a nuclear fuel assembly with over 17 million mesh cells. The two-phases explored are water and steam, with a standard $k - \varepsilon$ turbulence model. Wall boiling was introduced and bubble diameter and nucleation site density, both of which are set from mathematical models. Even with a complex geometry including mixing vanes at various heights through the bundle and very high flow rates, temperatures, and pressures, the average void fraction at four levels was within 12% of experimental resuts. The authors note a few improvements to the study that could be addressed, such as turbulence following the vapor bubbles. Additionally, they stress the importance of experimental data in verifying the CFD models.

In another recent study, Krepper and Rzehak (2012) looked at two-phase vertical parallel flow through a subchannel of a pressurized water reactor (PWR) including heat transfer. Verification of the 1/8th subchannel was done by simulating 1/4 and an entire channel with similar results. Vertical flow was injected into the bottom of the subchannel with an initial heated length followed by an unheated section downstream. The liquid phase was considered the continuous phase, with the vapor phase represented as discrete bubbles with d = 0.6 mm and a nucleation site density was chosen such that the measured wall temperatures matched the simulation temperatures. Cross-section averaged void distributions were calculated using three different turbulence schemes, a SST model, a RSM model, and a $k - \omega$ RSM model. Void distributions, when compared to the experimental data, agreed more with the two RSM models than the SST model.

Many other studies of multiphase flow CFD simulations are available. These include Kim et al. (2008) who simulated steam-water two-phase parallel flow through a nuclear reactor tube bundle using the $k - \varepsilon$ turbulence model. Their simulation results provided pressure drop and velocities throughout the simulated bundle.

#### 2.3.2.1 Volume of Fluid Numerical Techniques

A survey of the literature published in the last few years reveals dozens of studies using VOF techniques. Many of these studies explore relatively simple flow geometries, such as flow through pipes and ducts, bubble and droplet flows or free surface flows. While only

the pipe flow is closely related with the current study, it is important to note that VOF methods in CFD analysis are increasing in popularity as computational power is more readily available and the results are promising. Very few published works have been presented on VOF methods applied to tube bundles or external flow around tubes. However, some research of internal tube flows have been done using the VOF method.

Ragab et al. (2008) studied the flow pattern transition in horizontal and inclined tubes for oil transport. Gas-liquid two-phase flow in a pipe of $D_{in} = 50.8$ mm (2 in), with varying gas and liquid inlet velocities and fixed outlet temperature and pressure. Their mesh consisted of up to 122892 mesh elements for the inclined pipe. Their results show favorable agreement between the simulation data and existing flow pattern maps and experimental data for the flow geometry. Images of the interface between the gas and liquid regions are also supplied, showing clear boundaries indicative of slug flow. There was no mention of using a laminar or turbulent scheme in their simulations.

In a study of nucleate boiling of HFE-7100, Kunkelmann and Stephan (2010) used a 2D VOF method with the Level-Set (LSF) function to simulate bubble growth from a flat plate. The use of the VOF and LS techniques was required as they were attempting to model evaporation from the interface. With a constant contact angle of 40°, they note an increase in heat transfer as the bubble contact line recedes back as it departs from the surface, in agreement with numerous studies yet contrary to their primary experimental comparison source. The discrepancy is attributed to a number of possible sources, including measurement techniques in the experimental work.

Very recently, Gebauer et al. (2013) used the VOF method to study condensation on smooth and enhanced single tubes and tube bundles of R-134a and propane. A smooth tube and two types of finned tubes, including high performance finned tubes, are modeled under adiabatic and diabatic condensation conditions. Half of the tube was modeled assuming symmetric condensation around the tube. The inlet boundary condition changed depending on the simulation, but liquid overfeed (simulating condensation from tubes above) and

vapor injection for the diabatic conditions were available. Initial simulations for smooth and enhanced tubes for condensate retention angle agreed well with analytical models and experimental data. For the condensation heat transfer models, they note greater than 21% deviation from experimental results for the high performance tubes, likely caused by the simplified geometry used in the simulation. Their bundle results show lower heat transfer coefficients than experimental results, likely caused by the symmetry assumptions for the liquid overfeed, leading to sheet mode drainage from the upper tubes where no sheet mode was found in their experimental results.

A few other studies using VOF techniques relating to this research have been reported. Banerjee and Isaac (2003) explored various turbulence models for stratified open channel flows, which could be implemented in a modified manner for flow at the top of a critically charged, non-submerged tube bundle. Andersson et al. (2004) simulated in-tube flow of air-water two-phase flow. Using the SST turbulence and VOF models, volume fraction contour plots show decent agreement with experimental results. Various in-tube flow patterns including slug and annular flow were detected.

## 2.4 Summary

Two sections of literature were reviewed in this chapter. It is clear that extensive research has been done on experimental tube bundles with a variety of testing conditions such as tube surface enhancement, adiabatic or diabatic conditions, bundle layout, fluid type, and thermodynamic conditions. Various types of measurement techniques for the identification of flow patterns have also been developed using both intrusive and non-intrusive methods. These techniques allow for flow pattern maps to be generated for the specified bundle design and conditions.

The numerical analysis of tube bundles has also been studied, though it has received increasing attention in recent years as computational power becomes more available. Various combinations of phase modeling, turbulence modeling, and energy transfer have been

explored with little consensus on the best techniques avaialble. It appears that individual problems have their own preferred set of models that generate the most favorable results. Because there is no accepted combination of simulation models that always generates accurate results, the need for further experimental datasets is evident. These data sets must be very precise and provide enough resolution to allow accurate verification of CFD simulation results.

# Chapter 3

# Facility Description

## 3.1 Introduction

The original purpose of this experimental facility was the determination of heat transfer coefficients on enhanced tubes with variable tube pitches (Gorgy, 2011). The facility test section has been modified to accommodate shell-side flow visualization inside the tube bundle and in the headspace above the tube bundle. The test section, described later in Section 3.2, is a shell-and-tube heat exchanger with water as the tube-side heating fluid and R-134a on the shell-side in vertical cross-flow over the enhanced tubes. The test section resides at the top of the testing facility.

The test facility for this work consists of five fluid loops; the refrigerant loop, the primary test section water loop, the primary preboiler water loop, the hot water loops for the test section and preboiler, and the glycol loop. The refrigerant loop circulates refrigerant through the test section, condenser, and preboiler. The preboiler acts to raise the quality of the entering sub-cooled refrigerant to the desired test section inlet quality. The primary test section water loop provides the water to the test section heat exchanger tubes, while the primary preboiler water loop circulates water between the preboiler and secondary preboiler heat exchanger. The secondary water loops transfer water from the hot water reservoir to the secondary heat exchangers. Finally, the glycol loop pumps glycol from the storage tank to the condenser and refrigerant storage tank.

After the test section description, each fluid loop will be described in detail in the following sections and subsections. Accompanying each loop description is a process flow diagram (PFD) of the pipes and equipment; a complete facility PFD is given in Appendix B. At the end of this chapter is a description of the instrumentation calibration procedure for the pressure and temperature sensors.

## 3.2 Test Section

The test section is a shell-and-tube heat exchanger configured as a rectangular pressure vessel simulating a small subset of tubes from a larger evaporator. The test section consists of five water channels (A through E); each channel passes through the test section four times resulting in a five tube, four pass shell-and-tube heat exchanger design. Refrigerant flows vertically in a cross-flow configuration on the shell-side of the test section. The inside dimensions of the test section are nominally 1 m (39.2 in) long with a width of 0.0984 m (3.875 in) and a height of 0.425 m (16.75 in). The aluminum insert plates are positioned inside the test section to allow various tube pitch configurations; in this work, a single fixed tube pitch-to-diameter ratio (P/D) of 1.167 is used. Figure 3.1 shows the internal dimensions of the test section. With this pitch-to-diameter ratio, the spacing between the insert plates is 0.0667 m (2.625 in). Figure 3.2 gives the dimension between the insert plates.

As stated previously, the test section is a rectangular heat exchanger. Flow symmetry is encouraged in a rectangular vessel by adding inactive half rounds on the sides of the test section. This is accomplished by securing solid half rounds to the insert plates beside the two-tube rows. The test section thus contains four passes of five tubes, simulating a larger evaporator by promoting flow symmetry at the rectangular walls. Figure 3.3 shows the tube bundle along with the inactive tubes, half rounds, and refrigerant inlet tees. A more complete description of the refrigerant inlet tees is provided in Section 3.2.3.

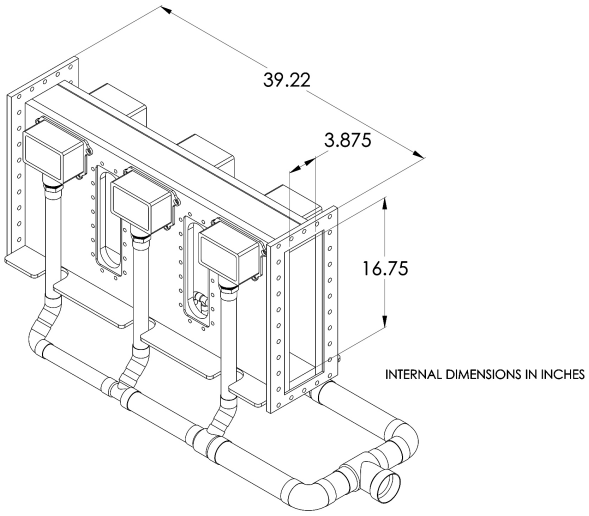


Figure 3.1: Internal dimensions of test section. Tube bundle, end plates, and instrumentation hidden for clarity.

### 3.2.1 Bundle Design

The test section can accommodate a number of tube pitch-to-diameter ratios. For this work, a single fixed P/D ratio of 1.167 has been selected. The tube outside diameter ($D_{out}$) is 19.05 mm (0.75 in). Given P/D and $D_{out}$, the spacing between tubes, or pitch (P), may be calculated as 22.22 mm (0.875 in). The enhanced tubes are mechanically rolled into the end plates using a tube expander. As shown in Figure 3.1, the active length of the test section and tube bundle is 1 m (39.2 in). Each enhanced tube has an active length of 1 m (39.2 in) with a plain length on each end of 0.158 m (6.25 in). This plain end allows for mechanical rolling into the end plates.

Figure 3.3 shows the tube layout. Detailed dimensions for the tube bundle and test section are given in Appendix A. Figure 3.3 also shows that one central water channel (called A2, described in Section 3.4.1 and Figure 3.10) has been replaced with a clear polycarbonate tube with $D_{out}$ of 19.05 mm (0.75 in) and an inside diameter ($D_{in}$) of 6.35 mm (0.25 in). This polycarbonate tube is used for visualization of flow patterns inside the tube bundle. A borescope with a 90° direction of view (DOV) is inserted into the polycarbonate tube and used to provide visual access to the tube bundle. Further details of the borescope and other

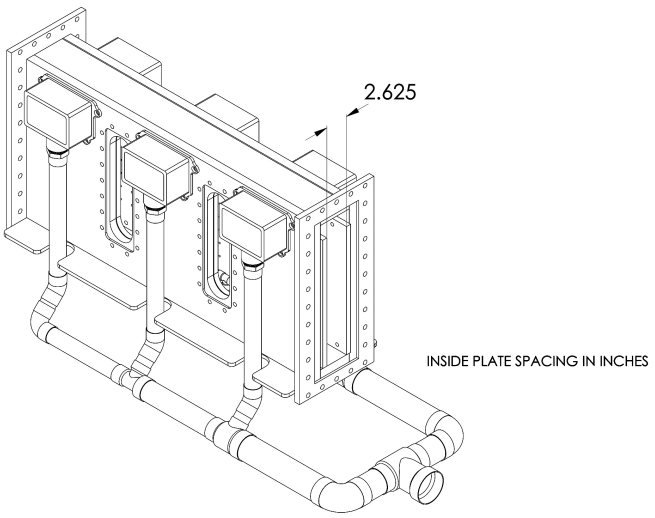


Figure 3.2: Spacing between insert plates. Tube bundle, end plates, and instrumentation hidden for clarity.

visualization equipment is available in Section 3.6.

### 3.2.2 Installation Procedure

Installation of the tube bundle is a multi-step process. The test section is first cleaned with isopropyl alcohol and paper towels to remove any large particulates such as copper or steel shavings that may be present from the tear-down of the previous bundle. Following the isopropyl alcohol cleaning, acetone is used to remove oil left from the vacuum pump during refrigerant recovery and from oil used to lubricate the cutter bit during the tube removal process.

With the test section cleaned, the end plate gaskets (3.175 mm (0.125 in) thick Garlok Gylon® Style 3504) are put in place, followed by the 25.4 mm (1 in) thick carbon steel end plates. The end plate bolts, washers, lock washers, and nuts are lightly secured. The enhanced tubes are cut to length and inserted into the end plate tube holes. Once all tube length dimensions are confirmed, the tubes and end plates are removed.

Construction begins by placing the insert plate assembly inside the test section. The insert assembly consists of both aluminum insert plates, spacers, half rounds, and the suction

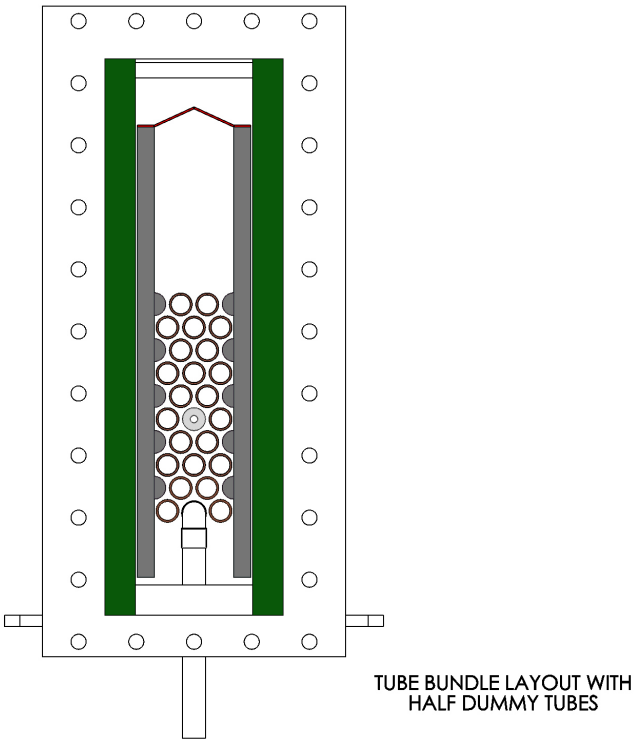


Figure 3.3: End view with tube bundle. half rounds are attached to the insert plates.

duct. Thin pieces of aluminum sheet metal are installed below the insert plates to position the insert plates properly in the bundle. Calipers are used to confirm dimensions from the bottom of the test section to the half tubes installed on the insert plates. Aluminum sheet metal pieces are used to shim the insert plates in position laterally, and calipers are used to measure the spacing between the insert plates and the spacing between the inside of the insert plates and inside of the test section.

Once the insert assembly is positioned in the test section, the refrigerant inlet tees are installed into the bottom of the test section. Swagelok fittings with nylon ferrules seal the refrigerant inlet tees. The inlet tees are aligned by placing the end plates and bottom four inactive copper tubes onto the test section and visually aligning the inlet tees parallel with the inactive smooth copper tubes. The end plates and inactive copper tubes are removed once the inlet tees are properly aligned and secured.

The sight glasses are inserted through the outside of the test section and are pressed flat

against the half rounds. If the dimensions measured previously are correct, the sight glasses should be aligned properly in the test section; if the sight glasses do not fit, they must be removed and realignment of the insert assembly is done. 3.175 mm (0.125 in) thick neoprene rubber strips, of equal width and height of the insert plates, are adhered to the ends of the insert plates with a small amount of vacuum grease. The grease allows the rubber to stay in place until the end plates are secured.

Two neoprene rubber O-rings, size 116, are inserted into the end plate O-ring grooves machined for the polycarbonate tube. Vacuum grease is used as a lubricant on the O-rings and polycarbonate tube. One end of the polycarbonate tube is inserted from the inner side of an end plate and pushed through approximately 0.127 m (5 in).

The end plate Gylon gaskets are put in place on both end plate flanges. The end plate with the polycarbonate tube installed is placed on the test section and lightly secured with bolts at the corners. The opposite end plate is positioned with the polycarbonate tube sliding through the O-rings. This method of installing the polycarbonate tube prevents major scratches to the surface of the tube. SAE Grade 8 bolts are installed in a star pattern to 122 N-m (90 ft-lb) of torque; increments of 20.3 to 40.7 N-m (15 to 20 ft-lb) is suggested to promote uniform stresses on the gasket around the end plate flange.

Before rolling the enhanced tubes into the test section, the bottom four inactive tubes are inserted, and the alignment of the inlet tees is confirmed. Access to the inlet tees is available through the sight glass openings if an inlet is misaligned. Once correct alignment of the inlet tees is confirmed, tubes are placed into the test section in groups of their length; the inactive tubes are installed first, followed by channels B and D, then channels C and E, and finishing with channel A. The channel naming scheme can be seen in Figure 3.10. The final positioning of the tubes is such that equal lengths of smooth tube are beyond either end plate. The mechanical tube expander pulls the tube through the end plate slightly which causes uneven end lengths. To offset this, the tubes are installed such that the pull of the expander forces the tubes into the correct position. For the smooth and enhanced tube

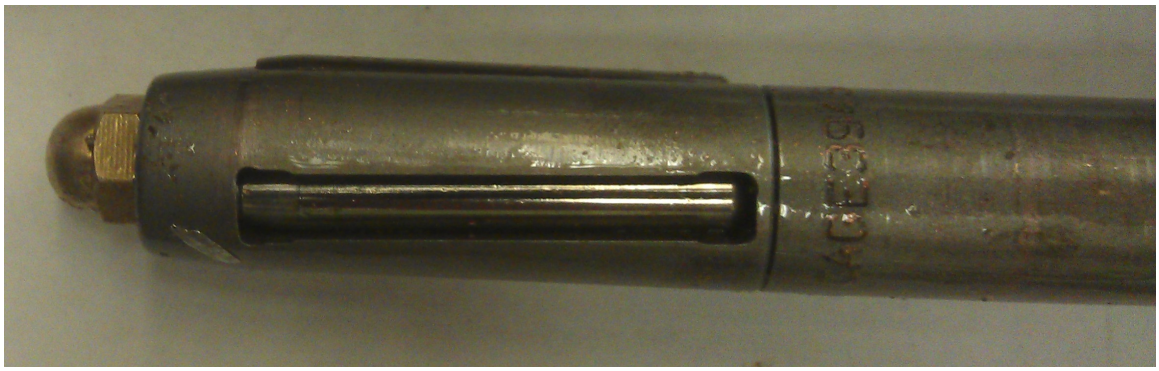

Figure 3.4: Tube expander device. Used for $D_{out}$ = 19.05 mm (0.75 in) and tube gauges between 18-22.

bundles, the tubes were pulled approximately 0.45 in. This dimension changes depending on expander speed and lubrication, so it is suggested that a new dimension is calculated for each bundle using a spare smooth tube and a single tube test section with spare flanges.

The tube expander used is pictured in Figure 3.4. This tube expander (Thomas C. Wilson, Expander No. 39453) is designated for 18-22 gauge tubes with a $D_{out}$ of 19.05 mm (0.75 in). The tubes are expanded into the end plate using a corded drill attached to the expander. A second person prevents excessive tube movement during installation by holding the opposite end of the tube using channel lock pliers. The corded drill should apply a slow, steady torque to the expander until significant resistance is felt in the drill. The corded drill is reversed to remove the expander. Oil is applied to the expander rollers after each tube.

Once all tubes are secured, all four side sight glasses and the end plate sight glass are installed. First, gaskets are applied to the test section box (1.587 mm (.0625 in) in thick Garlok Gylon® Style 3545) at the side sight glass locations (Papailias RS-OB 3x12) and the end plate sight glass location (Papailias RS 1x3). Then, the sight glasses are placed on the gaskets followed by neoprene rubber cushioning gaskets. Finally, the outer flanges are placed on the sight glass and secured with threaded studs. The end plate sight glass studs are tightened to 67.8 N-m (50 ft-lb) of torque in steps, suggested to be 33.9, 47.4, and 67.8 N-m (25, 35, and 50 ft-lb). The side sight glass studs are tightened to 67.8 N-m (50 ft-lb) of torque in increments of 6.8 N-m (5 ft-lb). All test section refrigerant instrumentation

is installed to seal the system (one thermistor at each tube pass, one pressure transducer assembly at each tube pass, refrigerant outlet thermistor, outlet pressure transducer, and pressure relief valve).

Leak checking is performed after securing the tubes, Swagelok fittings, and sight glasses. The system is filled with nitrogen to 206 kPa (30 psi), followed by recording pressure and temperature using the data acquisition system system. A system leak rate of 5 Pa/min (7.25 $\times$ $10^{-4}$ psi/min) or less is desirable. Large leaks are found using a simple bubble solution sprayed onto sealing surfaces. Small leaks require replacing the nitrogen with refrigerant by returning the system to a vacuum state and introducing a small amount of refrigerant. A portable refrigerant leak detector (Bacharach H-10PM) is used for smaller leaks not detectable with the bubble solution. After monitoring for a sufficient amount of time to detect leaks (some leaks are evident immediately while some leaks require multiple hours of monitoring) steps are taken to seal any leaks. Further tightening of the sight glasses or expanding of the tubes may be necessary; it is important to not overtighten the sight glasses to prevent fractures and overexpanding the tubes to prevent end plate deformation.

Copper tube fittings are placed on the enhanced tubes to dry-fit and align all water-side plumbing. All fittings must be sanded down and free of any solder remaining from previous use. The dry-fitting ensures all parts properly align and allow the installer to cut inlet and outlet tubing to length. The fittings must accommodate any camera equipment. The water channels are plumbed from the inlet at the bottom of the test section with the outlet at the top. Once the dry-fitting is complete, all instrumentation is removed from the test section.

Before soldering the fittings, the polycarbonate tube must be removed from the end plate being soldered. The polycarbonate tube is lightly lubricated with vacuum grease and pushed through the end plate so that one free end is hanging inside the test section. Soldering flux is applied to the sealing surfaces of the copper fittings and enhanced tubes; a logical order should be followed while installing the fittings. It was easiest for this installation to install the fittings from bottom to top, and from the inside to the outside of the tube bundle. MAPP

gas torches were used to solder the joints with silver solder. The refrigerant instrumentation is replaced and all water side instrumentation is installed; the water instrumentation includes five thermistors at the inlet, five thermistors at the outlet, two thermistors at channels D2 inlet and E2 inlet, two thermistors at channels D3 inlet and E3 inlet, five thermistors at pass 4 inlet, and four pressure transducers at the inlet and outlet of passes 1 and 4. Details of the instrumentation is provided in Section 3.2.4.

A leak check is performed on both the refrigerant and water sides. Leak checking of the refrigerant is done as described previously Water is filled through a riser upstream of the primary water loop pump and the pump speed is slowly increased until a leak is found. If a leak is found, the system must be drained of water so that the leaking fitting can be removed, cleaned, refluxed, and resoldered. This procedure is continued until the primary water loop pump is at full power with no detectable leaks.

### 3.2.3 Fluid Path and Distribution

Refrigerant enters the test section at the bottom of the tube bundle. The refrigerant inlet consists of four copper tees directing the flow downward. The refrigerant impacts the bottom face plate of the test section before returning to flow upward into the tube bundle. The bottom four tubes in the bundle are adiabatic smooth tubes to promote even flow distribution. As the refrigerant rises through the bundle, it boils and leaves the bundle as either a two-phase fluid or as a saturated vapor, depending on operating conditions. The refrigerant passes through the perforated suction duct mounted to the aluminum insert plates and exits the test section through the outlets. Once the refrigerant leaves the test section, it continues to flow towards the condenser and enters the test facility refrigerant loop (see Section 3.3 for details).

The test section water is fed into the bottom of the bundle. Water enters all five active tubes, listed as channel A1 through E1, and continues to flow through the enhanced tubes. At the inlet of pass two, channels B-E continue to flow through the test section. However,

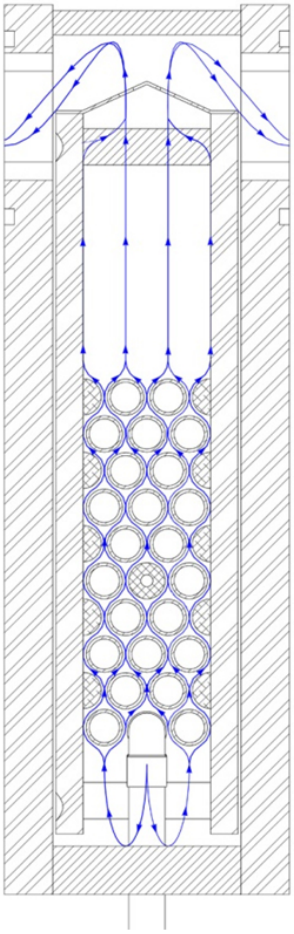

Figure 3.5: Diagram of the refrigerant flow path through the test section. Refrigerant enters through the downward facing tees at the bottom and exits through the suction duct and outlets.

due to the polycarbonate tube, pass A2 cannot flow through the test section. To ensure all water is traveling through the test section in the same direction in passes 3 and 4, pass A2 flows on the outside of the test section. Once all water channels exit the test section at the outlet of pass 4, the flow reunites into one larger diameter copper tube and flows to the rest of the test facility primary water loop (see Section 3.4.1 for details).

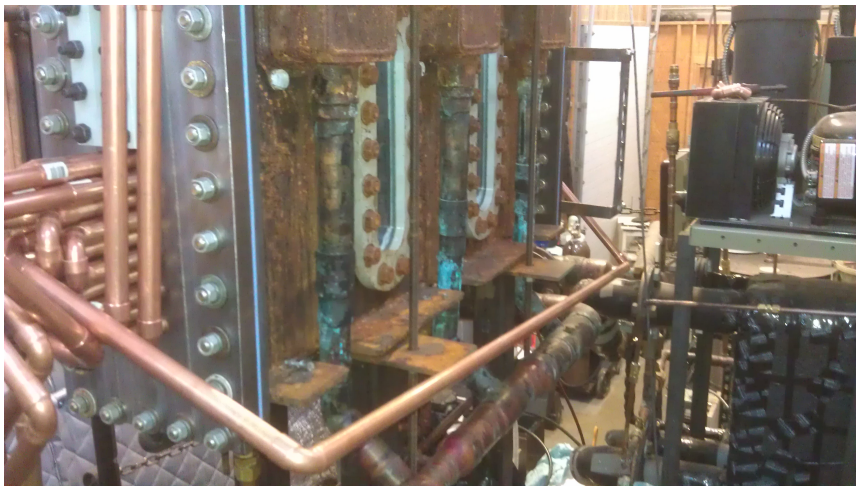

Figure 3.6: Picture of water channel A2 passing the outside of the test section. Picture is of dry-fitting stage with no insulation for clarity.

### 3.2.4 Test Section Instrumentation

Instrumentation throughout the test section consists of thermistors, resistance temperature detectors (RTDs) and pressure transducers. Both the refrigerant flow path and the water flow path have temperature and pressure instrumentation at various points.

#### 3.2.4.1 Test Section Refrigerant Instrumentation

Instrumentation on the refrigerant loop in the test section consists of pressure transducers, RTDs, and thermistors. At each tube row, temperatures and pressures are recorded. The half tube grooves, shown in Figure 3.7 allow temperature and pressure measurements to be made deep in the bundle. Each of these tube row pressure measurements are made with a 0-517.1 kPa (0-75 PSI) range pressure transducer (Viatran 245AKA), while the tube row refrigerant temperatures are measured using 100 Ω RTDs. Pressure transducers (Viatran 245AKA) and thermistors (Measurement Specialties 55036) measure the outlet refrigerant vapor conditions. Figure 3.8 shows a model of the refrigeration instrumentation.

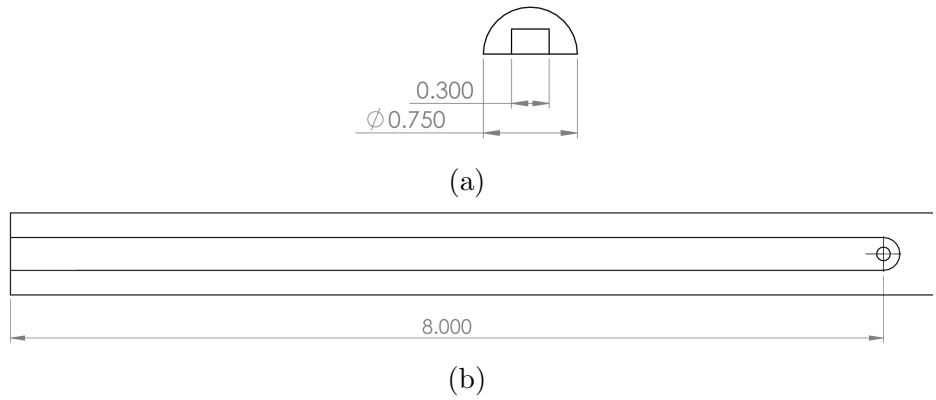


Figure 3.7: Groove dimensions for the half tubes looking at the (a) end view, (b) side view. Grooves in the half tubes allow thermistor and pressure transducer access to the tube bundle. Not to scale.

#### 3.2.4.2 Water Test Section Instrumentation

The water instrumentation in the test section tubes also consists of pressure transducers and thermistors. Pressure measurements are taken at the following locations: channel A1 inlet, channel A1 outlet, channel A4 inlet, and channel A4 outlet. Pressure transducers (Viatran 245ARA) with a range of 0-2068.4 kPa (0-300 PSI) are used at the A1 inlet and A1 outlet locations, while pressure transducers with a range of 0-1034.2 kpa (0-150 PSI) (Viatran 245ANA) are used at the A4 inlet and A4 outlet locations.

Temperatures are taken at the bundle inlet of every channel ($T_{W,i}$), the inlet of every channel at pass 4 ($T_{W,4i}$), and the bundle outlet of every channel ($T_{W,o}$). Additionally, inlet temperatures are taken at channel D2 ($T_{W,D2i}$), E2 ($T_{W,E2i}$), D3 ($T_{W,D3i}$), and E3 ($T_{W,E3i}$) for quality calculations at the polycarbonate tube row. These temperatures are measured using thermistors with a range of up to 200 °C (Measurement Specialties 55036). Temperature access is achieved by using Swagelok fittings brazed to the tubes at the end of each pass.

## 3.3 Refrigeration Loop

A PFD of the refrigeration loop is given in Figure 3.9. Subcooled liquid refrigerant is pumped through the facility using a magnetic-drive pump, E-4 in Figure 3.9 (Liquiflo 39R).

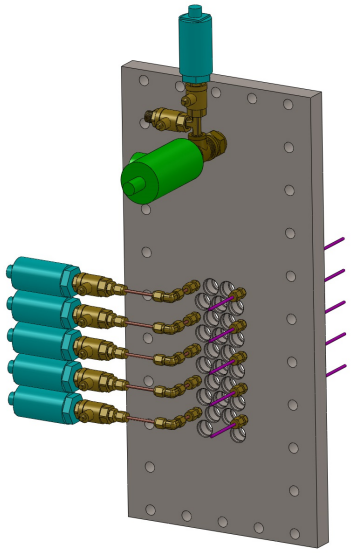

Figure 3.8: CAD model of the test section refrigerant instrumentation. Thermistors (pink), pressure transducers (blue), and pressure relief (green) are shown mounted to end plate.

This pump has a maximum flow rate of 57.0 LPM (15.1 GPM) with a maximum operating pressure of 1551 kPa (225 PSI) and minimum operating temperature of -40 °C (-40 °F). The refrigerant pump is controlled with the LabVIEW virtual instrument software (VI) on the facility computer, which sends its signal to a variable-frequency drive (VFD) (Dayton AC Inverter 3HX73). Refrigerant leaves the pump and passes through a filter (Parker Refrigeration Filter Drier 407G) before passing through a Coriolis flow meter (Micro Motion ELITE CMF050M). This flow meter, I-1, allows for flow rates up to 113.3 kg/s (4.17 lb/s) with low uncertainties of ±0.10% of the flow reading.

Downstream of the Coriolis flow meter is the preboiler, E-5. The preboiler is a water-heated shell-and-tube heat exchanger where refrigerant flows on the shell-side of the heat exchanger. The preboiler water loop will be described later in Section 3.4.2. Following the preboiler, the refrigerant passes through a ball valve, V-18, and then enters the test section. Details of the test section flow path can be found in Section 3.2.3.

Once the refrigerant exits the test section as a two-phase mixture or saturated vapor , the flow passes into the condenser, E-1 (FlatPlate C60). The condenser has a capacity of

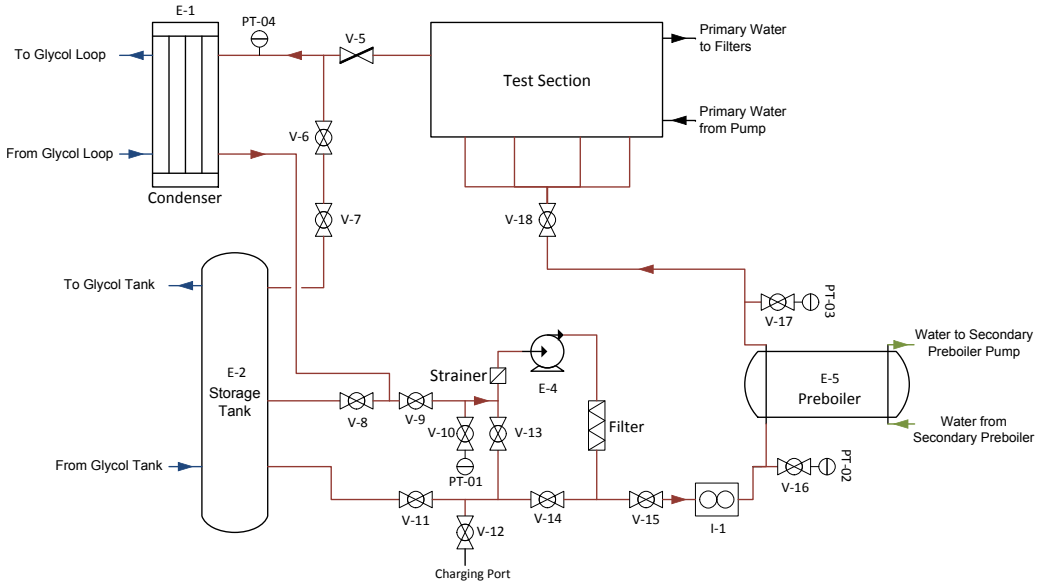


Figure 3.9: Refrigeration loop PFD. Pumps, filters, valves, and other equipment are labeled for reference.

211 kW (60 ton refrigeration) with a heat transfer area of 14.4 $m^2$ (155 $ft^2$). The cooling fluid used in the condenser is a 50/50 water-glycol mixture. The water-glycol mixture is supplied from an on-site storage tank, and the entire glycol loop is discussed in more detail in Section 3.5. The refrigerant leaves the condenser as a subcooled liquid and travels downward to a strainer (Parker). Downstream of the strainer, the refrigerant returns to the pump. Other valves shown in Figure 3.9 are used to add or remove refrigerant from the system. Multiple pressure transducers, RTDs, and thermistors are used in the monitoring and recording of the refrigeration loop conditions. The preboiler inlet temperature and pressure are measured using a pressure transducer (Viatran 245AKA) with an operating range of 0-517.1 kPa (0-75 PSI) and a 30,000 Ω thermistor, PT-02, shown in Figure 3.9. At the preboiler outlet, pressure and temperature of the two-phase refrigerant are measured using a similar pressure transducer (Viatran 245AKA) and a 1000 Ω RTD, PT-03.

Instrumentation on the refrigerant side of the test section is discussed in Section 3.2.4.1. Downstream of the test section, the condenser inlet temperature is measured using a 1000 Ω RTD. The refrigerant pump inlet pressure and temperature are measured using a pressure

transducer (Viatran 245ARA-DH) with an operating pressure of 0-689.5 kPa (0-100 PSI) and a 1000 Ω RTD, PT-01.

## 3.4 Water Loops

There are multiple water loops throughout the test facility. These water loops are the primary test section water loop, the preboiler water loops, and the hot water loop. The following sections will describe the individual water loops and the instrumentation and equipment in each loop.

### 3.4.1 Test Section Primary Loop

The main feature of the test section primary water loop is the five water channels through the test section. The water approaches the bundle in one larger diameter pipe and splits into five channels before entering the test section; these channels are labeled A through E. Each channel passes through the bundle four times and are labeled 1-4. The channel and pass labeling can be seen in Figure 3.10. Just prior to the primary water loop pump, all five channels merge back into one pipe.

Figure 3.11 shows a PFD of the primary water loop. The primary water loop is driven by a pump (ITT A-C Type 2000), E-17, capable of 125 GPM. This pump is controlled through the VI and a VFD (Dayton AC Inverter 1LNF1). As the water leaves the pump, it rises up to the test section and splits into five separate copper tubes, one for each channel of the test section. The water is fed into the test section from the bottom of the bundle (pass 1 in Figure 3.10) and exits the top of the bundle through pass 4 in Figure 3.10. As the water enters pass 2 of the bundle, channel A is rerouted outside of the bundle because no water flows through the polycarbonate tube. The rerouting of channel A allows all five channels of the bundle to enter the test section flowing in the same direction at every pass.

Water leaves the bundle at the outlet of pass 4 and travels downward in separate copper tubes. Downstream of the test section, channels B-E have separate gate valves, V-26, that

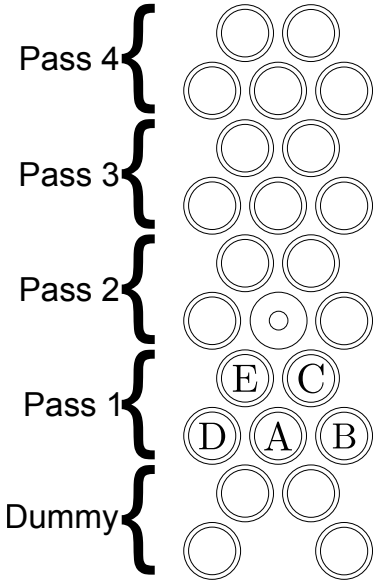


Figure 3.10: Water pass labels, looking from the inlet/outlet side of the test section. Water inlet is pass 1, water outlet is pass 4.

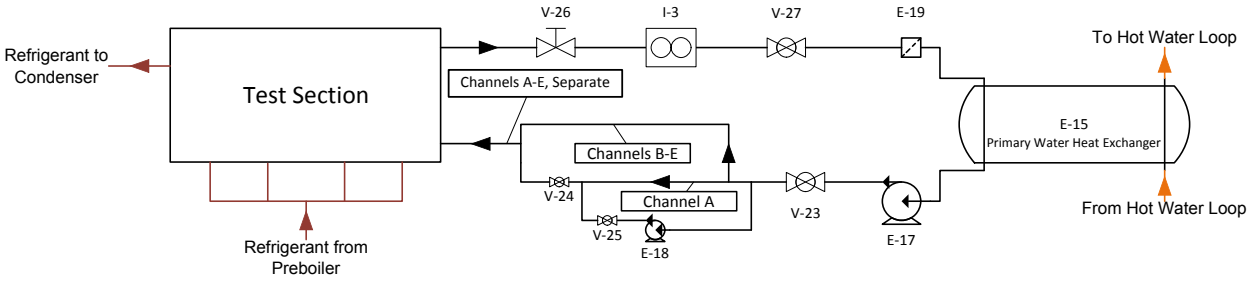


Figure 3.11: Primary water loop PFD. Pumps, filters, valves, and other equipment are labeled for reference.

control individual flow rates to ensure uniform heat transfer in each channel. Channel A's control valve, V-24, is located upstream of the test section. Additionally, each channel has its own Coriolis mass flow meter (Micro Motion ELITE CMF025), I-3, directly downstream of the gate valves. These Coriolis flow meters have a maximum flow rate of 2180 kg/h (79.9 lb/min) and an uncertainty of $\pm 0.10\%$ of the reading.

Downstream of the mass flow meters, the five channels merge into a single copper tube and flow through a set of filters, E-19, in a stainless steel housing, and finally to the primary water heat exchanger, E-15. This water-water shell-and-tube heat exchanger is heated with

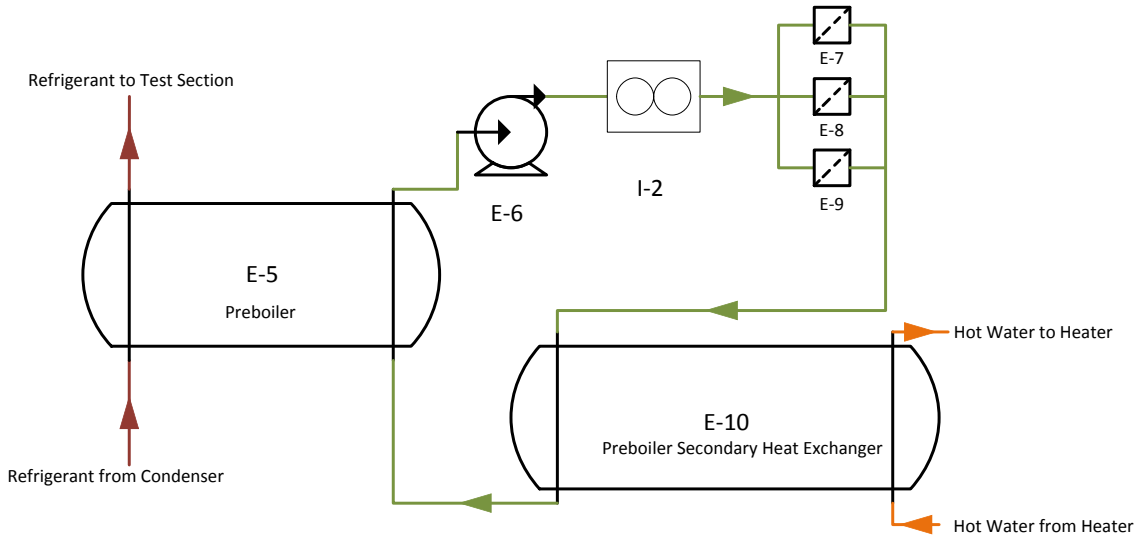


Figure 3.12: Primary preboiler water loop PFD. Pumps, filters, valves, and other equipment are labeled for reference.

water from the hot water loop (see Section 3.4.4 for information on the hot water loop) to reheat the test section water flowing on the tube-side of the heat exchanger. After leaving the primary water heat exchanger, the water returns to the primary water pump.

### 3.4.2 Primary Preboiler Loop

Figure 3.12 shows a PFD of the primary preboiler water loop. As stated in Section 3.3, the preboiler is a water-heated shell-and-tube heat exchanger. The primary preboiler water is circulated with a pump (Goulds 3BF 1H2C0), E-6, into a Coriolis flow meter (Micro Motion ELITE CMF100 ), I-2. The pump is controlled through the VI, which sends a signal to a VFD (Dayton AC Inverter 1KBR5). Downstream of the flow meter are three filters, E-7, E-8, and E-9, that remove particulates in the water loop. After the filters, the water flows into the secondary preboiler heat exchanger, E-10. The preboiler water passes through the shell-side of the water-water secondary preboiler heat exchanger and returns to the primary preboiler. The heating fluid in the secondary preboiler is the secondary preboiler water loop, which is discussed in more detail in Section 3.4.3.

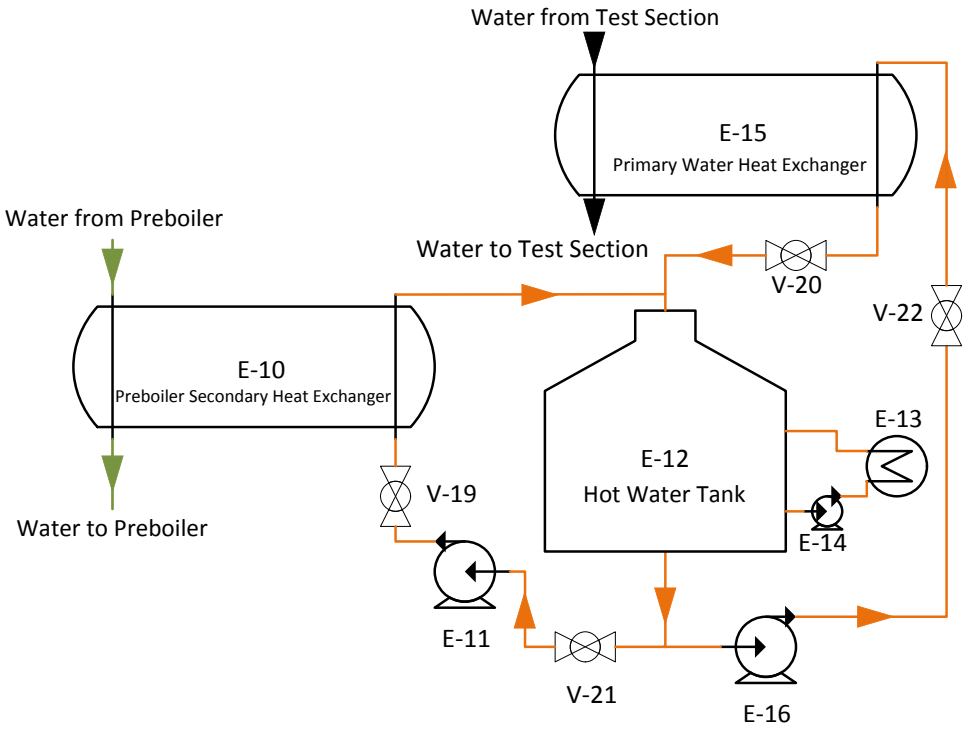


Figure 3.13: Hot water loop PFD. Pumps, valves, and other equipment are labeled for reference.

### 3.4.3 Secondary Preboiler Loop

The secondary preboiler loop acts to reheat the water in the primary preboiler loop. Hot water is pumped, by pump E-11 in Figure 3.13, from the hot water tank to the secondary preboiler heat exchanger, E-10 in Figure 3.12. In the secondary preboiler, water from the primary preboiler loop flows through the shell-side of the heat exchanger with hot water flowing on the tube-side of the heat exchanger. This water path is part of the hot water loop discussed in Section 3.4.4.

### 3.4.4 Hot Water Loop

A PFD of the hot water loop is shown in Figure 3.13. Hot water is supplied to the system by a 450.5 L (119 gal) water heater (American Standard ST-120-AS), E-12. The hot water tank has a temperature controller (Barber-Colman 7SC) to monitor and control the hot water temperature. Hot water is pumped from the tank towards the facility using

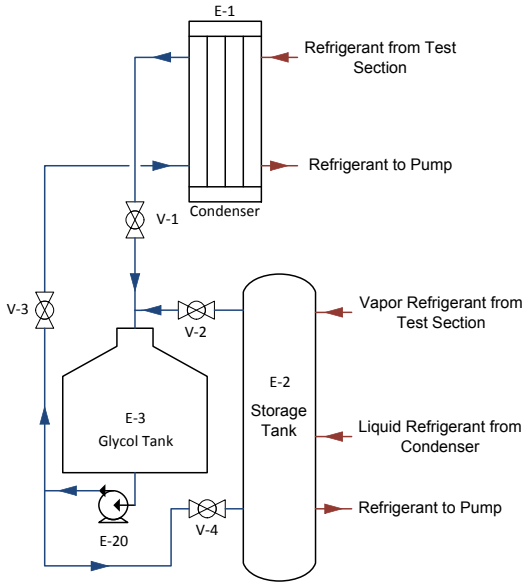


Figure 3.14: Glycol loop PFD. Pumps, filters, valves, and other equipment are labeled for reference.

two pumps: the first pump (Goulds 3BF1H2C0), E-11, supplies the secondary preboiler heat exchanger with hot water while the other pump (Goulds 3BF1H2C0), E-16, supplies the test section primary water heat exchanger. Downstream of each of these pumps is are gate valves, V-19 and V-22 respectively, providing flow control for the heat exchangers. The pump upstream of the secondary preboiler is controlled using a circuit breaker while the pump upstream of the primary water heat exchanger is controlled by a VFD (Magnetek GPD315). The hot water exits these two heat exchangers and returns to the hot water tank. Water is circulated inside the tank using a pump (Amtrol PCE300RF), E-13, controlled by a breaker.

## 3.5 Glycol Loop

A PFD of the glycol loop is shown in Figure 3.14. A 50/50 water-glycol mixture is supplied from a large storage tank, E-3, and pumped to the system by a 10 HP centrifugal pump, E-20. This pump is controlled through the VI, which sends a signal to a VFD (Magnetek GPD506). The glycol mixture flows through the refrigerant condenser, E-1, and

returns the refrigerant to a subcooled state. Three methods control the amount of heat transfer that occurs the condenser: the pump speed can be changed through the VI, a valve upstream of the condenser, V-1, on the glycol line can restrict the glycol flow into the condenser, and the glycol tank temperature set point can be changed. For a majority of the test conditions, the temperature of the glycol was adjusted at the chiller and changing the pump speed was the primary method of adjusting the heat transfer in the condenser.

## 3.6 Flow Visualization System

The visualization equipment used with this experimental facility include a high speed camera, borescope, and laptop computer. The high speed camera (Photron FASTCAM SA5) records video at multiple frame rates from 1000 to 3000 frames per second (FPS) with a resolution of 512x512 pixels. Attached to the high speed camera is a borescope (Hawkeye Pro Slim PS22-NVK). The borescope includes a 90°mirror tube that allows viewing of the tube bundle in any direction. A fiber optic cable provides light to the borescope from a halogen lamp (Thorlabs OSL1).

The borescope is inserted through the polycarbonate tube; the end of the mirror tube is approximately 12 inches inside the tube bundle, placing the mirror near the first side sight glass. The mirror tube is rotated such that the borescope views directly to the side (viewing water channel D), or at an upward angle (viewing water channel E). These positions are visible in Figure 3.15. The black lines in Figure 3.15 represent the borescope's 42° field of view (FOV).

## 3.7 Data Acquisition System

The data acquisition system contains two main components; a data acquisition switch and multimeter (Agilent 34980A Multifunction Switch) and a desktop computer. The switch contains three cards with 40 channels that can be connected to the multimeter. The unit communicates with the desktop computer through a USB cable. Data acquisition is done

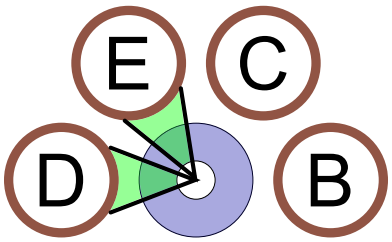


Figure 3.15: Diagram of the borescope mirror tube rotation inside the tube bundle. Borescope has a 42° FOV.

using National Instruments' LabVIEW 8.5 software. Thermistors, RTDs, pressure transducers, and Coriolis flow meters are connected to the data acquisition switch for a total of 51 measurements. The LabVIEW VI records data every 20 seconds for 5 minutes and writes the raw measurements (voltage, resistance, and frequency), calibrated data, and VI calculations (such as qualities and Reynolds numbers) to comma separated values (.csv) files.

## 3.8 Instrument Calibration Procedure

The thermistors, RTDs, and pressure transducers throughout the entire test facility were calibrated prior to the start of the experimental data collection. The temperature sensors were calibrated using a constant temperature bath (Fluke 7321 Deep-Well Compact Bath), which itself is calibrated yearly to reference thermistors, and the pressure transducers were calibrated using a deadweight tester (Amtek RK-200).

The temperature sensors were immersed in water with the bath temperature fixed at 4 °C. 120 data points were collected at each temperature setting, with the bath traversing a range from 4-40 °C. Raw resistance measurements were recorded using LabVIEW and exported in a .csv file. Calibration was done using a least-squares regression of the resistances and set temperatures using a calibration equation. For thermistors, the calibration equation was

$$T = (A + Bln(R) + Cln(R)^2 + Dln(R)^3)^{-1}(1 \times 10^{25}) - 273.15 \tag{3.1}$$

For the RTD sensors, the calibration equation was

$$T = A + B(R) + C(R)^2 + D(R)^3 + E(R)^4 \tag{3.2}$$

For both Equations (3.1) and (3.2), the sum of the errors between the calculated and expected temperatures were minimized by changing the calibration coefficients.

The pressure transducers were calibrated in groups of like-range. Each pressure transducer was attached to a manifold connected to the outlet of the deadweight tester. Nitrogen was used to pressurize the system. Weights were applied to the deadweight tester providing increments of 34.5 kPa (5 PSI) for pressure transducers with a range 0-517.1 kPa (0-75 PSI), 68.9 kPa (10 PSI) increments for pressure transducers with a range 0-1034.2 kPa (0-150 PSI), and 68.9 kPa (10 PSI) increments for pressure transducers with a range 0-2068.4 kPa (0-300 PSI). Due to the number of weights available, the maximum pressure calibrated was 1034.2 kPa (150 PSI).

Around 40 pressure readings were taken at each pressure level and voltage values were recorded. The voltage values were then calibrated using the equation

$$p = A + B(V) \tag{3.3}$$

A standard linear least squares regression was performed for each pressure transducer.

The coefficients found from calibration were then used in the LabVIEW software to convert resistance and voltage measurements to temperatures and pressures prior to LabVIEW writing the data to a file. Thus, files containing both raw and calibrated data were recorded.

## 3.9 Summary

This chapter described the facility used to acquire flow visualization inside an evaporator tube bundle with a tube P/D of 1.167. The 19 active copper tubes are arranged in a rotated equilateral triangular arrangement with tube A2 replaced with a clear polycarbonate tube for visualization access.

Temperatures, pressures, and fluid flow rates are monitored and recorded throughout the facility, allowing for precise control of test conditions. The test section and preboiler water

loops are reheated using hot water supplied from a tank, whose temperature is regulated using building steam and a temperature controller. The glycol supplied to the facility is cooled using a chiller shared with other test facilities in the lab. Control of the test facility is done through a PC using National Instruments' LabVIEW software sending signals to multiple VFDs and manual control of valves in the system. Data is collected from a multimeter and switch data acquisition system and stored for data reduction and analysis.

# Chapter 4

# Computational Fluid Dynamics Numerical Analysis

In order to perform numerical analysis using computational fluid dynamics, it is important that the governing equations are derived and it is shown how the problem can be discretized or otherwise implemented into commercial codes. First, a presentation of the governing equations for single-phase flow will be presented. Then, the single-phase equations will be modified to consider multi-phase systems. This extension will include some additional equations to help determine interfaces between the two phases. Finally, a brief introduction to the turbulence modeling method will be given.

## 4.1 Single-Phase Fluid Dynamics Equations

Single-phase fluid flow has been studied extensively; as such, the governing equations used in commercial CFD codes are widely known and available. Regardless, these fluid dynamics equations are derived below to provide a complete description of the problem presented in this work. As the assumption of adiabatic flow was made for this research, only the the conservation of mass and momentum equations are given.

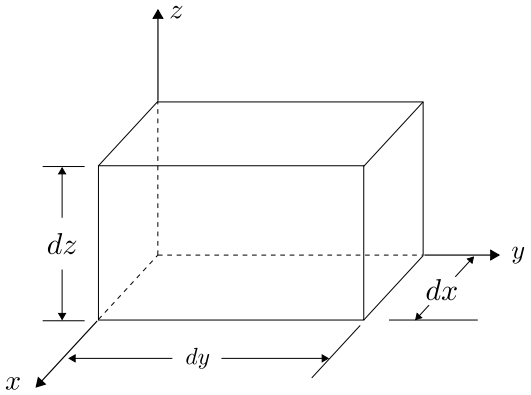


Figure 4.1: Differential volume element for Computational Fluid Dynamics derivations, including side lengths.

### 4.1.1 Conservation of Mass: The Continuity Equation

The first step in describing a fluid flow field is creating a mass balance through some volume. In this case, consider a differential element with side lengths $dx$, $dy$, and $dz$. Additionally, the element is assumed small enough that the properties of the fluid at the faces are represented by a two-term Taylor series expansion. We consider this fluid element to be fixed in space such that flow passes through the six faces of the cube and the center of the cube is at the center of mass of the fluid volume. Fluid properties such as density ($\rho$), velocity ($\boldsymbol{u}$), temperature ($T$), and pressure ($p$) are all dependent on the spatial coordinates and time; that is, $\rho = \rho(x, y, z, t)$, $\boldsymbol{u} = \boldsymbol{u}(x, y, z, t)$, $T = T(x, y, z, t)$, $p = p(x, y, z, t)$. Additionally, the representation of the velocity vector is given as

$$\boldsymbol{u} = ui + vj + wk \tag{4.1}$$

A differential volume element is shown in Figure 4.1. For this differential volume element, the rate of increase of mass inside the element can be given by

$$\frac{\partial}{\partial t}\left(\rho dxdydz\right) = \frac{\partial \rho}{\partial t}\left(dxdydz\right) \tag{4.2}$$

Conservation of mass requires that the rate of increase of mass inside the fluid element must be equal to the rate of mass flowing into the element. We can describe the rate of mass flowing into an element as a mass flow rate through each of the six faces of the element. In general, the mass flow rate can be given by

$$\dot{m} = \rho u A \tag{4.3}$$

For the case of a fixed differential volume element, the mass flowing through one face, for example the left most face at $x = 0$ as

$$\dot{m}_x = -\left(\rho u\right) dydz \tag{4.4}$$

and at the opposite face where $x = dx$ and mass is flowing out of the volume

$$\dot{m}_{x+\Delta x} = \left(\left(\rho u\right) + \frac{\partial\left(\rho u\right)}{\partial x} dx\right) dydz \tag{4.5}$$

The partial derivative terms in Eq. (4.5) arises from our Taylor series expansion assumption. Following this, we can use similar expressions for the other faces with the convention that mass flow into the volume element is negative while mass flow out of the volume is positive. This leads to the lengthy expression

$$\begin{aligned}
\dot{m} = &-\left(\rho u\right) dydz + \left(\rho u + \frac{\partial\left(\rho u\right)}{\partial x} dx\right) dydz \\
&-\left(\rho v\right) dxdz + \left(\rho v + \frac{\partial\left(\rho v\right)}{\partial y} dy\right) dxdz \\
&-\left(\rho w\right) dxdy + \left(\rho w + \frac{\partial\left(\rho w\right)}{\partial z} dz\right) dxdy
\end{aligned} \tag{4.6}$$

This expression can be simplified to

$$\begin{aligned}
\dot{m} &= \frac{\partial\left(\rho u\right)}{\partial x} dxdydz + \frac{\partial\left(\rho v\right)}{\partial y} dxdydz + \frac{\partial\left(\rho w\right)}{\partial z} dxdydz \\
&= \left(\frac{\partial\left(\rho u\right)}{\partial x} + \frac{\partial\left(\rho v\right)}{\partial y} + \frac{\partial\left(\rho w\right)}{\partial z}\right) dxdydz
\end{aligned} \tag{4.7}$$

In order for mass to be conserved, we know that the rate of mass increase inside the differential volume plus the rate of mass leaving the volume must be zero, thus we can combine Eq. (4.2) and Eq. (4.7) to show that

$$\frac{\partial \rho}{\partial t} dxdydz + \left(\frac{\partial\left(\rho u\right)}{\partial x} + \frac{\partial\left(\rho v\right)}{\partial y} + \frac{\partial\left(\rho w\right)}{\partial z}\right) dxdydz = 0 \tag{4.8}$$

Dividing this equation by $dxdydz$ allows Eq. (4.8) to be rewritten in a the more compact and commonly used form

$$\frac{\partial \rho}{\partial t} + \nabla \cdot \left(\rho \mathbf{u}\right) = 0 \tag{4.9}$$

### 4.1.2 Conservation of Momentum: The Navier-Stokes Equation

Following a derivation of the continuity equation (conservation of mass), it is necessary to formulate an equation for the conservation of momentum of a fluid element. In Section 4.1.1, the continuity equation was derived for an infinitesimally small control volume fixed in space with fluid flowing through the element. An alternative, but equivalent, model for analyzing a differential control volume is following the control volume as it moves along with the surrounding flow. This model is commonly used to define the conservation of momentum equations, as in Anderson (1995), which can be rearranged after the derivation into the conservative form of an infinitesimally small control volume fixed in space. Following the convention used in Anderson (1995), a derivation of the conservation of momentum for an infinitesimal fluid element is presented in this section. Details are given for the x-direction only, for simplicity, but the equations are easily expanded to the y- and z-direction.

The phrase "conservation of momentum" is simply a rephrasing of Newton's second law of motion, or simply

$$\mathbf{F} = m\mathbf{a} \tag{4.10}$$

The forces acting on our fluid element flowing with the field can be separated into two categories. The first type of forces, called body forces, act on the mass of the element. The primary body force in this derivation is gravity, although other body forces could act on the fluid element. The second type of forces, called surface forces, act on the surfaces of the fluid element. For our fluid element, only shear stresses, normal stresses, and pressure act on the surfaces of the element.

The first type of forces are simple to express. Given that the force per unit mass acting in the x-direction are indicated by $f_x$, the body forces in the x-direction can be given as

$$F_{b,x} = (\rho f_x)\, dxdydz \tag{4.11}$$

Figure 4.2 shows the x-direction surface forces applied to the differential volume element. For the stresses $\tau_{xx}, \tau_{yx}$, and $\tau_{zx}$, the first subscript letter represents the stress is acting on

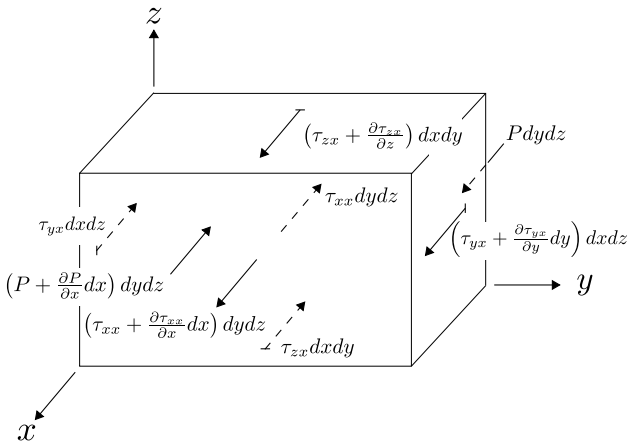


Figure 4.2: Forces acting on the differential volume element. Forces are shown in the x-direction only for clarity.

a face perpendicular to that axis, while the second subscript letter represents the direction the stress is acting in.

Summing the forces in the x-direction of Figure 4.2, it is shown that

$$\begin{aligned} F_{s,x} = {} & pdydz - \left(p+\frac{\partial p}{\partial x}dx\right)dydz + \left(\tau_{xx}+\frac{\partial\tau_{xx}}{\partial x}dx\right)dydz - \tau_{xx}dydz \\ & + \left(\tau_{yx}+\frac{\partial\tau_{yx}}{\partial y}dy\right)dxdz - \tau_{yx}dxdz + \left(\tau_{zx}+\frac{\partial\tau_{zx}}{\partial z}\right)dxdy - \tau_{zx}dxdy \end{aligned} \tag{4.12}$$

Eq. (4.12) can be simplified greatly to

$$\begin{aligned} F_{s,x} &= -\frac{\partial p}{\partial x}dxdydz + \frac{\partial\tau_{xx}}{\partial x}dxdydz + \frac{\partial\tau_{yx}}{\partial y}dxdydz + \frac{\partial\tau_{zx}}{\partial z}dxdydz \\ &= \left(-\frac{\partial p}{\partial x} + \frac{\partial\tau_{xx}}{\partial x} + \frac{\partial\tau_{yx}}{\partial y} + \frac{\partial\tau_{zx}}{\partial z}\right)dxdydz \end{aligned} \tag{4.13}$$

Now, as both the body and surface forces have been defined, the sum of forces in the x-direction is given as

$$\begin{aligned} \sum F_x &= F_{b,x} + F_{s,x} \\ &= (\rho f_x)\,dxdydz + \left(-\frac{\partial p}{\partial x} + \frac{\partial\tau_{xx}}{\partial x} + \frac{\partial\tau_{yx}}{\partial y} + \frac{\partial\tau_{zx}}{\partial z}\right)dxdydz \\ &= \left[(\rho f_x) + \left(-\frac{\partial p}{\partial x} + \frac{\partial\tau_{xx}}{\partial x} + \frac{\partial\tau_{yx}}{\partial y} + \frac{\partial\tau_{zx}}{\partial z}\right)\right]dxdydz \end{aligned} \tag{4.14}$$

Similar equations for the sum of forces in the y- and z-direction are given as

$$\sum F_y = \left[(\rho f_y) + \left(-\frac{\partial p}{\partial y} + \frac{\partial \tau_{xy}}{\partial x} + \frac{\partial \tau_{yy}}{\partial y} + \frac{\partial \tau_{zy}}{\partial z}\right)\right] dxdydz \tag{4.15}$$

and

$$\sum F_z = \left[(\rho f_z) + \left(-\frac{\partial p}{\partial z} + \frac{\partial \tau_{xz}}{\partial x} + \frac{\partial \tau_{yz}}{\partial y} + \frac{\partial \tau_{zz}}{\partial z}\right)\right] dxdydz \tag{4.16}$$

At this point, the LHS of Eq. (4.10) has been defined. For the RHS of Eq. (4.10), the mass of the fluid element can be defined as

$$m = \rho dxdydz \tag{4.17}$$

The acceleration of the fluid element is simply the time rate of change of the velocity. For a fluid element moving with the flow, the substantial derivative must be introduced. The substantial derivative of a fluid property that varies with time and space, $\Psi(t, x, y, z)$, is defined as

$$\frac{D\Psi}{Dt} = \frac{\partial \Psi}{\partial t} + \frac{\partial \Psi}{\partial x}\frac{dx}{dt} + \frac{\partial \Psi}{\partial y}\frac{dy}{dt} + \frac{\partial \Psi}{\partial z}\frac{dz}{dt} \tag{4.18}$$

Additionally, the time derivatives of the x, y, and z positions are simply velocities, thus Eq. (4.18) can be rewritten as

$$\frac{D\Psi}{Dt} = \frac{\partial \Psi}{\partial t} + \frac{\partial \Psi}{\partial x}u + \frac{\partial \Psi}{\partial y}v + \frac{\partial \Psi}{\partial z}w \tag{4.19}$$

If the x-component of velocity is substituted into Eq. (4.19) as the fluid property $\Psi$, Eq. (4.19) transforms into

$$\frac{Du}{Dt} = \frac{\partial u}{\partial t} + \frac{\partial u}{\partial x}u + \frac{\partial u}{\partial y}v + \frac{\partial u}{\partial z}w \tag{4.20}$$

From this, it is clear that $\frac{Du}{Dt}$ is the time rate of change of velocity of a fluid element flowing with the fluid. By definition, the time rate of change of velocity is equal to acceleration, thus the LHS of Eq. (4.20) can be substituted into Eq. (4.10) with Eq. (4.17) to give

$$ma_x = \rho dxdydz\left(\frac{Du}{Dt}\right) \tag{4.21}$$

Substituting Eq. (4.21) and Eq. (4.14) into Eq. (4.10) yields

$$\rho dxdydz\left(\frac{Du}{Dt}\right)=\left[(\rho f_x)+\left(-\frac{\partial p}{\partial x}+\frac{\partial \tau_{xx}}{\partial x}+\frac{\partial \tau_{yx}}{\partial y}+\frac{\partial \tau_{zx}}{\partial z}\right)\right]dxdydz \tag{4.22}$$

Simplifying Eq. (4.22) yields

$$\rho\frac{Du}{Dt}=(\rho f_x)+\left(-\frac{\partial p}{\partial x}+\frac{\partial \tau_{xx}}{\partial x}+\frac{\partial \tau_{yx}}{\partial y}+\frac{\partial \tau_{zx}}{\partial z}\right) \tag{4.23}$$

Similarly, equations for conservation of y and z momentum are given as

$$\rho\frac{Dv}{Dt}=(\rho f_y)+\left(-\frac{\partial p}{\partial y}+\frac{\partial \tau_{xy}}{\partial x}+\frac{\partial \tau_{yy}}{\partial y}+\frac{\partial \tau_{zy}}{\partial z}\right) \tag{4.24}$$

and

$$\rho\frac{Dw}{Dt}=(\rho f_z)+\left(-\frac{\partial p}{\partial z}+\frac{\partial \tau_{xz}}{\partial x}+\frac{\partial \tau_{yz}}{\partial y}+\frac{\partial \tau_{zz}}{\partial z}\right) \tag{4.25}$$

The notation of Equations (4.23), (4.24), and (4.25) indicates that these momentum conservation equations are in a nonconservative form owing to the substantial derivative. Simple modifications can be done to put these equations into a conservative form similar to the continuity equation above. For this, the $\nabla$ operator is used, simplifying a substantial derivative to

$$\begin{aligned}\rho\frac{Du}{Dt}&=\rho\left[\frac{\partial u}{\partial t}+\frac{\partial u}{\partial x}u+\frac{\partial u}{\partial y}v+\frac{\partial u}{\partial z}w\right]\\&=\rho\frac{\partial u}{\partial t}+(\rho\mathbf{u})\cdot\nabla u\end{aligned} \tag{4.26}$$

Further simplification to Eq. (4.26) can be done. First, the time derivative of $\rho u$ can be expanded as

$$\frac{\partial(\rho u)}{\partial t}=\rho\frac{\partial u}{\partial t}+u\frac{\partial \rho}{\partial t} \tag{4.27}$$

Solving Eq. (4.27) for the term appearing in Eq. (4.26) yields

$$\rho\frac{\partial u}{\partial t}=\frac{\partial(\rho u)}{\partial t}-u\frac{\partial \rho}{\partial t} \tag{4.28}$$

It can also be shown that, using a vector identity, that

$$\nabla \cdot (\rho u \mathbf{u}) = (\rho \mathbf{u}) \cdot \nabla u + u \nabla \cdot (\rho \mathbf{u}) \tag{4.29}$$

Rearranging Eq. (4.29) yields

$$(\rho \mathbf{u}) \cdot \nabla u = \nabla \cdot (\rho u \mathbf{u}) - u \nabla \cdot (\rho \mathbf{u}) \tag{4.30}$$

Substituting Equations (4.28) and (4.30) into Eq. (4.26) gives

$$\begin{aligned} \rho \frac{Du}{Dt} &= \frac{\partial (\rho u)}{\partial t} - u \frac{\partial \rho}{\partial t} + \nabla \cdot (\rho u \mathbf{u}) - u \nabla \cdot (\rho \mathbf{u}) \\ &= -u \left[ \frac{\partial \rho}{\partial t} + \nabla \cdot (\rho \mathbf{u}) \right] + \frac{\partial (\rho u)}{\partial t} + \nabla \cdot (\rho u \mathbf{u}) \end{aligned} \tag{4.31}$$

where the first term on the RHS of Eq. (4.31) is the LHS of the continuity equation, Eq. (4.9). Thus, by definition, this term must be zero and Eq. (4.31) can be further simplified to

$$\rho \frac{Du}{Dt} = \frac{\partial (\rho u)}{\partial t} + \nabla \cdot (\rho u \mathbf{u}) \tag{4.32}$$

Finally, Eq. (4.32) can be substituted into Eq. (4.23) giving, with similar analysis for the y- and z-directions,

$$\frac{\partial (\rho u)}{\partial t} + \nabla \cdot (\rho u \mathbf{u}) = (\rho f_x) + \left( -\frac{\partial p}{\partial x} + \frac{\partial \tau_{xx}}{\partial x} + \frac{\partial \tau_{yx}}{\partial y} + \frac{\partial \tau_{zx}}{\partial z} \right) \tag{4.33a}$$

$$\frac{\partial (\rho v)}{\partial t} + \nabla \cdot (\rho v \mathbf{u}) = (\rho f_y) + \left( -\frac{\partial p}{\partial y} + \frac{\partial \tau_{xy}}{\partial x} + \frac{\partial \tau_{yy}}{\partial y} + \frac{\partial \tau_{zy}}{\partial z} \right) \tag{4.33b}$$

$$\frac{\partial (\rho w)}{\partial t} + \nabla \cdot (\rho w \mathbf{u}) = (\rho f_z) + \left( -\frac{\partial p}{\partial z} + \frac{\partial \tau_{xz}}{\partial x} + \frac{\partial \tau_{yz}}{\partial y} + \frac{\partial \tau_{zz}}{\partial z} \right) \tag{4.33c}$$

Equations (4.33a), (4.33b), and (4.33c) are the conservation of momentum equations in conservative form, similar to the conservation of mass equation. These final three equations are general equations of fluid motion.

#### 4.1.2.1 Shear Force Representation

While Equations (4.33a), (4.33b), and (4.33c) describe an entire flow field, it is significantly easier to model the stresses involved in the equations. One method of doing so involves assuming the fluid is newtonian, that is, the shear stress varies linearly with the strain rate. Kundu (1990) gives the total stress tensor as

$$\tau_{ij} = -(p + \frac{2}{3}\mu\nabla \cdot \mathbf{u})\delta_{ij} + 2\mu e_{ij} \tag{4.34}$$

where

$$e_{ij} = \frac{1}{2}\left(\frac{\partial u_i}{\partial x_j} + \frac{\partial u_j}{\partial x_i}\right) \tag{4.35}$$

and the subscripts i and j represent the axes of the coordinate system.

Eq. (4.34) uses Einstein notation for the indices, including the Kronecker delta, $\delta_{ij}$. The pressure term in Eq. (4.34) has been included already in the derivation of the Navier-Stokes equations. The remaining terms represent $\tau_{xx}, \tau_{yy}, \tau_{zz}, \tau_{xy}, \tau_{xz}, \tau_{yx}, \tau_{yz}, \tau_{zx}$, and $\tau_{zy}$. These stress terms can thus be expanded as

$$\tau_{xx} = \frac{2}{3}\mu\left(\nabla \cdot \mathbf{u}\right) + 2\mu\frac{\partial u}{\partial x} \tag{4.36a}$$

$$\tau_{yy} = \frac{2}{3}\mu\left(\nabla \cdot \mathbf{u}\right) + 2\mu\frac{\partial v}{\partial y} \tag{4.36b}$$

$$\tau_{zz} = \frac{2}{3}\mu\left(\nabla \cdot \mathbf{u}\right) + 2\mu\frac{\partial w}{\partial z} \tag{4.36c}$$

$$\tau_{xy} = \tau_{yx} = \mu\left[\frac{\partial u}{\partial y} + \frac{\partial v}{\partial x}\right] \tag{4.36d}$$

$$\tau_{xz} = \tau_{zx} = \mu\left[\frac{\partial u}{\partial z} + \frac{\partial w}{\partial x}\right] \tag{4.36e}$$

$$\tau_{yz} = \tau_{zy} = \mu\left[\frac{\partial y}{\partial z} + \frac{\partial w}{\partial y}\right] \tag{4.36f}$$

Note that the pressure terms in Eq. (4.34) have been left out of Equations (4.36a) - (4.36f). The symmetry in the off-axis terms of the stress tensor is required for conservation of angular

momentum for the fluid element. With some manipulation Eq. (4.33) can be expressed as a simplified vector equation using divergence and gradient operators as

$$\frac{\partial(\rho\mathbf{u})}{\partial t} + \nabla \cdot (\rho\mathbf{u}\mathbf{u}) = -\nabla p + \nabla \cdot \overline{\overline{\tau}} + \rho\mathbf{f} \tag{4.37}$$

as given in the ANSYS Fluent Theory Guide (2011). This is the momentum conservation equation that most CFD software solves, including Fluent. Simplifications to the stress tensor $\overline{\overline{\tau}}$ can be made for incompressible fluids as the term $\nabla \cdot \mathbf{u} = 0$.

## 4.2 Turbulence Modeling

Turbulent flows cause many problems with CFD analysis; the fluctuation of vector and scalar quantities in the flow field can, in some cases, be too computationally expensive to explicitly solve. There are a number of modeling methods available to resolve the issues turbulent flow brings to a CFD simulation, including RANS, LES, and Direct Numerical Simulation (DNS), among others. In this work, the RSM turbulence model is used in the CFD calculations. General RANS turbulence modeling is described in the following subsections with a description of the RSM method following.

### 4.2.1 Reynolds-Averaged Navier-Stokes Turbulence Model

The RANS turbulence model makes use of Reynolds decomposition. For example, the x-component of velocity, $u_x$, would have a mean value and fluctuations around the mean. Using the Reynolds decomposition, this is described as

$$u_x = \overline{u}_x + u'_x \tag{4.38}$$

where $\overline{u}_x$ and $u'_x$ are the mean and fluctuating parts of the x-component of the velocity field, respectively. A similar expression for other velocity components and flow parameters, such as density, can also be written. Substituting Eq. (4.38) into the general equation for the x-component of momentum, Eq. (4.33a), and rearranging according to Glasgow (2010) yields

$$\frac{\partial(\rho\overline{u})}{\partial t} + \nabla \cdot (\rho\overline{u}\overline{\mathbf{u}}) = -\left[\frac{\partial \overline{p}}{\partial x} + \frac{\partial}{\partial x}(\tau_{xx} - \rho\overline{u'u'}) + \frac{\partial}{\partial y}(\tau_{yx} - \rho\overline{u'v'}) + \frac{\partial}{\partial z}(\tau_{zx} - \rho\overline{u'w'})\right] \quad (4.39)$$

Similar equations to (4.39) can be derived for y- and z-direction momentum, as well as a similar treatment for the continuity equation. From these equations, nine new terms called Reynolds stresses appear in the form $\rho\overline{u_i'u_j'}$ in indicial notation. Because of the number of unknowns (14) now in the system of equations, closure schemes must be used to make the problem tractable. One such closure scheme is the RSM scheme.

### 4.2.2 Reynolds Stress Model (RSM)

The RSM method of closing the turbulent RANS equations focuses on the transport of the Reynolds stresses, $\rho\overline{u_i'u_j'}$. From the Fluent theory guide (ANSYS, Inc., 2011), the transport of Reynolds stresses is given by

$$\frac{\partial}{\partial t}(\rho\overline{u_i'u_j'}) + C_{ij} = D_{T,ij} + D_{L,ij} + P_{ij} + G_{ij} + \phi_{ij} + \epsilon_{ij} + F_{ij} + S_{user} \quad (4.40)$$

where $C_{ij}$, $D_{T,ij}$, $D_{L,ij}$, $P_{ij}$, $G_{ij}$, $\phi_{ij}$, $\epsilon_{ij}$, $F_{ij}$, and $S_{user}$ are the convection, turbulent diffusion, molecular diffusion, and production of Reynolds stresses, buoyancy produced and pressure strain caused from Reynolds stresses, the dissipation of Reynolds stresses, production of Reynolds stresses caused by system rotation, and additional source terms of Reynolds stresses as defined by the user, respectively. All of these terms and their models are described in length in the Fluent theory guide (2011). These terms have been used in VOF multiphase simulations, including Banerjee and Isaac (2003).

RSM is more computationally expensive than other models, such as the $k$-$\epsilon$ or $k$-$\omega$ models. As discussed in Section 2.3.1, many turbulence models can be applied to problems similar to tube bundle flows, including $k-\varepsilon$, $k-\omega$, RSM, SST, and LES. The RSM turbulence model was chosen for two reasons. The primary reason was the computational power available. LES simulations are generally more computationally expensive, thus a RANS turbulence model was selected; in addition, LES simulations are currently not available with the VOF model in Fluent. Secondly, according to ANSYS, Inc. (2011), the RSM model has

the capability to more accurately capture the parameters of more complex flow fields than other RANS models. With more experimental data sets and available time, a study comparing the various turbulence models and their results could help select a more appropriate turbulence model for the given geometry.

## 4.3 Multi-Phase Fluid Dynamics Equations

Expanding the equations of conservation of mass and momentum to permit multiphase flow is a complex process depending on the schemes selected. From ANSYS, Inc. (2011), the conservation of volume fraction can be expressed as

$$\frac{1}{\rho_q}\left[\frac{\partial}{\partial t}(\alpha_q\rho_q) + \nabla\cdot(\alpha_q\rho_q\mathbf{u}_q) = S_{\alpha_q} + \sum_{p=1}^{n}(\dot{m}_{pq} - \dot{m}_{qp})\right] \tag{4.41}$$

In Eq. (4.41), $\alpha$ is the volume fraction of phase $q$, $S_{\alpha_q}$ is a source term set to zero by default, and the two $\dot{m}$ terms are mass transfer between the two phases, also set to zero in this research. It is clear that

$$\sum_{q=1}^{n}\alpha_q = 1 \tag{4.42}$$

For this work, an explicit scheme is used for multiphase volume fraction modeling and an implicit scheme for time discretization. The volume fractions at the current step are thus calculated based on the values from the previous time step, yielding

$$\frac{\alpha_q^{n+1}\rho_q^{n+1} - \alpha_q^n\rho_q^n}{\Delta t}V + \sum_f(\rho_q U_f^n \alpha_{q,f}^n) = \left[\sum_{p=1}^{n}(\dot{m}_{pq} - \dot{m}_{qp}) + S_{\alpha q}\right]V \tag{4.43}$$

where $U$ is the volume flux through the face of the cell based on the normal velocity, $V$ is the volume of the cell, and the subscript $f$ is the face value of a variable and $n+1$ is the current time step. The geometric reconstruction scheme is used for interface construction; this method fits a linear curve through each cell representing the volume fraction of phase 2 present in the cell.

Material properties for multiphase systems are volume-averaged; thus, an expression for the volume-average density is given as

$$\rho = \alpha_2 \rho_2 + (1 - \alpha_2)\rho_1 \tag{4.44}$$

With Eq. (4.44), the conservation of momentum equation can be reformed as, in a slightly expanded form to see volume-averaged properties,

$$\frac{\partial}{\partial t}(\rho \mathbf{u}) + \nabla \cdot (\rho \mathbf{u}\mathbf{u}) = -\nabla p + \nabla \cdot \left[\mu(\nabla \mathbf{u} + \nabla \mathbf{u}^T)\right] + \rho \mathbf{f} \tag{4.45}$$

It is important to note that the phases share a conservation of momentum equation, and thus a velocity field, and that the equation is dependent on volume-averaged properties such as $\rho$ and $\mu$.

### 4.3.1 Level-Set Function

In general, the level-set function allows interface tracking by using the level-set function in each cell of the model. In cells where the level-set function is between 0 and 1, the software knows the interface lies in that cell. Mathematically, this is represented by

$$\varphi(x,t) = \begin{cases} +|d|, & \text{if } x \in \text{the primary phase} \\ 0, & \text{if } x \in \Gamma \\ -|d|, & \text{if } x \in \text{the secondary phase} \end{cases} \tag{4.46}$$

where $d$ is the distance of the cell from the interface and $\Gamma$ is the zero level-set (ANSYS, Inc., 2011). Additionally, surface tension of the interface is found using the normal and curvature of the interface. After each time step, the level-set function must be re-initialized to prevent large errors from propagating due to the deformation of the interface. Finally, the level-set function can only be used with the VOF method and without mass transfer, thus it fits perfectly with the current research project. Further details, including details on the re-initializing process, can be found in ANSYS, Inc. (2011).

## 4.4 CFD Analysis Case Setup

In general, CFD analysis has five broad steps in the solution process; these steps are problem definition and geometry creation, mesh generation and refinement, application of

material properties and boundary conditions, choice of solution method and solving the system, and post processing and interpreting the results. Commercial CFD codes, such as ANSYS 14, the package used in this work, provide many tools and graphical user interfaces to make this process easier. However, these steps require attention to detail and experience to help ensure solution correctness and convergence. The next subsections will walk through the process of setting up the CFD simulations whose results are presented in Section 7.2 and Appendix E.

### 4.4.1 Problem Definition and Geometry Creation

The problem definition has been discussed at length throughout this paper. However, simplifications are made to ease the CFD simulation process. For the numerical simulations, a 2-D slice of the evaporator tube bundle is chosen. Adiabatic upward crossflow of R-134a over the tube bundle will be analyzed, meaning both liquid and vapor must be injected into the bundle and allowed to mix prior to measurements. Analysis of the results will examine vapor volume fraction in a single mesh element; this is analogous to a local void fraction measurement in experimental work by an optical probe. A PDF statistical analysis of the vapor volume fraction will be performed in an attempt to identify flow patterns based on $C_{M3}$ and $C_{M4}$ values as explored in the literature review.

The 2-D slice of the tube bundle greatly reduces the computational resources required. Inlet to the bundle requires both a liquid and vapor feed. To simplify the inlet geometry, long vertical openings at the interstitial gap of a two-tube row are used as the inlet sections. Figure 4.3 shows a close-up of the vertical inlets. Because the simulation was set up with the assumption of adiabatic flow, both liquid and vapor must be injected into the bundle to approximate two-phase flow; the 12 liquid inlets are shown in green with the three vapor inlets shown in red.

Above the long inlets, the bundle geometry is identical to the experimental setup in that the experimental insert plates are modeled as wall boundaries, not symmetry planes. This

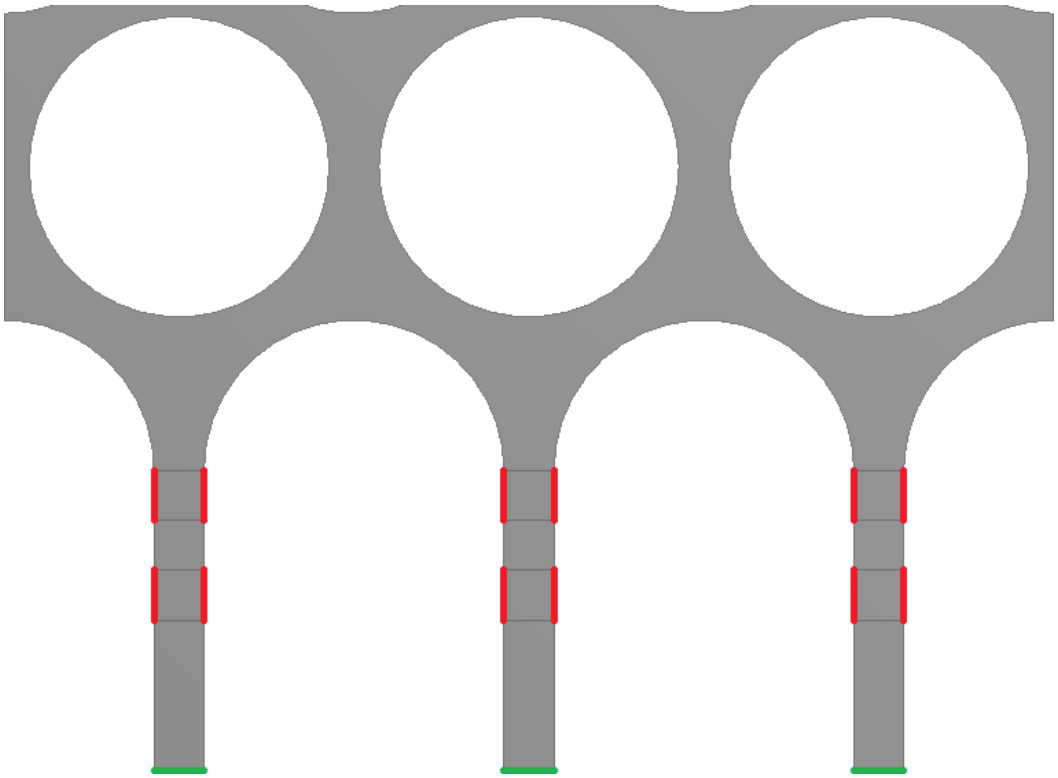

Figure 4.3: Bundle inlets for CFD analysis. Liquid inlets are shown in green with vapor inlets shown in red.

modeling decision was made to allow a comparison between the numerical flow patterns and the flow pattern maps for an identical experimental bundle geometry given in van Rooyen (2011). Five tubes with four tube passes in a staggered bundle layout with P/D = 1.167 is modeled. The geometry was initially created in SolidWorks 2012 as a 3-D model and imported into ANSYS Design Modeler where the model was flattened into a 2-D model. All boundaries were created and named in ANSYS DesignModeler; tube walls and side walls were grouped and considered solid wall boundaries. The 12 liquid inlets, three vapor inlets, and three fluid outlets were grouped separately. A picture of the final geometry is given in Figure 4.4.

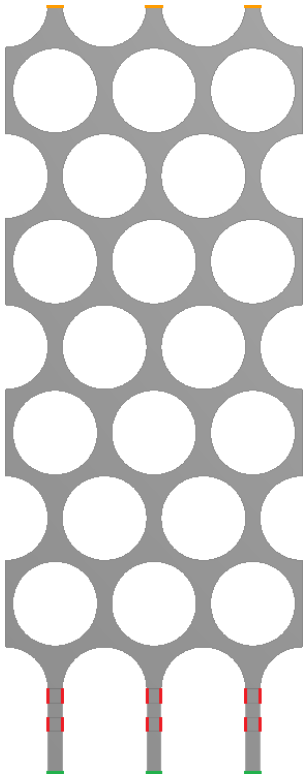

Figure 4.4: Final geometry for CFD analysis. Liquid inlets are shown in green, vapor inlets shown in red, and fluid outlets shown in orange.

### 4.4.2 Mesh Generation and Refinement

Using the ANSYS Workbench, geometry is passed from the DesignModeler to ANSYS Meshing. As a first attempt at meshing, default values are used and a mesh is generated with quadrilateral mesh elements. This mesh is shown in Figure 4.5. It is clear from the generated mesh that refinement is needed; many areas of the initial mesh have only one or two elements across the width of the geometry.

As a second attempt at mesh generation, a mesh size yielding seven elements across the minimum cross sectional area between two tubes is used. The distance between two tubes is found by

$$\begin{aligned}\left(\frac{P}{D}\right) D - D &= 1.167\,(19.05\ \text{mm}) - 19.05\ \text{mm} \\ &= 3.1814\ \text{mm}\end{aligned} \tag{4.47}$$

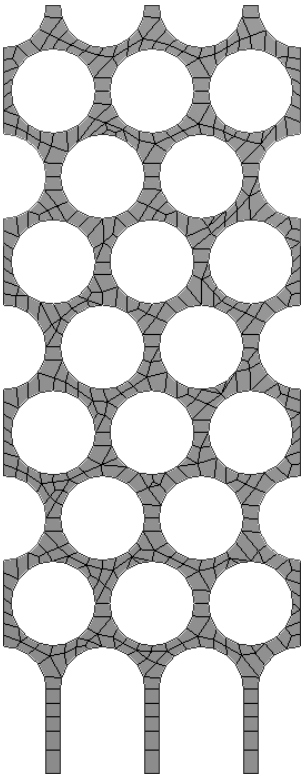

Figure 4.5: Initial mesh using default values from ANSYS Meshing.

Thus, the element size to give approximately seven elements between two tubes is

$$(3.1814 \text{ mm})/7 \approx 0.45 \text{ mm}$$

Instead of assigning the entire field with a specified element size, mesh refinement techniques were used. In this case, the two approaches would yield similar results as there are no large areas where larger mesh elements would be beneficial. Edge selection was used to select every edge in the geometry. Selection groups were used to keep similar features, such as inlets or tube walls, selected and refined together if further refinement on only one feature was needed. In this particular case, a uniform mesh refinement was used, with a mesh size of 0.45 mm on all boundaries. A mesh ratio of 1.2 was implemented to control the size of mesh elements away from the refined walls.

The final generated mesh is shown in Figure 4.6a and has 15840 nodes and 14021 elements. Table 4.1 gives details of the meshes used in the mesh refinement process.

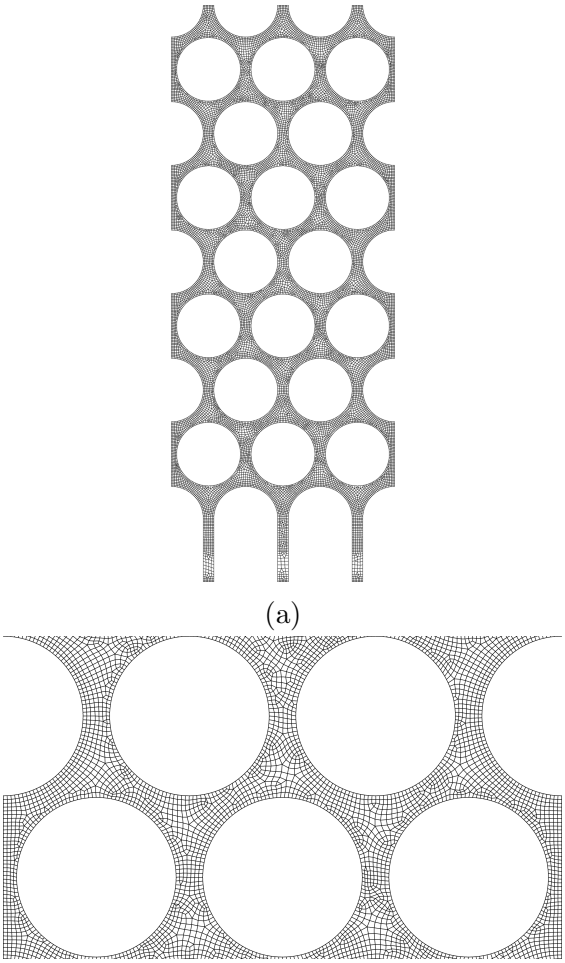

(a)

(b)

Figure 4.6: Finalized mesh using mesh refinement in ANSYS Meshing, showing (a) the entire generated mesh, (b) close-up of mesh refinement between two tubes.

Table 4.1: Table of mesh information

| Mesh Name | Number of Nodes | Number of Elements | Refinement Size (mm) |
|---|---|---|---|
| Coarse | 5278 | 4361 | 0.90 |
| Medium (Chosen) | 15840 | 14021 | 0.45 |
| Fine | 92709 | 87395 | 0.15 |

### 4.4.3 Application of Material Properties and Boundary Conditions

Once the mesh has been finalized, physical properties and models are added to the problem. For this research, R-134a is the working fluid. Two fluids are created, representing

saturated liquid and vapor R-134a. Density and viscosity of each phase are given to Fluent; here, saturated conditions at 5 °C are used in REFPROP to generate fluid properties. The temperature of 5 °C was chosen to closely match the flow pattern map testing conditions in van Rooyen (2011).

Once the phase properties are set, the primary phase is defined as liquid R-134a and the secondary phase is defined as vapor R-134a. For this work, the phase determination is not important. However, the addition of heat transfer and boiling models requires that the primary phase transitions into the secondary phase. Surface tension force modeling, including wall adhesion, is also defined in the phase interaction window between the liquid and vapor phases. A constant surface tension value of 10.0844 $mN/m$ is selected from the saturated conditions at 5 °C.

The boundary conditions for the walls, tubes, inlet and outlet are now set. The inlet conditions are mass flow rate conditions. The thermodynamic quality and mass flux determine the vapor and liquid flow rates into the bundle. For example, a mass flux of 10 $kg/m^2 \cdot s$ has a total refrigerant flow rate of 0.095 $kg/s$. This yields, for a quality of 10%, a vapor mass flow rate of 0.0095 $kg/s$ and liquid mass flow rate of 0.086 $kg/s$. The vapor flow rate through the liquid inlet, and liquid flow rate through the vapor inlet, are both set to zero so pure liquid and vapor are injected through their respective inlet boundaries.

The outlet boundary condition is set as a pressure boundary with a specified gauge pressure of 0 Pa, relative to the operating pressure. In this case, the operating pressure is irrelevant as no flow parameters depend on absolute pressure values. Setting the outlet pressure to 0 Pa prevents pressure-driven flow in the bundle, and flow is caused only by the vapor and liquid densities, inlet velocities, and pressure drop as the fluid flows through the geometry. Both vapor and liquid phases can leave through the outlet boundaries. While using the VOF model, a backflow volume fraction must be set at the pressure boundary. In this work, a backflow volume fraction of the vapor phase is set to zero. Thus, when vortices or downward velocity vectors intersect the outlet condition, Fluent injects liquid into the

simulation.

Turbulence parameters must also be set for inlet and outlet boundaries. For all of the boundaries, a turbulence intensity of 5% and turbulent length scale based on the minimum distance between tubes is defined as

$$\ell = 0.07L \tag{4.48}$$

where L is the smallest distance in the flow, between the flat walls and outer tubes.

The tube surfaces and walls are defined as a stationary wall boundary with contact angle of 90°and zero wall roughness. No slip can occur on the wall boundaries.

### 4.4.4 Simulation Models

As decribed partly in Section 4.2 and Section 4.3, this simulation models a two-phase, adiabatic flow using the RSM turbulence model, the VOF multiphase model, and the level-set function for interface tracking.

The RSM turbulence model was selected for its ability to accurately model turbulence in chaotic flows. The RSM linear pressure-strain turbulence model requires many coefficients and model constants to be set; all of these are left at default values including the near-wall treatment and calculation of boundary Reynolds stresses from the turbulent kinetic energy equation.

The VOF multiphase model was selected for its ability to track interfaces through the flow, allowing for accurate measurement of vapor volume fractions to determine flow patterns. A volume fraction cutoff of $1 \times 10^{-6}$ was set for low vapor volume fractions. No parameters are set for the level-set function.

### 4.4.5 Choice of Solution Method and Solving the System

The coupled pressure-velocity solver is used. Many spatial discretization parameters are set to second order upwind for increased solution accuracy. The geometric reconstruction volume fraction option is selected, which allows for piecewise-linear interfaces in the mesh

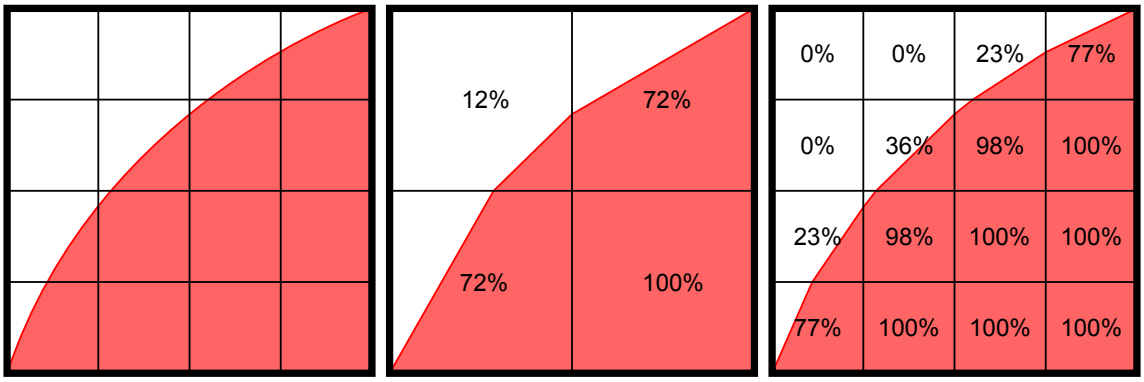


(a) (b) (c)

Figure 4.7: Example of a geo-reconstruct interface based on the volume fraction of individual mesh elements and their derivatives showing (a) the actual interface, (b) geo-reconstruct interface and volume fractions with coarse mesh, and (c) geo-reconstruct interface and volume fractions with fine mesh using linear piece-wise interfaces.

elements. Figure 4.7 shows an example interface that may be generated from the geo-reconstruct scheme using a coarse mesh and a fine mesh. As the mesh refinement increases, the geo-reconstructed surface more closely resembles the actual interface, and the individual mesh elements begin to have more accurate volume fraction values.

The simulation begins with the entire flow field initialized with zero velocity and entirely filled with liquid followed by an initialization simulation. The initialization simulation acts to fill the bundle with liquid and vapor with a minimum computational effort. This initialization is performed with a variable $\Delta t$, set by Fluent to ensure the Courant number is less than 0.9. By setting $Co = 0.9$, convergence issues with local velocities moving fluid elements further than one mesh cell are avoided while stepping the time forward as much as possible. The time step has converged once the continuity, momentum, turbulence parameters, and level-set function equations have reached the convergence criterion set at 0.001. After the initialization simulation is complete and the bundle has vapor throughout, a fixed time step simulation, with $\Delta t = 5 \times 10^{-5}$ s is performed. Data are recorded every 20 time steps for results every 1 ms, similar to the high speed video recordings at 1000 fps. This fixed time step simulation is run for 1 s, again similar to the high speed video recordings. The final

results will be used to determine flow patterns based on a statistical method presented in Chapter 7 using an averaging time window of $\Delta t = 0.02$ s. Identical convergence criterion to the initialization simulation are used for the fixed time step simulations.

## 4.5 Summary

In this chapter, the equations governing fluid flow are derived and applied to CFD simulations. A brief discussion of the turbulence and multiphase models is given from the software documentation. Finally, the general procedure of running a CFD simulation is given. Details for preparing the CFD simulations, including the creation of model geometry, mesh generation and refinement, material parameters and boundary conditions, and simulation models and solution methods, are given.

The final step to a CFD simulation requires post processing the results and analyzing the calculated values. This last step is presented in Chapter 7.

# Chapter 5

# Data Reduction

## 5.1 Introduction

Two tube bundles were tested for the experimental results; the first bundle consisted of smooth tubes only with a P/D = 1.167. The second tube bundle used Wolverine Tube, Inc. Turbo ESP tubes, also with a P/D = 1.167. Both tube bundles rerouted water channel A2 outside of the bundle and replaced channel A2 inside the bundle with a clear polycarbonate tube for flow pattern visualization.

The LabVIEW VI software was adapted from a previous experiment using the same test facility and different bundle (Gorgy, 2011). Raw data from all pressure transducers, thermistors, RTDs, and flow meters were collected by the LabVIEW program in intervals of 20 seconds for 5 minutes. A number of calculations were performed from this data, including refrigerant mass flux, heat flux, and quality. The following sections of this chapter detail the calculations to reduce the raw data into quantities used for system analysis.

## 5.2 Refrigerant Mass Flux

The refrigerant mass flow rate, $\dot{m}_R$, referred to in many sections is measured from the Coriolis mass flow meter I-1 in Figure 3.9. The mass flux for the tube bundle is calculated based on the minimum cross sectional area inside the test section. Thus, the refrigerant mass flux, $G_R$, is defined as

$$G_R = \frac{\dot{m}_R}{A_{min}} \tag{5.1}$$

The minimum cross sectional area, $A_{min}$, is the spacing between two neighboring tubes times the length of the test section. Additionally, every tube row has three intertube spaces; thus, $A_{min}$ is calculated to be

$$\begin{aligned} A_{min} &= 3\left(\frac{P}{D}D - D\right)L \\ &= 3\left[(1.167)\,(.01905\ \text{m}) - .01905\ \text{m}\right](1\ \text{m}) \\ &= .009544\ \text{m}^2 \end{aligned} \tag{5.2}$$

In each bundle, tests are run with mass fluxes of 10, 15, 20, 25, and 35 $kg/m^2 \cdots$ with some quality limitations due to the facility capacities.

## 5.3 Water Channel Heat Flux

The heat flux for each water channel is calculated from the change of enthalpy of the water. As described in Chapter 3, a water channel is named water channel A through E and describes the entire path that water can take through one tube column. For an open system with negligible potential energy change, kinetic energy change, and work done, an energy balance can be reduced to

$$q = \dot{m}_W\left[(i_{W,i} - i_{W,o})\right] \tag{5.3}$$

where q is the rate of heat transfer from the water to the refrigerant. For an incompressible fluid, the specific enthalpy, $i_W$ in Eq. (5.3) can be expressed as

$$i_W = c_{p,W}T + \nu p \tag{5.4}$$

Substituting Eq. (5.4) into Eq. (5.3), assuming constant specific heat, $c_{p,W}$, and a negligible change in pressure yields

$$q = \dot{m}\left[c_p(T_i - T_o)\right] \tag{5.5}$$

where $c_{p,W}$ is calculated at the mean of $T_{W,i}$ and $T_{W,o}$.

Finally, dividing Eq. (5.5) by the total external surface area gives us an expression for the heat flux through the tube as

$$\begin{aligned} q'' &= \frac{q}{\pi D_{out} L} \\ &= \frac{\dot{m} c_p (T_i - T_o)}{\pi D_{out} L} \end{aligned} \tag{5.6}$$

In Eq. (5.6), inlet and outlet temperatures ($T_i$ and $T_o$) are directly measured from the test facility. For the smooth tubes and Turbo ESP tubes, an outside diameter of $D_{out} = 19.05$ mm (0.75 in) was used. Additionally, the nominal active length of all tubes is 1 m (39.37 in); therefore, for the total bundle heat flux calculations, the RHS denominator of Eq. (5.6) contains a length of 4 m (157.48 in) for channels B-E and a length of 3 m (118.11 in) for channel A. The shorter length of channel A is a result of the polycarbonate tube in A2 acting as an inactive water pass.

Each of the five tube average heat flux calculations is used to find a bundle heat transfer rate following

$$q = \sum_{k=1}^{5} q''_k \pi D_{out} L \tag{5.7}$$

where the subscript k represents an individual water channel. Again, the active length of channels B-E in Eq. (5.7) is 4 m and the active length of channel A is 3 m.

## 5.4 Preboiler Heat Transfer and Quality

Determination of refrigerant quality at the polycarbonate tube row is necessary for classifying flow patterns in the tube bundle. Multiple calculations are required to determine the quality at the polycarbonate tube row as all of the passes are not fully instrumented. Calculations begin by finding the bundle inlet quality which subsequently is found from preboiler calculations.

At the preboiler inlet, the refrigerant is considered to be subcooled or a saturated liquid. During testing, it was found that a majority of test conditions had a subcooled refrigerant

entering the preboiler. The preboiler refrigerant inlet temperature ($T_{PB,i}$) and pressure ($p_{PB,i}$) measurements were passed to REFPROP 8.0. REFPROP returns the refrigerant preboiler inlet enthalpy ($i_{PB,i}$). Using a calculation similar to Eq. (5.5), the heat transfer through the preboiler on the water side is calculated as

$$q_{PB} = \dot{m}_{W,PB} c_{p,W,PB} \left(T_{W,PB,i} - T_{W,PB,o}\right) \tag{5.8}$$

The refrigerant preboiler outlet enthalpy, $i_{,PB,o}$, can then be calculated by

$$i_{PB,o} = \frac{q_{PB}}{\dot{m}_R} + i_{PB,i} \tag{5.9}$$

The preboiler outlet quality, $x_{PB,o}$ is determined by passing REFPROP $i_{PB,o}$ and $p_{PB,o}$ as

$$x_{PB,o} = f(i_{PB,o}, p_{PB,o}) \tag{5.10}$$

## 5.5 Tube Bundle Refrigerant Quality

The quality calculated from the test section measurements is an average quality at a specific tube row for the entire length of the tube bundle. This section describes the method of determining refrigerant quality in the tube bundle; a subsection details the difficulties encountered in calculating the smooth tube qualities due to some instrumentation not being installed in the smooth tube bundle. Changes were made to instrumentation after the smooth tube bundle to make the process of determining refrigerant quality more precise in the enhanced tube bundle.

In general, the enthalpy of a two phase fluid can be calculated as

$$\begin{aligned} i &= (1-x)\, i_f + x i_g \\ &= i_f + x\left(i_g - i_f\right) \\ &= i_f + x i_{fg} \end{aligned} \tag{5.11}$$

With the enthalpy of a fluid at any quality defined, an energy balance of the heat transfer from the tubes can be performed. The heat transfer rate to the refrigerant is given by

$$q_R = \dot{m}_R \left(i_o - i_i\right) \tag{5.12}$$

Substituting Eq. (5.11) into Eq. (5.12) yields

$$\begin{aligned} q_R &= \dot{m}_R \left[ (i_f + x_o i_{fg}) - (i_f + x_i i_{fg}) \right] \\ &= \dot{m}_R \left( x_o - x_i \right) i_{fg} \end{aligned} \tag{5.13}$$

From Eq. (5.13), one can solve for $x_o$ as

$$x_o = \frac{q_R}{\dot{m}_R i_{fg}} + x_i \tag{5.14}$$

As the refrigerant side heat transfer rate must be equal to the water side heat transfer rate, $q_R$ in Eq. (5.14) can be replaced with the water heat transfer rate from Eq. (5.5)

$$x_o = \frac{\dot{m}_W c_p \left( T_i - T_o \right)}{\dot{m}_R i_{fg}} + x_i \tag{5.15}$$

This quality calculation forms the basis for finding refrigerant qualities at different tube rows in the bundle. The tube bundle inlet quality is calculated using the preboiler outlet enthalpy and test section inlet pressure, $i_{PB,o}$ and $p_{TS,i}$. These refrigerant properties are passed to REFPROP to determine the test section inlet quality, $x_{TS,i}$ as

$$x_{TS,i} = f(i_{PB,o}, p_{TS,i}) \tag{5.16}$$

$x_{PB,o}$ and $x_{TS,i}$ should be very similar as no heat transfer occurs between the two locations, but due to pressure drop through the connecting pipe, small variations in $x_{PB,o}$ and $x_{TS,i}$ exist.

After determining $x_{TS,i}$, other qualities throughout the tube bundle are calculated with a form of Eq. (5.15). This yields a refrigerant quality after the first tube pass, $x_1$, of

$$x_1 = \frac{\dot{m}_{W,all} c_{p,W} \left( T_{W,1i,ave} - T_{W,2i,ave} \right)}{\dot{m}_R i_{fg}} + x_i \tag{5.17}$$

Following the calculation of $x_1$, a similar set of quality calculations can be done to find the refrigerant quality at the side of the polycarbonate tube and angled above the polycarbonate tube, $x_{2s}$ and $x_{2a}$, respectively. The calculations for $x_{2s}$ and $x_{2a}$ are

$$x_{2s} = \frac{\frac{\dot{m}_{W,BD}}{2} c_{p,w} (T_{W,BD2i} - T_{W,BD3i})}{\dot{m}_R i_{fg}} + x_1 \tag{5.18}$$

$$x_{2a} = \frac{\dot{m}_{W,BD} c_{p,w} (T_{W,BD2i} - T_{W,BD3i})}{\dot{m}_R i_{fg}} + x_1 \tag{5.19}$$

where the subscript $BD$ represents either the sum of the mass flow rate of water through channels B and D, $\dot{m}_{W,BD}$, or the average water temperatures of channels B and D entering pass 2 or 3, $T_{W,BD2i}$ and $T_{W,BD3i}$ respectively. The use of heat transfer from only channels B and D in Eq. (5.18) and Eq. (5.19) is due to the viewing direction; for both the side and angled views, heat transfer has only occurred on water channels B and D. Additionally, the division of $\dot{m}_{W,BD}$ in Eq. (5.18) by 2 forces the calculation of $x_{2s}$ to only consider heat transfer occurring on the bottom half of channels B and D. More advanced models determining the percentage of heat transfer occurring on the bottom half of a tube could be used to further refine these quality calculations. It is expected that this would marginally change the value of $x_{2s}$ while no change would be seen in $x_{2a}$.

### 5.5.1 Smooth Tube Bundle Refrigerant Quality

In the smooth tube bundle, the refrigerant temperature and pressure at every tube row was measured. However, water instrumentation was only installed at $T_{W,ki}$, $T_{W,k3o}$ and $T_{W,k4o}$ for each water channel, along with the pressures $p_{W,Ai}$, $p_{W,A1o}$, $p_{W,A3o}$, and $p_{W,A4o}$. Approximation of the refrigerant quality at the polycarbonate tube row requires the water temperatures at the inlet and outlet of pass 2. Finding these temperatures is a multi-step process beginning with the determination of the test section inlet quality, $x_{TS,i}$, as calculated in Section 5.4 and the overall heat transfer coefficient for the first three tube rows, $U_{3k}$.

It is clear that the water side heat transfer rate in the tube bundle must be equal to the refrigerant side heat transfer rate. The water side heat transfer rate for the first three passes of a single water channel, k, is given as

$$q_{3k} = \dot{m}_{W,k} c_{p,W} (T_{W,k1i} - T_{W,k3o}) \tag{5.20}$$

For the refrigerant side heat transfer, an overall heat transfer coefficient for the first three passes, $U_{3k}$, for each channel is used. The refrigerant side heat transfer rate is given as

$$q_{3k} = U_{3k} A \Delta T_{lm,3k} \tag{5.21}$$

The refrigerant side and water side heat transfer rates can then be equated as

$$U_{3k} A \Delta T_{lm,3k} = \dot{m}_{W,k} c_{p,W} \Delta T_{W,k} \tag{5.22}$$

Finding the overall heat transfer coefficient is required for determining $T_{k1o}$ and $T_{k2o}$. The first step is calculating $\Delta T_{lm,3,k}$; this LMTD applies to the first three tube passes of a single channel. The calculation of $\Delta T_{lm,3,k}$ value is done using the following equation

$$\Delta T_{lm,3,k} = \frac{(T_{W,k3o} - T_{R,3,sat}) - (T_{W,k1i} - T_{R,i,sat})}{ln\left(\frac{T_{W,k3o} - T_{R,3,sat}}{T_{W,k1i} - T_{R,i,sat}}\right)} \tag{5.23}$$

In Eq. (5.23), the temperatures represented by $T_{W,k1i}$ and $T_{W,k3o}$ are the temperatures entering pass 1 and leaving pass 3 of each channel, respectively. $T_{R,i,sat}$ and $T_{R,3,sat}$ are the refrigerant saturation temperatures at the inlet of the test section and row 3 of the tube bundle based on the average refrigerant pressure in the test section. If dryout occurs lower in the tube bundle, the value used for $T_{R,3,sat}$ may be slightly lower than its actual temperature because the refrigerant pressures of a superheated vapor will be higher. However, the amount of superheating should be small. The result of Eq. (5.23) is thus five values of $\Delta T_{lm,3,k}$, one for each water channel A through E.

With $\Delta T_{lm,3,k}$, overall tube heat transfer coefficient for the first three passes of a tube, $U_{3,k}$, can be calculated as

$$U_{3k} = \frac{\dot{m}_{W,k} c_{p,W} \Delta T_{W,3k}}{A \Delta T_{lm,3k}} \tag{5.24}$$

In order to calculate $T_{W,k1o}$ and $T_{W,k2o}$, an assumption is made that the refrigerant temperature does not appreciably change between the tubes; this assumption is reasonable as the refrigerant is in a phase transition and in Eq. (5.23) the refrigerant saturation temperatures are based on the average refrigerant pressure in the tube bundle. This assumption simplifies Eq. (5.23) to

$$\Delta T_{lm,k} = \frac{(T_{W,ko} - T_{W,ki})}{ln\left(\frac{T_{W,ko} - T_{R,o}}{T_{W,ki} - T_{R,i}}\right)} \tag{5.25}$$

Eq. (5.22) can now be used to find $T_{W,k1o}$ and $T_{W,k2o}$. Substituting Eq. (5.25) for $\Delta T_{lm,3k}$ as well as the temperature difference of the water into Eq. (5.22), Eq. (5.22) becomes

$$U_{3k}A\frac{(T_{W,ko}-T_{W,ki})}{ln\left(\frac{T_{W,ko}-T_{R,o,sat}}{T_{W,ki}-T_{R,i,sat}}\right)}=\dot{m}_{W,k}c_{p,W}(T_{W,ki}-T_{W,ko}) \tag{5.26}$$

Solving Equation (5.26) for $T_{W,ko}$ yields

$$T_{W,ko}=(T_{W,ki}-T_{R,i,sat})\exp\left(\frac{-\pi D_{out}LU_{3k}}{\dot{m}_{W,k}c_{p,W}}\right)+T_{R,o,sat} \tag{5.27}$$

When calculating $T_{W,ko}$ for the first tube pass, inlet temperatures are the bundle inlet conditions, $T_{W,k1i}$ and $T_{R,i,sat}$, outlet temperatures are the temperatures after one tube pass, $T_{W,k2i}$ and $T_{R,1,sat}$, and the length, $L$, used is 1 m. For $T_{W,2}$, the inlet temperatures are the temperatures after one tube pass, $T_{W,k2i}$ and $T_{R,1,sat}$, the outlet temperatures are the temperatures after two tube passes, $T_{W,k2o}$ and $T_{R,2,sat}$ and the length is again 1 m.

An additional assumption has been made in Eq. (5.27). This equation assumes that the overall heat transfer coefficient for the first three tube rows, $U_{3k}$, is approximately equal to the heat transfer coefficient for a single tube row. The tube bundle is plumbed from the bottom to the top, so the first tube row will have the highest heat transfer coefficient and thus a higher heat transfer coefficient than the one used in Eq. (5.27). However, for a first approximation of the quality, the value of $U_{3k}$ is assumed to be sufficient.

At this point, each water channel has approximated $T_{W,k1}$ and $T_{W,k2}$. From these values, qualities throughout the tube bundle can be calculated using Equations (5.17) through (5.19).

## 5.6 Uncertainty Analysis

The uncertainty analysis is performed primarily using Mathcad software for speed and ease of use. The quality at the polycarbonate tube row, both at the side view and angled view, along with the polycarbonate tube row heat flux and refrigerant mass flow rate uncertainties are calculated for each data point collected for the smooth tube and enhanced tube bundles.

### 5.6.1 Measurement Uncertainties

The first set of uncertainties needed to calculate the final uncertainty values for quality, heat flux, and mass flux are the measurement uncertainties of various temperatures, pressures, and mass flow rates.

#### 5.6.1.1 Temperature Uncertainty

Two types of temperature measuring devices are used in the system for different temperature measurements. Throughout the test section, thermistors are used to find water temperatures while RTDs are used to find the refrigerant temperatures. In the rest of the test facility, a few locations use RTDs to measure temperature, including the preboiler refrigerant outlet temperature. A complete description of the temperature sensors used is available in Appendix C.

The thermistor interchangeability given by the manufacturer is $\pm 0.1^{\circ}$ C. Using a traditional propagation of uncertainties (Wheeler and Ganji, 2010), more accurate estimates of uncertainty can be found by looking at the uncertainty of the data acquisition equipment and calibration procedure. In this case, the data acquisition switch and multimeter have a combined resistance uncertainty, according to the manufacturer, of $\pm 0.008\%$ reading $+0.001$ range. For the thermistors, the reading is nominally $10k\Omega$ and the range is set to $100k\Omega$, yielding a resistance uncertainty of $u_{Res} = \pm 1.80\Omega$. The calibration curves have an average slope of $dT/d\Omega = -1.689 \times 10^{-3}$ °C/Ω. Additionally, the temperature bath used for calibration has a standard uncertainty of $u_{TB} = \pm 0.01^{\circ}$ C. Combining these uncertainties, we see that the overall temperature uncertainty is

$$\begin{aligned} u_{Therm} &= \sqrt{u_{TB}^2 + \left(\frac{dT}{d\Omega} u_{Res}\right)^2 + u_{Manuf}^2} \\ &= \pm 0.1005 \ ^{\circ}\text{C} \cong \pm 0.1 \ ^{\circ}\text{C} \end{aligned} \tag{5.28}$$

Thus, for simplicity, the manufacturers interchangeability will be used for uncertainty calculations. Similarly, the manufacturers uncertainty for RTDs is $u_{RTD} = \pm 0.15 \ ^{\circ}C$.

#### 5.6.1.2 Pressure Uncertainty

Similar to the temperature uncertainty, the manufacturers give an uncertainty of $u_P = 0.05\%$ of the range. For the refrigerant pressure transducers with a full range of 0-517.1 kPa (0-75 PSI), the uncertainty is

$$\begin{aligned} u_P &= 0.05\%(517.1 \text{ kPa}) \\ &= \pm 0.258 kPa \end{aligned} \tag{5.29}$$

A similar analysis of the measurement system uncertainty as performed for the temperatures could be done; however, the most significant form of uncertainty is the instrument uncertainty listed by the manufacturer.

#### 5.6.1.3 Flow Rate Uncertainty

All of the flow meters are Coriolis flow meters manufactured by Micro Motion. Their ELITE model line has flow rate uncertainties of $\pm 0.1\%$ of the flow rate.

### 5.6.2 Uncertainty of REFPROP Values

While the values returned from REFPROP are returned from verified equations, the returned values still have an uncertainty based on the values passed to REFPROP. As an example, the uncertainty of the preboiler refrigerant inlet enthalpy. REFPROP expects the temperature and pressure of the inlet refrigerant, thus

$$i_{PB,in} = f(T, P) \tag{5.30}$$

To find the uncertainty in the refrigerant inlet enthalpy, propagation of uncertainties on the temperature and pressure passed to REFPROP can be used. This gives the uncertainty of the enthalpy as

$$u_{i_{PB,in}} = \sqrt{\left(\frac{\partial i}{\partial P} u_P\right)^2 + \left(\frac{\partial i}{\partial T} u_T\right)^2} \tag{5.31}$$

The derivatives in Eq. (5.30) are found by incrementing pressure or temperature while holding the other constant and looking at the changes in enthalpy in REFPROP. Similar

calculations are done for any REFPROP calculation, except the water specific heat, where it was found to have negligible uncertainty.

### 5.6.3 Quality Uncertainty

The thermodynamic quality of the refrigerant at the polycarbonate tube row is required for accurately determining the test condition. As described in Section 5.5, the quality is at a tube row is calculated using Equations (5.18) and (5.19). Thus, their uncertainty is given by

$$u_{x_2} = \sqrt{\left(\frac{\partial x_2}{\partial \dot{m}_W} u_{\dot{m}_W}\right)^2 + \left(\frac{\partial x_2}{\partial T_1} u_{T_1}\right)^2 + \left(\frac{\partial x_2}{\partial T_2} u_{T_2}\right)^2 + \left(\frac{\partial x_2}{\partial \dot{m}_R} u_{\dot{m}_R}\right)^2 + \left(\frac{\partial x_2}{\partial x_1} u_{x_1}\right)^2} \tag{5.32}$$

For this equation, all uncertainties are known from Section 5.6.1 for the enhanced tube bundle except for $u_{x_1}$. For the smooth tube bundle, $u_{T_1}$ is also unknown. $x_1$, calculated in Eq. (5.17), has an uncertainty given by an equation similar to Eq. (5.32), with temperatures at the inlet and outlet of water pass 1 and the inlet quality, $x_i$. Of course, the uncertainty of $x_i$ is then needed, which is calculated from

$$u_{x_i} = \sqrt{\left(\frac{\partial x_i}{\partial i_{PB,o}} u_{i_{PB,o}}\right)^2 + \left(\frac{\partial x_i}{\partial P_{TS,i}} u_{P_{TS,i}}\right)^2} \tag{5.33}$$

This uncertainty arises from REFPROP returning a thermodynamic quality based on the preboiler outlet enthalpy and test section inlet pressure. $u_{P_{TS,i}}$ is known from the measurement uncertainty, while $u_{i_{PB,o}}$ is unknown. Further uncertainty calculations are used to find the uncertainties needed to fully define the quality uncertainty. Additionally, the smooth tube bundle requires uncertainties for $\Delta T_{lm}$ at the water outlets of passes 1 and 2, which require still more uncertainty calculations. For complete details on the uncertainty calculations, an example Mathcad file is provided in Appendix F. The thermodynamic quality at the polycarbonate tube row ranges in relative uncertainty from $\pm 0.117\%$ at high qualities to $\pm 5.0\%$ at low qualities.

### 5.6.4 Heat Flux Uncertainty

The final uncertainty needed is from the heat flux of the tube being visualized. Channel D's heat flux is calculated from Eq. (5.6). Thus, its uncertainty is given by

$$u_{q''} = \sqrt{\left(\frac{\partial q''}{\partial \dot{m}_{WD}} u_{\dot{m}_{WD}}\right)^2 + \left(\frac{\partial q''}{\partial T_{D1}} u_{T_{D1}}\right)^2 + \left(\frac{\partial q''}{\partial T_{D2}} u_{T_{D2}}\right)^2} \tag{5.34}$$

In Eq. (5.34), the area is assumed to have negligible uncertainty compared to the measurement uncertainties from the temperatures and pressures.

The uncertainty of the water channel D heat flux ranges in relative uncertainty from $\pm 7.2\%$ to $\pm 46.6\%$.

## 5.7 Summary

Throughout this chapter, the methods of reducing the collected data into the desired test condition values has been explained; the thermodynamic quality and heat flux from the second pass of water channel D is of particular interest. From the raw data, qualities at the polycarbonate tube row were found for both the smooth and enhanced tube bundles, with a LMTD method for finding the smooth tube water temperatures. Additionally, the uncertainty analysis has been described to find the uncertainties of the thermodynamic quality and heat flux of the polycarbonate tube row.

# Chapter 6

# Experimental Results

In this chapter both the smooth and enhanced tube bundle experimental results are presented. In each of these sections, a test matrix for the tube bundle states the experimental conditions used. Then, a brief description of the data collection method is given. An example analysis of the results is presented with images showing the observed flow patterns.

## 6.1 Smooth Tube Bundle Visualization Results

The results from the smooth tube bundle are presented in this section. For the smooth tube bundle, videos were recorded at 1000 fps and 3000 fps using the borescope and high speed camera for one second. The videos were replayed at 1/100th speed to determine the flow patterns in each test condition.

### 6.1.1 Smooth Bundle Test Matrix

A test matrix for the smooth tube bundle is given in Table 6.1. As mentioned in the facility description in Chapter 3 and the data reduction in Chapter 5, the smooth tube testing facility had fewer thermistors on the water side of the test section. This necessitates the LMTD method, after experimentation, to determine the water temperatures and thus thermodynamic quality of the refrigerant at the polycarbonate (PC) tube row. Additionally, the heat flux at the polycarbonate tube row was not monitored; instead, the nominal overall bundle heat flux was fixed near 16 $kW/m^2$ when possible. Some testing conditions, where

Table 6.1: List of all smooth tube bundle testing conditions

| Mass Flux, $kg/m^2 \cdot s$ | Bundle Heat Flux, $kW/m^2$ | TS Inlet Quality, % | PC Row Heat Flux, $kW/m^2$ | PC Row Quality, % | Flow Pattern |
|---|---|---|---|---|---|
| 10 | 14 | 2 | 17.6 | 45 | Bubbly/Intermittent |
| 10 | 16 | 0 | 17.8 | 39 | Bubbly/Intermittent |
| 15 | 12 | 54 | 17.3 | 77 | Intermittent |
| 15 | 16 | 35 | 17.2 | 60 | Intermittent |
| 15 | 17 | 27 | 18.5 | 55 | Intermittent |
| 15 | 18 | 30 | 17.0 | 60 | Intermittent |
| 15 | 18 | 35 | 24.0 | 68 | Intermittent |
| 20 | 12 | 61 | 19.7 | 83 | Annular |
| 20 | 12 | 65 | 16.1 | 82 | Annular |
| 20 | 13 | 27 | 12.7 | 42 | Intermittent |
| 20 | 13 | 57 | 19.2 | 78 | Intermittent |
| 20 | 14 | 54 | 16.3 | 73 | Intermittent |
| 20 | 17 | 48 | 18.5 | 66 | Intermittent |
| 20 | 17 | 51 | 18.3 | 69 | Intermittent |
| 20 | 18 | 50 | 17.2 | 69 | Intermittent |
| 20 | 20 | 45 | 17.9 | 65 | Intermittent |
| 25 | 13 | 20 | 13.5 | 30 | Bubbly/Intermittent |
| 25 | 15 | 63 | 21.4 | 83 | Annular/Dryout |
| 25 | 16 | 43 | 16.3 | 56 | Intermittent |
| 25 | 16 | 62 | 23.2 | 82 | Annular |
| 25 | 16 | 63 | 18.4 | 78 | Intermittent/Annular |
| 25 | 16 | 62 | 19.8 | 80 | Intermittent |
| 35 | 11 | 70 | 15.3 | 86 | Intermittent/Annular |
| 35 | 15 | 67 | 23.3 | 86 | Annular |
| 35 | 15 | 72 | 18.0 | 82 | Intermittent |
| 35 | 20 | 57 | 21.8 | 72 | Intermittent |

the entire bundle was not fully submerged and dryout was observed, were not able to meet this heat flux condition.

The relative uncertainties for the polycarbonate tube row heat flux range from ±7.2% to ±46.6% while the relative uncertainties for the side and angled polycarbonate tube row quality range from ±0.12% at high qualities to ±5.0% at low qualities.

### 6.1.2 Smooth Bundle Flow Pattern Identification

The flow patterns were captured using the high speed camera, borescope, and light source. During each test condition listed in Table 6.1, four total videos were recorded. The first pair, taken at 1000 fps and 3000 fps, view water channel D. This view is called the "side" view as it looks directly to the side of the polycarbonate tube. The second pair of videos, also taken at 1000 fps and 3000 fps, view water channel E. This view is known as the "angled" view as it looks upward at an angle towards channel E. Refer to Figure 3.15 for a diagram of the two viewing angles.

The side view shows the flow through the minimum cross sectional area of the tube bundle while the angled view shows the vertical section of the bundle that contains no tubes throughout the width. In many cases, different flow patterns are visible at these two views. The flow patterns reported in Table 6.1 are the flow patterns of the side view, as the minimum cross sectional area is traditionally used in literature to describe and classify flow patterns in the bundle. Figure 6.1 shows a set of five images taken from the test condition of 15 $kg/m^2 \cdot s$ mass flux, 16 $kW/m^2$ bundle heat flux, 35% inlet quality, 17.2 $kW/m^2$ PC row heat flux, and 60% PC row quality at 1000 fps. The images are spaced 10 ms apart, thus the total time between the first and last image is 40 ms.

The flow pattern in Figure 6.1 is classified as intermittent. Figure 6.1b are the same five images in Figure 6.1a with post processing applied to assist in detecting the vapor edges, allowing easier detection of flow structures in still images. In general, an intermittent flow pattern is classified as a combination of bubbly and annular flows. Separation of the annular flow by bubbly flow generates large vapor slug structures, typical of intermittent flows. These vapor slugs are visible, for example, in the last two images of Figure 6.1 rising from the bottom of the image. The solid black line approximately one-third up the image is the leading edge of a vapor slug. Additionally, bubbly flow is visible in the first three images in the upper portion of the frames. Ellipses outlined with a dark border and having a highlight are indicative of individual bubbles.

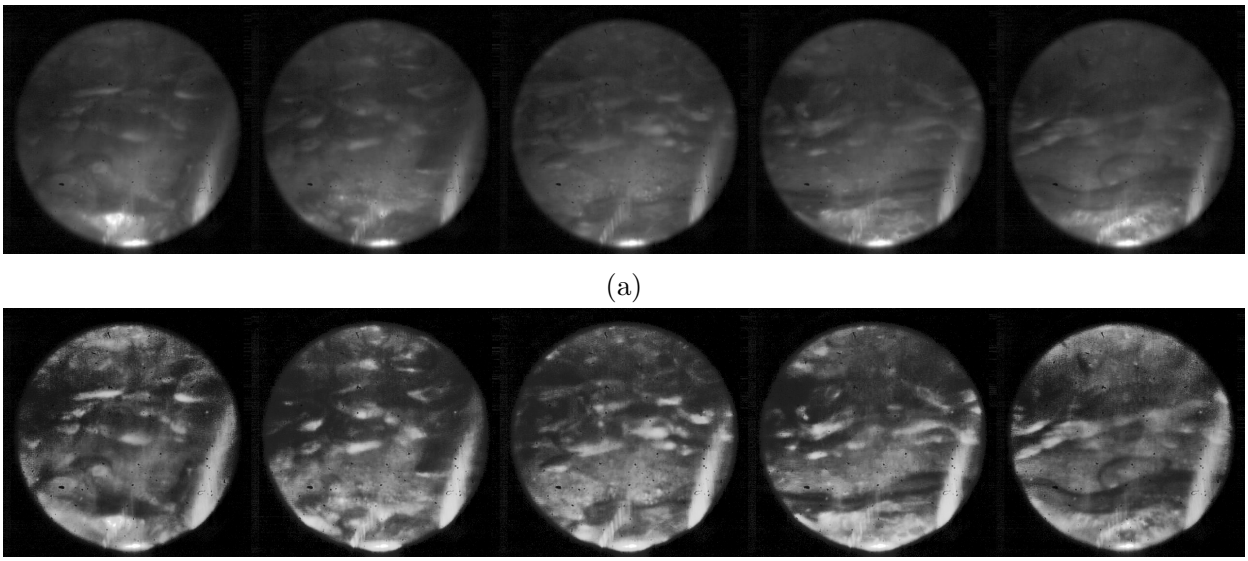

(a)

(b)

Figure 6.1: Smooth tube video images with a mass flux of 15 $kg/m^2 \cdot s$, heat flux of 16 $kW/m^2$, inlet quality of 35%, polycarbonate tube row heat flux of 17.2 $kW/m^2$, and polycarbonate tube row quality of 60% at 1000 fps, side view. Time step between images is 10 ms.

The use of high speed video significantly aides the detection and classification of flow patterns. Primarily, the time difference between each frame of the recorded video (0.33 - 1 ms)is much shorter than the given images in Figure 6.1 (10 ms); however, shorter time intervals between images are not given here as the difference between two subsequent frames is minimal and many still images would be required to view a significant change in the flow pattern. Secondly, the images are slightly out of focus due to the thickness of the polycarbonate tube, the fast motion of the bubbles, light refraction through the various media, and any focusing imperfections in the borescope. The use of high speed video reduces the influence of the motion blur as each image is only visible for a short amount of time.

## 6.2 Enhanced Tube Bundle Visualization Results

Similar to the smooth tube bundle, the results from the flow pattern visualization in the enhanced tube bundle is presented in this section. After reviewing the video from the smooth

tube bundle, it was decided that the 3000 fps video did not provide any additional insight to the flow pattern structures that were not visible in the 1000 fps video. Additionally, the faster frame rate requires more illumination to produce satisfactory images while the light source is already being used at maximum intensity. Thus, for the enhanced tube bundle tests, video was taken primarily at 1000 fps, and occasionally at 2000 fps to reduce the motion blur from increased vapor velocities.

### 6.2.1 Enhanced Bundle Test Matrix

All test conditions for the enhanced tube bundle are listed in Table 6.2. Unlike the smooth tube bundle, both the heat flux and the quality at the polycarbonate tube row were monitored with additional thermistors in the water channels. The experimental conditions fixed the polycarbonate tube row heat transfer fixed at 20 $kW/m^2$ and the vapor quality at the polycarbonate tube was changed by adjusting the test section inlet quality.

The relative uncertainties for the polycarbonate tube row heat flux range from ±5.1% to ±18.8% while the relative uncertainties for the side and angled polycarbonate quality range from ±0.14% to ±1.6%. The uncertainties in measurements for the enhanced tube bundle are generally lower than those of the smooth tube bundle due to the increased instrumentation in the water channels.

### 6.2.2 Enhanced Bundle Flow Pattern Identification

The general method of flow pattern identification for the enhanced tube bundle is similar to that of the smooth tube bundle; however, only two videos were recorded at most test conditions. These two videos were the side view and angled view recorded at 1000 fps. At some high vapor velocity test conditions, video was also recorded at 2000 fps for both views to reduce motion blur effects. The flow patterns for each test condition are listed in Table 6.2.

Detection of flow patterns in the enhanced tube bundle is slightly easier than the smooth tube bundle. The tube enhancements visible through the borescope provide a clear object

Table 6.2: List of all enhanced tube bundle testing conditions

| Mass Flux, $kg/m^2 \cdot s$ | Bundle Heat Flux, $kW/m^2$ | TS Inlet Quality, % | PC Row Heat Flux, $kW/m^2$ | PC Row Quality, % | Flow Pattern |
|---|---|---|---|---|---|
| 10 | 14 | 27 | 19.2 | 80 | Intermittent/Annular |
| 10 | 17 | 0 | 20.6 | 57 | Bubbly/Intermittent |
| 15 | 14 | 51 | 20.0 | 82 | Intermittent/Annular |
| 15 | 15 | 0 | 21.1 | 35 | Intermittent |
| 15 | 15 | 40 | 18.5 | 75 | Intermittent |
| 15 | 18 | 25 | 19.1 | 67 | Annular |
| 20 | 11 | 71 | 11.1 | 101 | Dryout |
| 20 | 11 | 72 | 10.6 | 102 | Dryout |
| 20 | 15 | 0 | 21.2 | 25 | Intermittent |
| 20 | 15 | 14 | 20.7 | 41 | Bubbly/Intermittent |
| 20 | 15 | 45 | 17.2 | 70 | Intermittent/Annular |
| 20 | 16 | 56 | 15.9 | 83 | Intermittent/Annular |
| 20 | 16 | 57 | 15.8 | 83 | Intermittent/Annular |
| 25 | 15 | 00 | 21.1 | 20 | Bubbly/Intermittent |
| 25 | 15 | 40 | 19.0 | 62 | Annular |
| 25 | 18 | 10 | 19.5 | 33 | Intermittent |
| 25 | 18 | 38 | 18.5 | 44 | Intermittent |
| 25 | 18 | 58 | 18.5 | 81 | Annular |
| 35 | 17 | 44 | 18.2 | 62 | Annular |
| 35 | 17 | 61 | 17.7 | 78 | Annular |
| 35 | 18 | 08 | 19.3 | 24 | Intermittent |
| 35 | 18 | 20 | 17.5 | 37 | Intermittent/Annular |

to focus the camera. With the borescope focused in this way, a region of pure liquid between the polycarbonate tube and the visible enhancements will have no distortion of the images. Figure 6.2a shows a series of images with only liquid between the polycarbonate tube and enhanced tube in the bottom portion of the image. The consistent enhancement images are visible by observing little variation in clarity and light reflection between the five images, spaced 1 ms apart.

When vapor enters the borescope view, the enhancements become distorted due to the wavy vapor interface traveling upward through the tube gap. On the trailing edge of vapor bubbles, or in high vapor velocity flows, the tube enhancements become completely obscured

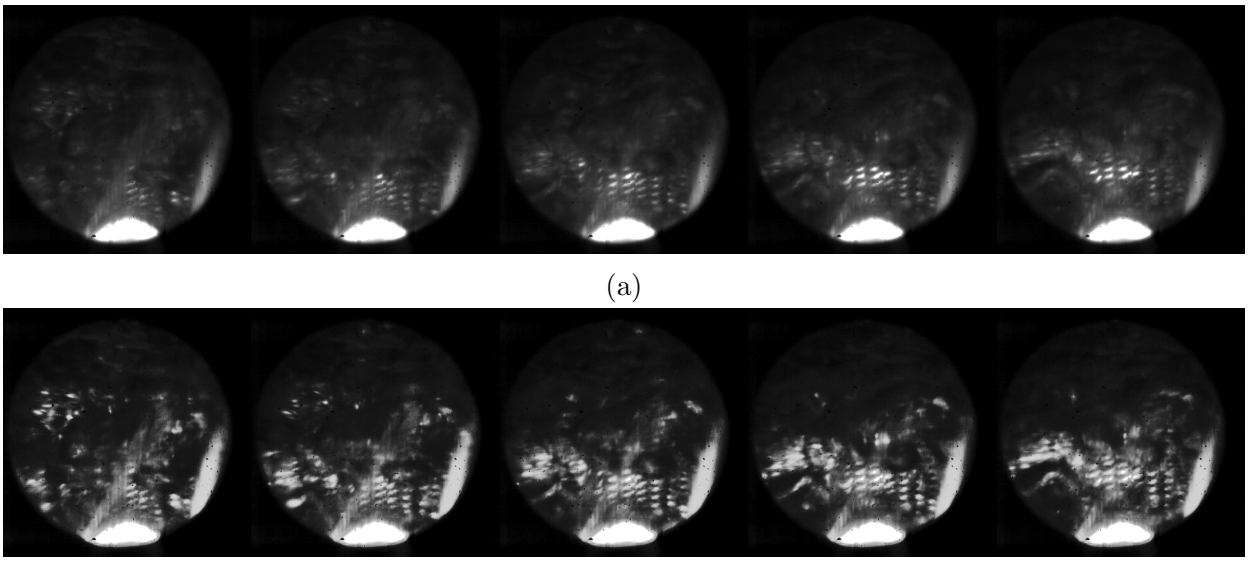

(a)

(b)

Figure 6.2: Tube enhancements as viewed through the borescope with the liquid only region visible. Time between images is 1 ms. Figure (a) are raw video images, (b) are post-processed images.

by the extremely wavy vapor and liquid interface.

Figure 6.3 shows a set of images from the testing condition of 15 $kg/m^2 \cdot s$ mass flux, 15 $kW/m^2$ bundle heat flux, 0% inlet quality, 21.1 $kW/m^2$ PC row heat flux, and 35% PC row quality at 1000 fps. The flow pattern of this testing condition is classified as intermittent, though in the five images shown, primarily bubbly flow is visible. At other points in the video, large vapor slugs are the predominant flow pattern, leading to the classification of intermittent flow.

In the first two images of Figure 6.3, a solitary elliptical bubble is visible in the bottom third of the image. As the bubble flows upward, its shape becomes more spherical in the third and fourth images. In the final image, this bubble has begun to coalesce with a neighboring vapor region. Also on the bottom third of the set of images is a rising vapor slug. The leading edge of this slug appears to be conical shaped and proceeds from the lower left portion of the first and second image and progresses towards the center of the remaining frames. This axial motion of bubbles and vapor regions is typical in many of the

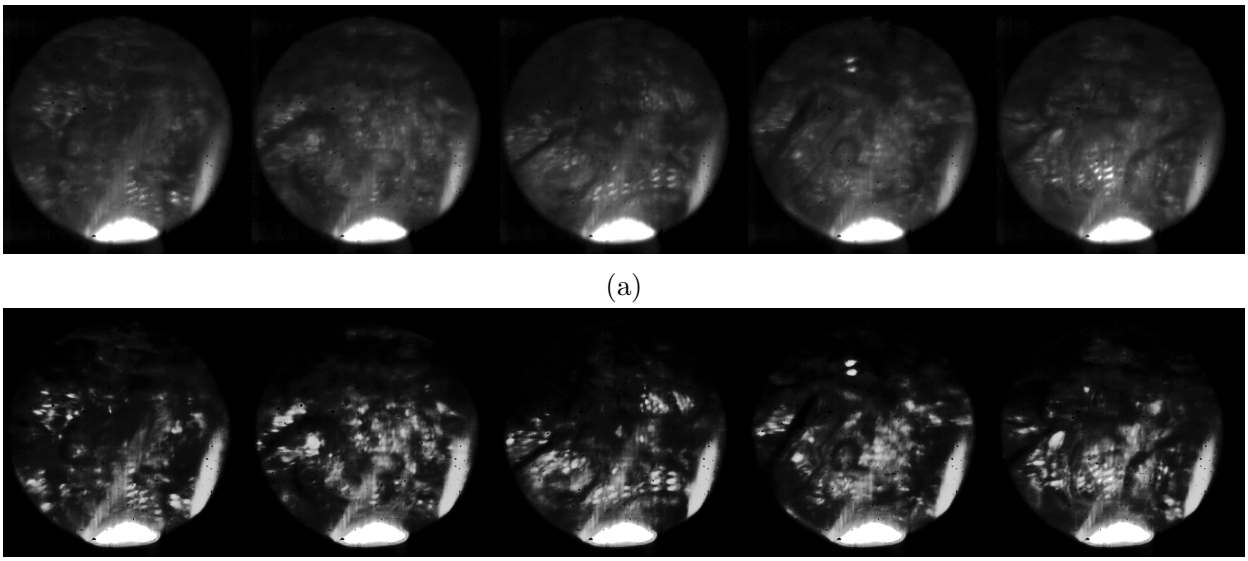

(a)

(b)

Figure 6.3: Enhanced tube video images with a mass flux of 15 $kg/m^2 \cdot s$, heat flux of 15 $kW/m^2$, inlet quality of 0%, polycarbonate tube row heat flux of 21.1 $kW/m^2$, and polycarbonate tube row quality of 35% at 1000 fps, side view. Time step between images is 10 ms.

recorded videos.

## 6.3 Summary

The analysis method for the smooth and enhanced experimental tube bundles has been presented. Examples of still images from each bundle have also been given. The flow patterns in each testing condition can be classified as either instantaneous or long-term flow patterns. In nearly all tests, individual bubbles can be seen at some instance in the images; this does not immediately classify the flow as bubbly flow. In those same videos, large vapor slugs can also be seen convecting smaller bubbles behind and occasionally coalescing with them. The reported flow patterns are a best attempt at classifying the long-term flow patterns by watching the entire video and determining the most appropriate flow pattern.

While reasonable agreement was found with the enhanced tube bundle, the results presented in this chapter highlight the difficulty and imprecision of using qualitative results to

classify flow patterns. Instead, attempts should be made to determine flow patterns quantitatively, using experimental or numerical methods. An attempt to classify flow patterns using CFD simulations and PDFs is presented in Chapter 7.

# Chapter 7

# Numerical Results

Following the experimental results description in Chapter 6, the numerical CFD results are presented in this chapter. First, a test matrix of the simulation conditions is given, followed with a grid independence study to show the mesh size does not influence the results. Finally, the results of the CFD simulations is presented through a PDF analysis of the vapor volume fraction at various locations in the tube bundle.

## 7.1 Test Matrix

Table 7.1 gives the refrigerant mass flux and inlet quality of the eight simulation points. The table also provides the detected flow pattern from each simulation. The flow pattern classification procedure is given in Section 7.2.4.

Table 7.1: List of all CFD simulation conditions

| Mass Flux, $kg/m^2 \cdot s$ | TS Inlet Quality, % | Closest Experimental PC Quality % | Flow Pattern |
|---|---|---|---|
| 10 | 10 | N/A | Intermittent |
| 10 | 80 | 80 | Annular |
| 15 | 33 | 35 | Intermittent |
| 20 | 22 | 22 | Intermittent |
| 25 | 18 | 20 | Intermittent |
| 25 | 45 | 44 | Annular |
| 25 | 82 | 81 | Annular |
| 35 | 24 | 24 | Annular |

The simulation conditions selected in Table 7.1 were chosen in an attempt to match the experimental testing conditions. As the simulation is adiabatic, the inlet quality was set matching an experimental polycarbonate tube row quality. Thus, after a number of tube rows in the simulation, bubble coalescence and breakup caused by the tube bundle will ideally provide a similar flow pattern to what was seen in the experimental tube bundle. Additionally, as only a finite amount of simulation time was available, the CFD simulation conditions were chosen to provide a wide range of possible flow parameters to plot on the adiabatic flow pattern map for a tube bundle of P/D=1.167 and R-134a as the working fluid, given in van Rooyen (2011). The range of flow parameters include low and high mass fluxes and vapor qualities.

## 7.2 CFD Simulation Results

In the following subsections, the CFD simulation results are presented. First, an analysis of the grid size is given, showing the three tested grid sizes and the determination of the most appropriate mesh. Following the grid independence study, the flow pattern classification procedure using the vapor volume fraction and PDF method is described, followed by an example of the CFD results using the vapor volume fraction and PDF of the vapor volume fraction.

### 7.2.1 Grid Independence Results

The purpose of a grid independence study is to determine if the chosen mesh size influences the simulation results. In general, a number of grid sizes is chosen and simulations are completed on each and the results are compared once the solution has converged.

Figure 7.1 shows the three selected grid sizes. The coarse mesh, in Figure 7.1a, doubled the size of the refined mesh, in Figure 7.1b presented in Section 4.4.2. The fine mesh, in Figure 7.1c, reduced the mesh size of the refined mesh by 33%. Figure 7.2 shows an enlarged view of the mesh between tubes.

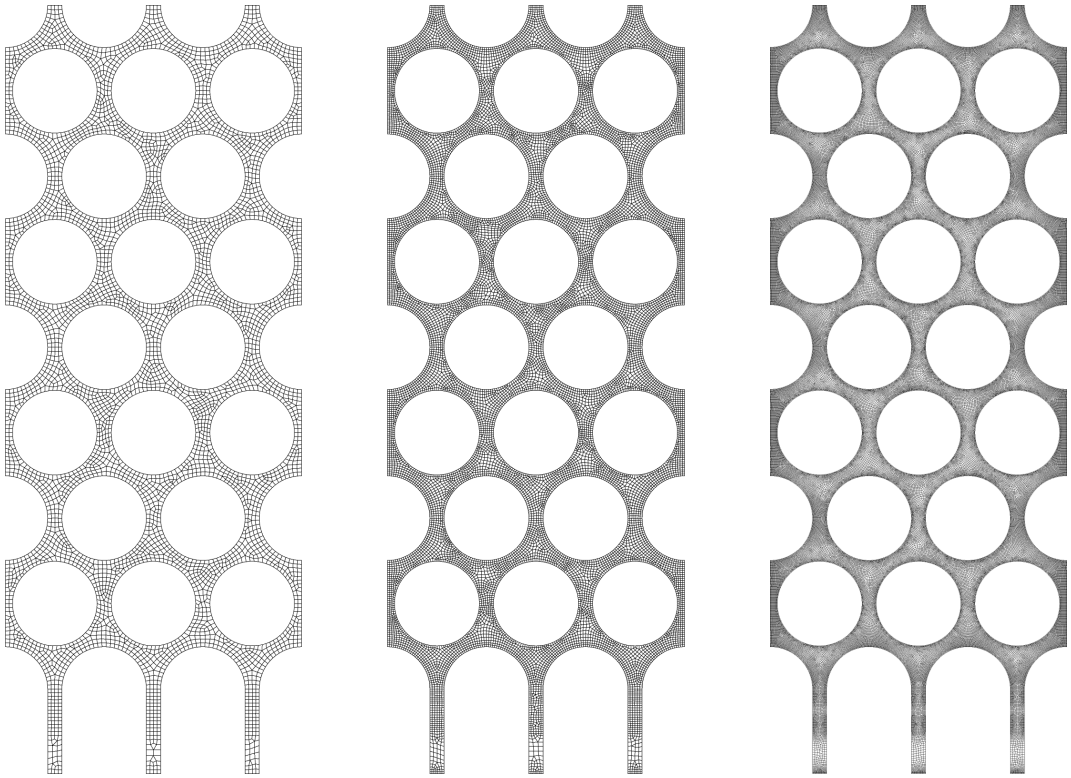

(a) (b) (c)

Figure 7.1: Overall view of meshes used in grid independence study showing the (a) coarse mesh, (b) medium mesh, and (c) fine mesh.

Three identical simulations are set up for the three mesh sizes at a mass flux of 25 $kg/m^2 \cdot s$ and inlet quality of 20%. The bundle average vapor volume fraction was recorded at each time step. At first, a linear increase of the bundle vapor volume fraction exists as the vapor progresses through the bundle. The vapor leaves the bundle through the upper outlets, the average vapor volume fraction begins to oscillate, and converges on a steady state value. Figure 7.3 compares the bundle averaged vapor volume fraction at each time step for the duration of the simulation.

The bundle averaged vapor volume fraction from Figure 7.3 clearly reaches a steady-state value for both the coarse and medium meshes. The fine mesh, which increases linearly similar to the coarse and medium meshes, was not run for the full time length due to computational resource restrictions. However, the rate of increase of bundle averaged vapor

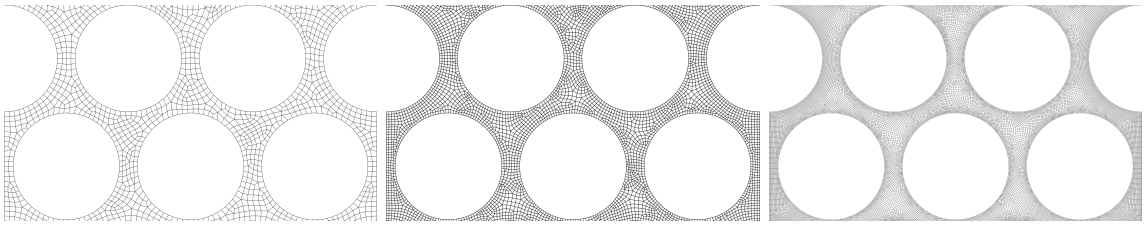

(a) (b) (c)

Figure 7.2: Closeup view of meshes used in grid independence study showing the (a) coarse mesh, (b) medium mesh, and (c) fine mesh.

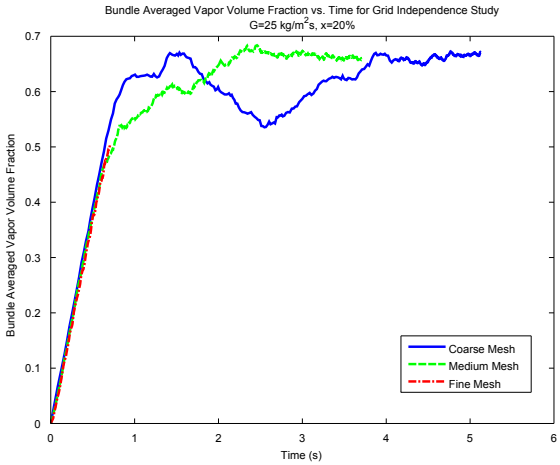


Figure 7.3: Average vapor volume fraction of the entire tube bundle for the three mesh structures.

volume fraction for all three meshes are similar.

The coarse and medium meshes both overshoot the steady-state vapor volume fraction. The outlet boundary condition allows for return flow, but the return flow is set to a pure liquid as explained in Section 4.4.3. Thus, the overshoot can be explained by the initial vapor formations quickly pushing through the outlet and preventing liquid from returning through the top. This leads to an elevated vapor volume fraction throughout the bundle. As the initial vapor passes through the outlets and mixing occurs near the top of the bundle, the outlets begin to have reverse flow of liquid returning into the domain, reducing the average vapor volume fraction.

Both the coarse and medium meshes achieve a steady-state bundle average vapor volume

fraction of around 66%. Generally, the mesh size which provides accurate results for the desired quantities at the lowest computational cost is selected for the remaining simulations. However, consideration of the interface definition is important in this work, thus the medium grid is chosen for the remaining simulations. The influence of the grid size on the interface definition is provided in Section 7.2.2.

### 7.2.2 Grid Influence on Interfaces

Not only does the grid size affect the potential results of the simulation, but the grid size also helps determine the resolution of the fluid interface as it is tracked through the bundle. As defined in Section 4.3.1, the interface must lie inside a fluid element. The larger a fluid element is, the less refined the interface will appear. While mass is still conserved for the larger element sizes, the interface geometry becomes less precise as the level-set function has fewer elements that it can track the interface through. For example, a mesh with four times as many elements may see two with a vapor volume fraction of 0%, one element with 50% and one with 100%, where a coarser mesh would have a volume fraction of 37.5%. The increase mesh resolution thus provides a significant increase in interface resolution.

While the purpose of a grid independence study is to verify that the mesh does not influence the simulation results, the mesh size is also important for determining precise semi-instantaneous vapor volume fractions using the PDF method described in Section 7.2.4. For example, a slow moving fluid with a large mesh may cause the PDF definition to see an intermediate void fraction far from 0 or 1 for a fixed $\Delta t$. By refining the mesh size, and thus decreasing the size of the interface, a finer mesh will contain more vapor volume fractions equal to 0 or 1. For the same $\Delta t$, the PDF may calculate a void fraction much closer to 0 or 1. The simulation with a finer mesh will more closely resemble experimental data acquisition methods.

An example of the influence of mesh size on the interface definition is given in Figure 7.4. From these images, it is immediately clear that a finer mesh provides more resolution of the

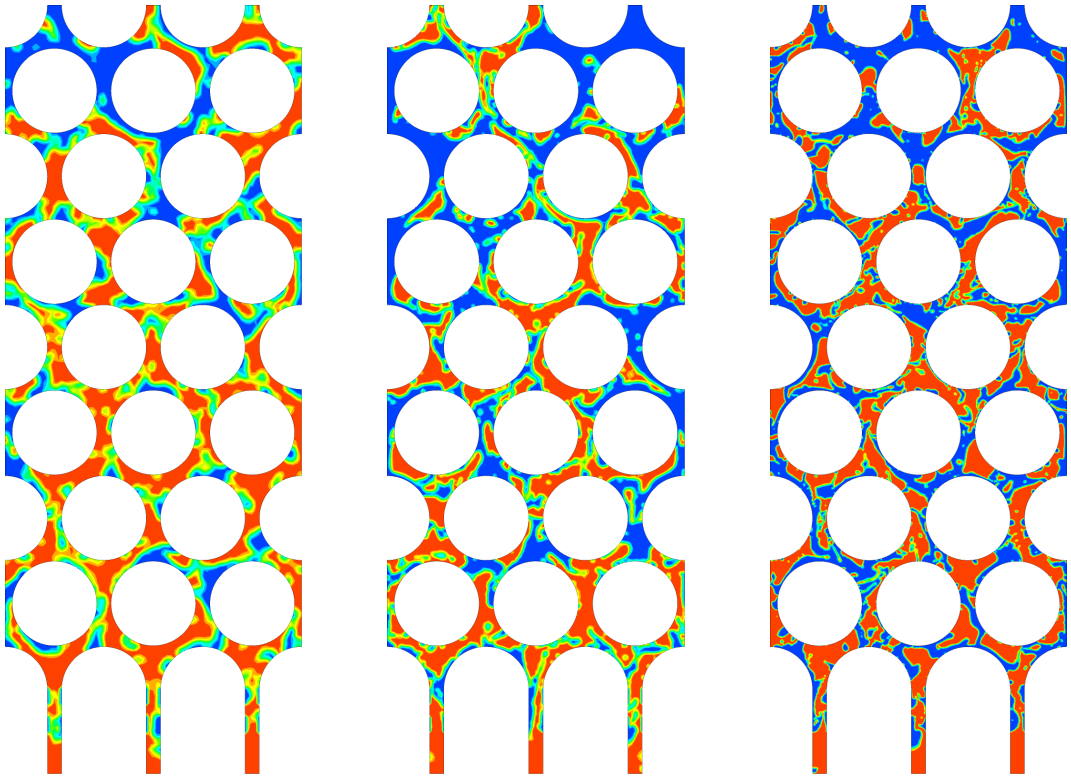

(a) (b) (c)

Figure 7.4: Grid influence on the two-phase interface using the (a) coarse, (b) medium, and (c) fine mesh from the grid independence study.

interface. Additionally, it is also apparent a finer mesh will provide fewer intermediate values of the vapor volume fraction during the PDF analysis method described in Section 7.2.3.1; the measurement location will record more data points with a vapor volume fraction of either 0 or 1 in a finer mesh simulation.

### 7.2.3 Analysis of Vapor Volume Fraction Past a Point

The CFD simulation case setup was described previously in Section 4.4. The setup was identical for the eight test cases simulated. In order to determine the flow pattern in the tube bundle, measurements of the vapor volume fraction are taken from the Fluent results at six locations. The choice of six locations is used to provide more data points at a reduced computational cost. A simulation comparing the results of running a simulation for 1 s and

recording data at six locations was compared to a simulation of 6 s with results taken at one location and is compared in Section 7.2.4.1. Before presenting the flow pattern results from any CFD simulation, the definition of the probability density function used to determine flow patterns must be given.

#### 7.2.3.1 Probability Density Function Definition

The probability density function method has been used in many studies to determine flow patterns (Ali et al. (1993); Aprin et al. (2007); Noghrehkar et al. (1999)). The value $P(\varepsilon)$ is the probability that the void fraction, $\varepsilon$, is less than some value. Then, $dP(\varepsilon)/d\varepsilon = p(\varepsilon)$ is the probability per unit void fraction that the void fraction lies between $\varepsilon$ and $\varepsilon + d\varepsilon$. If $N$ is the total number of void fraction values recorded, then $n_i$ is defined as the number of void fraction measurements that lie between $\varepsilon$ and $\varepsilon + d\varepsilon$, given that the void fraction is discretized into equally spaced intervals. The ratio of $n_i$ and $N\Delta\varepsilon$ is therefore equal to $p(\varepsilon)$. Additionally, if the recorded signal is a high-low signal similar to optical or electrical probes, then the void fraction can also be represented by the fraction of time that the signal is in the high state, thus

$$\frac{n_i/N}{\Delta\varepsilon_i} = \frac{1}{\Delta\varepsilon}\sum_{k=1}^{n_i}\frac{t_{G,k}}{T_{Rec}} \tag{7.1}$$

If the window of time discretizations, $\Delta t_{G,k}$ is small enough, the PDF of void fractions can be represented by either the left or right hand side of Equation (7.1). In experimental results, such as that of Aprin et al. (2007), the void fraction is calculated as

$$\varepsilon_j(t) = \frac{t_{G,k}}{\Delta t} \tag{7.2}$$

that is, the void fraction is the fraction of time the probe tip is in vapor for the given time window, $\Delta t$. For the CFD simulations where the interface, as a function of the mesh size, can generate fractional values of the vapor volume fraction between 0 and 1, the PDF of the void fraction can be estimated as

$$PDF_{\varepsilon_i} = \frac{n_i/N}{\Delta\varepsilon} \tag{7.3}$$

where i is the void fraction window. In these results, the void fraction is discretized into 20 intervals, setting $\Delta\varepsilon = 0.05$. Additionally, the time is discretized such that $\Delta t = 0.02\ s$.

The PDFs are generated by measuring the vapor volume fraction at a specific point every 0.001 s in the bundle and averaging over the 0.02 s window. Then, this average vapor volume fraction is put into the $\Delta\varepsilon$ bins similar to a histogram. After calculating these 0.02 s average vapor volume fraction for the entire time series, the right hand side of Eq. (7.3) contains the number of times a vapor volume fraction value fell within the $\Delta\varepsilon$ range, generating a PDF of the vapor volume fraction.

### 7.2.4 Analysis of Flow Pattern Observations

Determining the flow patterns from the CFD simulation results requires taking the vapor volume fraction at a location, averaging the value over a fixed $\Delta t$, and plotting into a histogram with fixed-width $\Delta\varepsilon$ bins, as described in Section 7.2.3.1. The vapor volume fractions are recorded at six locations throughout the bundle to provide an increased number of measurements. This technique is validated in Section 7.2.4.1 below. Following the validation of the measurement method, an example of the flow pattern analysis is given in Section 7.2.4.2.

#### 7.2.4.1 Comparison of Six Result Locations to One Result Location

Experimental data, especially with invasive techniques like optical or electrical probes, is taken at a single location for a set time and a high sampling rate. Taking additional data downstream of an optical or electrical probe may influence the downstream void fraction values. However, the CFD techniques used here are computationally intensive, so running a simulation for an extended length of time is impractical. One method of acquiring more data, as no invasive techniques are used with CFD simulations, is to sample from multiple locations simultaneously. In this work, data was collected at six sampling locations during the 1 second simulation time, for a total of six seconds of collected data. This time length nearly matches the experimental procedure for $n$-pentane and propane in Aprin et al. (2007)

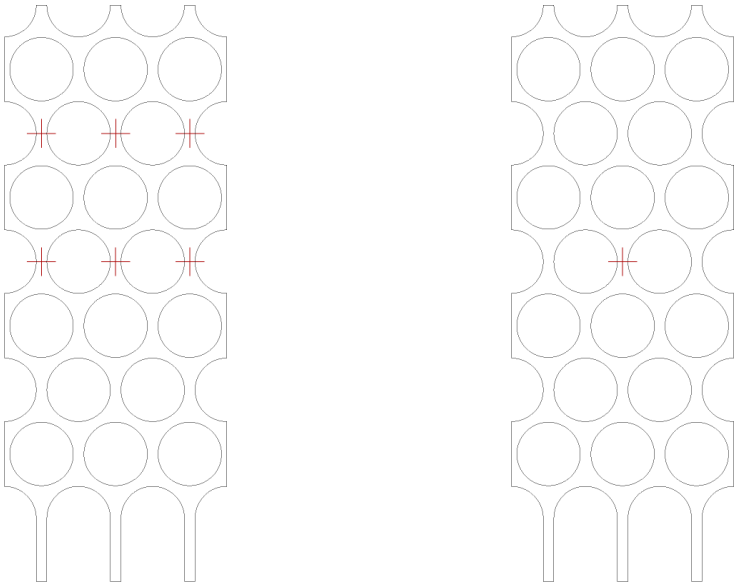

(a) (b)

Figure 7.5: Positions of the measurement locations for the (a) six-location simulation, run for 1 s, and (b) the single-location simulation, run for 6 s.

of 6.4 s, although their sampling rate was set at 5 kHz, where the sampling rate in this study is set at 1 kHz. It is expected that taking data at multiple locations will yield independent vapor volume fraction measurements, as long as the data points are far enough apart that the flow is allowed to mix further as it moves downstream.

The six-location measurement method was verified using a one-location measurement simulation run for 6 s. The 6 s simulation was performed at a mass flux of 10 $kg/m^2 \cdot s$ and an inlet quality of 10%. Figure 7.5a shows the position of the six measurement locations for the 1 s simulation, while Figure 7.5b shows the position of the single measurement location for the 6 s simulation.

The vapor volume fractions were recorded every 0.001 s for both the six- and single-location simulations and averaged over 0.02 s for creating the PDFs. Figures 7.6a and 7.6b show the PDFs generated for the six- and single-location simulations, respectively, for a fixed simulation time step of $\Delta t_{sim} = 0.001s$.

The results from Figure 7.6 show that both the six-location simulation, run for 1 s,

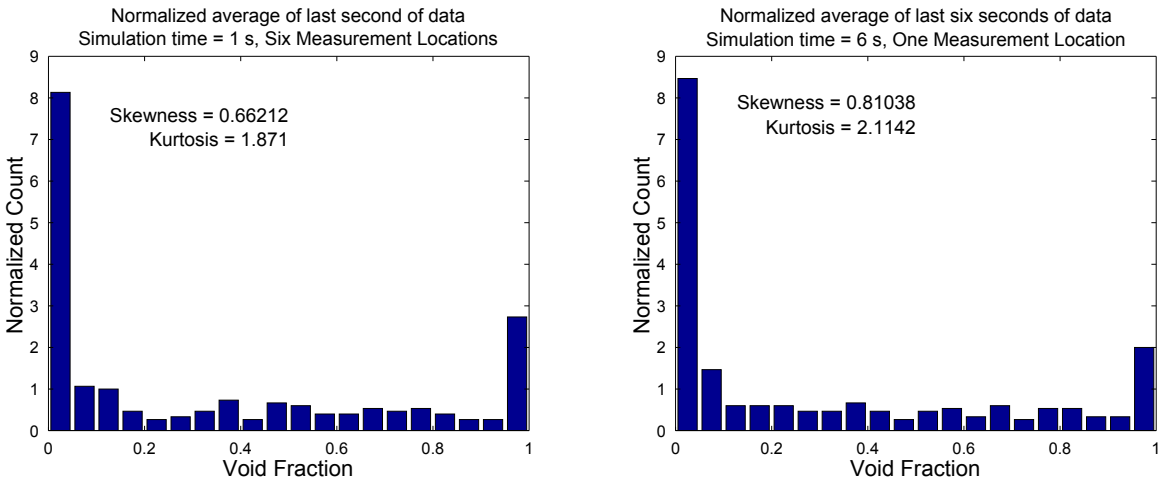


(a) (b)

Figure 7.6: Comparison of the vapor volume fraction PDFs generated from the (a) six-location simulation, run for 1 s, and (b) the single-location simulation, run for 6 s.

and the single-location, run for 6 s, have very similar normalized PDFs. The skewness coefficient for both plots, $C_{M3} = 0.66212$ for the six-location simulation and $C_{M3} = 0.81038$ for the one-location simulation, give the PDF positive skew, indicating a larger number of low void fractions. The kurtosis for both plots, $C_{M4} = 1.8710$ for the six-location simulation and $C_{M4} = 2.1142$ for the one-location simulation, is less than 3, indicating that the flow pattern is intermittent. The percent error between the one-location measurement and six-location measurement skewness is 18.3% while the percent error of the kurtosis is 11.5%. These percent differences are deemed acceptable, showing that the six-location measurement technique will give reasonable results compared to running the same simulation for a longer time period. For the analysis of flow patterns in the CFD simulations, the six-location measurement technique for 1 s simulations is used exclusively.

#### 7.2.4.2 Flow Pattern Analysis Example

The example presented here uses a mass flux of 20 $kg/m^2 \cdot s$ and inlet quality of 22%. After completing the CFD simulation, the vapor volume fraction for the entire domain at every time step is loaded. Three intermediate vapor volume contour images, spaced 0.01 s

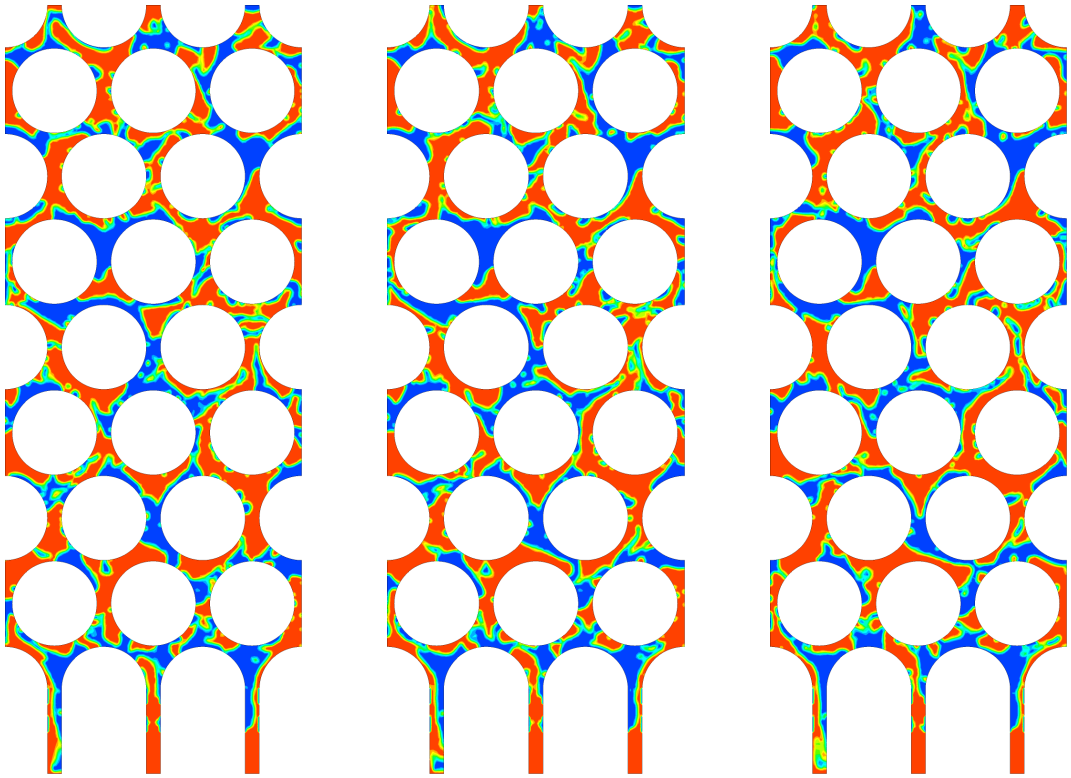

(a) (b) (c)

Figure 7.7: Example of the simulated flow patterns for a mass flux of 20 $kg/m^2 \cdot s$ and inlet quality of 22%. Each image is spaced apart 0.01 s.

apart, are given in Figure 7.7 as an example of the flow pattern seen for this simulation.

At the six measurement locations shown in Figure 7.5a, the vapor volume fraction is recorded for each time step to a .csv file. This data file is loaded into Matlab which stores each location and the time vector into separate vectors.

Once the six volume fraction vectors are loaded, the software looks for the first non-zero vapor volume fraction value at any measurement location, indicating that vapor has progressed to the measurement sites. After this time value, every instantaneous volume fraction measurement is recorded and plotted in a histogram with bin widths of $\Delta\varepsilon = 0.05$. This histogram, shown in Figure 7.8a gives an early indication of the flow pattern characteristics. Not much value is given to this histogram, as the measurement locations higher in the bundle will still be recording volume fraction values of zero until the vapor

progresses past those locations.

Once the first histogram containing all volume fraction values after the first non-zero value is plotted, the software strips off the initialization phase of the simulation, leaving only the last second of simulation time with fixed $\Delta t = 0.001$ s. The software averages every 20 measurements as described by the PDF method. The average vapor volume fractions for the last second are then placed into a histogram with fixed bin widths of $\Delta\varepsilon = 0.05$. This histogram is shown in Figure 7.8b.

Finally, the histogram in Figure 7.8b is normalized by the total number of measurements. This normalized histogram follows the PDF analysis method as described in Section 7.2.3.1, and is shown in Figure 7.8c.

In addition to the histograms at each step, values for $C_{M3}$ and $C_{M4}$ are displayed on each plot. For this example, $C_{M3} = -0.90822$ and $C_{M4} = 2.5475$. As described in Section 2.2.1, a value of $C_{M4} < 3$ indicates intermittent flow. Additionally, $C_{M3} < 0$ indicates that more vapor structures resembling annular flow are seen. This can be interpreted as intermittent flow with significantly more large vapor slugs than small vapor bubbles.

A final figure, Figure 7.8d, is plotted. This is simply the flow pattern map proposed by van Rooyen (2011) for adiabatic flow in a tube bundle with P/D = 1.167. The simulation data point is plotted for convenient comparison of $C_{M3}$ and $C_{M4}$ with the experimental flow pattern map.

## 7.3 Summary

In this chapter, the numerical simulation analysis method has been presented. A grid independence study was performed showing that the selected medium mesh size is adequate in determining void fractions in the bundle while preserving the liquid-vapor interfaces. The analysis method used to determine flow patterns by measuring vapor volume fraction was also presented, including a detailed formulation of the PDF method used in experimental work and its adaptation to the CFD simulations in this research. Using the PDF anal-

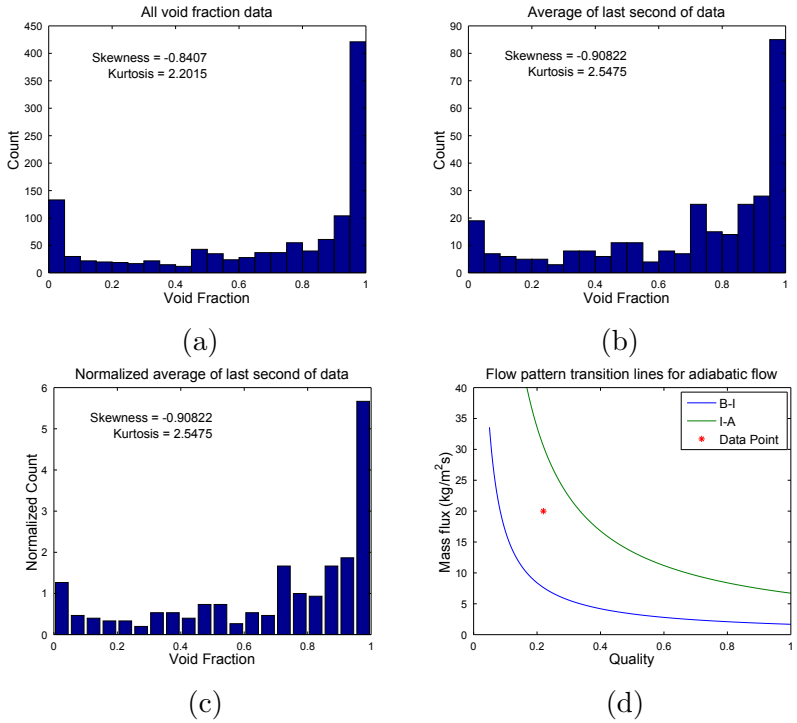


Figure 7.8: CFD results for x=22%, G=20 kg/m$^2$s. Flow pattern map adapted from van Rooyen (2011)

ysis method, an example simulation was presented showing the resulting flow pattern as determined by the coefficients of skewness, $C_{M3}$, and kurtosis, $C_{M4}$.

# Chapter 8

# Discussion

In Chapter 6 and Chapter 7, the methods of analyzing the experimental and CFD results were presented. This chapter summarizes all of the results for the experimental and numerical research. The first section details the findings from the experimental smooth and enhanced tube bundle flow patterns. Comparison of the flow patterns with flow pattern maps from literature is completed. Following the experimental summary is the presentation of the CFD findings. These findings are supplemented with further analysis of the flow patterns at low mass flux and inlet quality, as well as the influence of measurement height in the bundle.

Following the presentation of all data is a section detailing possible future work to be completed. An ever growing need for experimental data sets for empirical model generation is needed; additionally, exploring other models used for CFD simulations could greatly impact the design of tube bundles used in the industry.

## 8.1 Summary of Experimental Results

Analysis of the flow patterns was done for each recorded video at both views for all frame rates to ensure accurate flow pattern descriptions according to the example in Sections 6.1.2 and 6.2.2. The flow patterns were then plotted on a flow pattern map to compare the experimental results with the results of other researchers. These flow pattern map comparisons are presented in the subsequent sections.

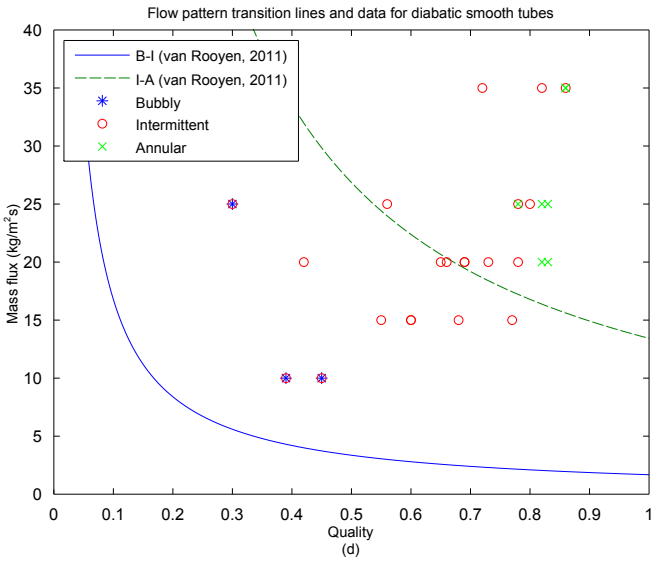


Figure 8.1: Plot of smooth tube bundle flow patterns mapped against the flow pattern map presented in van Rooyen (2011), assuming 20 $kW/m^2$ on the polycarbonate tube row. $u_{g,trans} = 0.1\ m/s$ and $u_{g,trans} = 0.8\ m/s$.

### 8.1.1 Smooth Bundle Flow Pattern Map

Figure 8.1 shows a flow pattern map for the smooth tube bundle. The transition lines are provided by van Rooyen (2011) for diabatic enhanced tube bundle at a heat flux of 20 $kW/m^2s$ with transition vapor velocities of 0.1 $m/s$ and 0.8 $m/s$. It is immediately clear that the flow patterns do not closely match the map provided. There are a number of reasons for this, primarily the tube surface geometry. Enhanced tubes generate more vapor as smaller bubbles, causing flow patterns to shift to higher qualities as the fast vapor generation causes bubbles to coalescence into larger vapor slugs. Additional differences between the flow pattern map experimental basis and the current results include the inexact method of determining the polycarbonate tube row heat flux during testing and unknown transition vapor velocities to plot accurate transition boundaries.

No completely bubbly flows were detected in the smooth tube tests. However, three test conditions were found to have significant bubbly flow interspersed with larger vapor structures. Additionally, while completely annular flows were detected, two annular test

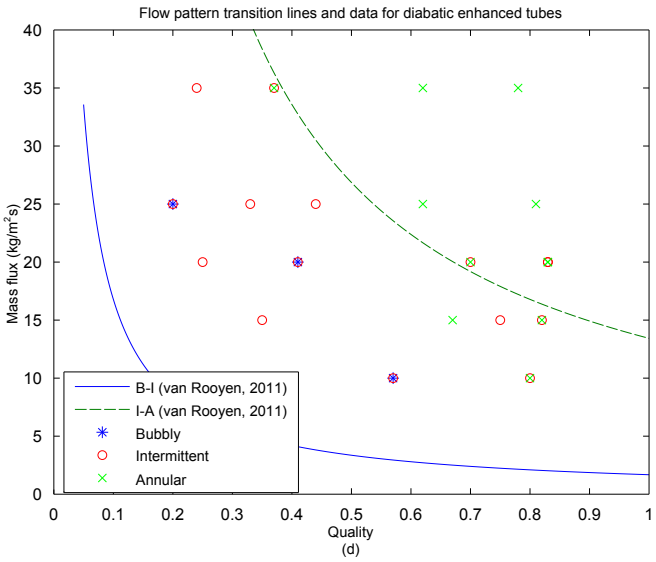


Figure 8.2: Plot of enhanced tube bundle flow patterns mapped against the flow pattern map presented in van Rooyen (2011), assuming 20 $kW/m^2$ on the polycarbonate tube row. $u_{g,trans} = 0.1\ m/s$ and $u_{g,trans} = 0.8\ m/s$.

conditions had significant amounts of individual vapor slugs indicating intermittent flow as well as annular flow. The cases where significant amounts of two different flow patterns were observed, the data point is plotted as having both flow patterns and should be interpreted as a possible transition condition.

### 8.1.2 Enhanced Bundle Flow Pattern Map

Figure 8.2 shows the flow pattern map results for the enhanced tube bundle. A brief look at the flow pattern map for the enhanced tube bundle shows better agreement than the results for the smooth tube bundle. Again, no bubbly flows were seen but transitional flows were detected at several testing conditions. One test condition classified as purely annular flow appears in the intermittent region while the bubbly/intermittent transition flow patterns are significantly farther into the intermittent region than the proposed transition line.

## 8.2 Conclusion of Experimental Results

When the flow patterns for both tube bundles are plotted against the flow pattern map proposed by van Rooyen (2011), it is clear that differences exist between this experimental work and previous results. The smooth tube bundle flow patterns show only moderate agreement with the flow pattern map. Many differences between the experimental conditions in this work and in van Rooyen (2011) exist, contributing to the discrepancy. These differences include tube type, heat flux, vapor velocity, and flow pattern identification techniques.

The enhanced tube bundle flow patterns agree much closer with the flow pattern map. Only a few of the detected flow patterns in this work fall outside the flow pattern map transition lines. The closer agreement is most probably due to the similar tube type and more precise measurement of heat flux at the polycarbonate tube row.

## 8.3 Summary of CFD Flow Pattern Results

After performing the analysis detailed in Section 7.2.4.2 for every CFD simulation point, the flow patterns are decided based on the $C_{M3}$ and $C_{M4}$ values of the normalized last second of averaged vapor volume fraction histograms. Using the criteria put forth by Aprin et al. (2007) and used throughout this work, the flow patterns are identified and plotted against the adiabatic flow pattern map of van Rooyen (2011). Figure 8.3 shows the transition regions and the flow patterns detected for each simulation point.

### 8.3.1 Revisit of Low Mass Flux and Quality Simulation

As can be seen, all but one flow pattern agrees with the flow pattern map. The lowest inlet quality and mass flux point does not agree with the flow pattern map. The normalized PDF for this simulation point, with an inlet quality of 10% and mass flux of 10 $kg/m^2 \cdot s$, is shown in Figure 8.4.

The calculated values of $C_{M3}$ and $C_{M4}$ clearly indicate this point to be intermittent. However, the skewness value is moderately positive, suggesting that the flow is nearing the

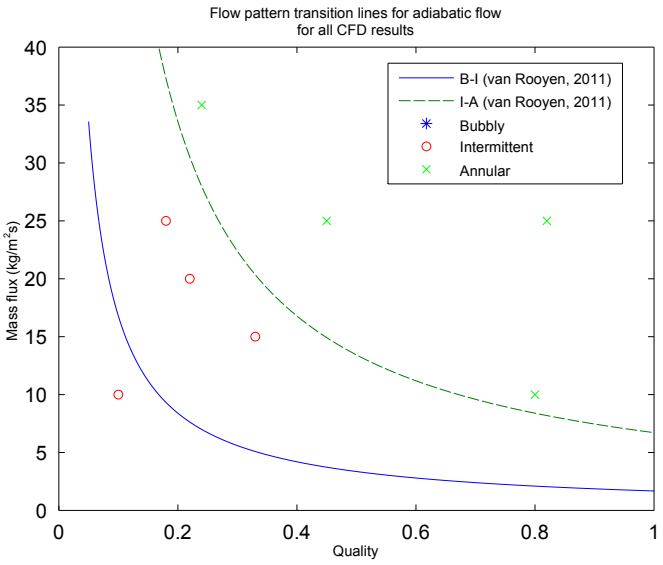


Figure 8.3: Summary of the detected flow patterns from each CFD simulation point, plotted on the adiabatic flow pattern map of van Rooyen (2011). $u_{g,trans} = 0.1\ m/s$ and $u_{g,trans} = 0.4\ m/s$.

transition region of bubbly-intermittent flow. After analyzing the CFD interfaces through an animation of every data point, it is found that the long inlets to the tube bundle may be creating a vapor hold-up region caused by falling liquid. The vapor stays in the inlet region until the buoyancy force of the trapped vapor slug allows it to push past the liquid above. This mechanism promotes larger vapor structures to be formed in the inlet region than might otherwise be seen in an experimental bundle. These larger vapor structures may then fail to break up before reaching the measurement locations, causing the PDF results to be skewed towards intermittent and annular flow.

A second geometry was created to investigate the possible issue of liquid preventing vapor from leaving the inlet region. This new geometry contains a much shorter inlet region and is shown in Figure 8.5. Identical mesh refinement properties and boundary conditions to the long inlet geometry is used. However, due to the shorter inlet sections, only six vapor inlets exist prior to the first set of semicircular tubes at the bottom of the bundle, rather than the 12 vapor inlets for the long inlet geometry. Identical model properties to the long inlet geometry is used to determine the flow characteristics in the new, short inlet geometry.

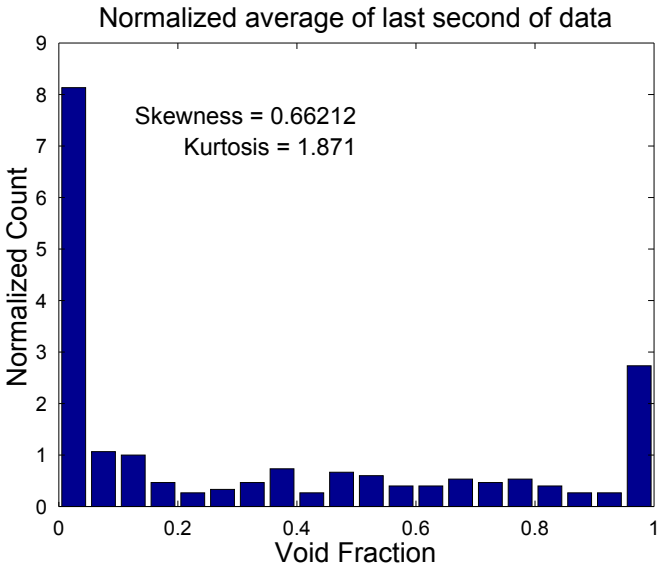


Figure 8.4: Normalized PDF of the only misidentified flow pattern with an inlet quality of 10% and mass flux of 10 $kg/m^2 \cdot s$. Flow pattern map from van Rooyen (2011).

Figure 8.6 shows a comparison of the long inlet and short inlet vapor volume fractions and interface geometry at similar simulation times.

A similar PDF analysis of the vapor volume fraction was performed for the short inlet geometry. Using the same six measurement locations, the normalized PDF in Figure 8.7b is constructed and can be compared with the normalized PDF for the long inlet geometry in Figure 8.7a.

From both the flow patterns shown by the vapor interfaces in Figure 8.6b and the normalized PDF in Figure 8.7b, the flow pattern is approaching bubbly flow. However, the flow pattern is still classified as intermittent using this geometry. The increase in bubbly flow for the shorter inlet section validates the idea of liquid suppressing vapor from leaving the long inlet sections, yet additional improvements may be possible to obtain statistically bubbly flow, such as decreased mesh size to sharpen the vapor interface or a change of $\Delta t$ in the PDF definition to reduce the effects of a wider interface.

It is not needed to revisit other simulations with the short inlet geometry. Increasing the mass flux and quality of refrigerant entering the bundle increases the rate of vapor

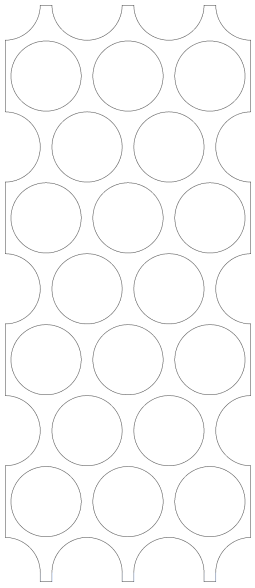

Figure 8.5: Short inlet geometry for verification of long inlet simulation at an inlet quality of 10% and mass flux of 10 $kg/m^2 \cdot s$.

generation and reduces the effects of vapor hold-up found in the low quality, low mass flux simulation.

### 8.3.2 Analysis of Height Influence on Void Fraction

An analysis of the void fraction at multiple heights was carried out with a mass flux of 10 $kg/m^2 \cdot s$ and inlet quality of 10%. Six separate locations were recorded for 7 s of simulation time. Figure 8.8 shows the six measurement locations of the tube bundle.

Using the same simulation procedure as before, an initialization simulation was run to fill the bundle with vapor and liquid. The Matlab software recorded all vapor volume fractions after the first non-zero value as well as the last 7 s of data, recorded at an interval of 0.001 s. Using the last 7 s, PDFs of the void fraction at each location were calculated. These PDFs are shown in Figure 8.9 for all measurement locations, from the highest to lowest point.

As the flow patterns are determined by the skewness and kurtosis coefficients, these values are plotted on Figure 8.10 with the tube row number as the independent variable. It appears that there is a downward trend for both the skewness and kurtosis, however

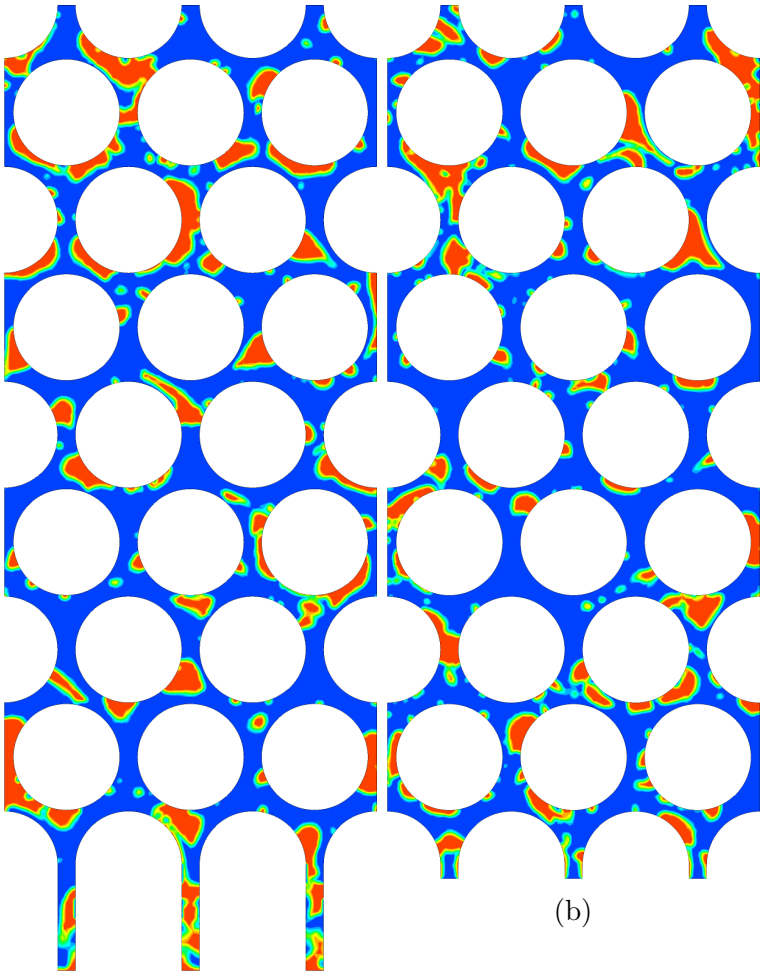

(a) (b)

Figure 8.6: Comparison of the long inlet and short inlet flow patterns at identical simulation times for the simulation of 10% inlet quality and mass flux of 10 $kg/m^2 \cdot s$.

the change in both values is relatively small with the skewness decreasing by 22% and the kurtosis by 14%. At both the highest and lowest measurement locations in the tube bundle, the flow would still be classified as intermittent flow ($C_{M4} < 3$) with slightly more bubbly flow than annular flow ($C_{M3} > 0$).

## 8.4 Conclusion of Numerical Results

All of the numerical simulations were compared to an existing adiabatic flow pattern map by van Rooyen (2011) for a staggered tube bundle with P/D=1.167 and R-134a as the

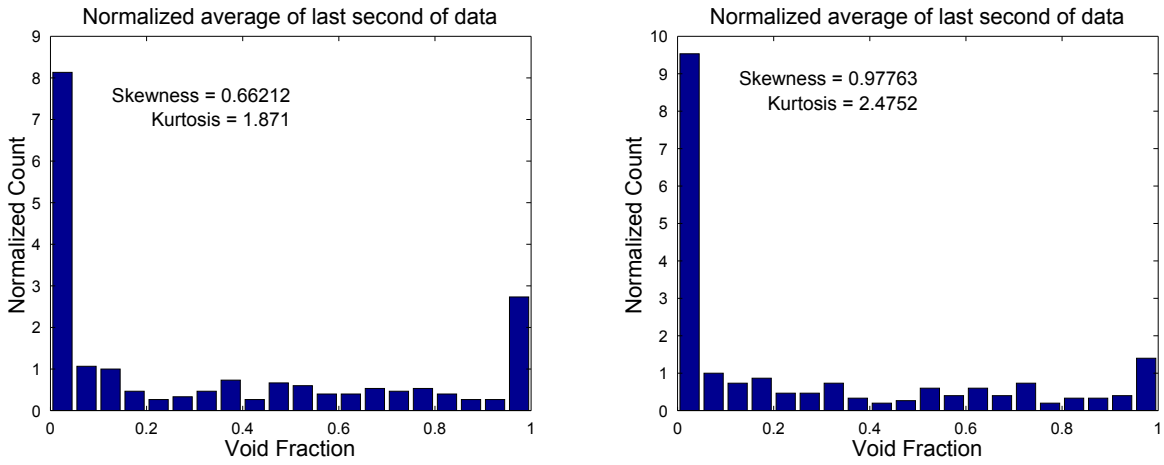


(a) (b)

Figure 8.7: Comparison of the normalized PDFs for the long and short inlet geometries at an inlet quality of 10% and mass flux of 10 $kg/m^2 \cdot s$.

working fluid. Nearly all flow patterns are correctly identified with the numerical methods presented here, except the lowest mass flow rate and inlet quality. For this condition, the inlet length was explored as a possible source of error at such low vapor velocities. The normalized PDF of void fraction for the short inlet length shows an increase in bubbly flow, though it is still classified as intermittent. A complete set of PDFs for every CFD simulation is provided in Appendix E.

## 8.5 Future Work

As with any developing field, future research is needed to progress the state-of-the-art. Tube bundle research consists of many areas including heat transfer, pressure drop, fouling, tube vibration, and bundle characteristics. These research areas lead to new empirical models for designing tube bundles. Ideas for further research relating directly to this work are presented in the subsections below.

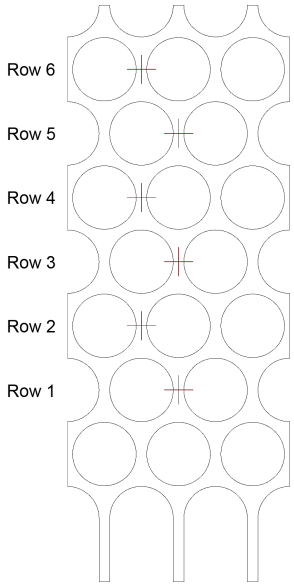


Figure 8.8: Measurement locations in the tube bundle to explore the effect of height in the tube bundle on void fraction measurements.

#### 8.5.0.1 Future Experimental Analysis Opportunities

Because this research consisted primarily of simple bundle visualization techniques, there are many areas to be improved for a wider applicability, increased accuracy, and scope of results. In general, various bundle configurations using different tube types, P/D ratios, and working fluids can all be explored. Additional experimental data sets will help validate and verify CFD simulations as the numerical analysis field progresses.

While testing various bundle geometries and parameters will increase the amount of experimental data available, new visualization techniques can also be introduced. In this research, the flow was visualized outside of an adiabatic, clear polycarbonate tube with an opposite diabatic tube. Other research has used diabatic flow while visualizing from an end plate or side sight glass, while further studies have taken in-bundle visualizations in adiabatic regions. A drive to somehow allow for internal visualization of completely diabatic regions should be pursued. This may involve a borescope run through an active tube with a very small sight window removed for visual access, running a very thin fiberscope along the shell-side of an active tube, or a combination of the two. Advancements in optics may be

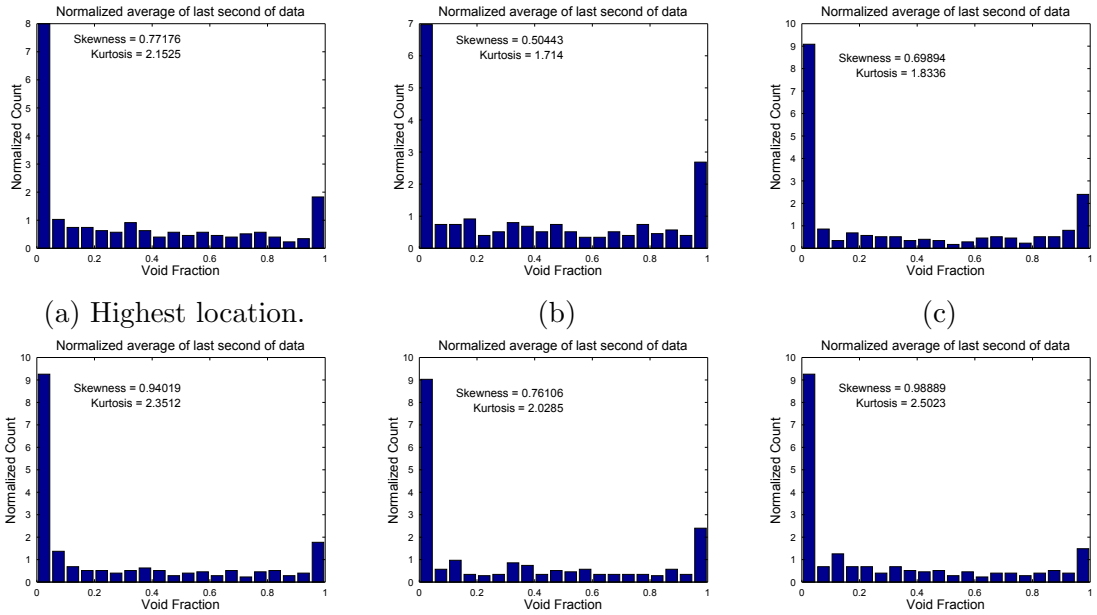


(a) Highest location. (b) (c)

(d) (e) (f) Lowest location.

Figure 8.9: Void fraction PDFs at various heights in the tube bundle for the simulation of 10% inlet quality and mass flux of 10 $kg/m^2 \cdot s$.

necessary to produce the resolution needed for thin fiberscopes. Additional improvements to focusing mechanics and video capture technology to reduce the effects of motion blur, light refraction, and manual focus could also greatly impact the flow visualization in tube bundles.

Simultaneous video recordings at various heights, widths, and angles could also prove beneficial for bundle designing and CFD validation and verification. High speed video recorded simultaneously, or at a known time offset fixed by vapor and bubble velocity, may allow tracking of vapor structures throughout a bundle. Taking high speed video of the same location from different view points would better visualize the three dimensional movements of vapor and liquid, as well as provide insight on the change of vapor structures moving between minimum and maximum bundle cross sectional areas between tube rows. Similar problems as described above would still need to be addresses, especially the use of active tubes at the visualization site. Particle image velocimetry (PIV) inside the bundle using suspended particles would increase the accuracy of vapor and liquid velocity measure-

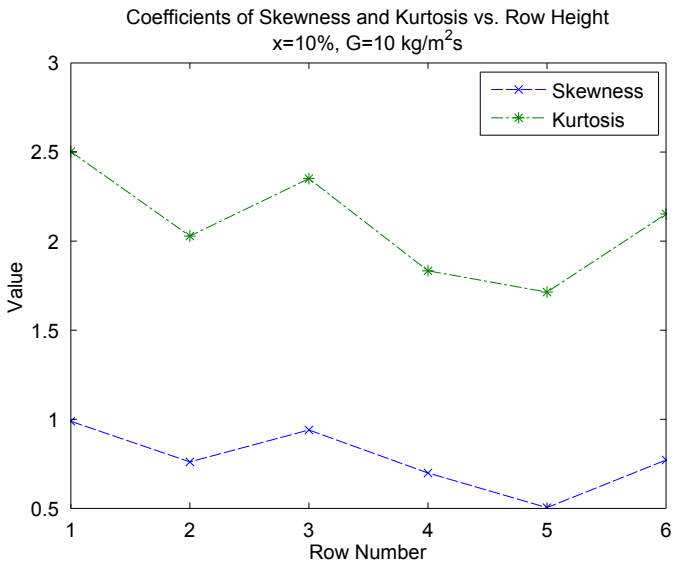


Figure 8.10: Variation of the skewness and kurtosis of the void fraction PDFs with a change in height for a simulation mass flux of 10 $kg/m^2 \cdot s$ and inlet quality of 10%.

ments, though difficulties arise with inserting foreign material into the refrigerant stream, potentially causing damage to tubes, equipment, and problems with refrigerant recovery and removal of particles from the system.

#### 8.5.0.2 Future Numerical Analysis Opportunities

As computers, clusters, and supercomputers become less expensive, more powerful, and more available for CFD simulations, an endless number of new research opportunities exist. Direct expansion of the work presented in this thesis can be performed with current desktop computer hardware by exploring different turbulence models, bundle geometries, and fluid properties in adiabatic simulations. These simulations could then be validated by experimental datasets.

With increased computational power, other CFD simulation options are available. One of the most important improvements to this work would be implementing heat transfer either through empirical models or solving the energy equation allowing for mass transfer between phases. This work could extend to small scales by incorporating wall superheat

changes as bubbles grow and detach from tube surfaces, the implementation of enhanced surfaces, pressure change of bubbles as they rise through a bundle causing size and mass transfer transients, and other mechanics of tube bundle flows. Incorporating boiling will most likely require significant computational resources, so it is likely simulations will begin with simple bundles or single subchannels. Once the simulation models are validated and the results verified, improvements can be made by increasing the size of the computational domain.

3D simulations using the VOF method for interface tracking are another area of possible research. Researchers could validate 3D simulations using flow visualization techniques from experimental bundles. Following the verification of the simulations, and with appropriate computational power and boiling models well validated for tube bundles, work could begin to couple 3D flows and boiling to very closely simulate experimental work.

## 8.6 Summary

This chapter presented a summary of the experimental and numerical research. All observed flow patterns for the two experimental tube bundles and the CFD simulations were compared with a flow pattern map from the literature. Moderate agreement was found for the experimental tube bundle results while excellent agreement was found for the CFD simulations. For the CFD simulation that did not agree with the flow pattern map, two additional analyses were run, including shortening the inlet geometry and observing the effect of height on flow patterns. Both of these adjustments shifted the detected flow pattern towards bubbly flow and agreement with the flow pattern map. Finally, examples of future research opportunities were presented to extend the current experimental database available in literature and advance the use of CFD techniques in designing tube bundles.

# Chapter 9

# Conclusion

This research, facilitated by the Institute for Environmental Engineering at Kansas State University under Dr. Steve Eckels, explored the flow patterns generated in an evaporator tube bundle. A literature review covering void fraction measurement techniques, flow pattern definitions, and computational fluid dynamics techniques was completed, laying the foundation for the methods used in this research. A complete description of the experimental test facility was given in Chapter 3 and derivations to the governing equations of CFD analysis were performed in Chapter 4. The data reduction method was then presented in Chapter 5, allowing for calculation of refrigerant quality, shell-side heat flux, and uncertainties.

The analysis methods used for determining flow patterns were presented in Chapters 6 and 7. The first half of the analysis concentrated on the experimental results of a diabatic bundle with R-134a as the working fluid, with smooth and enhanced tube bundles with P/D=1.167. The flow patterns were recorded with a high speed video camera and borescope setup, allowing for deep visualization inside a boiling tube bundle. The flow patterns for both tube bundles were plotted on a flow pattern map and compared with existing experimental results in Chapter 8. Reasonable agreement was found for the enhanced tube bundle where flow parameters were more closely controlled and matched the flow pattern map experimental conditions, while the results of the smooth tube bundle varied significantly from expected results.

The CFD analysis consisted of creating PDFs of vapor volume fraction at various locations in the 2D bundle geometry with P/D=1.167. The PDF method was described and used in literature for experimental measurement of void fraction and adapted here for CFD measurements of vapor volume fraction. The PDF analysis shows how the skewness coefficient, $C_{M3}$, and kurtosis coefficient, $C_{M4}$, can be used to determine flow patterns at any location in the tube bundle. For the simulations performed, where refrigerant mass flux and inlet quality was varied, excellent agreement with an experimentally determined flow pattern map was found, as shown in Chapter 8. For one mass flux and inlet quality, extended analysis was performed looking at the effects of the inlet geometry and effect of measurement height on flow patterns.

This research has shown, through an analysis of boiling flow patterns in an evaporator tube bundle, that flow patterns are difficult to determine solely from experimental research. These difficulties include both instantaneous and time-averaged flow patterns during testing, the flow traveling in upward, downward, and axial directions causing chaotic mixing, and the camera equipment may not acquire images clear enough to adequately describe the flow. Literature has shown many techniques of measuring void fraction and liquid and vapor phase velocities, which have been used to create flow pattern maps. However, the use of the experimental techniques in this paper show only moderate agreement with these flow pattern maps. These flow pattern maps appear to be based solely on experimental data and rely on simple properties of the flow, such as velocity and density. while not incorporating physical modeling of the flow, including possible buoyancy, surface tension, tube surface geometry, and many other factors. More general flow pattern maps should be based on physical properties of the flow, such as buoyancy, surface tension, tube surface geometry, and pressure.

While the experimental analysis in this research did not agree particularly well with existing flow pattern maps, the numerical techniques though CFD modeling showed significant improvement. The CFD techniques involved with this research use state-of-the-art

modeling techniques including multiphase flow with turbulence. The statistical methods are analogous to successful experimental techniques presented in the literature. The continued development of CFD models and computer hardware will vastly improve the accuracy and speed of computational simulations. These simulations will then significantly lower the cost of designing tube bundles to sustain their defined stresses while maintaining proper heat transfer and pressure drop characteristics. It is strongly recommended that the use of CFD simulations be expanded by including more detailed modeling with verification and validation from experimental results.

# Bibliography

Ali, M. I. and Kawaji, M. (1991). Effect of flow channel orientation on two-phase flow in a narrow passage between flat plates. In *ASME/JSME Thermal Engineering Proceedings*, pages 183 – 190, Reno, NV, USA.

Ali, M. I., Sadatomi, M., and Kawaji, M. (1993). Adiabatic two-phase flow in narrow channels between two flat plates. *Canadian Journal of Chemical Engineering*, 71(5):657 – 666.

Anderson, Jr., J. D. (1995). *Computational fluid dynamics: The basics with applications*. McGraw-Hill.

Andersson, V., Holm, M., and Sunden, B. (2004). Simulation of two-phase flow in a heat exchanger distributor application. In *Proceedings of 2004 ASME IMECE*, volume 260, pages 609 – 616.

ANSYS, Inc. (2011). *ANSYS® FLUENT Theory Guide, Release 14.0*.

Aprin, L., Mercier, P., and Tadrist, L. (2007). Experimental analysis of local void fractions measurements for boiling hydrocarbons in complex geometry. *International Journal of Multiphase Flow*, 33(4):371 – 93.

Banerjee, R. and Isaac, K. (2003). Evaluation of turbulence closure scheme for stratified two phase flow. In *Proceedings of 2003 ASME IMECE*, volume 259, pages 689 – 705.

Benhamadouche, S. and Laurence, D. (2003). LES, coarse LES, and transient RANS comparisons on the flow across a tube bundle. *International Journal of Heat and Fluid Flow*, 24(4):470 – 479.

Bertola, V. (2003). Experimental characterization of gas-liquid intermittent subregimes by phase density function measurements. *Experiments in Fluids*, 34(1):122 – 129.

Burnside, B., Miller, K., McNeil, D., and Bruce, T. (2005). Flow velocities in an experimental kettle reboiler determined by particle image velocimetry. *International Journal of Heat and Mass Transfer*, 48(5):1000 – 1016.

Chen, Y., Groll, M., Mertz, R., and Kulenovic, R. (2005). Visualization and mechanisms of pool boiling of propane, isobutane and their mixtures on enhanced tubes with reentrant channels. *International Journal of Heat and Mass Transfer*, 48(12):2516 – 28.

Cornwell, K., Duffin, N., and Schuller, R. (1980). An experimental study of the effects of fluid flow on boiling within a kettle reboiler tube bundle. *ASME Paper No. 80-HT-45*.

Dehbi, A. and Badreddine, H. (2013). CFD prediction of mixing in a steam generator mock-up: Comparison between full geometry and porous medium approaches. *Annals of Nuclear Energy*, 58:178 – 187.

Dowlati, R., Kawaji, M., and Chan, A. (1988). Void fraction and friction pressure drop in two-phase flow across a horizontal tube bundle. In *AIChE Symposium Series*, volume 84, pages 126 – 132, Houston, TX.

Gan, G., Riffat, S., and Shao, L. (2000). CFD modelling of pressure loss across tube bundles of a heat exchanger for closed-wet cooling towers. *International Journal of Ambient Energy*, 21(2):77 – 84.

Gebauer, T., Al-Badri, A. R., Gotterbarm, A., Hajal, J. E., Leipertz, A., and Fröba, A. P. (2013). Condensation heat transfer on single horizontal smooth and finned tubes and tube bundles for R-134a and propane. *International Journal of Heat and Mass Transfer*, 56(12):516 – 524.

Gebbie, J. and Jensen, M. (1997). Void fraction distributions in a kettle reboiler. *Experimental Thermal and Fluid Science*, 14(3):297 – 311.

Glasgow, L. A. (2010). *Transport phenomena: An introduction to advanced topics*. John Wiley & Sons, Inc.

Gorgy, E. (2011). *Experimental evaluation of heat transfer impacts of tube pitch on highly enhanced surface tube bundle*. PhD thesis, Kansas State University.

Grant, I. and Chisholm, D. (1979). Two-phase flow on the shell-side of a segmentally baffled shell-and-tube heat exchanger. *Transactions of the ASME. Journal of Heat Transfer*, 101(1):38 – 42.

Hahne, E., Spindler, K., Chen, Q., and Windisch, R. (1990). Local void fraction measurements in finned tube bundles. *Heat Transfer, Proceedings of the International Heat Transfer Conference*, pages 41 – 41.

Haquet, J. and Gouirand, J. (1995). Local two-phase flow measurements in a cross-flow steam-generator tube bundle geometry: the Minnie II XF program. In *Multiphase Flow 1995. Proceedings of the Second International Conference on Multiphase Flow*, pages 613 – 618, Amsterdam, Netherlands.

Ibrahim, T. A. and Gomaa, A. (2009). Thermal performance criteria of elliptic tube bundle in crossflow. *International Journal of Thermal Sciences*, 48(11):2148 – 2158.

Iwaki, C., Cheong, K., Monji, H., and Matsui, G. (2005). Vertical, bubbly, cross-flow characteristics over tube bundles. *Experiments in Fluids*, 39(6):1024 – 1039.

Jones Jr., O. C. and Zuber, N. (1975). Interrelation between void fraction fluctuations and flow patterns in two-phase flow. *International Journal of Multiphase Flow*, 2(3):273 – 306.

Kim, J.-I., Jung, J.-W., and Kim, M.-Y. (2008). Flow distribution analysis in a nuclear steam generator tube bundle using computational fluid dynamics. In *Societe Francaise*

*d'Energie Nucleaire - International Congress on Advances in Nuclear Power Plants - ICAPP 2007*, volume 1, pages 358 – 364.

Kondo, M. and Nakajima, K. I. (1980). Experimental investigation of air-water two phase upflow across horizontal tube bundles: Part I–flow pattern and void fraction. *Bulletin of the JSME*, 23(177):385 – 393.

Krepper, E. and Rzehak, R. (2012). CFD analysis of a void distribution benchmark of the nupec psbt tests: Model calibration and influence of turbulence modelling. *Science and Technology of Nuclear Installations*.

Kundu, P. K. (1990). *Fluid Mechanics*. Academic Press, Inc.

Kunkelmann, C. and Stephan, P. (2010). Numerical simulation of the transient heat transfer during nucleate boiling of refrigerant HFE-7100. *International Journal of Refrigeration*, 33(7):1221 – 1228.

Lávička, D. (2011). CFD simulation the thermal-hydraulic characteristic within fuel rod bundle near grid spacers. *World Academy of Science, Engineering and Technology*, 55:168 – 173.

Lo, S. and Osman, J. (2012). CFD modeling of boiling flow in PSBT 5x5 bundle. *Science and Technology of Nuclear Installations*.

Lu, G., Zhao, G., Ren, J., Xiang, W., and Ai, H. (2010). Investigation on flow patterns and transition characteristics in a tube-bundle channel. In *ASME International Mechanical Engineering Congress and Exposition, Proceedings*, volume 9, pages 1579 – 1582.

Mizutani, Y., Tomiyama, A., Hosokawa, S., Sou, A., Kudo, Y., and Mishima, K. (2007). Two-phase flow patterns in a four by four rod bundle. *Journal of Nuclear Science and Technology*, 44(6):894 – 901.

Noghrehkar, G., Kawaji, M., and Chan, A. (1999). Investigation of two-phase flow regimes in tube bundles under cross-flow conditions. *International Journal of Multiphase Flow*, 25(5):857 – 874.

Nukiyama, S. (1934). Film boiling water on thin wires. *Japan Society of Mechanical Engineering*, 37.

Ragab, A., Brandstaetter, W., and Shalaby, S. (2008). CFD-simulation of multiphase flows in horizontal and inclined pipelines. *Oil Gas European Magazine*, 34(1):34 – 40.

Ridluan, A. and Tokuhiro, A. (2008a). Benchmark simulation of turbulent flow through a staggered tube bundle to support CFD as a reactor design tool. Part I: SRANS CFD simulation. *Journal of Nuclear Science and Technology*, 45(12):1293 – 1304.

Ridluan, A. and Tokuhiro, A. (2008b). Benchmark simulation of turbulent flow through a staggered tube bundle to support CFD as a reactor design tool. Part II: URANS CFD simulation. *Journal of Nuclear Science and Technology*, 45(12):1305 – 1315.

Schrage, D., Hsu, J., and Jensen, M. (1987). Void fractions and two-phase friction multipliers in a horizontal tube bundle. In *AIChE Symposium Series*, volume 83, pages 1 – 8, Pittsburgh, PA, USA.

Tutu, N. (1982). Pressure fluctuations and flow pattern recognition in vertical two phase gas-liquid flows. *International Journal of Multiphase Flow*, 8(4):443 – 447.

Ueno, T., Tomomatsu, K., Takamatsu, H., and Nishikawa, H. (1997). Void fraction and interface velocity in gas-liquid upward two-phase flow across tube bundles. In *Eighth International Topical Meeting on Nuclear Reactor Thermal-Hydraulics. NURETH-8. New Horizons in Nuclear Reactor Thermal-Hydraulics*, volume 1, pages 229 – 238, Tokyo, Japan.

Ulbrich, R. and Mewes, D. (1994). Vertical, upward gas-liquid two-phase flow across a tube bundle. *International Journal of Multiphase Flow*, 20(2):249 – 272.

van Rooyen, E. (2011). *Boiling on a Tube Bundle: Heat Transfer, Pressure Drop and Flow Patterns*. PhD thesis, École Polytechnique Fédérale de Lausanne.

van Rooyen, E., Agostini, F., Borhani, N., and Thome, J. R. (2012). Boiling on a tube bundle: Part I–flow visualization and onset of dryout. *Heat Transfer Engineering*, 33(11):913 – 929.

Vince, M. and Lahey, R.T., J. (1982). On the development of an objective flow regime indicator. *International Journal of Multiphase Flow*, 8(2):93 – 124.

Wheeler, A. J. and Ganji, A. R. (2010). *Introduction to Engineering Experimentation*. Prentice Hall, 3rd edition.

Xu, G., Tso, C., and Tou, K. (1998). Hydrodynamics of two-phase flow in vertical up and down-flow across a horizontal tube bundle. *International Journal of Multiphase Flow*, 24(8):1317 – 1342.

Yeh, C.-H. and Ferng, Y.-M. (2012). CFD investigating hydraulic characteristics in a triangular-pitch rod bundle. In *Transactions of the American Nuclear Society*, volume 107, pages 1293 – 1296.

# Appendix A

# Dimensioned Drawings

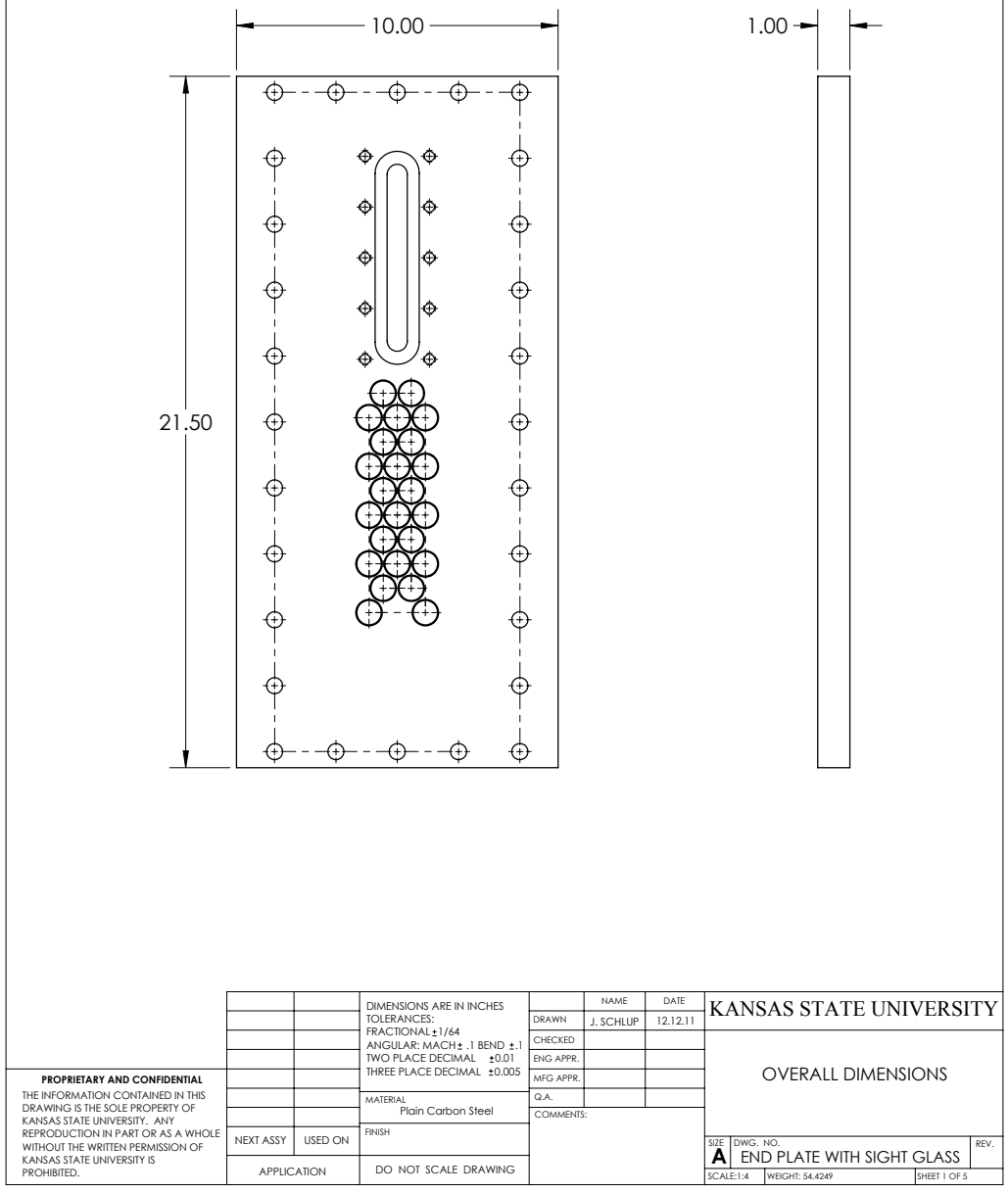


| | | | | | |
|---|---|---|---|---|---|
| | | DIMENSIONS ARE IN INCHES<br>TOLERANCES:<br>FRACTIONAL ±1/64<br>ANGULAR: MACH ± .1 BEND ±.1<br>TWO PLACE DECIMAL ±0.01<br>THREE PLACE DECIMAL ±0.005 | | NAME | DATE |
| | | | DRAWN | J. SCHLUP | 12.12.11 |
| | | | CHECKED | | |
| | | | ENG APPR. | | |
| | | | MFG APPR. | | |
| | | | Q.A. | | |
| | | MATERIAL<br>Plain Carbon Steel | COMMENTS: | | |
| | | FINISH | | | |
| NEXT ASSY | USED ON | DO NOT SCALE DRAWING | | | |
| APPLICATION | | | | | |



KANSAS STATE UNIVERSITY

OVERALL DIMENSIONS

| SIZE | DWG. NO. | REV. |
|---|---|---|
| A | END PLATE WITH SIGHT GLASS | |
| SCALE:1:4 | WEIGHT: 54.4249 | SHEET 1 OF 5 |

Figure A.1: Outside dimensions of sight glass end plate.

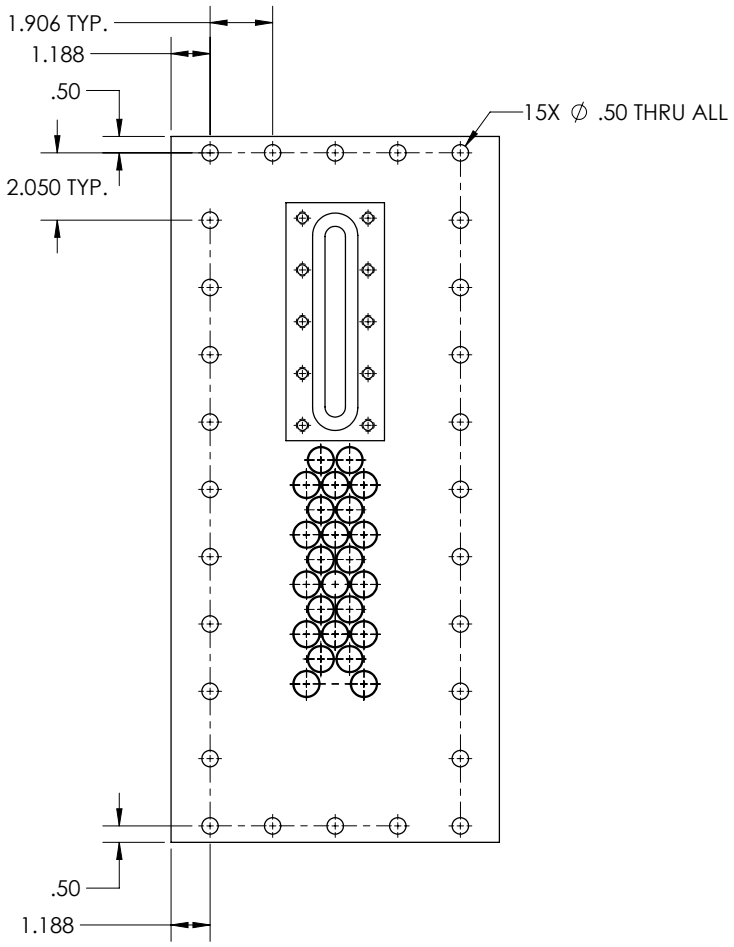


| | | | | | |
|---|---|---|---|---|---|
| | | DIMENSIONS ARE IN INCHES<br>TOLERANCES:<br>FRACTIONAL ±1/64<br>ANGULAR: MACH ± .1 BEND ±.1<br>TWO PLACE DECIMAL ±0.01<br>THREE PLACE DECIMAL ±0.005 | | NAME | DATE |
| | | | DRAWN | J. SCHLUP | 12.12.11 |
| | | | CHECKED | | |
| | | | ENG APPR. | | |
| | | | MFG APPR. | | |
| | | | Q.A. | | |
| | | MATERIAL<br>Plain Carbon Steel | COMMENTS: | | |
| | | FINISH | | | |
| NEXT ASSY | USED ON | | | | |
| APPLICATION | | DO NOT SCALE DRAWING | | | |



KANSAS STATE UNIVERSITY

SEALING HOLE LOCATIONS

| SIZE | DWG. NO. | REV. |
|---|---|---|
| A | END PLATE WITH SIGHT GLASS | |
| SCALE:1:4 | WEIGHT: 54.4249 | SHEET 2 OF 5 |

Figure A.2: Mounting hole locations of sight glass end plate.

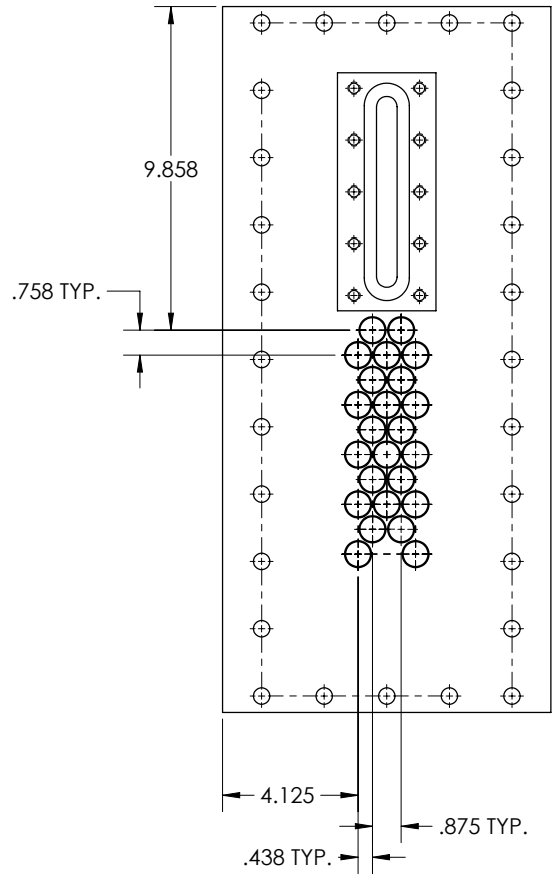


| | | | | | |
|---|---|---|---|---|---|
| | | DIMENSIONS ARE IN INCHES<br>TOLERANCES:<br>FRACTIONAL ±1/64<br>ANGULAR: MACH ± .1 BEND ±.1<br>TWO PLACE DECIMAL ±0.01<br>THREE PLACE DECIMAL ±0.005 | | NAME | DATE |
| | | | DRAWN | J. SCHLUP | 12.12.11 |
| | | | CHECKED | | |
| | | | ENG APPR. | | |
| | | | MFG APPR. | | |
| | | | Q.A. | | |
| | | MATERIAL<br>Plain Carbon Steel | COMMENTS: | | |
| NEXT ASSY | USED ON | FINISH | | | |
| APPLICATION | | DO NOT SCALE DRAWING | | | |



KANSAS STATE UNIVERSITY

TUBE HOLE LOCATIONS

| SIZE | DWG. NO. | REV. |
|---|---|---|
| A | END PLATE WITH SIGHT GLASS | |
| SCALE:1:4 | WEIGHT: 54.4249 | SHEET 3 OF 5 |

Figure A.3: Tube hole locations of sight glass end plate.

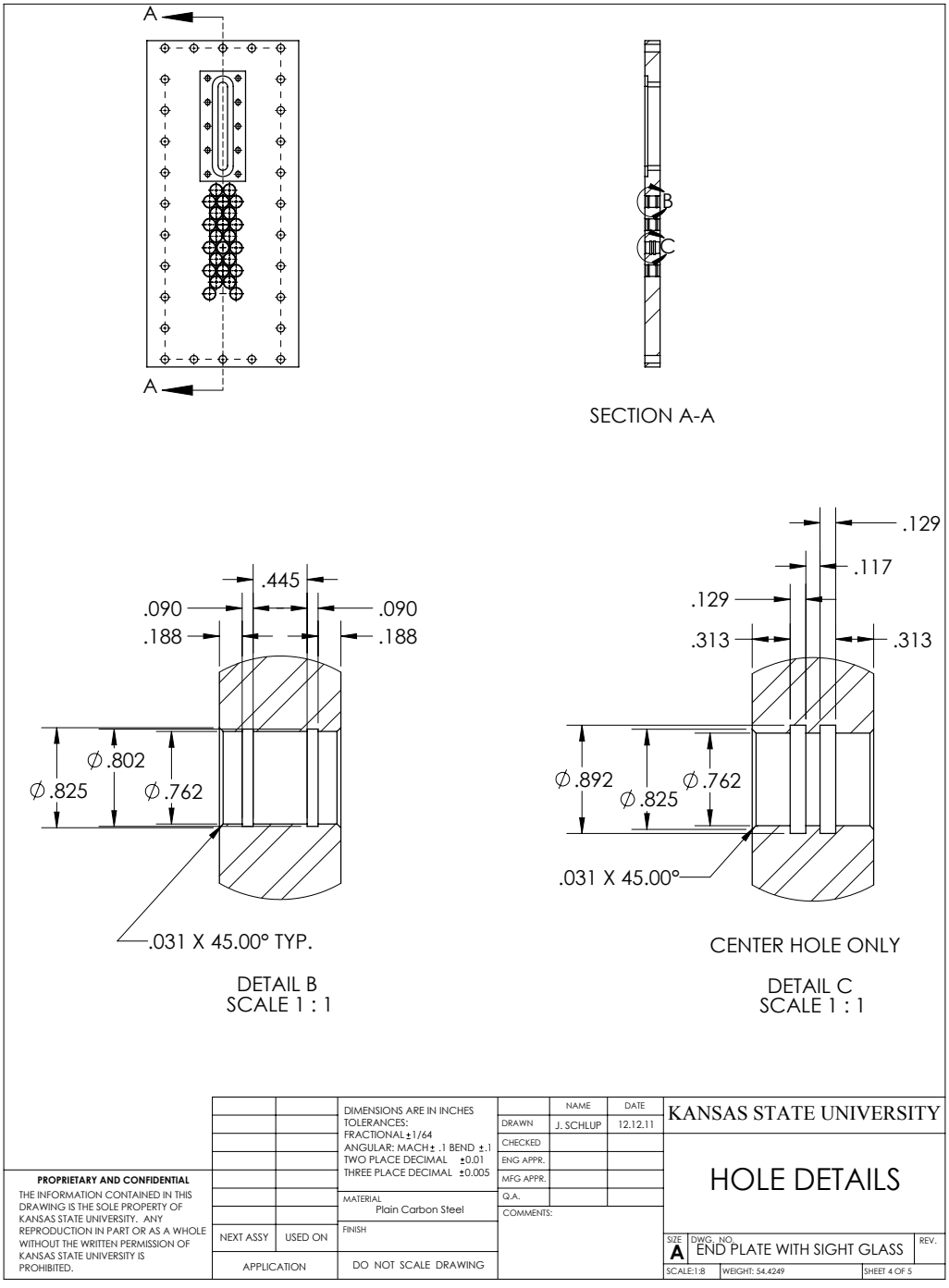


Figure A.4: Expansion groove details of sight glass end plate.

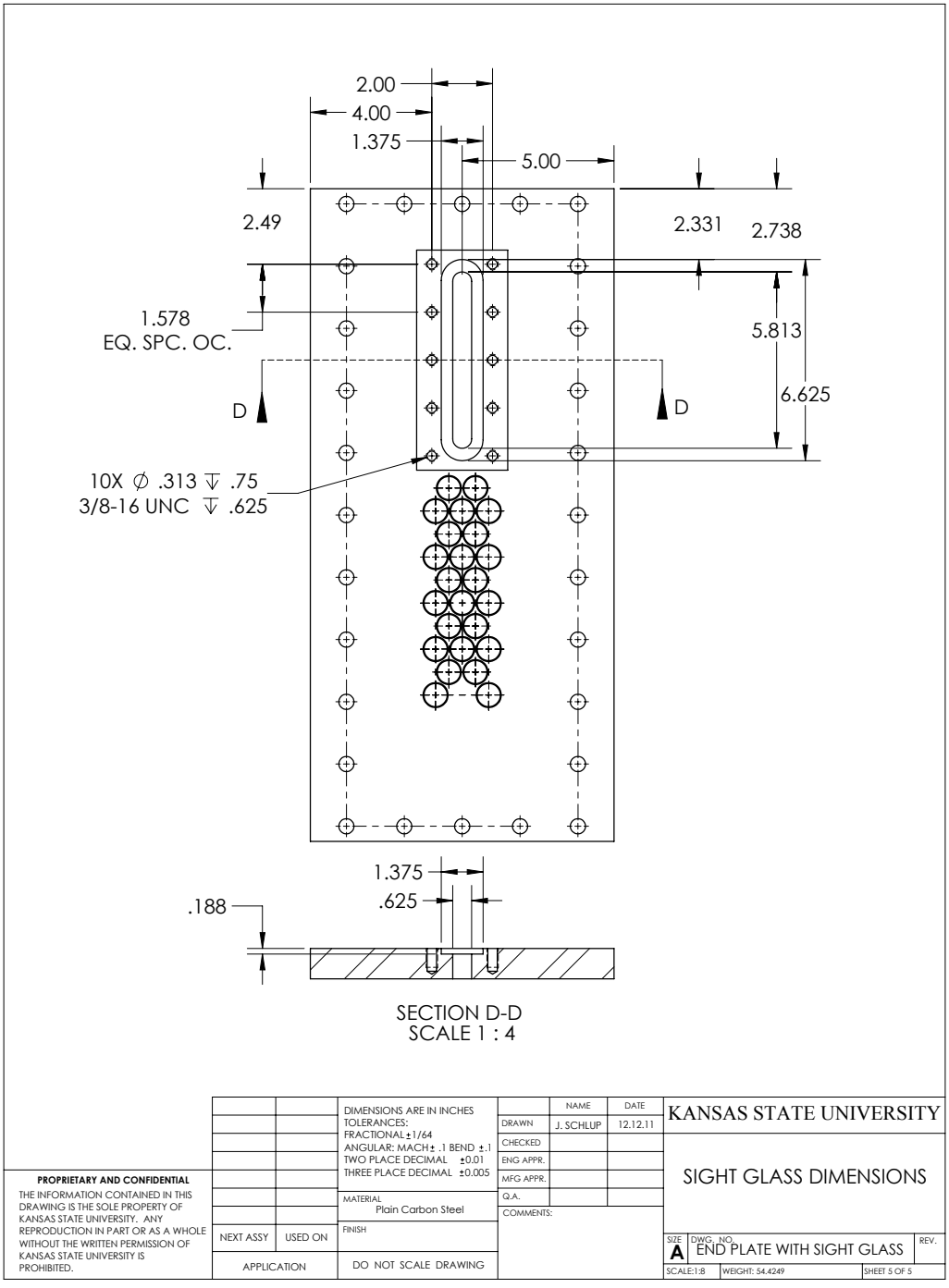


Figure A.5: Sight glass detailed dimensions.

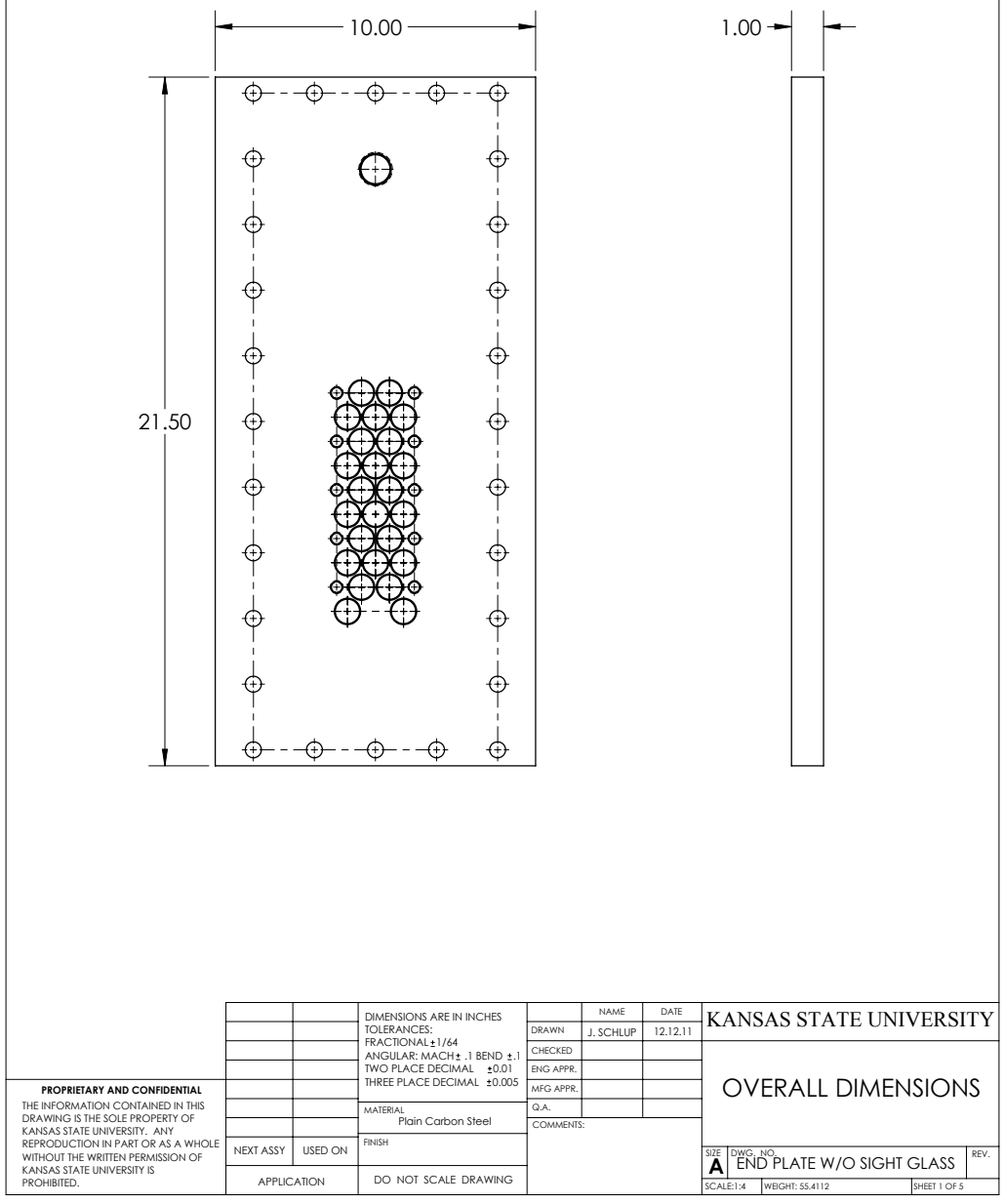


Figure A.6: Outside dimensions of pressure relief end plate.

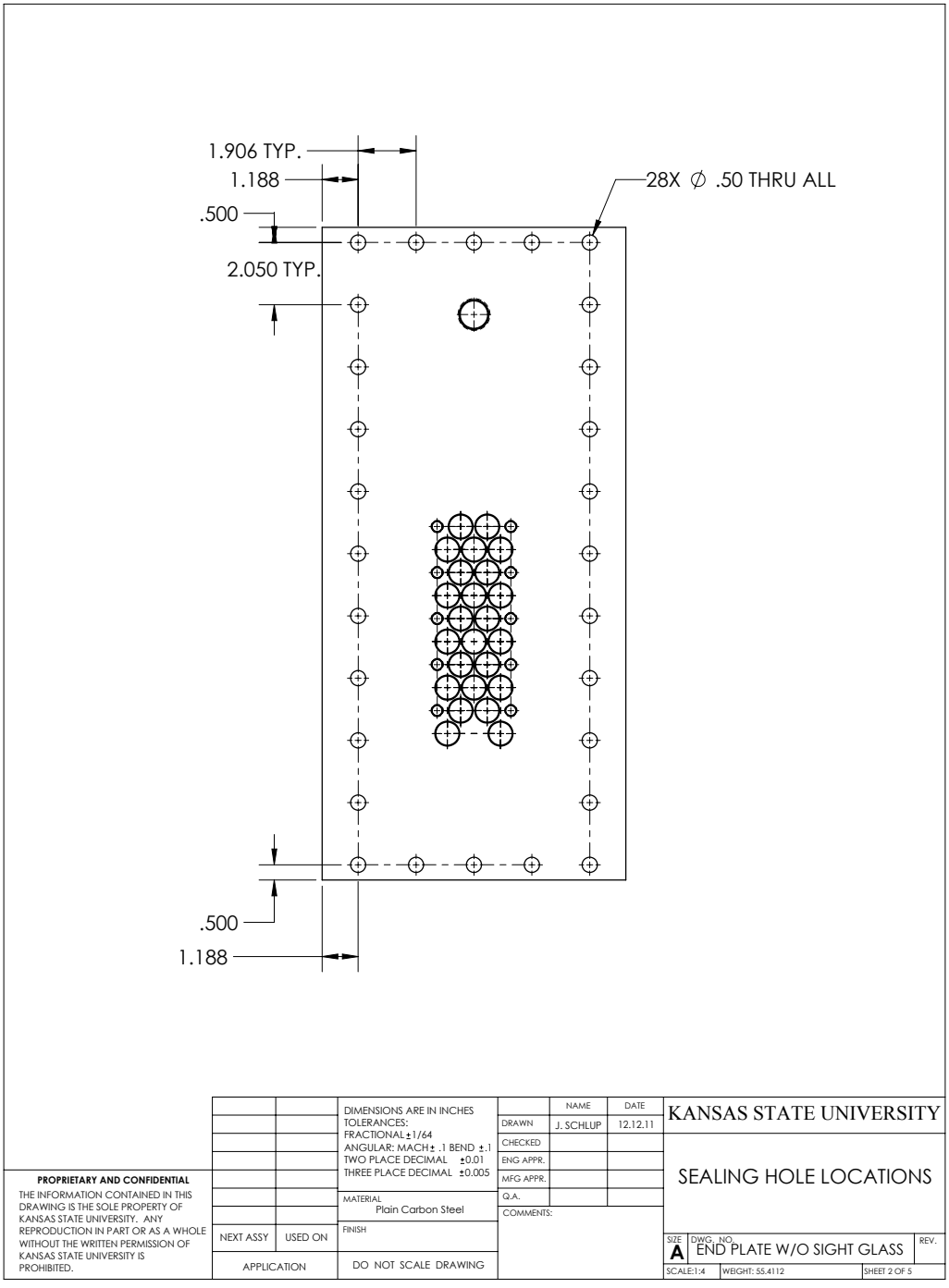


Figure A.7: Mounting hole locations of pressure relief end plate.

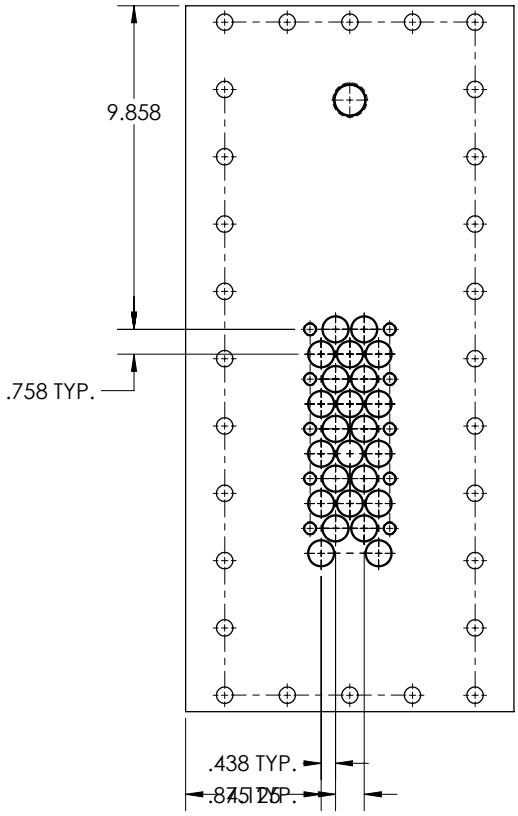


| | | | | | | |
|---|---|---|---|---|---|---|
| | | DIMENSIONS ARE IN INCHES<br>TOLERANCES:<br>FRACTIONAL ±1/64<br>ANGULAR: MACH ± .1 BEND ±.1<br>TWO PLACE DECIMAL ±0.01<br>THREE PLACE DECIMAL ±0.005 | | NAME | DATE | KANSAS STATE UNIVERSITY |
| | | | DRAWN | J. SCHLUP | 12.12.11 | |
| | | | CHECKED | | | TUBE HOLE LOCATIONS |
| | | | ENG APPR. | | | |
| | | | MFG APPR. | | | |
| | | MATERIAL<br>Plain Carbon Steel | Q.A. | | | |
| | | | COMMENTS: | | | |
| NEXT ASSY | USED ON | FINISH | | | | SIZE A DWG. NO. END PLATE W/O SIGHT GLASS REV. |
| APPLICATION | | DO NOT SCALE DRAWING | | | | SCALE:1:4 WEIGHT: 55.4112 SHEET 3 OF 5 |



Figure A.8: Tube hole locations of pressure relief end plate.

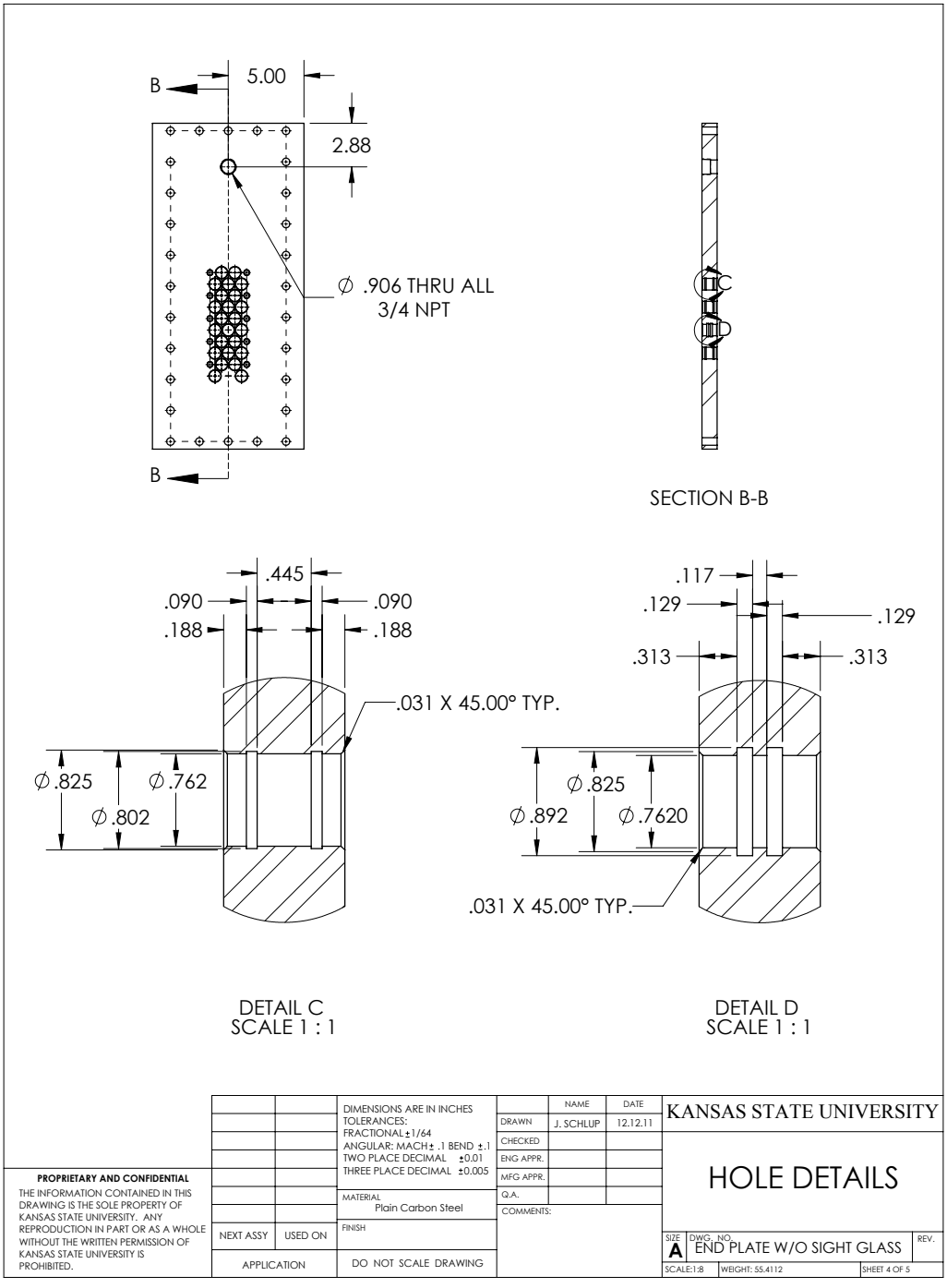


Figure A.9: Expansion groove details of pressure relief end plate.

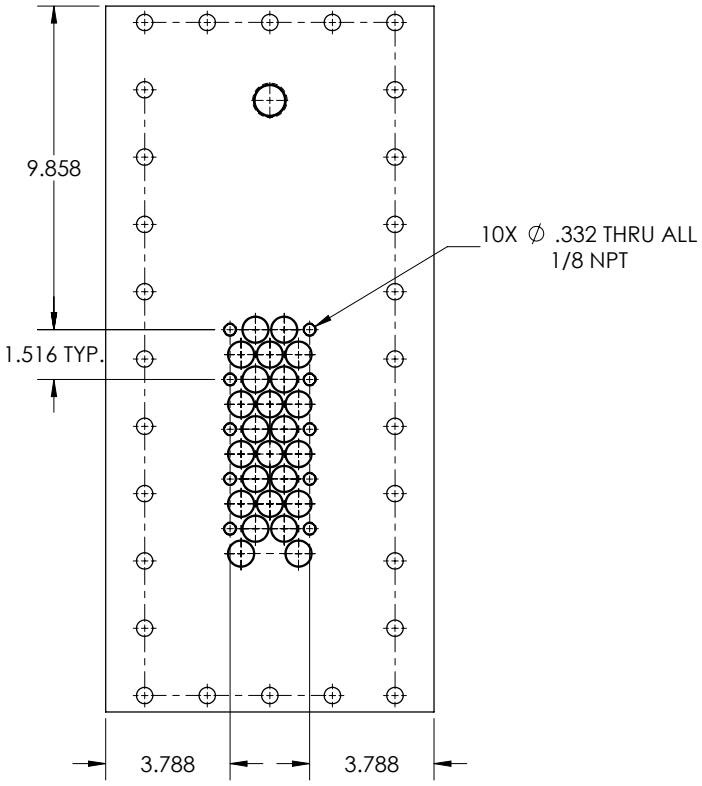


| | | | | | |
|---|---|---|---|---|---|
| | | DIMENSIONS ARE IN INCHES<br>TOLERANCES:<br>FRACTIONAL ±1/64<br>ANGULAR: MACH ± .1 BEND ±.1<br>TWO PLACE DECIMAL ±0.01<br>THREE PLACE DECIMAL ±0.005 | | NAME | DATE |
| | | | DRAWN | J. SCHLUP | 12.12.11 |
| | | | CHECKED | | |
| | | | ENG APPR. | | |
| | | | MFG APPR. | | |
| | | | Q.A. | | |
| | | MATERIAL<br>Plain Carbon Steel | COMMENTS: | | |
| NEXT ASSY | USED ON | FINISH | | | |
| APPLICATION | | DO NOT SCALE DRAWING | | | |



KANSAS STATE UNIVERSITY

PRESSURE TAP LOCATIONS

| SIZE | DWG. NO. | REV. |
|---|---|---|
| A | END PLATE W/O SIGHT GLASS | |
| SCALE:1:8 | WEIGHT: 55.4112 | SHEET 5 OF 5 |

Figure A.10: Instrumentation tap detailed dimensions.

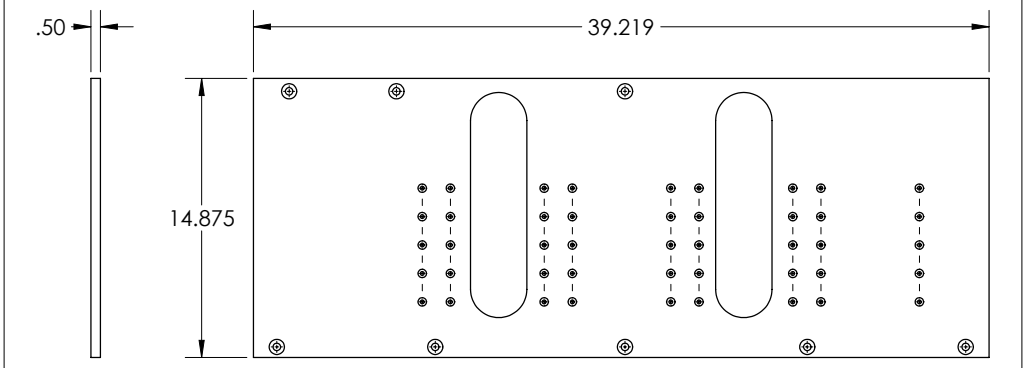


| | | | | | |
|---|---|---|---|---|---|
| | | DIMENSIONS ARE IN INCHES<br>TOLERANCES:<br>FRACTIONAL ±1/64<br>ANGULAR: MACH ± .1 BEND ±.1<br>TWO PLACE DECIMAL ±0.01<br>THREE PLACE DECIMAL ±0.005 | | NAME | DATE |
| | | | DRAWN | J. SCHLUP | 12.12.11 |
| | | | CHECKED | | |
| | | | ENG APPR. | | |
| | | | MFG APPR. | | |
| | | | Q.A. | | |
| | | MATERIAL<br>Aluminum | COMMENTS: | | |
| NEXT ASSY | USED ON | FINISH | | | |
| APPLICATION | | DO NOT SCALE DRAWING | | | |



KANSAS STATE UNIVERSITY

OVERALL DIMENSIONS

| SIZE | DWG. NO. | REV. |
|---|---|---|
| A | INSERT LEFT SIDE | |
| SCALE:1:7 | WEIGHT: 9.42254 | SHEET 1 OF 5 |

Figure A.11: Outside dimensions of left insert plate.

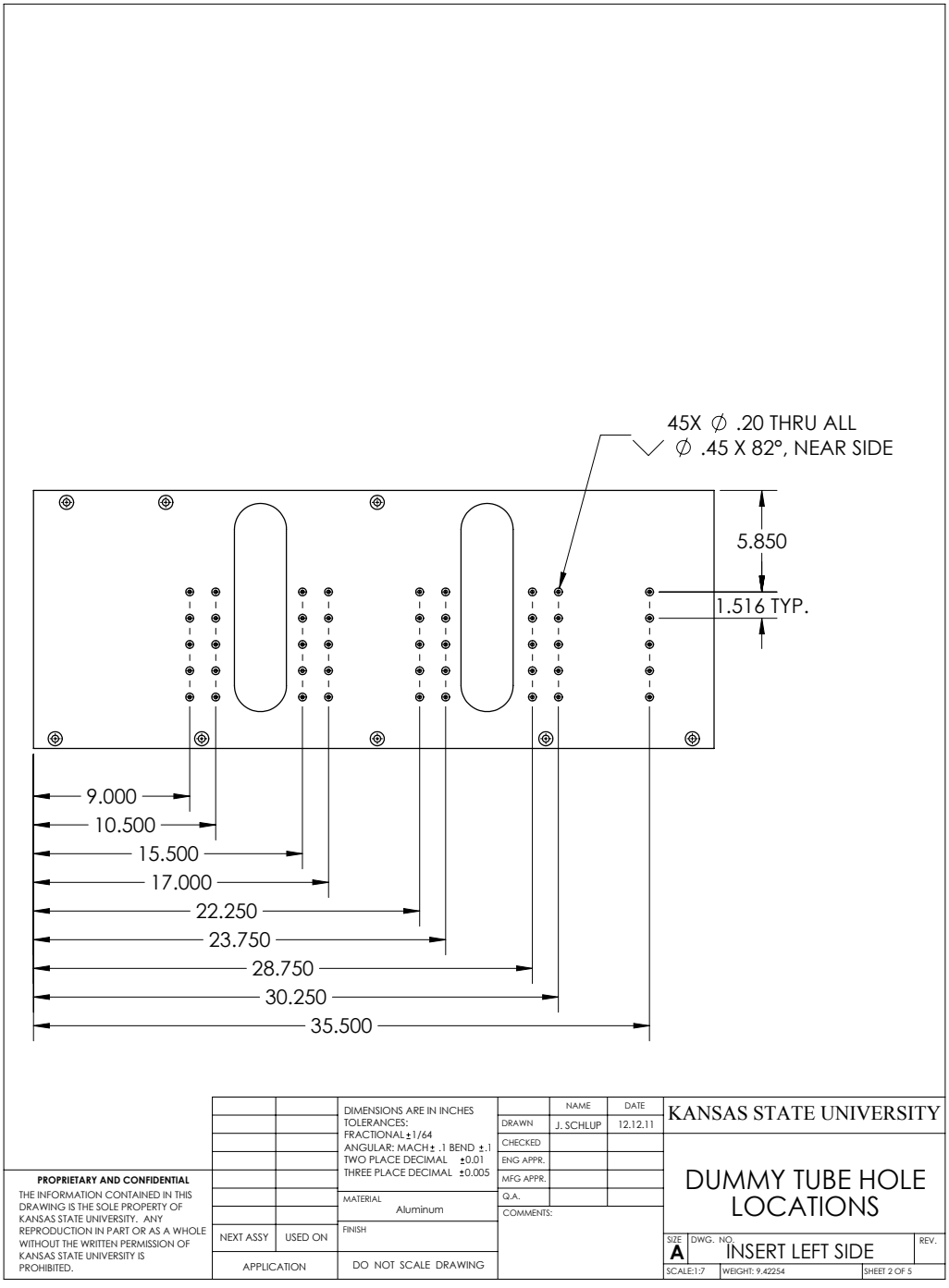


Figure A.12: Half round hole locations of left insert plate.

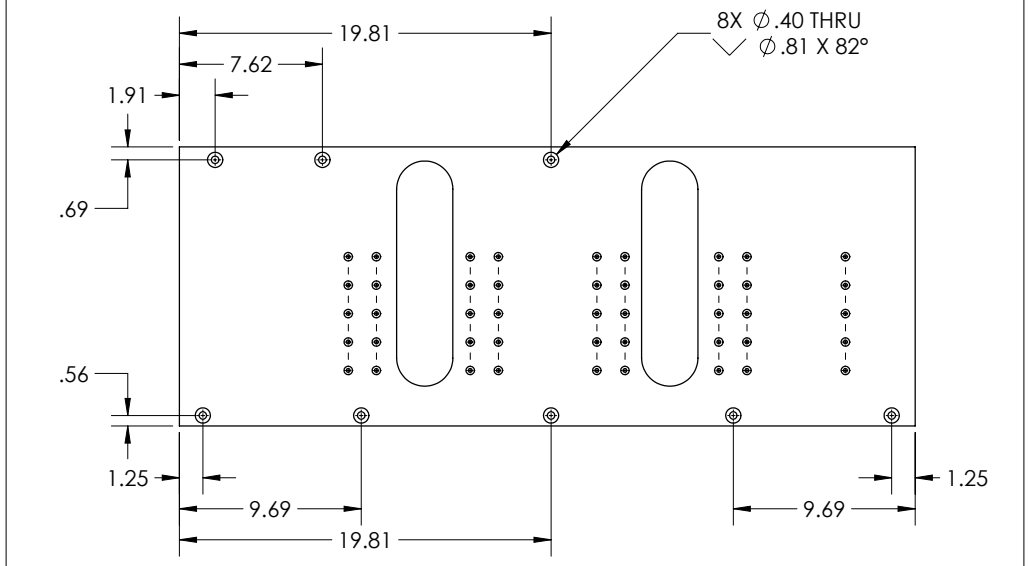


| | | | | | |
|---|---|---|---|---|---|
| | | DIMENSIONS ARE IN INCHES<br>TOLERANCES:<br>FRACTIONAL ±1/64<br>ANGULAR: MACH ± .1 BEND ±.1<br>TWO PLACE DECIMAL ±0.01<br>THREE PLACE DECIMAL ±0.005 | | NAME | DATE |
| | | | DRAWN | J. SCHLUP | 12.12.11 |
| | | | CHECKED | | |
| | | | ENG APPR. | | |
| | | | MFG APPR. | | |
| | | | Q.A. | | |
| | | MATERIAL<br>Aluminum | COMMENTS: | | |
| NEXT ASSY | USED ON | FINISH | | | |
| APPLICATION | | DO NOT SCALE DRAWING | | | |

**PROPRIETARY AND CONFIDENTIAL**
THE INFORMATION CONTAINED IN THIS DRAWING IS THE SOLE PROPERTY OF KANSAS STATE UNIVERSITY. ANY REPRODUCTION IN PART OR AS A WHOLE WITHOUT THE WRITTEN PERMISSION OF KANSAS STATE UNIVERSITY IS PROHIBITED.

KANSAS STATE UNIVERSITY

SPACER HOLE LOCATIONS

| SIZE | DWG. NO. | REV. |
|---|---|---|
| A | INSERT LEFT SIDE | |
| SCALE:1:7 | WEIGHT: 9.42254 | SHEET 3 OF 5 |

Figure A.13: Spacer hole locations of left insert plate.

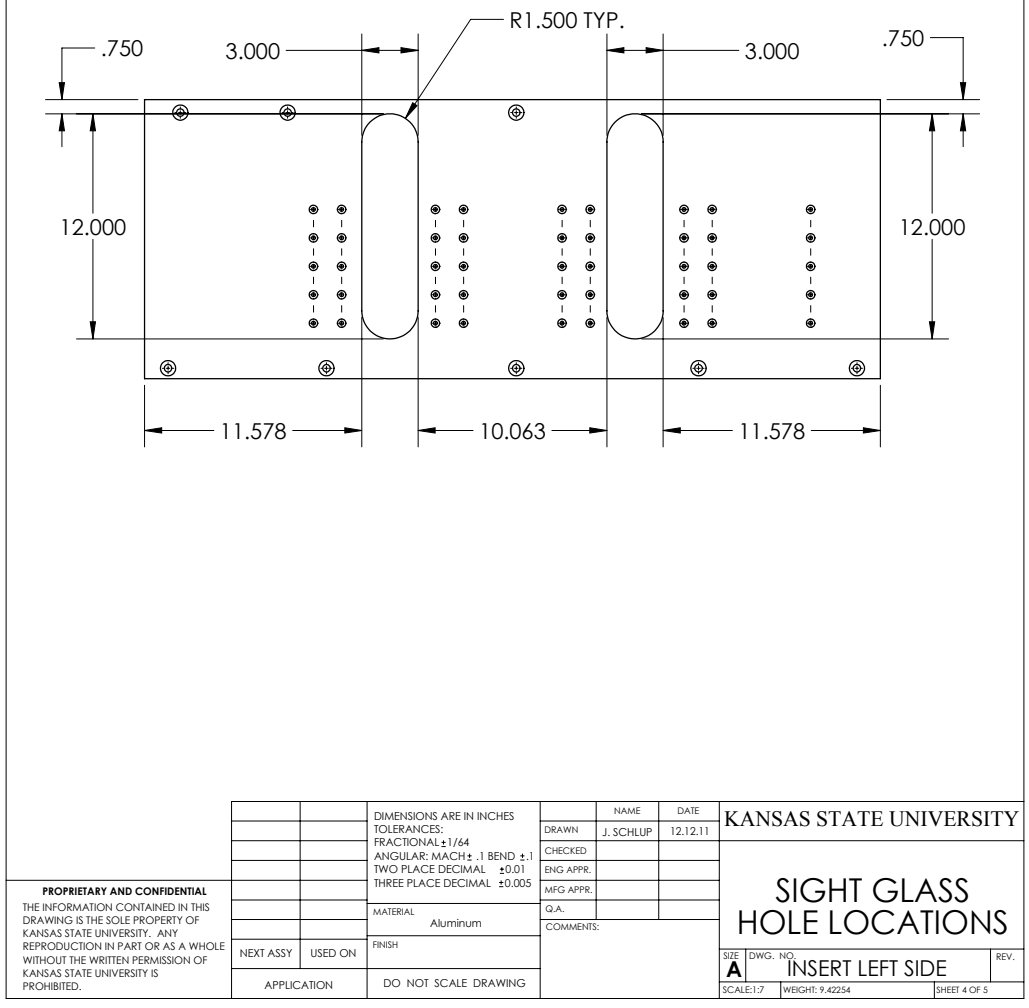


| | | | | | |
|---|---|---|---|---|---|
| | | DIMENSIONS ARE IN INCHES<br>TOLERANCES:<br>FRACTIONAL ±1/64<br>ANGULAR: MACH ± .1 BEND ±.1<br>TWO PLACE DECIMAL ±0.01<br>THREE PLACE DECIMAL ±0.005 | | NAME | DATE |
| | | | DRAWN | J. SCHLUP | 12.12.11 |
| | | | CHECKED | | |
| | | | ENG APPR. | | |
| | | | MFG APPR. | | |
| | | | Q.A. | | |
| | | MATERIAL<br>Aluminum | COMMENTS: | | |
| NEXT ASSY | USED ON | FINISH | | | |
| APPLICATION | | DO NOT SCALE DRAWING | | | |



KANSAS STATE UNIVERSITY

SIGHT GLASS HOLE LOCATIONS

| SIZE | DWG. NO. | REV. |
|---|---|---|
| A | INSERT LEFT SIDE | |
| SCALE:1:7 | WEIGHT: 9.42254 | SHEET 4 OF 5 |

Figure A.14: Sight glass opening dimensions of left insert plate.

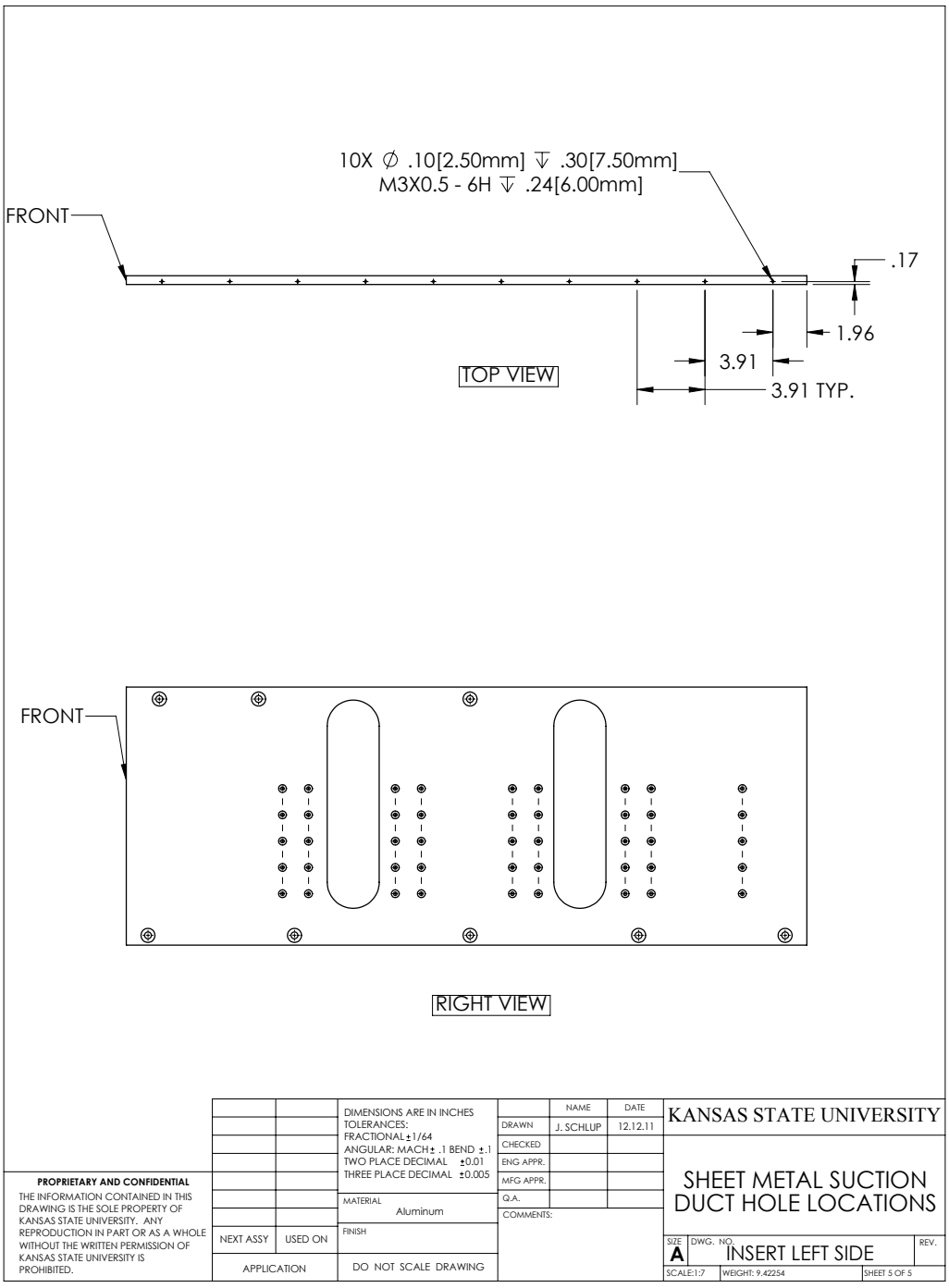


Figure A.15: Suction duct hole locations of left insert plate.

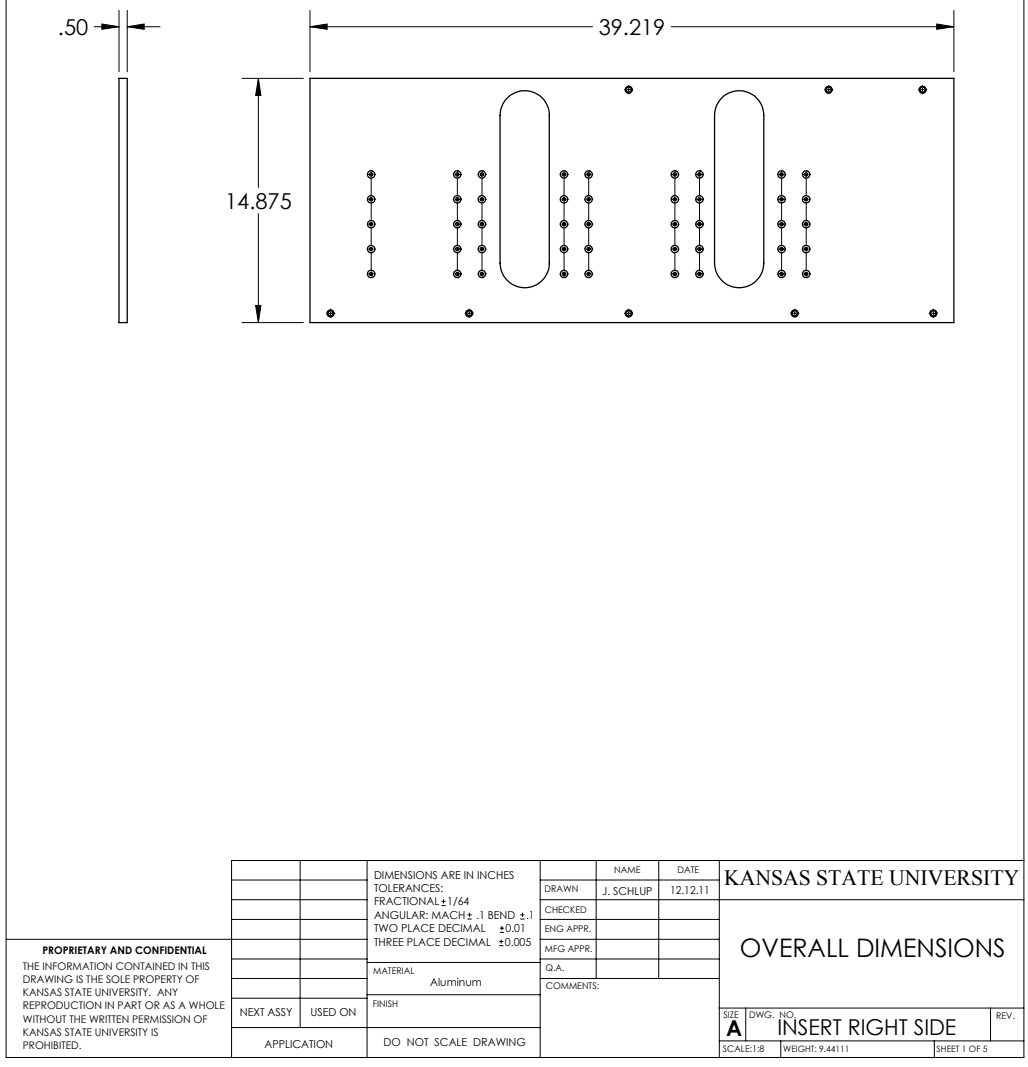


Figure A.16: Outside dimensions of right insert plate.

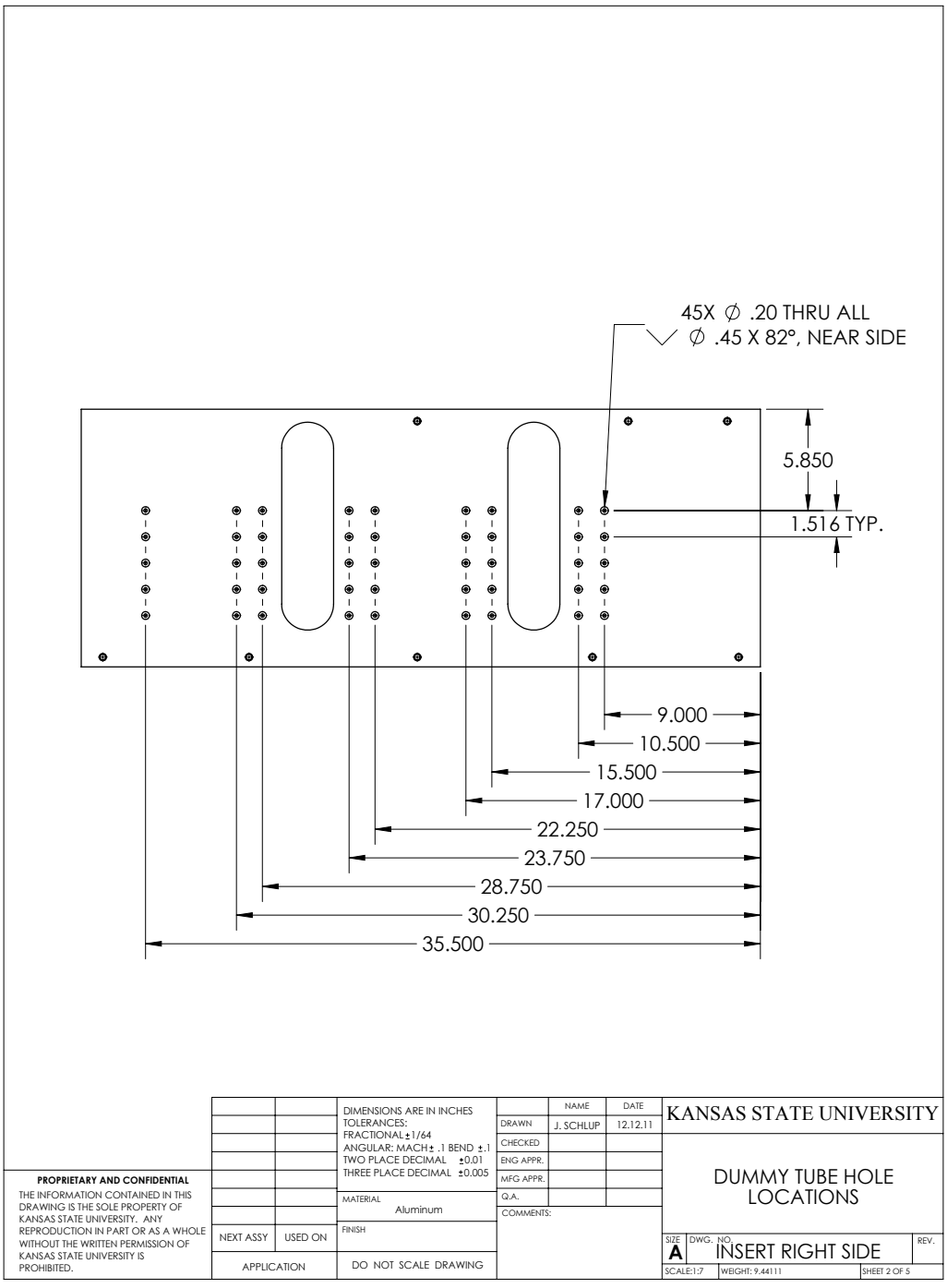


Figure A.17: Half round hole locations of right insert plate.

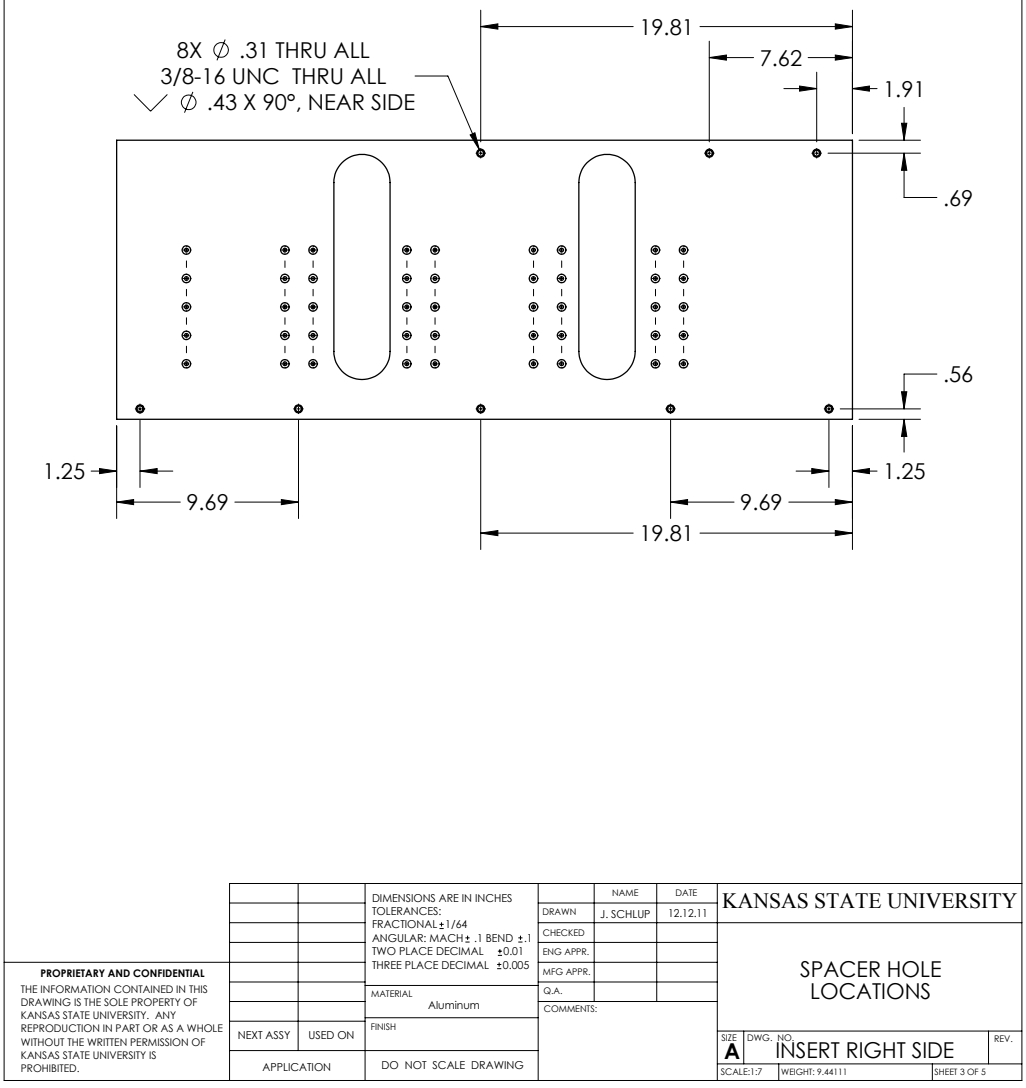


Figure A.18: Spacer hole locations of right insert plate.

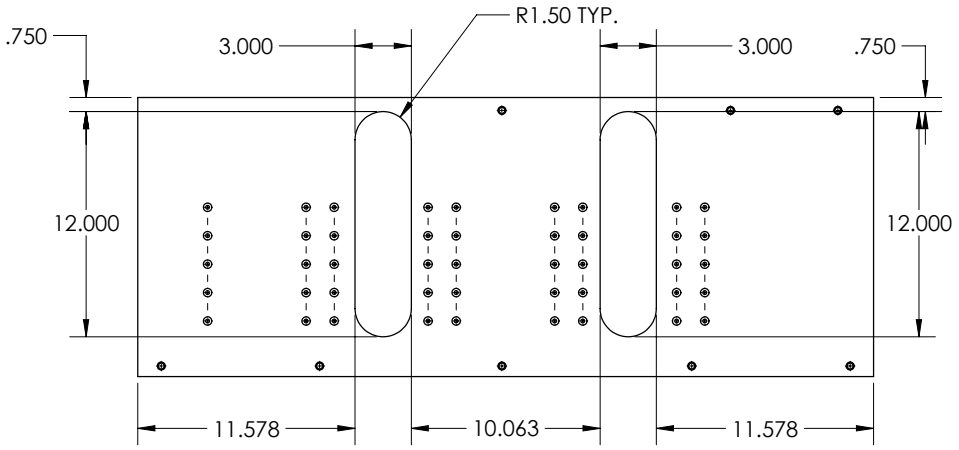


| | | | | | |
|---|---|---|---|---|---|
| | | DIMENSIONS ARE IN INCHES<br>TOLERANCES:<br>FRACTIONAL ±1/64<br>ANGULAR: MACH ± .1 BEND ±.1<br>TWO PLACE DECIMAL ±0.01<br>THREE PLACE DECIMAL ±0.005 | | NAME | DATE |
| | | | DRAWN | J. SCHLUP | 12.12.11 |
| | | | CHECKED | | |
| | | | ENG APPR. | | |
| | | | MFG APPR. | | |
| | | | Q.A. | | |
| | | MATERIAL<br>Aluminum | COMMENTS: | | |
| NEXT ASSY | USED ON | FINISH | | | |
| APPLICATION | | DO NOT SCALE DRAWING | | | |

**PROPRIETARY AND CONFIDENTIAL**

THE INFORMATION CONTAINED IN THIS DRAWING IS THE SOLE PROPERTY OF KANSAS STATE UNIVERSITY. ANY REPRODUCTION IN PART OR AS A WHOLE WITHOUT THE WRITTEN PERMISSION OF KANSAS STATE UNIVERSITY IS PROHIBITED.

KANSAS STATE UNIVERSITY

SIGHT GLASS
HOLE LOCATIONS

| SIZE | DWG. NO. | REV. |
|---|---|---|
| A | INSERT RIGHT SIDE | |
| SCALE:1:7 | WEIGHT: 9.44111 | SHEET 4 OF 5 |

Figure A.19: Sight glass opening dimensions of right insert plate.

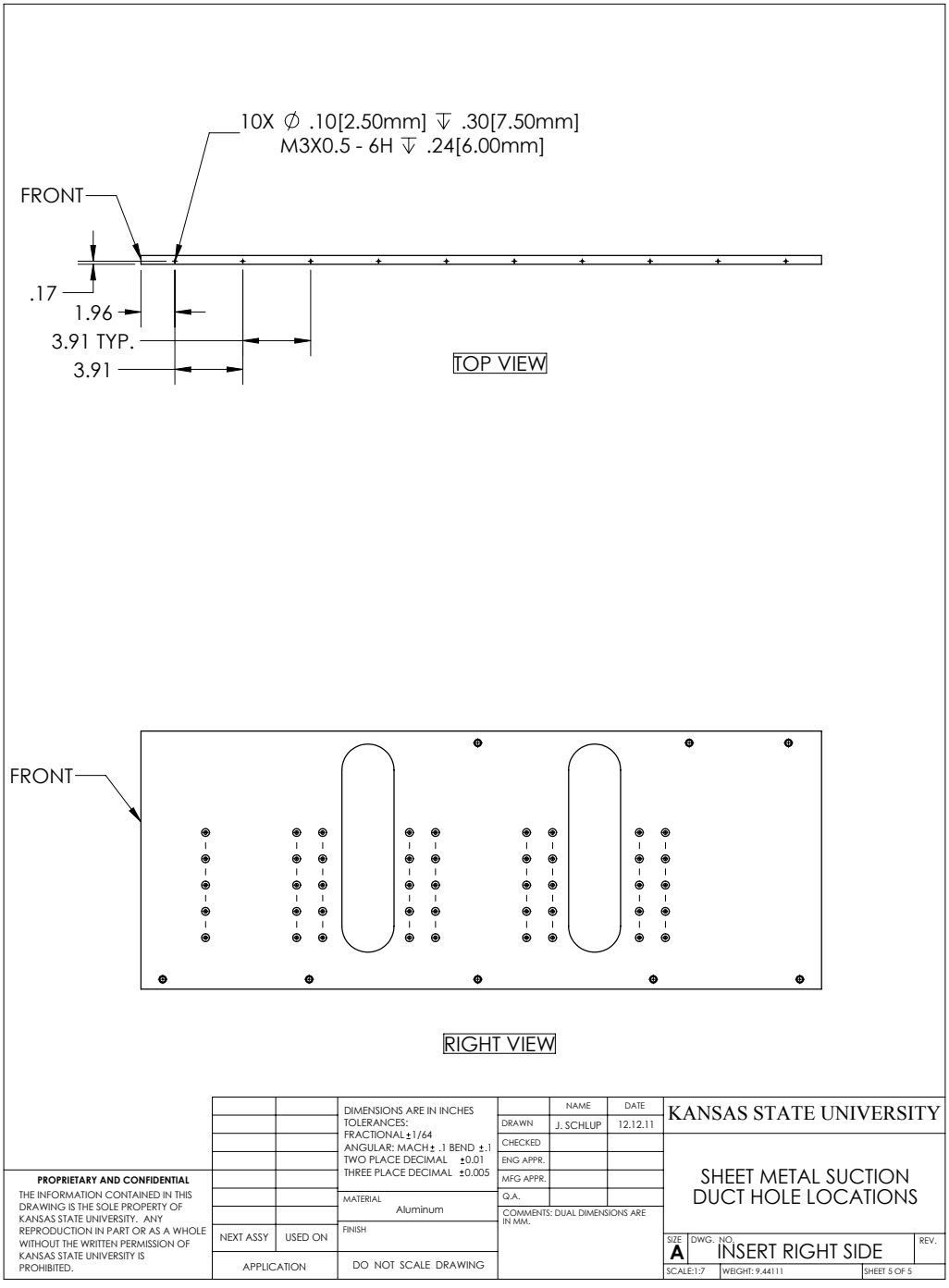


Figure A.20: Suction duct hole locations of right insert plate.

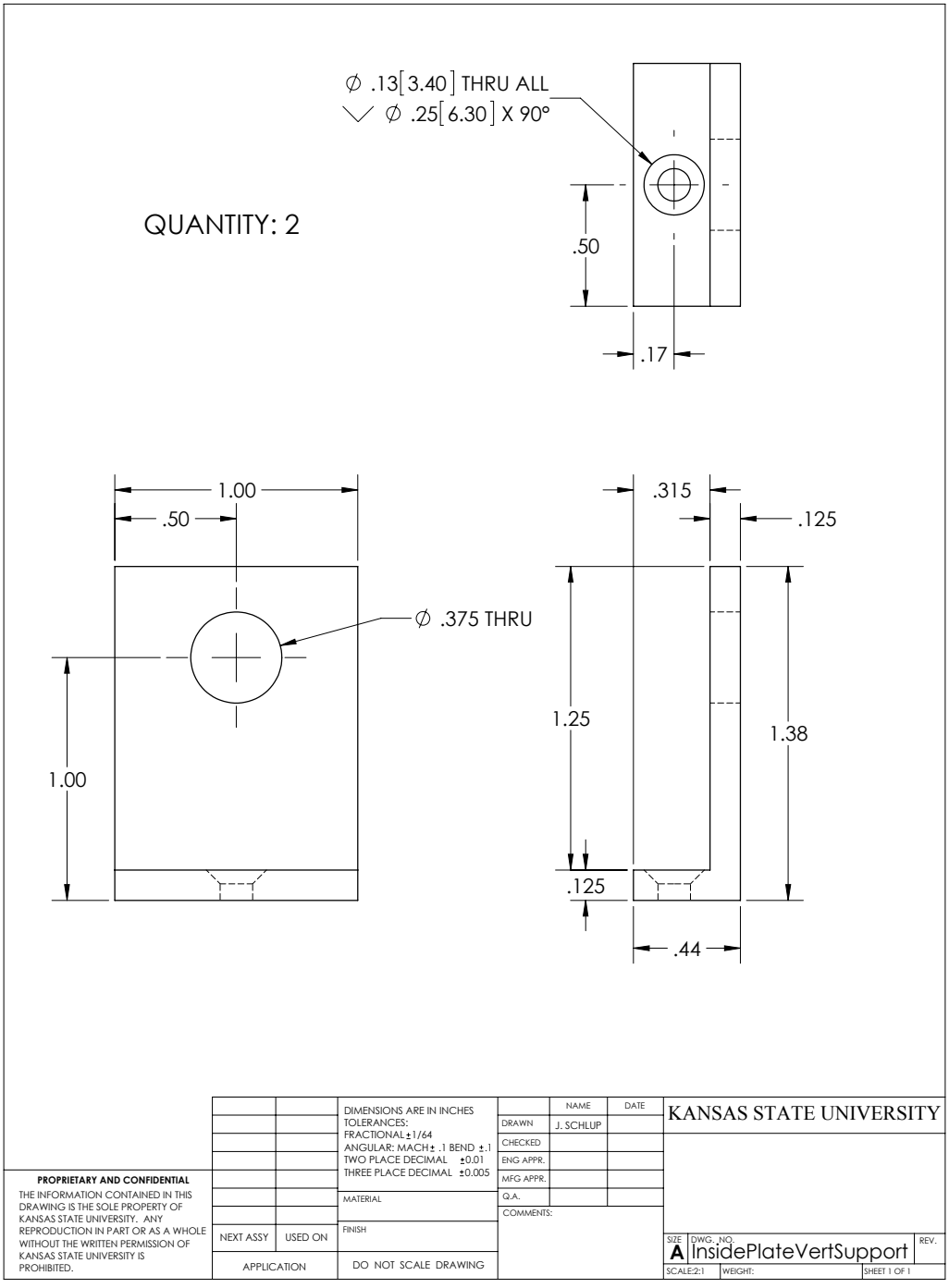


Figure A.21: Vertical support for insert plates.

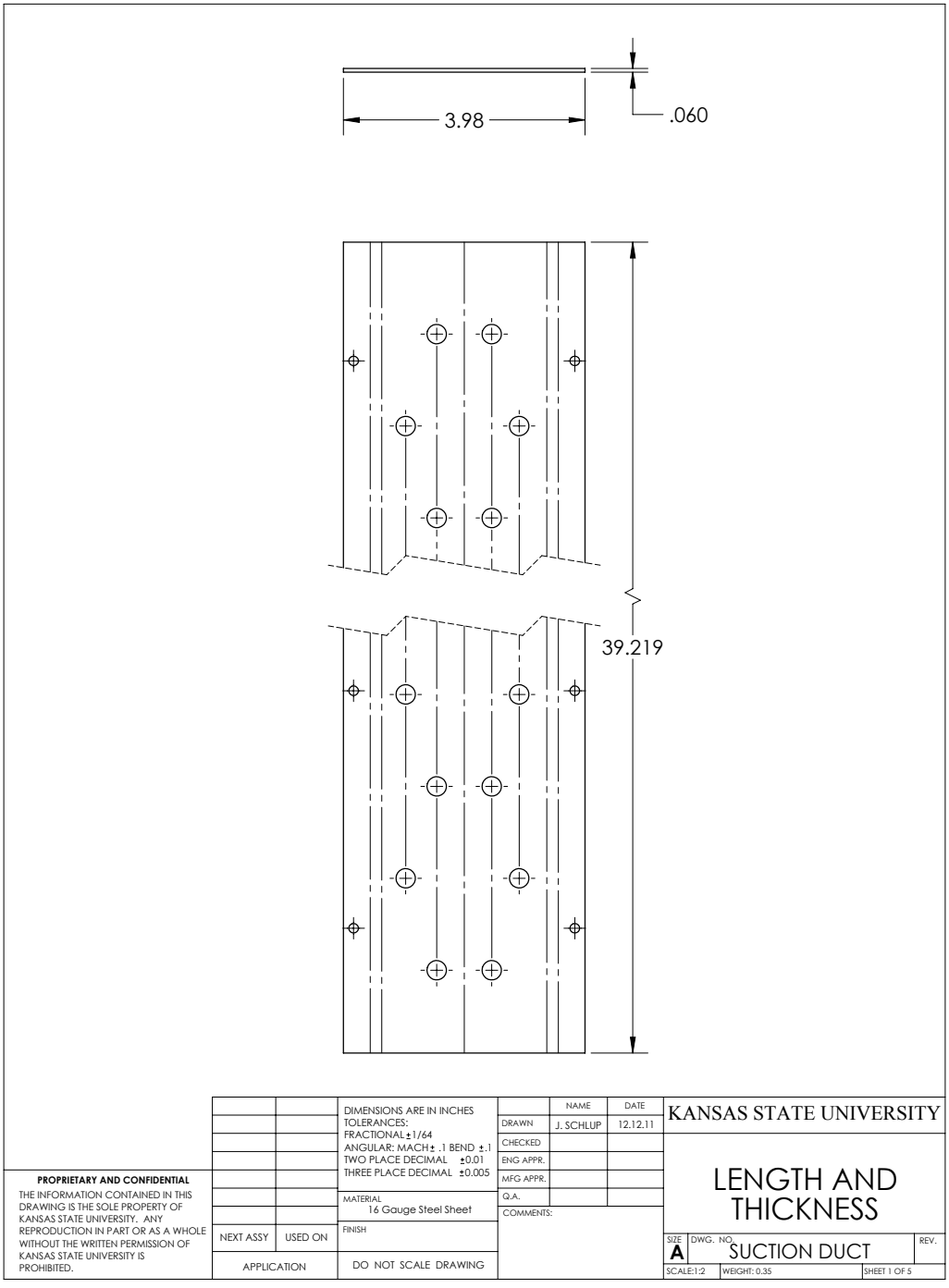


Figure A.22: Overall dimensions of suction duct.

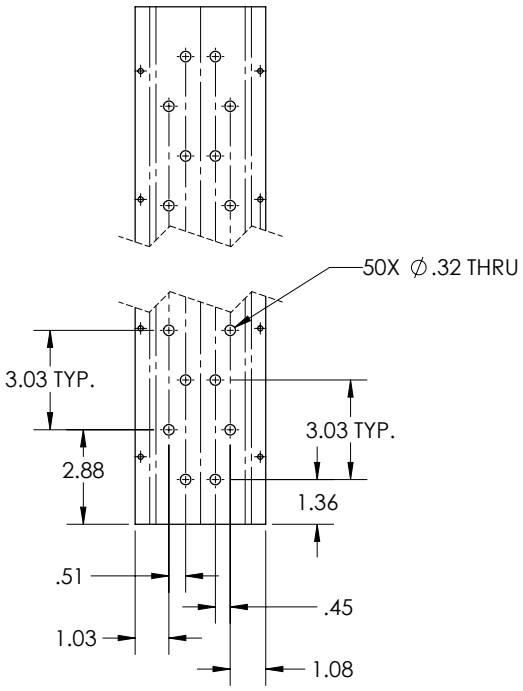


| | | | | | |
|---|---|---|---|---|---|
| | | DIMENSIONS ARE IN INCHES<br>TOLERANCES:<br>FRACTIONAL ±1/64<br>ANGULAR: MACH ± .1 BEND ±.1<br>TWO PLACE DECIMAL ±0.01<br>THREE PLACE DECIMAL ±0.005 | | NAME | DATE |
| | | | DRAWN | J. SCHLUP | 12.12.11 |
| | | | CHECKED | | |
| | | | ENG APPR. | | |
| | | | MFG APPR. | | |
| | | | Q.A. | | |
| | | MATERIAL<br>16 Gauge Steel Sheet | COMMENTS: | | |
| NEXT ASSY | USED ON | FINISH | | | |
| APPLICATION | | DO NOT SCALE DRAWING | | | |

**PROPRIETARY AND CONFIDENTIAL**

THE INFORMATION CONTAINED IN THIS DRAWING IS THE SOLE PROPERTY OF KANSAS STATE UNIVERSITY. ANY REPRODUCTION IN PART OR AS A WHOLE WITHOUT THE WRITTEN PERMISSION OF KANSAS STATE UNIVERSITY IS PROHIBITED.

KANSAS STATE UNIVERSITY

FLOW HOLE LOCATIONS

| SIZE | DWG. NO. | REV. |
|---|---|---|
| A | SUCTION DUCT | |
| SCALE:1:4 | WEIGHT: 0.35 | SHEET 2 OF 5 |

Figure A.23: Vapor hole locations of suction duct.

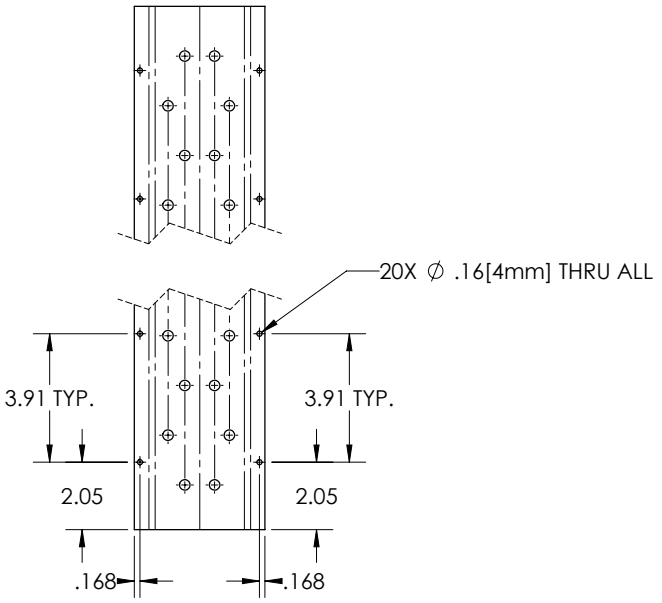


| | | | | | |
|---|---|---|---|---|---|
| | | DIMENSIONS ARE IN INCHES<br>TOLERANCES:<br>FRACTIONAL ±1/64<br>ANGULAR: MACH ± .1 BEND ±.1<br>TWO PLACE DECIMAL ±0.01<br>THREE PLACE DECIMAL ±0.005 | | NAME | DATE |
| | | | DRAWN | J. SCHLUP | 12.12.11 |
| | | | CHECKED | | |
| | | | ENG APPR. | | |
| | | | MFG APPR. | | |
| | | | Q.A. | | |
| | | MATERIAL<br>16 Gauge Steel Sheet | COMMENTS: DUAL DIMENSIONS ARE IN MM. THE LARGER, 7 MM HOLE OCCURS ONLY ONCE PER SIDE, AT HOLE LOCATION 9. | | |
| | | FINISH | | | |
| NEXT ASSY | USED ON | | | | |
| APPLICATION | | DO NOT SCALE DRAWING | | | |

KANSAS STATE UNIVERSITY

SIDE PLATE
HOLE LOCATIONS

SIZE A | DWG. NO. SUCTION DUCT | REV.

SCALE:1:4 | WEIGHT: 0.35 | SHEET 3 OF 5



Figure A.24: Attachment hole locations of suction duct.

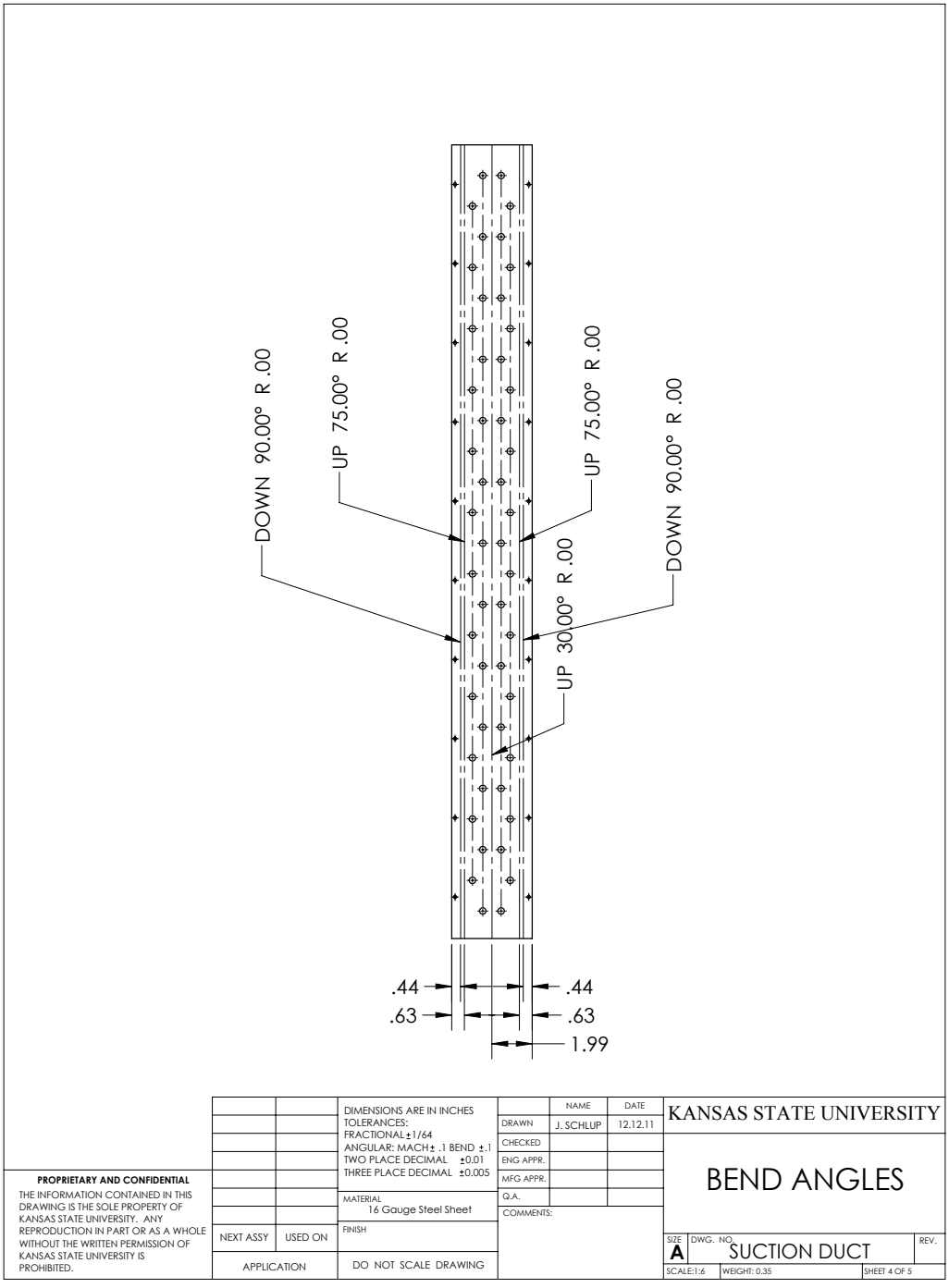


Figure A.25: Sheet metal bend angles for suction duct.

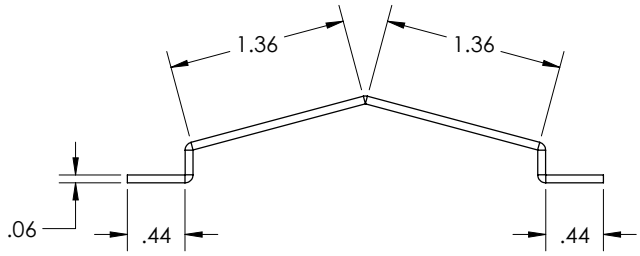


| | | | | | | |
|---|---|---|---|---|---|---|
| | | DIMENSIONS ARE IN INCHES<br>TOLERANCES:<br>FRACTIONAL ±1/64<br>ANGULAR: MACH ± .1 BEND ±.1<br>TWO PLACE DECIMAL ±0.01<br>THREE PLACE DECIMAL ±0.005 | | NAME | DATE | KANSAS STATE UNIVERSITY |
| | | | DRAWN | J. SCHLUP | 12.12.11 | |
| | | | CHECKED | | | |
| | | | ENG APPR. | | | FOLDED DIMENSIONS |
| | | | MFG APPR. | | | |
| | | | Q.A. | | | |
| | | MATERIAL<br>16 Gauge Steel Sheet | COMMENTS: | | | |
| | | FINISH | | | | SIZE A DWG. NO. SUCTION DUCT REV. |
| NEXT ASSY | USED ON | | | | | SCALE:1:1 WEIGHT: 0.35 SHEET 5 OF 5 |
| APPLICATION | | DO NOT SCALE DRAWING | | | | |



Figure A.26: Sheet metal bend lengths for suction duct.

# Appendix B

# Facility Process Flow Diagram

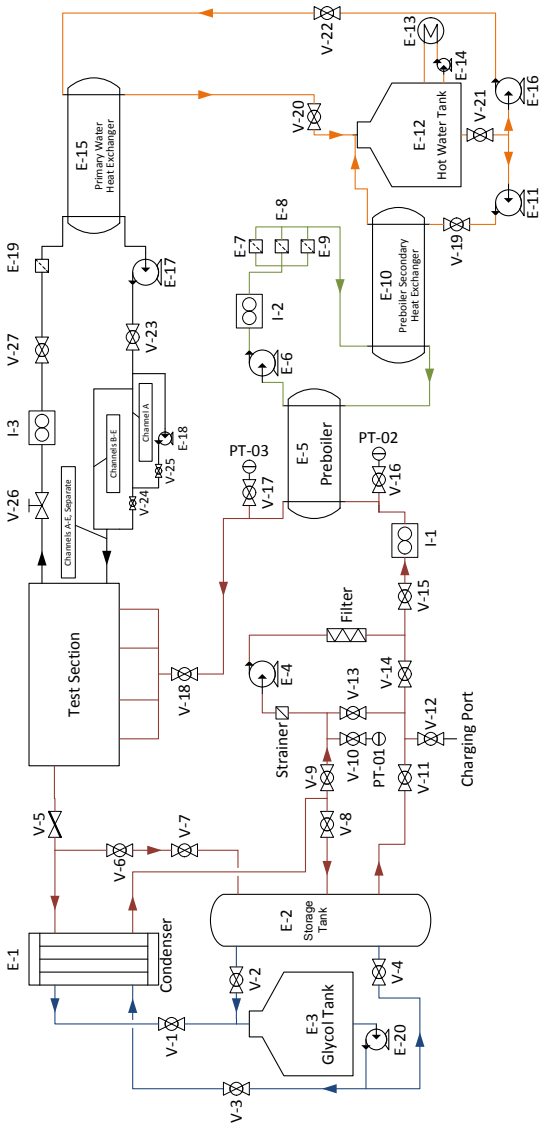


Figure B.1: Process flow diagram of the entire test facility. All equipment is labeled as referenced in Chapter 3.

# Appendix C

# Instrumentation Channels

| Labeled Name | Description | Card Channel | Comments |
|---|---|---|---|
| AIT | Channel A Inlet Temperature (Therm) | 1001 | Resistance Measurement 10 $k\Omega$, 6 1/2 Digits |
| AOT | Channel A Outlet Temperature (Therm) | 1002 | |
| A4IT | Channel A4 Inlet Temperature (Therm) | 1003 | |
| B4IT | Channel B4 Inlet Temperature (Therm) | 1004 | |
| C4IT | Channel C4 Inlet Temperature (Therm) | 1005 | |
| D4IT | Channel D4 Inlet Temperature (Therm) | 1006 | |
| E4IT | Channel E4 Inlet Temperature (Therm) | 1007 | |
| EOT | Channel E Outlet Temperature (Therm) | 1008 | |
| D2IT | Channel D2 Inlet Temperature (Therm) | 1009 | |
| E2IT | Channel E2 Inlet Temperature (Therm) | 1010 | |
| D3IT | Channel D3 Inlet Temperature (Therm) | 1011 | |
| E3IT | Channel E3 Inlet Temperature (Therm) | 1012 | |
| TSOT | Test Section Outlet Temperature (Therm) | 1013 | |
| PBIT | Preboiler Inlet Temperature (RTD) | 1031 | Resistance Measurement 10 $k\Omega$, 6 1/2 Digits |
| PBOT | Preboiler Outlet Temperature (RTD) | 1032 | |
| PBWOT | Preboiler Water Outlet Temperature (RTD) | 1034 | |
| TSIP | Test Section Inlet Pressure | 2014 | Voltage Measurement (0-5 VDC) |
| TSP1 | Test Section 1st Row Pressure | 2015 | |
| TSP2 | Test Section 2nd Row Pressure | 2016 | |
| TSP3 | Test Section 3rd Row Pressure | 2017 | |
| TSP4 | Test Section 4th Row Pressure | 2018 | |
| A1IP | Tube A1 Inlet Pressure | 2019 | |
| A1OP | Tube A1 Outlet Pressure | 2020 | |
| A4IP | Tube A4 Inlet Pressure | 2021 | |
| A4OP | Tube A4 Outlet Pressure | 2022 | |
| PBIP | Preboiler Inlet Pressure | 2023 | |
| PBOP | Preboiler Outlet Pressure | 2024 | |
| RPIP | Refrigerant Pump Inlet Pressure | 2025 | |
| TSOP | Test Section Outlet Pressure | 2026 | |

*Continued on next page*

Table C.1 – *Continued from previous page*

| Labeled Name | Description | Card Channel | Comments |
|---|---|---|---|
| TSTI | Test Section Inlet Temperature (RTD) | 2034 | |
| TST1 | Test Section 1st Row Temperature (RTD) | 2035 | Resistance Measurement 10 $k\Omega$, 6 1/2 Digit |
| TST2 | Test Section 2nd Row Temperature (RTD) | 2036 | |
| TST3 | Test Section 3rd Row Temperature (RTD) | 2037 | |
| TST4 | Test Section 4th Row Temperature (RTD) | 2038 | |
| CIT | Condenser Inlet Temperature (RTD) | 2039 | Resistance Measurement 1 $k\Omega$, 6 1/2 Digit |
| RPIT | Refrigerant Pump Inlet Temperature (RTD) | 2040 | |
| RFR | Refrigerant Flow Rate | 3002 | Frequency Measurement |
| BFR | Test Section Channel B Water Flow Rate | 3003 | |
| CFR | Test Section Channel C Water Flow Rate | 3004 | |
| DFR | Test Section Channel D Water Flow Rate | 3005 | |
| EFR | Test Section Channel E Water Flow Rate | 3006 | |
| PBFR | Preboiler Water Flow Rate | 3007 | |
| AFR | Test Section Channel A Water Flow Rate | 3008 | |
| PBWIT | Preboiler Water Inlet Temperature (Thermistor) | 3020 | Resistance Measurement, 100$k\Omega$, 6 1/2 Digits |
| AD | Test Section Channel A Density | 3021 | Current Measurement (4-20 mA) |
| BD | Test Section Channel B Density | 3022 | |
| CD | Test Section Channel C Density | 3023 | |
| DD | Test Section Channel D Density | 3024 | |
| ED | Test Section Channel E Density | 3025 | |
| PBD | Preboiler Water Density | 3026 | |
| RT | Refrigerant Temperature | 3027 | |
| RD | Refrigerant Density | 3028 | |
| EOT | Test Section Channel E Outlet Temperature (RTD) | 3029 | Resistance Measurement 1 $k\Omega$, 6 1/2 Digit |
| BIT | Test Section Channel B Inlet Temperature (RTD) | 3033 | |
| CIT | Test Section Channel C Inlet Temperature (RTD) | 3034 | |
| DIT | Test Section Channel D Inlet Temperature (RTD) | 3035 | |
| EIT | Test Section Channel E Inlet Temperature (RTD) | 3036 | |
| BOT | Test Section Channel B Outlet Temperature (RTD) | 3037 | |
| COT | Test Section Channel C Outlet Temperature (RTD) | 3038 | |
| DOT | Test Section Channel D Outlet Temperature (RTD) | 3039 | |
| | Dummy Channel | 3040 | |

Table C.1: DAQ card channel connections for system instrumentation. Any unlisted card channels are not in use.

# Appendix D

# CFD Analysis Code

This is the Matlab code used to analyze the generated .csv files from Fluent for all vapor volume fraction measurements. The first block of code contains all of the details for the void fraction PDF analysis, including the creation of all plots. Some of the labeling for these plots changes depending on which case is run.

```
%=================================================
%Matlab code to analyze PDF distributions of void
%fractions in a simulated shell and tube bundle.
%Written by: Jason Schlup, 2013
%Included packages: plot2svg
%=================================================

function fileanalysis (filename)
%=================================================
%This code is used for single file analysis

%clear all;
%filename = uigetfile ('*.csv',' Select vapor volume fraction file ');
%=================================================
fid = fopen(filename);
Header_text = textscan(fid, '%s', 10, 'delimiter', ',\n');

Block = 1;

while (~feof(fid))
    Data{1,Block}=cell2mat(textscan(fid,'%f %f','Delimiter',','));
    textscan(fid,'%s',10,'delimiter',',\n');
    Block=Block+1;
end

%Convert cell array to matrix
alldata = cell2mat(Data);

```

```
%Remove extra time columns
alldata(:,3:2:end)=[];

%Code for formatting plots by using file name.
[token,remain] = strtok(filename,'Q');
quality = token(end1:end);
massflux = remain(3:4);

rowcounter = 0;
i = 0;
%Checks for nonzero vapor volume fraction
while i == 0
    rowcounter = rowcounter + 1; %Tracks row number
    for j=2:size(alldata,2) %Loops through all columns
        i = alldata(rowcounter,j); %Sets i = vapor volume fraction value in row and column
        if i ~= 0 %If i is not zero, first non zero vapor volume fraction has been found, break out of
            loops
            break;
        end
    end
end

%Stores all vapor volume fraction after the first non zero vapor volume fraction has
%been sensed
alldataafterfirst = alldata(rowcounter:end,:);

%Takes the last second of data
lastseconddata = alldata(end999:end,:);
%Stores just the last second void fraction values in a new array
lastsecondvoidfrac = lastseconddata(:,2:end);
%Averages the last second of void fraciton values, using a delta t of 20
%time steps; in this case, delta t = 0.001s, thus using 0.02s time steps
%for averaging
averagelastseconddata = mean(reshape(lastsecondvoidfrac,20,[]))';

%Finds skewness coefficient of all of the void fraction data
skew_alldataafterfirst = skewness(alldataafterfirst(:,2));
%Finds kurtosis coefficient of all of the void fraction data
kurtosis_alldataafterfirst = kurtosis(alldataafterfirst(:,2));
%Finds skewness of the average last second void fraction data
skew_averagelastseconddata = skewness(averagelastseconddata);
%Finds kurtosis of the average last second void fraction data
kurtosis_averagelastseconddata = kurtosis(averagelastseconddata);

basefilename=filename(1:end4);
fclose(fid);

%Uncomment below to print to one PDF
%Print to one PDF
figure(1);
subplot(2,2,1)
```

```
79
80  %Histogram of all data after the first non zero void fraction measurement.
81  %Binned into 20 delta_epsilon
82
83  hist( alldataafterfirst (:,2) ,20)
84  text_loc_x = .5;
85  text_loc_y = max(hist( alldataafterfirst (:,2) ,20)) *.9;
86   stats_vals_all = ['Skewness = ',num2str(skew_alldataafterfirst),10, 'Kurtosis =
        ',num2str( kurtosis_alldataafterfirst )];
87  text( text_loc_x , text_loc_y , stats_vals_all , 'HorizontalAlignment','right' , 'FontSize',6) ;
88   title ('All_void_fraction_data', 'FontSize',8) ;
89  xlabel({'Void_Fraction';'(a)'}, 'FontSize',8) ;
90  set(gca, 'FontSize',8) ;
91  ylabel('Count','FontSize',8) ;
92  xlim([0 1]) ;
93
94  subplot(2,2,2)
95
96  %Histogram of last second of data, averaged with delta t = 0.02s, leading
97  %to 50 total histogram events. Binned into 20 delta epsilon
98  %figure(2);
99  hist(averagelastseconddata,20)
100 text_loc_x = .5;
101 text_loc_y = max(hist(averagelastseconddata,20))*.9;
102 stats_vals = ['Skewness = ',num2str(skew_averagelastseconddata),10,'Kurtosis = 
        ',num2str(kurtosis_averagelastseconddata)];
103 text( text_loc_x , text_loc_y , stats_vals , 'HorizontalAlignment','right' , 'FontSize',6) ;
104  title ('Average_of_last_second_of_data, \Deltat = 0.02s','FontSize',8) ;
105 xlabel({'Void_Fraction';'(b)'}, 'FontSize',8) ;
106 set(gca, 'FontSize',8) ;
107 ylabel('Count','FontSize',8) ;
108 xlim([0 1]) ;
109
110
111 subplot(2,2,3)
112
113 %Normalized histogram of last second of data, averaged with delta t = 0.02s
114 %figure(3);
115 [count_norm,bins_norm] = hist(averagelastseconddata,20);
116 bins_delta = bins_norm(2)bins_norm(1);
117 A=sum(count_norm)*bins_delta;
118 bar(bins_norm, count_norm/sum(count_norm)/bins_delta);
119  title ('Normalized_average_of_last_second_of_data, \Deltat = 0.02s','FontSize',8) ;
120 xlabel({'Void_Fraction';'(c)'}, 'FontSize',8) ;
121 set(gca, 'FontSize',8) ;
122 ylabel('Normalized_Count','FontSize',8);
123  text_loc_y = max(hist(averagelastseconddata,20))*.9/sum(count_norm)/bins_delta;
124 text( text_loc_x , text_loc_y , stats_vals , 'HorizontalAlignment','right' , 'FontSize',6) ;
125 xlim([0 1]) ;
126
127 %Commented out the void fraction measurement vs. time plot
```

```
% subplot(2,2,3)
%
% %Scatterplot of all void fraction values versus time
% %figure(4);
% plot(alldata(:,1),alldata(:,2:end));
% %plot(alldata(:,1),alldata(:,2))
% title(strcat('Void fraction measurements versus time',titlestr));
% xlabel('Time (s)');
% ylabel('Void Fraction');

subplot(2,2,4)

j_glower =0.250.15; %Transition vapor velocity from bubbly to intermittent
j_gupper=0.25+0.15; %Transition vapor velocity from intermittent to annular
rho_g=17.131; %Density of vapor R134a at 5C
for i=50:1000
    x(i)=i/1000.;
end
g_translower=j_glower*rho_g./x;
g_transupper=j_gupper*rho_g./x;
plot(x,g_translower,x,g_transupper,str2num(quality)/100.,str2num(massflux),'*');
xlim([0 1]);
ylim([0 40]);
h_legend = legend('B I','I A','Data Point');
set(h_legend,'FontSize',8);
title('Flow pattern transition lines for adiabatic flow','FontSize',8);
xlabel({'Quality';'(d)'},'FontSize',8);
ylabel('Mass flux (kg/m^2s)','FontSize',8);

%Header for all subplots
titlestr = sprintf(' x=%d%%, G=%d kg/m^2s',str2num(quality),str2num(massflux));
ha = axes('Position',[0 0 1 1],'Xlim',[0 1],'Ylim',[0
    1],'Box','off','Visible','off','Units','normalized','clipping' ,'off');
text(0.5, 1,strcat('\bf CFD analysis for
    ',titlestr),'HorizontalAlignment','center','VerticalAlignment', 'top')

print('painters','dpdf','r600',strcat(basefilename,'.pdf'))
%================================

figure(2);

%Histogram of all data after the first non zero void fraction measurement.
%Binned into 20 delta_epsilon

hist(alldataafterfirst(:,2),20)
text_loc_x = .5;
text_loc_y = max(hist(alldataafterfirst(:,2),20))*.9;
stats_vals_all = ['Skewness = ',num2str(skew_alldataafterfirst),10,'Kurtosis =
    ',num2str(kurtosis_alldataafterfirst)];
text(text_loc_x,text_loc_y, stats_vals_all ,'HorizontalAlignment','right','FontSize',14);
title('All void fraction data','FontSize',16);
```

```
176 xlabel('Void_Fraction','FontSize',16);
177 set(gca,'FontSize',12);
178 ylabel('Count','FontSize',16);
179 xlim([0 1]);
180 plot2svg(strcat(basefilename,'_alldata.svg'));
181
182 figure(3);
183
184 %Histogram of last second of data, averaged with delta t = 0.02s, leading
185 %to 50 total histogram events. Binned into 20 delta epsilon
186 %figure(2);
187 hist(averagelastseconddata,20)
188 text_loc_x = .5;
189 text_loc_y = max(hist(averagelastseconddata,20))*.9;
190 stats_vals = ['Skewness_=_',num2str(skew_averagelastseconddata),10,'Kurtosis_=_
      ',num2str(kurtosis_averagelastseconddata)];
191 text(text_loc_x,text_loc_y,stats_vals,'HorizontalAlignment','right','FontSize',14);
192 title('Average_of_last_second_of_data','FontSize',16);
193 xlabel('Void_Fraction','FontSize',16);
194 set(gca,'FontSize',12);
195 ylabel('Count','FontSize',16);
196 xlim([0 1]);
197 plot2svg(strcat(basefilename,'_avglastsec.svg'));
198
199 figure(4);
200
201 %Normalized histogram of last second of data, averaged with delta t = 0.02s
202 %figure(3);
203 [count_norm,bins_norm] = hist(averagelastseconddata,20);
204 bins_delta = bins_norm(2)bins_norm(1);
205 A=sum(count_norm)*bins_delta;
206 bar(bins_norm, count_norm/sum(count_norm)/bins_delta);
207 title('Normalized_average_of_last_second_of_data','FontSize',16);
208 xlabel('Void_Fraction','FontSize',16);
209 set(gca,'FontSize',12);
210 ylabel('Normalized_Count','FontSize',16);
211 text_loc_y = max(hist(averagelastseconddata,20))*.9/sum(count_norm)/bins_delta;
212 text(text_loc_x,text_loc_y,stats_vals,'HorizontalAlignment','right','FontSize',14);
213 xlim([0 1]);
214 plot2svg(strcat(basefilename,'_normavglastsec.svg'));
215
216 figure(5);
217 %Creation of flow pattern map with transition regions
218 j_glower =0.250.15; %Transition vapor velocity from bubbly to intermittent
219 j_gupper=0.25+0.15; %Transition vapor velocity from intermittent to annular
220 rho_g=17.131; %Density of vapor R134a at 5C
221 for i=50:1000
222     x(i)=i/1000.;
223 end
224 g_translower=j_glower*rho_g./x;
225 g_transupper=j_gupper*rho_g./x;
```

```
226 plot(x,g_translower,x,g_transupper,str2num(quality)/100.,str2num(massflux),'*');
227 xlim([0  1]);
228 ylim([0  40]);
229 h_legend = legend('B I','I  A','Data Point');
230 set(h_legend,'FontSize',14);
231  title ('Flow pattern transition lines for adiabatic flow','FontSize',16);
232 xlabel('Quality','FontSize',16);
233 ylabel('Mass flux (kg/m^2s)','FontSize',16);
234 set(gca,'FontSize',12);
235 plot2svg(strcat(basefilename,' flowpattern.svg'));
```

This second block of code is a simple script that runs the PDF analysis on all csv files in a directory, allowing for easy analysis on a large number of files. If the analysis is to be run on a single file, this code can be used, or to chose a particular file, the first block of code can be modified slightly to not call this function and instead ask for the specific file to be analyzed.

```
%#Build a list of file names with absolute path
clear all;
fPath = uigetdir('.','Select directory containing CSV files');
if fPath==0, error('No folder selected.'), end
fNames = dir( fullfile (fPath,'*.csv') );
fNames = strcat(fPath, filesep , {fNames.name});

for i=1:length(fNames)
      fileanalysis (fNames{i})
end
```

# Appendix E

# CFD Results

The following figures contain the results of the CFD analysis. For each test condition, four figures are presented. Figure (a) is a histogram containing all of the VVF results for the six data locations in the simulation. Only values after the first non-zero VVF value are recorded; this eliminates the "start-up" time for the bundle. However, these results include VVF for the variable time step simulation.

Figure (b) contains the average VVF of the last second, with an averaging time of $\Delta t$=0.02 s. This $\Delta t$ value was recommended by Aprin et al. (2007) as a time where the void fractions $\varepsilon(t)$ and $\varepsilon(t + \Delta t)$ are no longer correlated. Figure (c) contains the same VVF results but is instead a normalized PDF.

Figure (d) plots the given CFD test condition on the flow pattern map proposed for adiabatic R-134a flow in a tube bundle by van Rooyen (2011). This figure is not used to determine the flow pattern of the CFD results; instead, it is used as a comparison to experimental data for the CFD results. All flow pattern classifications are based on the statistical methods described in Section 7.2.3.

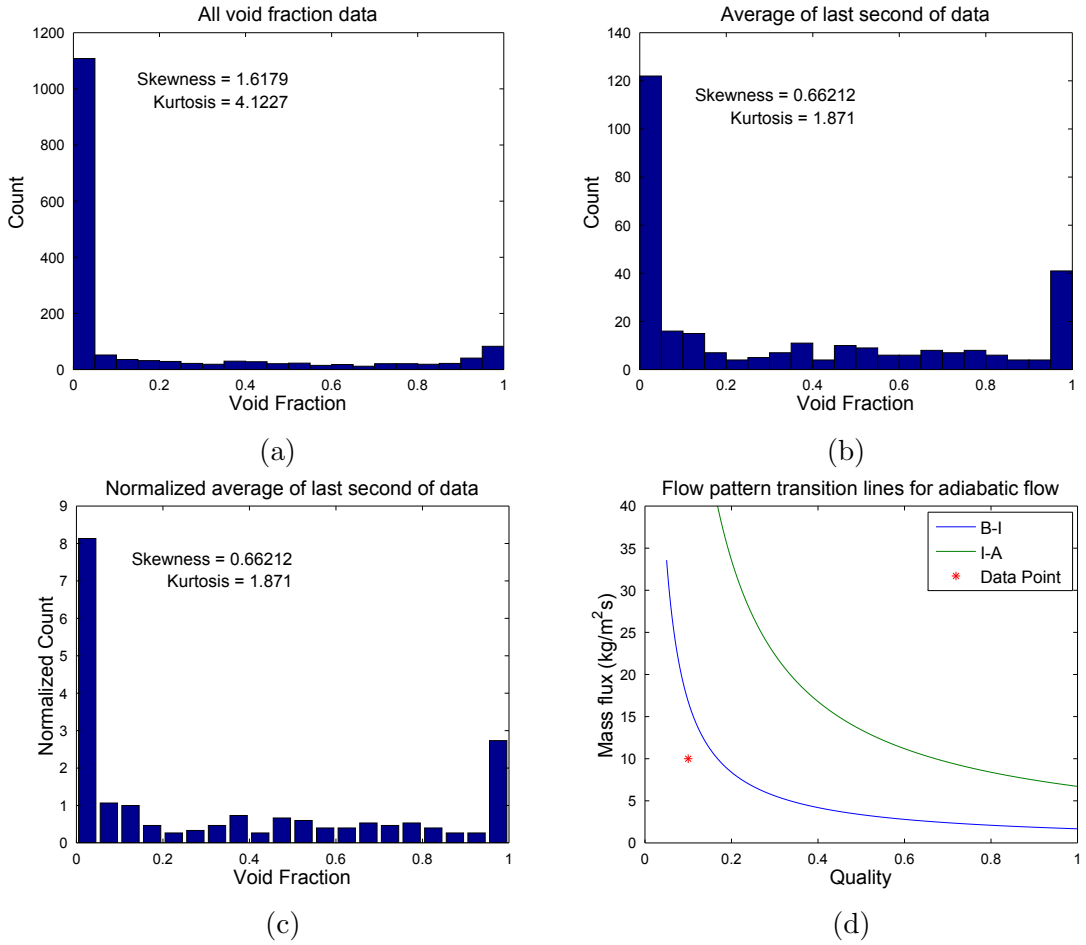


Figure E.1: CFD results for x=10%, G=10 $kg/m^2 \cdot s$.

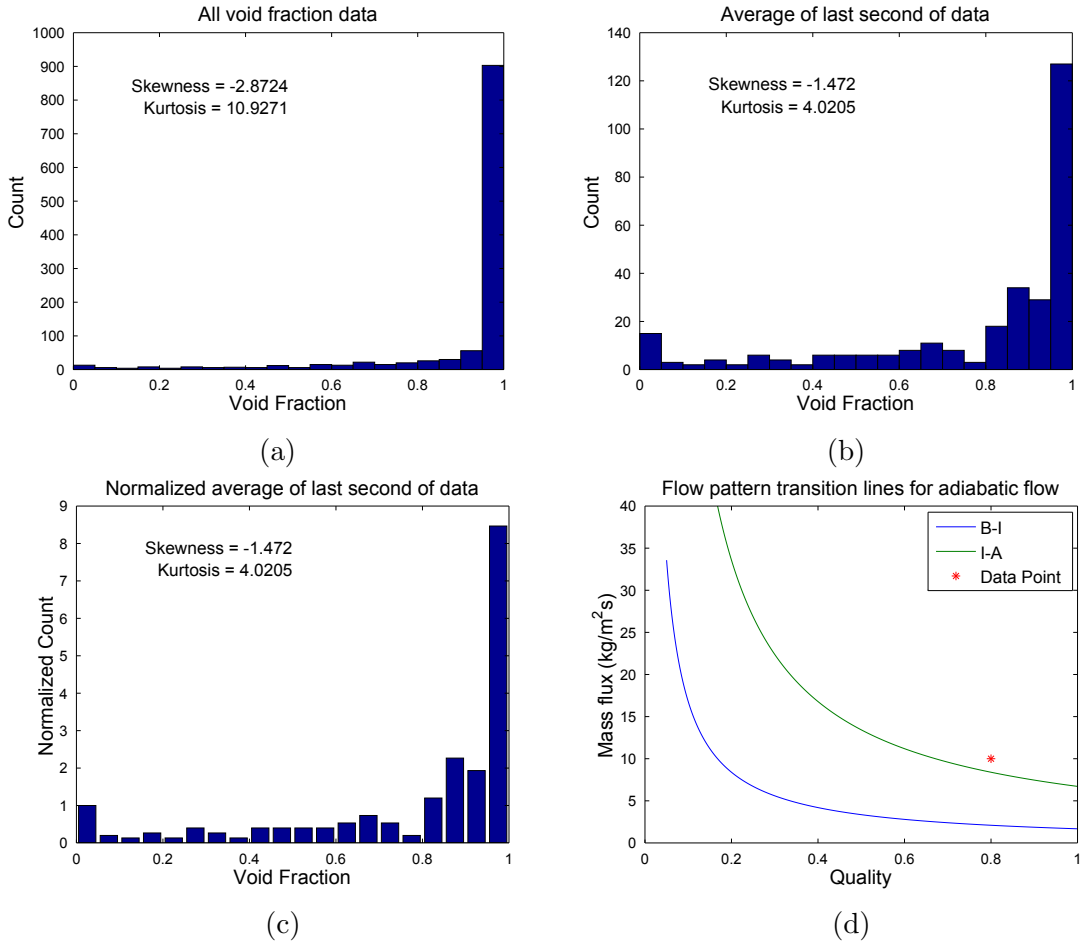


Figure E.2: CFD results for x=80%, G=10 $kg/m^2 \cdot s$.

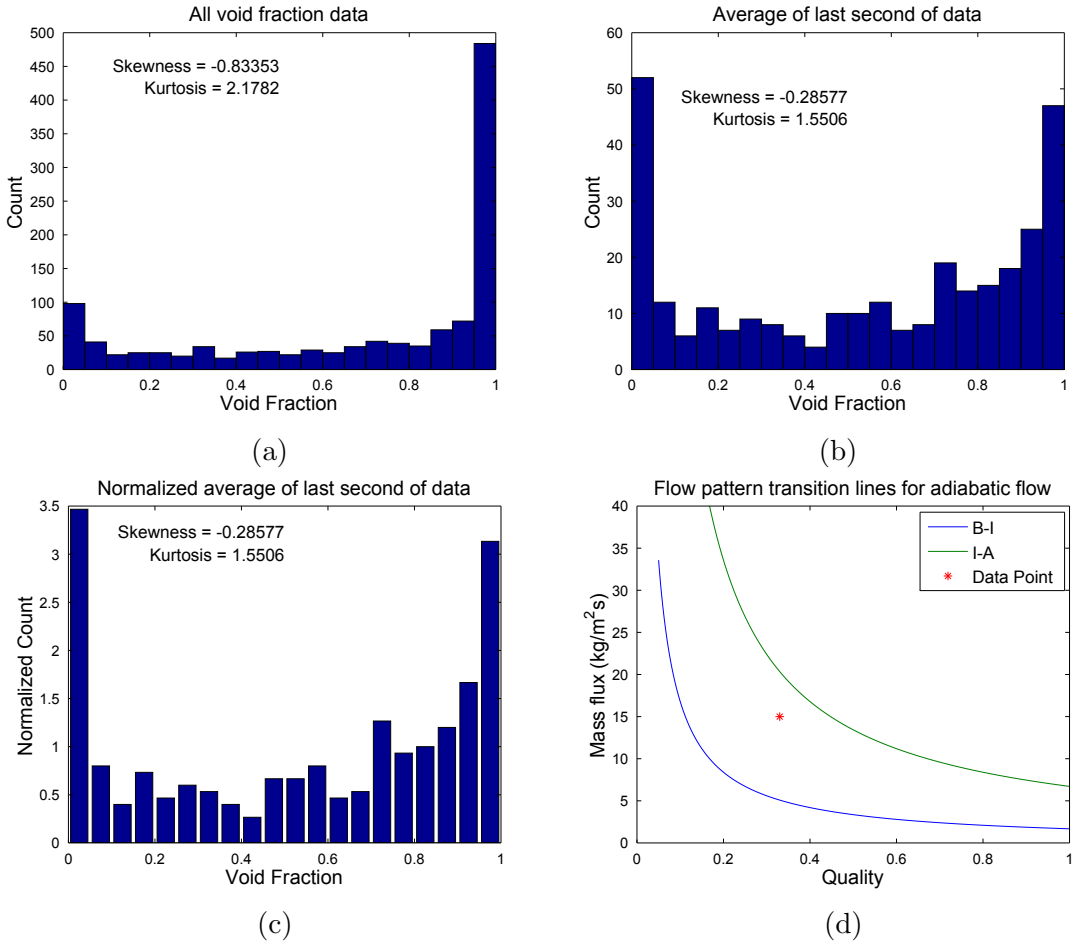


Figure E.3: CFD results for x=33%, G=15 $kg/m^2 \cdot s$.

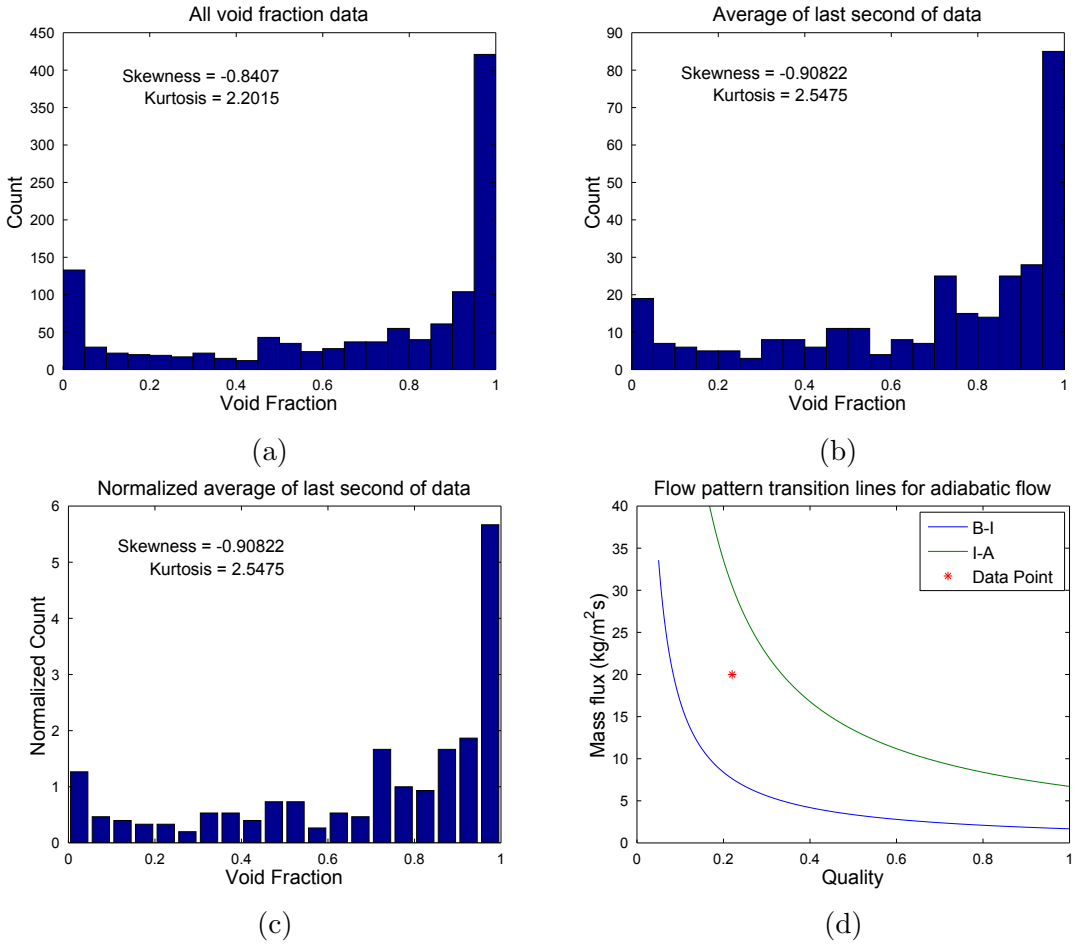


Figure E.4: CFD results for x=22%, G=20 $kg/m^2 \cdot s$.

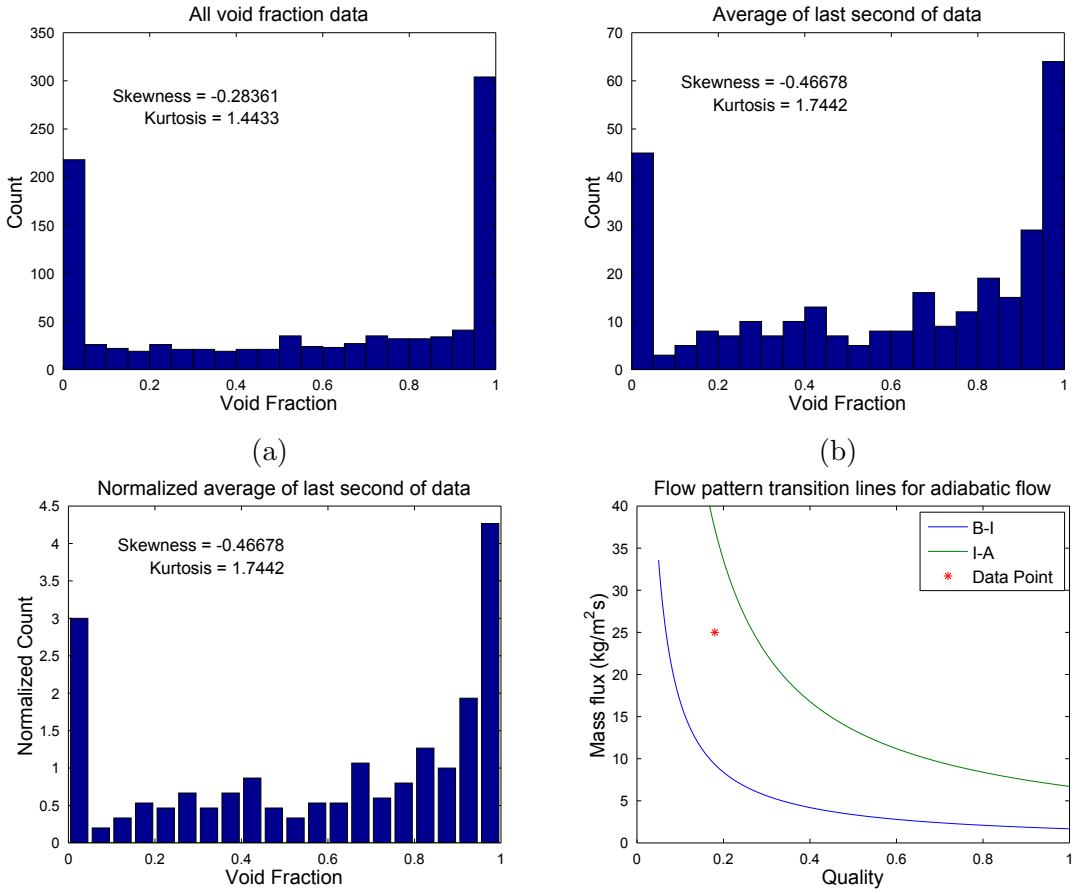


Figure E.5: CFD results for x=18%, G=25 $kg/m^2 \cdot s$.

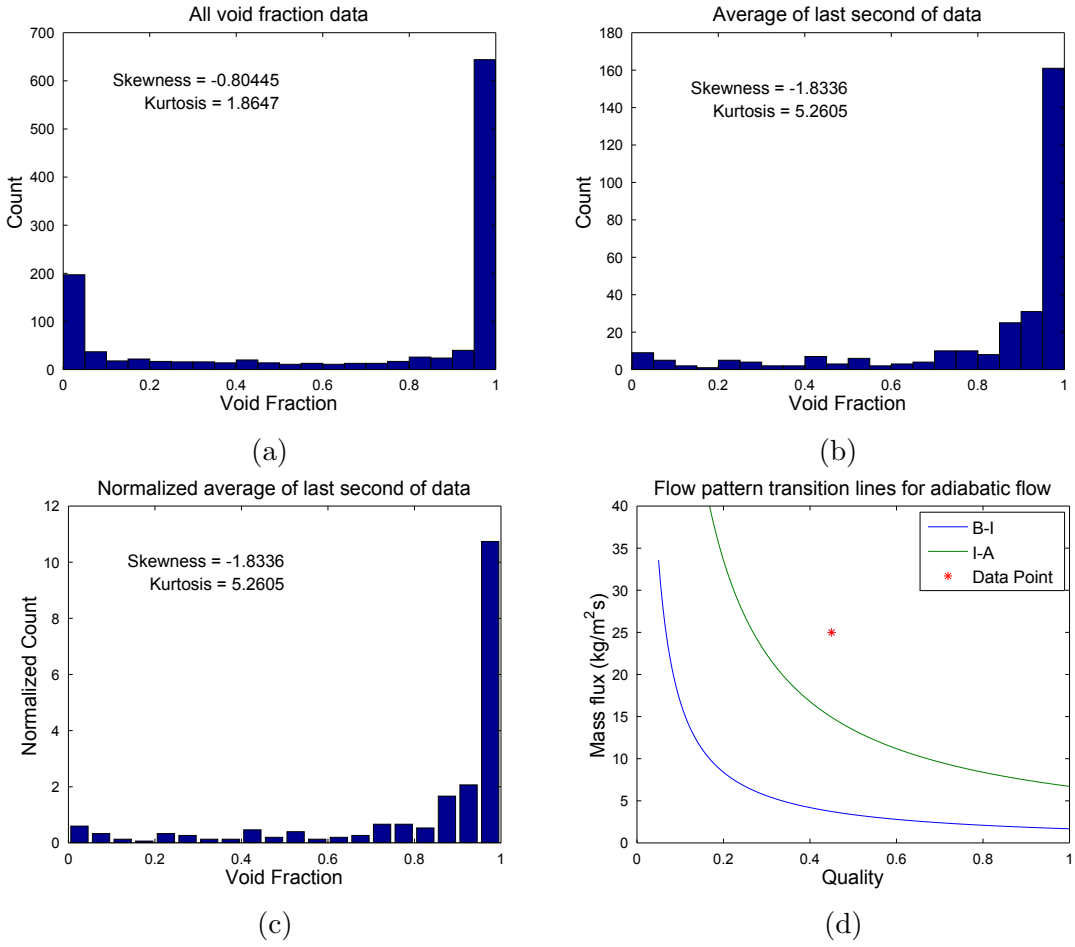


Figure E.6: CFD results for x=45%, G=25 $kg/m^2 \cdot s$.

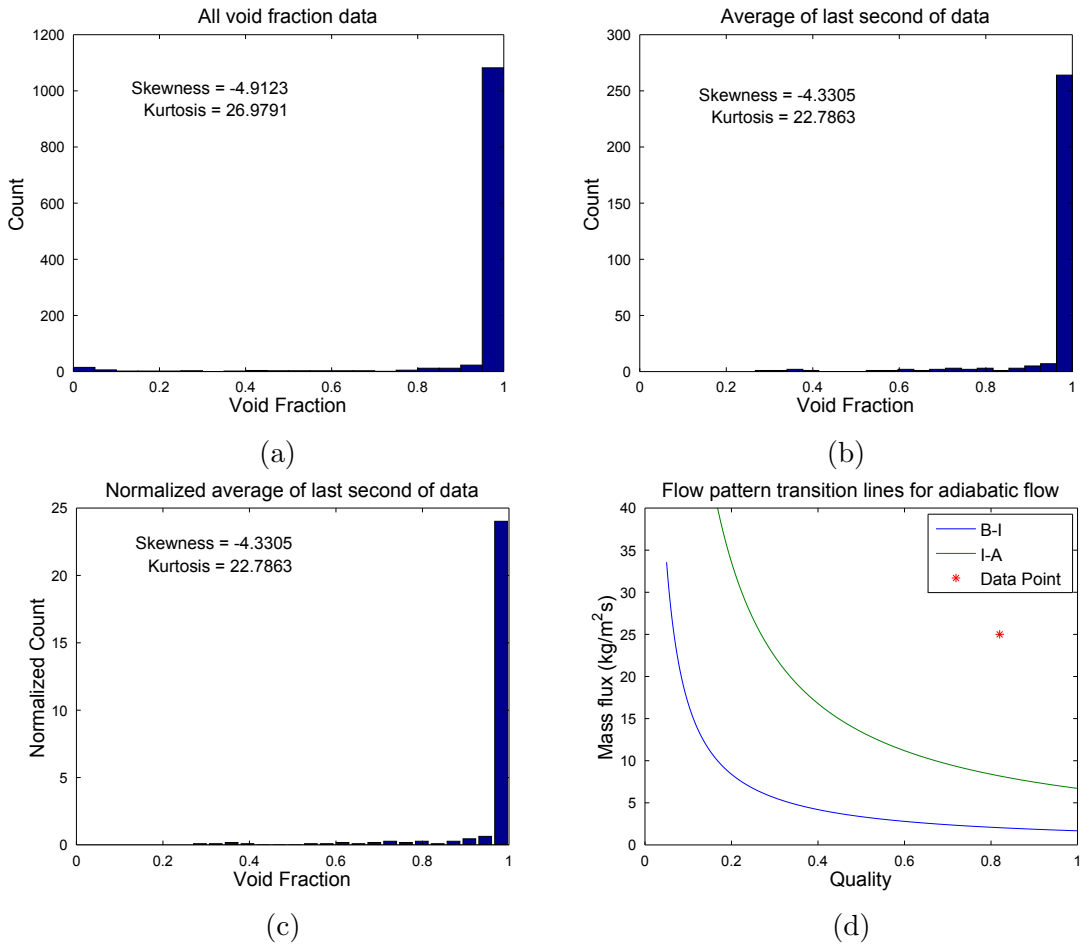


Figure E.7: CFD results for x=82%, G=25 $kg/m^2 \cdot s$.

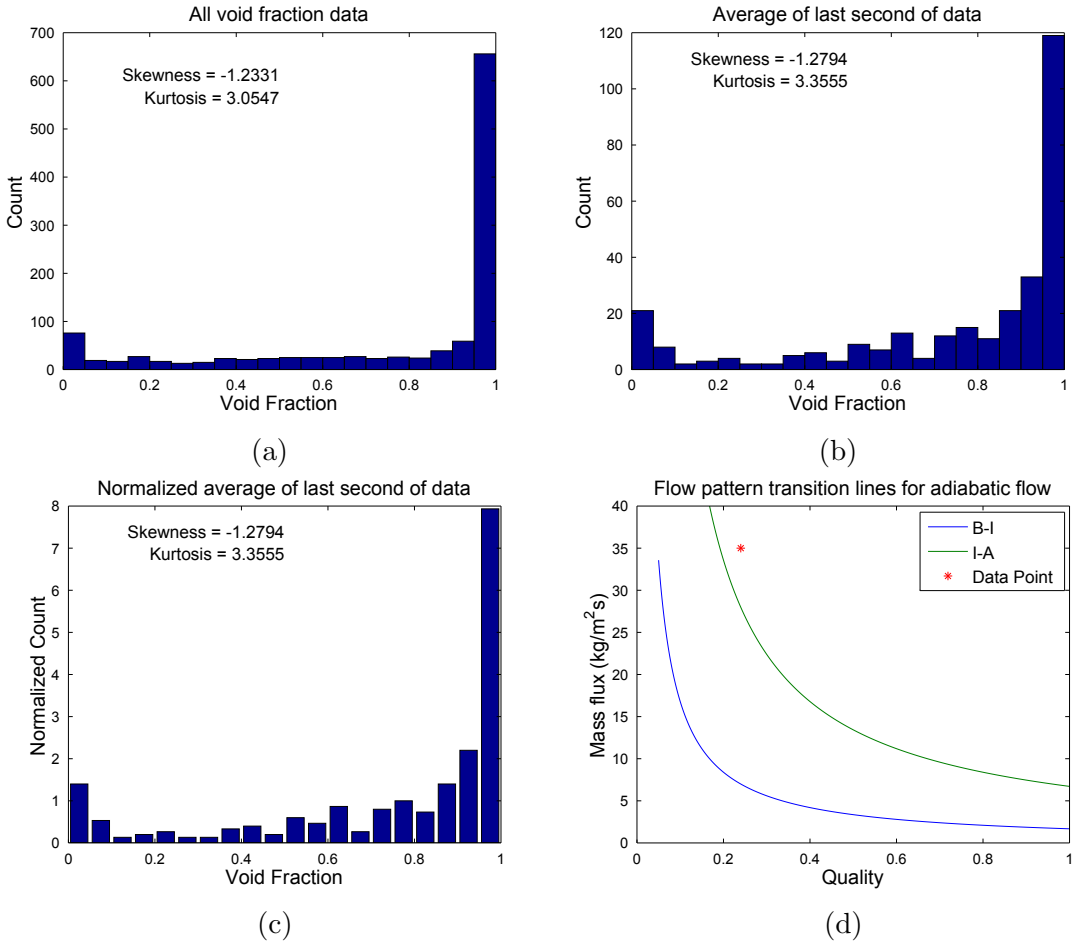


Figure E.8: CFD results for x=24%, G=35 $kg/m^2 \cdot s$.

# Appendix F

# Mathcad Uncertainty File

Figure F.1 shows screenshots of an example Mathcad uncertainty analysis file for the smooth tube bundle.

base := "E:\Jason Backup - Masters\Masters Backup\Data Files\Compiled Files\Smooth Tube\High Speed Videos\"

file := "10 14 0.0 05-04-12 11 21 33.xlsm"

filename := concat(base, file)

data := READEXCEL(filename, "Summary for Uncertainty Analys!")

kJ := 1000·J

area := π·0.75in·1m = 0.05985 $m^2$

A3 := area·3

Calculations

data =

| | 0 | 1 | 2 |
|---|---|---|---|
| 0 | "Flow Rate Water A (kg/s)" | "Flow Rate Water B (kg/s)" | "Flow Rate Water C (kg/s)" |
| 1 | 0.257 | 0.311 | 0.315 |
| 2 | 0.257 | 0.311 | 0.315 |
| 3 | 0.257 | 0.311 | 0.315 |
| 4 | 0.257 | 0.311 | ... |

umdot := .1%

$mdot_{WA} := data_{1,0} \cdot \frac{kg}{s} = 0.257 \frac{kg}{s}$

$mdot_{WB} := data_{1,1} \cdot \frac{kg}{s} = 0.311 \frac{kg}{s}$

$mdot_{WC} := data_{1,2} \cdot \frac{kg}{s} = 0.315 \frac{kg}{s}$

$mdot_{WD} := data_{1,3} \cdot \frac{kg}{s} = 0.324 \frac{kg}{s}$

$mdot_{WE} := data_{1,4} \cdot \frac{kg}{s} = 0.305 \frac{kg}{s}$

$umdot_{WA} := umdot \cdot mdot_{WA} = 2.573 \times 10^{-4} \frac{kg}{s}$

$umdot_{WB} := umdot \cdot mdot_{WB} = 3.106 \times 10^{-4} \frac{kg}{s}$

$umdot_{WC} := umdot \cdot mdot_{WC} = 3.149 \times 10^{-4} \frac{kg}{s}$

$umdot_{WD} := umdot \cdot mdot_{WD} = 3.241 \times 10^{-4} \frac{kg}{s}$

$umdot_{WE} := umdot \cdot mdot_{WE} = 3.048 \times 10^{-4} \frac{kg}{s}$

$$\mathrm{mdot}_{all}(AFR, BFR, CFR, DFR, EFR) := AFR + BFR + CFR + DFR + EFR \qquad uCp_W := .00019 \cdot \frac{kJ}{kg \cdot K}$$

$$\mathrm{mdot}_{BD}(BFR, DFR) := BFR + DFR$$

$$\mathrm{mdot}_{Wall} := \mathrm{mdot}_{all}(\mathrm{mdot}_{WA}, \mathrm{mdot}_{WB}, \mathrm{mdot}_{WC}, \mathrm{mdot}_{WD}, \mathrm{mdot}_{WE}) = 1.512 \frac{kg}{s}$$

$$\mathrm{mdot}_{WBD} := \mathrm{mdot}_{BD}(\mathrm{mdot}_{WB}, \mathrm{mdot}_{WD}) = 0.635 \frac{kg}{s}$$

$$\mathrm{umdot}_{all} := \left[ \left[ \frac{d}{d\mathrm{mdot}_{WA}} \left( \mathrm{mdot}_{all}(\mathrm{mdot}_{WA}, \mathrm{mdot}_{WB}, \mathrm{mdot}_{WC}, \mathrm{mdot}_{WD}, \mathrm{mdot}_{WE}) \cdot \mathrm{umdot}_{WA} \right) \right]^2 \ldots \right.$$
$$+ \left[ \frac{d}{d\mathrm{mdot}_{WB}} \left( \mathrm{mdot}_{all}(\mathrm{mdot}_{WA}, \mathrm{mdot}_{WB}, \mathrm{mdot}_{WC}, \mathrm{mdot}_{WD}, \mathrm{mdot}_{WE}) \cdot \mathrm{umdot}_{WB} \right) \right]^2 \ldots$$
$$+ \left[ \frac{d}{d\mathrm{mdot}_{WC}} \left( \mathrm{mdot}_{all}(\mathrm{mdot}_{WA}, \mathrm{mdot}_{WB}, \mathrm{mdot}_{WC}, \mathrm{mdot}_{WD}, \mathrm{mdot}_{WE}) \cdot \mathrm{umdot}_{WC} \right) \right]^2 \ldots$$
$$+ \left[ \frac{d}{d\mathrm{mdot}_{WD}} \left( \mathrm{mdot}_{all}(\mathrm{mdot}_{WA}, \mathrm{mdot}_{WB}, \mathrm{mdot}_{WC}, \mathrm{mdot}_{WD}, \mathrm{mdot}_{WE}) \cdot \mathrm{umdot}_{WD} \right) \right]^2 \ldots$$
$$\left. + \left[ \frac{d}{d\mathrm{mdot}_{WE}} \left( \mathrm{mdot}_{all}(\mathrm{mdot}_{WA}, \mathrm{mdot}_{WB}, \mathrm{mdot}_{WC}, \mathrm{mdot}_{WD}, \mathrm{mdot}_{WE}) \cdot \mathrm{umdot}_{WE} \right) \right]^2 \right]^{\frac{1}{2}}$$

$$\mathrm{umdot}_{all} = 6.781 \times 10^{-4} \frac{kg}{s} \qquad \frac{\mathrm{umdot}_{all}}{\mathrm{mdot}_{Wall}} \cdot 100 = 0.045$$

$$\mathrm{umdot}_{WBD} := \left[ \left[ \frac{d}{d\mathrm{mdot}_{WB}} \left( \mathrm{mdot}_{BD}(\mathrm{mdot}_{WB}, \mathrm{mdot}_{WD}) \cdot \mathrm{umdot}_{WB} \right) \right]^2 + \left[ \left[ \frac{d}{d\mathrm{mdot}_{WD}} \left( \mathrm{mdot}_{BD}(\mathrm{mdot}_{WB}, \mathrm{mdot}_{WD}) \cdot \mathrm{umdot}_{WD} \right) \right] \right]^2 \right]^{\frac{1}{2}}$$

$$\mathrm{umdot}_{WBD} = 4.489 \times 10^{-4} \frac{kg}{s} \qquad uT_{RTD} := .15K \qquad uT := 0.1 \cdot K \qquad uP_R := .258kPa$$

$$\frac{\mathrm{umdot}_{WBD}}{\mathrm{mdot}_{WBD}} \cdot 100 = 0.071$$

$$\mathrm{mdot}_R := \mathrm{data}_{1,15} \cdot \frac{kg}{s} \qquad \mathrm{umdot}_R := \frac{0.1}{100} \cdot \mathrm{mdot}_R = 7.375 \times 10^{-5} \frac{kg}{s}$$

$$Cp_1 := \mathrm{data}_{1,11} \frac{kJ}{kg \cdot K}$$

$$Tin := \mathrm{data}_{1,8} K \qquad T3 := \mathrm{data}_{3,9} \cdot K \qquad TR := \mathrm{data}_{1,13} \cdot K$$

$$\mathrm{LMTD3}_1(Tin, TRin, T3, TR3) := \frac{(T3 - TR3) - (Tin - TRin)}{\ln\left[\frac{(T3 - TR3)}{(Tin - TRin)}\right]} \qquad \mathrm{LMTD3} := \mathrm{LMTD3}_1(Tin, TR, T3, TR) = 12.96\,K$$

$$\mathrm{uLMTD3}_1(Tin, TRin, T4, TR3) := \left[ \left( \frac{d}{dTin} \mathrm{LMTD3}_1(Tin, TRin, T4, TR3) \cdot uT \right)^2 + \left( \frac{d}{dTRin} \mathrm{LMTD3}_1(Tin, TRin, T4, TR3) \cdot uT \right)^2 \ldots \right.$$
$$\left. + \left( \frac{d}{dT4} \mathrm{LMTD3}_1(Tin, TRin, T4, TR3) \cdot uT \right)^2 + \left( \frac{d}{dTR3} \mathrm{LMTD3}_1(Tin, TRin, T4, TR3) \cdot uT \right)^2 \right]^{\frac{1}{2}}$$

$$uLMTD3 := uLMTD3_1(Tin, TR, T3, TR) = 0.10045\,K \qquad \frac{uLMTD3}{LMTD3} = 0.775\cdot\%$$

$$q(mdot, Cp, Tin, Tout) := mdot\cdot Cp\cdot(Tin - Tout) \qquad q\left(mdot_{Wall}, Cp_1, Tin, T3\right) = 1.477 \times 10^4\,W$$

$$q3 := q\left(mdot_{Wall}, Cp_1, Tin, T3\right) = 14.769\cdot kW$$

$$uq(mdot, Cp, Tin, Tout) := \left[\left(\frac{d}{dmdot} q(mdot, Cp, Tin, Tout)\cdot umdot_{all}\right)^2 + \left(\frac{d}{dTin} q(mdot, Cp, Tin, Tout)\cdot uT\right)^2 \ldots + \left(\frac{d}{dTout} q(mdot, Cp, Tin, Tout)\cdot uT\right)^2\right]^{\frac{1}{2}}$$

$$uq3 := uq\left(mdot_{Wall}, Cp_1, Tin, T3\right) = 0.895\cdot kW \qquad \frac{uq3}{q3} = 6.06\cdot\%$$

$$U(q, A, LMTD) := \frac{q}{LMTD\cdot A}$$

$$U3 := U(q3, A3, LMTD3) = 6.347\cdot\frac{kW}{m^2 K}$$

$$uU(q, A, LMTD) := \left[\left(\frac{d}{dq} U(q, A, LMTD)\cdot uq3\right)^2 + \left(\frac{d}{dLMTD} U(q, A, LMTD)\cdot uLMTD3\right)^2\right]^{\frac{1}{2}}$$

$$uU3 := uU(q3, A3, LMTD3) = 0.388\cdot\frac{kW}{m^2 K} \qquad \frac{uU3}{U3} = 6.109\cdot\%$$

$$Tout(TWin, TRin, U, A, mdot, Cp, TRout) := (TWin - TRin)\cdot e^{\left(\frac{-U\cdot A}{mdot\cdot Cp}\right)} + TRout$$

$$T1 := Tout\left(Tin, TR, U3, area, mdot_{Wall}, Cp_1, TR\right) = 18.207\,K$$

$$uT1_1(TWin, TRin, U, A, mdot, Cp, TRout) := \left[\left(\frac{d}{dTWin} Tout(TWin, TRin, U, A, mdot, Cp, TRout)\cdot uT\right)^2 \ldots + \left(\frac{d}{dTRin} Tout(TWin, TRin, U, A, mdot, Cp, TRout)\cdot uT\right)^2 \ldots + \left(\frac{d}{dU} Tout(TWin, TRin, U, A, mdot, Cp, TRout)\cdot uU3\right)^2 \ldots + \left(\frac{d}{dmdot} Tout(TWin, TRin, U, A, mdot, Cp, TRout)\cdot umdot_{all}\right)^2 \ldots + \left(\frac{d}{dTRout} Tout(TWin, TRin, U, A, mdot, Cp, TRout)\cdot uT\right)^2\right]^{\frac{1}{2}}$$

$$uT1 := uT1_1\left(Tin, TR, U3, area, mdot_{Wall}, Cp_1, TR\right) = 0.174\,K \qquad \frac{uT1}{T1} = 0.953\cdot\%$$

$$T2 := Tout\left(T1, TR, U3, area, mdot_{Wall}, Cp_1, TR\right) = 17.43\,K$$

$$i_{fg} := data_{1,14} \cdot \frac{kJ}{kg} \qquad x_i := data_{1,16} = 9.426 \times 10^{-3}$$

$$x_o(mdot_W, Cp, Tin, Tout, mdot_R, i_{fg}, x_i) := \frac{mdot_W \cdot Cp \cdot (Tin - Tout)}{mdot_R \cdot i_{fg}} + x_i$$

$$x_1 := x_o(mdot_{Wall}, Cp_1, Tin, T1, mdot_R, i_{fg}, x_i) = 0.37277$$

$$Cp_2 := Cp_1$$

$$x_{2s} := x_o\left(\frac{mdot_{WBD}}{2}, Cp_2, T1, T2, mdot_R, i_{fg}, x_1\right) = 0.445$$

$$x_{2a} := x_o(mdot_{WBD}, Cp_2, T1, T2, mdot_R, i_{fg}, x_1) = 0.516$$

$$dhdP := .0002 \cdot \frac{kJ}{kg \cdot kPa}$$

$$dhdT := 1.35 \frac{kJ}{kg \cdot K}$$

$$uh_{PBin} := \left[(dhdP \cdot uP_R)^2 + (dhdT \cdot uT_{RTD})^2\right]^{\frac{1}{2}} = 0.203 \cdot \frac{kJ}{kg}$$

$$q_{PB1}(mdot, Cp, Tin, Tout) := mdot \cdot Cp \cdot (Tin - Tout)$$

$$mdot_{WPB} := data_{1,17} \cdot \frac{kg}{s} \qquad CpPB := data_{1,18} \cdot \frac{kJ}{kg \cdot K} \qquad Tin_{PB} := data_{1,19} \cdot K \qquad Tout_{PB} := data_{1,20} \cdot K \qquad h_{PBin} := data_{1,21} \cdot \frac{kJ}{kg}$$

$$umdot_{WPB} := umdot \cdot mdot_{WPB}$$

$$q_{PB} := q_{PB1}(mdot_{WPB}, CpPB, Tin_{PB}, Tout_{PB}) = 598.439\,W$$

$$uq_{PB1}(mdot, Cp, Tin, Tout) := \left[\left(\frac{d}{dmdot} q_{PB1}(mdot, Cp, Tin, Tout) \cdot umdot_{WPB}\right)^2 + \left(\frac{d}{dTin} q_{PB1}(mdot, Cp, Tin, Tout) \cdot uT_{RTD}\right)^2 \ldots \right.$$
$$\left. + \left(\frac{d}{dTout} q_{PB1}(mdot, Cp, Tin, Tout) \cdot uT_{RTD}\right)^2 + \left(\frac{d}{dCp} q_{PB1}(mdot, Cp, Tin, Tout) \cdot uCp_W\right)^2\right]^{\frac{1}{2}}$$

$$uq_{PB} := uq_{PB1}(mdot_{WPB}, CpPB, Tin_{PB}, Tout_{PB}) \qquad uq_{PB} = 821.947\,W \qquad \frac{uq_{PB}}{q_{PB}} \cdot 100 = 137.348$$

$$hPB_{out1}(q_{PB}, mdot_R, hin) := \frac{q_{PB}}{mdot_R} + hin$$

$$hPB_{out} := hPB_{out1}(q_{PB}, mdot_R, h_{PBin}) = 206.813 \cdot \frac{kJ}{kg}$$

$$uhPB_{out1}(q_{PB}, mdot_R, hin) := \left[ \left( \frac{d}{dq_{PB}} hPB_{out1}(q_{PB}, mdot_R, hin) \cdot uq_{PB} \right)^2 + \left( \frac{d}{dmdot_R} hPB_{out1}(q_{PB}, mdot_R, hin) \cdot umdot_R \right)^2 \dots \right.$$
$$\left. + \left( \frac{d}{dhin} hPB_{out1}(q_{PB}, mdot_R, hin) \cdot uh_{PBin} \right)^2 \right]^{\frac{1}{2}}$$

$$uhPB_{out} := uhPB_{out1}(q_{PB}, mdot_R, h_{PBin}) = 11.147 \cdot \frac{kJ}{kg} \qquad \frac{uhPB_{out}}{hPB_{out}} \cdot 100 = 5.39$$

$$dxdh_{TSi} := .00512 \cdot \frac{kg}{kJ}$$

$$dxdp_{TSi} := -.0004834 \cdot \frac{1}{kPa}$$

$$ux_{in} := \left[ \left( dxdh_{TSi} \cdot uhPB_{out} \right)^2 + \left( dxdp_{TSi} \cdot uP_R \right)^2 \right]^{\frac{1}{2}} = 0.057$$

$$qprime_{D1}(mdot, Cp, Tin, Tout, A) := \frac{mdot \cdot Cp \cdot (Tin - Tout)}{A}$$

$$qprime_D := qprime_{D1}(mdot_{WD}, Cp_2, T1, T2, area)$$

$$qprime_D = 17.615 \cdot \frac{kW}{m^2}$$

$$uqprime_{D1}(mdot, Cp, Tin, Tout, A) := \left[ \left( \frac{d}{dmdot} qprime_{D1}(mdot, Cp, Tin, Tout, A) \cdot umdot_{WD} \right)^2 + \left( \frac{d}{dTin} qprime_{D1}(mdot, Cp, Tin, Tout, A) \cdot uT \right)^2 \dots \right.$$
$$\left. + \left( \frac{d}{dTout} qprime_{D1}(mdot, Cp, Tin, Tout, A) \cdot uT \right)^2 + \left( \frac{d}{dCp} qprime_{D1}(mdot, Cp, Tin, Tout, A) \cdot uCp_W \right)^2 \right]^{\frac{1}{2}}$$

$$uqprime_D := uqprime_{D1}(mdot_{WD}, Cp_2, T1, T2, area) = 3.206 \cdot \frac{kW}{m^2} \qquad \frac{uqprime_D}{qprime_D} = 18.202 \cdot \%$$

$$ux_1 := \left[\left[\frac{d}{dmdot_{Wall}}\left[\left(x_o\left(mdot_{Wall}, Cp_1, Tin, T1, mdot_R, i_{fg}, x_i\right)\right)umdot_{all}\right]\right]^2 + \left[\frac{d}{dTin}\left[\left(x_o\left(mdot_{Wall}, Cp_1, Tin, T1, mdot_R, i_{fg}, x_i\right)\right)uT\right]\right]^2 \ldots \right.$$
$$\left. + \left[\frac{d}{dT1}\left[\left(x_o\left(mdot_{Wall}, Cp_1, Tin, T1, mdot_R, i_{fg}, x_i\right)\right)uT\right]\right]^2 + \left[\frac{d}{dmdot_R}\left[\left(x_o\left(mdot_{Wall}, Cp_1, Tin, T1, mdot_R, i_{fg}, x_i\right)\right)\cdot umdot_R\right]\right]^2 \ldots \right.$$
$$\left. + \left[\frac{d}{dx_i}\left[\left(x_o\left(mdot_{Wall}, Cp_1, Tin, T1, mdot_R, i_{fg}, x_i\right)\right)\cdot ux_{in}\right]\right]^2 + \left[\frac{d}{dCp_1}\left[\left(x_o\left(mdot_{Wall}, Cp_1, Tin, T1, mdot_R, i_{fg}, x_i\right)\right)\cdot uCp_W\right]\right]^2 \right]^{\frac{1}{2}}$$

$ux_1 = 8.448 \cdot \%$ $\quad \frac{ux_1}{x_1} = 22.662\,\%$

$$ux_{2s} := \left[\left[\frac{d}{dmdot_{Wall}}\left[\left(x_o\left(\frac{mdot_{WBD}}{2}, Cp_2, T1, T2, mdot_R, i_{fg}, x_1\right)\right)umdot_{WBD}\right]\right]^2 + \left[\frac{d}{dT1}\left[\left(x_o\left(\frac{mdot_{WBD}}{2}, Cp_2, T1, T2, mdot_R, i_{fg}, x_1\right)\right)uT\right]\right]^2 \ldots \right.$$
$$\left. + \left[\frac{d}{dT2}\left[\left(x_o\left(\frac{mdot_{WBD}}{2}, Cp_1, T1, T2, mdot_R, i_{fg}, x_1\right)\right)uT\right]\right]^2 + \left[\frac{d}{dmdot_R}\left[\left(x_o\left(\frac{mdot_{WBD}}{2}, Cp_1, T1, T2, mdot_R, i_{fg}, x_1\right)\right)\cdot umdot_R\right]\right]^2 \ldots \right.$$
$$\left. + \left[\frac{d}{dx_i}\left[\left(x_o\left(\frac{mdot_{WBD}}{2}, Cp_1, T1, T2, mdot_R, i_{fg}, x_1\right)\right)\cdot ux_1\right]\right]^2 + \left[\frac{d}{dCp_1}\left[\left(x_o\left(\frac{mdot_{WBD}}{2}, Cp_1, T1, T2, mdot_R, i_{fg}, x_1\right)\right)\cdot uCp_W\right]\right]^2 \right]^{\frac{1}{2}}$$

$ux_{2s} = 1.307 \cdot \%$ $\quad \frac{ux_{2s}}{x_{2s}} = 2.941\,\%$

$$ux_{2a} := \left[\left[\frac{d}{dmdot_{Wall}}\left[\left(x_o\left(mdot_{WBD}, Cp_2, T1, T2, mdot_R, i_{fg}, x_1\right)\right)umdot_{WBD}\right]\right]^2 + \left[\frac{d}{dT1}\left[\left(x_o\left(mdot_{WBD}, Cp_2, T1, T2, mdot_R, i_{fg}, x_1\right)\right)uT\right]\right]^2 \ldots \right.$$
$$\left. + \left[\frac{d}{dT2}\left[\left(x_o\left(mdot_{WBD}, Cp_1, T1, T2, mdot_R, i_{fg}, x_1\right)\right)uT\right]\right]^2 + \left[\frac{d}{dmdot_R}\left[\left(x_o\left(mdot_{WBD}, Cp_1, T1, T2, mdot_R, i_{fg}, x_1\right)\right)\cdot umdot_R\right]\right]^2 \ldots \right.$$
$$\left. + \left[\frac{d}{dx_i}\left[\left(x_o\left(mdot_{WBD}, Cp_1, T1, T2, mdot_R, i_{fg}, x_1\right)\right)\cdot ux_1\right]\right]^2 + \left[\frac{d}{dCp_1}\left[\left(x_o\left(mdot_{WBD}, Cp_1, T1, T2, mdot_R, i_{fg}, x_1\right)\right)\cdot uCp_W\right]\right]^2 \right]^{\frac{1}{2}}$$

$ux_{2a} = 2.615 \cdot \%$ $\quad \frac{ux_{2a}}{x_{2a}} = 5.064\,\%$

Calculations

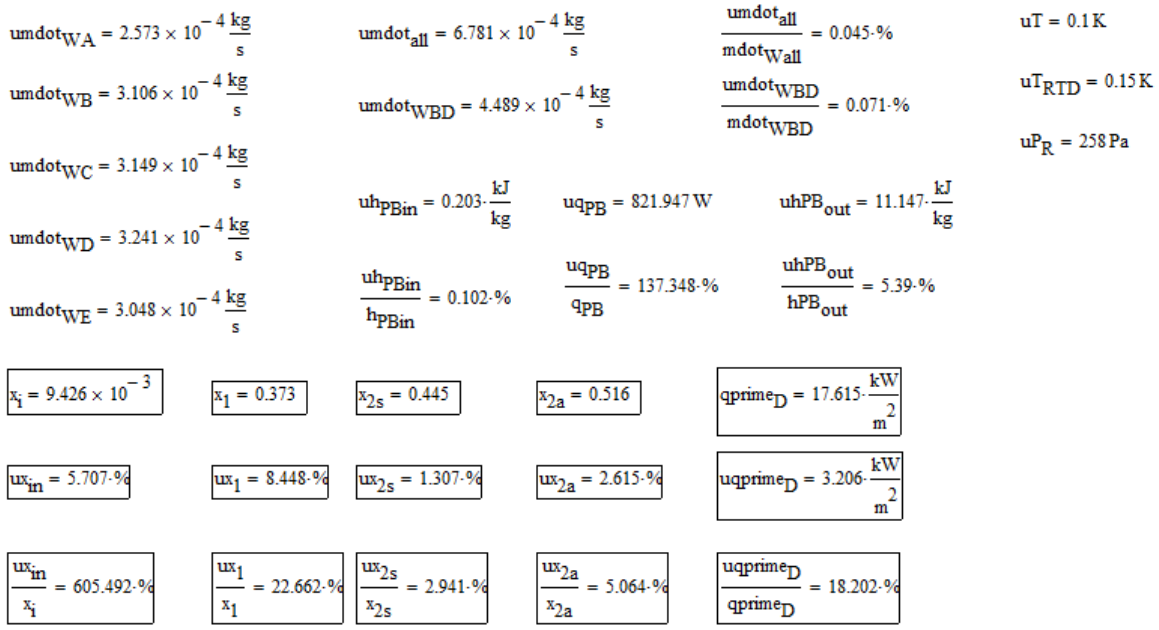


Figure F.1: Sample Mathcad uncertainty analysis file for the smooth tube bundle.

Figure F.2 shows screenshots of an example Mathcad uncertainty analysis file for the smooth tube bundle.

base := "E:\Jason Backup - Masters\Masters Backup\Data Files\Compiled Files\Enhanced Tube\High Speed Video\"

file := "35 18 0.20 19.5 0.37 03-05-13 16 28 24.xlsm"

filename := concat(base, file)

kJ := 1000·J

data := READEXCEL(filename, "Summary for Uncertainty Analys!")

area := π·0.75in·1m = 0.05985 $m^2$

Calculations

data =

| | 0 | 1 | 2 |
|---|---|---|---|
| 0 | "Flow Rate Water A (kg/s)" | "Flow Rate Water B (kg/s)" | "Flow Rate Water C (kg/s)" |
| 1 | 0.275 | 0.204 | 0.312 |
| 2 | 0.275 | 0.204 | 0.312 |
| 3 | 0.275 | 0.204 | 0.312 |
| 4 | 0.275 | 0.204 | ... |

umdot := .1%

$mdot_{WA} := data_{1,0} \cdot \frac{kg}{s} = 0.275 \frac{kg}{s}$

$umdot_{WA} := umdot \cdot mdot_{WA} = 2.754 \times 10^{-4} \frac{kg}{s}$

$mdot_{WB} := data_{1,1} \cdot \frac{kg}{s} = 0.204 \frac{kg}{s}$

$umdot_{WB} := umdot \cdot mdot_{WB} = 2.036 \times 10^{-4} \frac{kg}{s}$

$mdot_{WC} := data_{1,2} \cdot \frac{kg}{s} = 0.312 \frac{kg}{s}$

$umdot_{WC} := umdot \cdot mdot_{WC} = 3.117 \times 10^{-4} \frac{kg}{s}$

$mdot_{WD} := data_{1,3} \cdot \frac{kg}{s} = 0.331 \frac{kg}{s}$

$umdot_{WD} := umdot \cdot mdot_{WD} = 3.306 \times 10^{-4} \frac{kg}{s}$

$mdot_{WE} := data_{1,4} \cdot \frac{kg}{s} = 0.256 \frac{kg}{s}$

$umdot_{WE} := umdot \cdot mdot_{WE} = 2.565 \times 10^{-4} \frac{kg}{s}$

$$mdot_{all}(AFR, BFR, CFR, DFR, EFR) := AFR + BFR + CFR + DFR + EFR \qquad uCp_W := .00019 \cdot \frac{kJ}{kg \cdot K}$$

$$mdot_{BD}(BFR, DFR) := BFR + DFR \qquad umdot_{WA} = 2.754 \times 10^{-4} \frac{kg}{s}$$

$$mdot_{Wall} := mdot_{all}(mdot_{WA}, mdot_{WB}, mdot_{WC}, mdot_{WD}, mdot_{WE}) = 1.378 \frac{kg}{s}$$

$$mdot_{WBD} := mdot_{BD}(mdot_{WB}, mdot_{WD}) = 0.534 \frac{kg}{s}$$

$$umdot_{all} := \left[ \left[ \frac{d}{dmdot_{WA}} \left( mdot_{all}(mdot_{WA}, mdot_{WB}, mdot_{WC}, mdot_{WD}, mdot_{WE}) \cdot umdot_{WA} \right) \right]^2 \ldots \right.$$
$$+ \left[ \frac{d}{dmdot_{WB}} \left( mdot_{all}(mdot_{WA}, mdot_{WB}, mdot_{WC}, mdot_{WD}, mdot_{WE}) \cdot umdot_{WB} \right) \right]^2 \ldots$$
$$+ \left[ \frac{d}{dmdot_{WC}} \left( mdot_{all}(mdot_{WA}, mdot_{WB}, mdot_{WC}, mdot_{WD}, mdot_{WE}) \cdot umdot_{WC} \right) \right]^2 \ldots$$
$$+ \left[ \frac{d}{dmdot_{WD}} \left( mdot_{all}(mdot_{WA}, mdot_{WB}, mdot_{WC}, mdot_{WD}, mdot_{WE}) \cdot umdot_{WD} \right) \right]^2 \ldots$$
$$\left. + \left[ \frac{d}{dmdot_{WE}} \left( mdot_{all}(mdot_{WA}, mdot_{WB}, mdot_{WC}, mdot_{WD}, mdot_{WE}) \cdot umdot_{WE} \right) \right]^2 \right]^{\frac{1}{2}}$$

$$umdot_{all} = 6.241 \times 10^{-4} \frac{kg}{s}$$

$$\frac{umdot_{all}}{mdot_{Wall}} \cdot 100 = 0.045$$

$$umdot_{WBD} := \left[ \left[ \frac{d}{dmdot_{WB}} \left( mdot_{BD}(mdot_{WB}, mdot_{WD}) \cdot umdot_{WB} \right) \right]^2 + \left[ \left[ \frac{d}{dmdot_{WD}} \left( mdot_{BD}(mdot_{WB}, mdot_{WD}) \cdot umdot_{WD} \right) \right] \right]^2 \right]^{\frac{1}{2}}$$

$$umdot_{WBD} = 3.882 \times 10^{-4} \frac{kg}{s} \qquad \frac{umdot_{WBD}}{mdot_{WBD}} \cdot 100 = 0.073$$

$$mdot_R := data_{1,16} \cdot \frac{kg}{s}$$

$$Cp_1 := data_{1,12} \frac{kJ}{kg \cdot K}$$

$$Tin := data_{1,8} K$$

$$T1 := data_{1,9} \cdot K$$

$$i_{fg} := data_{1,15} \cdot \frac{kJ}{kg}$$

$$x_i := data_{1,17} \qquad \boxed{x_i = 0.204}$$

$$x_o(mdot_W, Cp, Tin, Tout, mdot_R, i_{fg}, x_i) := \frac{mdot_W \cdot Cp \cdot (Tin - Tout)}{mdot_R \cdot i_{fg}} + x_i$$

$$x_1 := x_o(mdot_{Wall}, Cp_1, Tin, T1, mdot_R, i_{fg}, x_i) = 0.35969$$

$$Cp_2 := data_{2,12} \cdot \frac{kJ}{kg \cdot K} \qquad Cp_2 = 4.2 \times 10^3 \frac{m^2}{K \cdot s^2}$$

$$T2 := data_{2,9} \cdot K \qquad T2 = 6.202\,K$$

$$x_{2s} := x_o\left(\frac{mdot_{WBD}}{2}, Cp_2, T1, T2, mdot_R, i_{fg}, x_1\right) = 0.373$$

$$x_{2a} := x_o(mdot_{WBD}, Cp_2, T1, T2, mdot_R, i_{fg}, x_1) = 0.386$$

$$uT := 0.1 \cdot K$$

$$umdot_R := \frac{0.1}{100} \cdot mdot_R = 3.319 \times 10^{-4} \frac{kg}{s}$$

$$uP_R := .258kPa$$

$$uT_{RTD} := .15K$$

$$dhdP := .0002 \cdot \frac{kJ}{kg \cdot kPa} \qquad dhdT := 1.35 \frac{kJ}{kg \cdot K}$$

$$uh_{PBin} := \left[(dhdP \cdot uP_R)^2 + (dhdT \cdot uT_{RTD})^2\right]^{\frac{1}{2}} = 0.203 \cdot \frac{kJ}{kg} \qquad q_{PB1}(mdot, Cp, Tin, Tout) := mdot \cdot Cp \cdot (Tin - Tout)$$

$$mdot_{WPB} := data_{1,21} \cdot \frac{kg}{s} \qquad CpPB := data_{1,22} \cdot \frac{kJ}{kg \cdot K} \qquad Tin_{PB} := data_{1,23} \cdot K \qquad Tout_{PB} := data_{1,24} \cdot K \qquad h_{PBin} := data_{1,25} \cdot \frac{kJ}{kg}$$

$$Tin_{PB} = 9.657\,K \qquad Tout_{PB} = 7.179\,K$$

$$umdot_{WPB} := umdot \cdot mdot_{WPB}$$

$$q_{PB} := q_{PB1}(mdot_{WPB}, CpPB, Tin_{PB}, Tout_{PB}) = 2.14 \times 10^4\,W \qquad CpPB = 4.197 \frac{1}{K} \cdot \frac{kJ}{kg} \qquad mdot_{WPB} = 2.059 \frac{kg}{s}$$

$$uq_{PB1}(mdot, Cp, Tin, Tout) := \left[\left(\frac{d}{dmdot} q_{PB1}(mdot, Cp, Tin, Tout) \cdot umdot_{WPB}\right)^2 + \left(\frac{d}{dTin} q_{PB1}(mdot, Cp, Tin, Tout) \cdot uT_{RTD}\right)^2 \ldots + \left(\frac{d}{dTout} q_{PB1}(mdot, Cp, Tin, Tout) \cdot uT_{RTD}\right)^2 + \left(\frac{d}{dCp} q_{PB1}(mdot, Cp, Tin, Tout) \cdot uCp_W\right)^2\right]^{\frac{1}{2}}$$

$$uq_{PB} := uq_{PB1}(mdot_{WPB}, CpPB, Tin_{PB}, Tout_{PB}) \qquad uq_{PB} = 1.833 \times 10^3\,W \qquad \frac{uq_{PB}}{q_{PB}} \cdot 100 = 8.563$$

$$hPB_{out1}(q_{PB}, mdot_R, hin) := \frac{q_{PB}}{mdot_R} + hin \qquad hPB_{out} := hPB_{out1}(q_{PB}, mdot_R, h_{PBin}) = 245.698 \cdot \frac{kJ}{kg}$$

$$uhPB_{out1}(q_{PB}, mdot_R, hin) := \left[ \left( \frac{d}{dq_{PB}} hPB_{out1}(q_{PB}, mdot_R, hin) \cdot uq_{PB} \right)^2 + \left( \frac{d}{dmdot_R} hPB_{out1}(q_{PB}, mdot_R, hin) \cdot umdot_R \right)^2 \ldots \right.$$
$$\left. + \left( \frac{d}{dhin} hPB_{out1}(q_{PB}, mdot_R, hin) \cdot uh_{PBin} \right)^2 \right]^{\frac{1}{2}}$$

$$uhPB_{out} := uhPB_{out1}(q_{PB}, mdot_R, h_{PBin}) = 5.526 \cdot \frac{kJ}{kg} \qquad \frac{uhPB_{out}}{hPB_{out}} \cdot 100 = 2.249$$

$$dxdh_{TSi} := .00512 \cdot \frac{kg}{kJ}$$

$$dxdp_{TSi} := -.0004834 \cdot \frac{1}{kPa}$$

$$ux_{in} := \left[ \left( dxdh_{TSi} \cdot uhPB_{out} \right)^2 + \left( dxdp_{TSi} \cdot uP_R \right)^2 \right]^{\frac{1}{2}} = 0.028$$

$$qprime_{D1}(mdot, Cp, Tin, Tout, A) := \frac{mdot \cdot Cp \cdot (Tin - Tout)}{A}$$

$$qprime_D := qprime_{D1}(mdot_{WD}, Cp_2, T1, T2, area) \qquad qprime_D = 17.455 \cdot \frac{kW}{m^2}$$

$$uqprime_{D1}(mdot, Cp, Tin, Tout, A) := \left[ \left( \frac{d}{dmdot} qprime_{D1}(mdot, Cp, Tin, Tout, A) \cdot umdot_{WD} \right)^2 + \left( \frac{d}{dTin} qprime_{D1}(mdot, Cp, Tin, Tout, A) \cdot uT \right)^2 \ldots \right.$$
$$\left. + \left( \frac{d}{dTout} qprime_{D1}(mdot, Cp, Tin, Tout, A) \cdot uT \right)^2 + \left( \frac{d}{dCp} qprime_{D1}(mdot, Cp, Tin, Tout, A) \cdot uCp_W \right)^2 \right]^{\frac{1}{2}}$$

$$uqprime_D := uqprime_{D1}(mdot_{WD}, Cp_2, T1, T2, area) = 3.281 \cdot \frac{kW}{m^2} \qquad \frac{uqprime_D}{qprime_D} \cdot 100 = 18.797$$

$$ux_1 := \left[ \left[ \frac{d}{dmdot_{Wall}} \left[ \left( x_o(mdot_{Wall}, Cp_1, Tin, T1, mdot_R, i_{fg}, x_i) \right) umdot_{all} \right] \right]^2 + \left[ \frac{d}{dTin} \left[ \left( x_o(mdot_{Wall}, Cp_1, Tin, T1, mdot_R, i_{fg}, x_i) \right) uT \right] \right]^2 \ldots \right.$$
$$+ \left[ \frac{d}{dT1} \left[ \left( x_o(mdot_{Wall}, Cp_1, Tin, T1, mdot_R, i_{fg}, x_i) \right) uT \right] \right]^2 + \left[ \frac{d}{dmdot_R} \left[ \left( x_o(mdot_{Wall}, Cp_1, Tin, T1, mdot_R, i_{fg}, x_i) \right) \cdot umdot_R \right] \right]^2 \ldots$$
$$\left. + \left[ \frac{d}{dx_i} \left[ \left( x_o(mdot_{Wall}, Cp_1, Tin, T1, mdot_R, i_{fg}, x_i) \right) \cdot ux_{in} \right] \right]^2 + \left[ \frac{d}{dCp_1} \left[ \left( x_o(mdot_{Wall}, Cp_1, Tin, T1, mdot_R, i_{fg}, x_i) \right) \cdot uCp_W \right] \right]^2 \right]^{\frac{1}{2}}$$

$$ux_1 = 0.031 \qquad \frac{ux_1}{x_1} \cdot 100 = 8.613$$


Figure F.2: Sample Mathcad uncertainty analysis file for the enhanced tube bundle.